Improving Computational Models of Solid Oxide Cells for Industrial Performance Optimization

Zur Erlangung des akademischen Grades eines
DOKTORS DER INGENIEURWISSENSCHAFTEN

von der KIT-Fakultät für Chemieingenieurwesen und Verfahrenstechnik des Karlsruher Instituts für Technologie (KIT)
genehmigte

DISSERTATION

von
M. Sc. Oscar Furst
aus Haguenau, Frankreich

Tag der mündlichen Prüfung: 06.05.2026

Erstgutachter: Prof. Dr. Olaf Deutschmann
Zweitgutachter: Prof. Dr. Wolfgang G. Bessler

Preface

This dissertation comprises three peer-reviewed scientific journal articles presenting efforts to improve the capabilities of computational models used to simulate the performance of solid oxide cell systems and the subsequent application of the developed tools in order to contribute to the development of related energy conversion technologies. The research was conducted between June 2021 and July 2025 at the Karlsruhe Institute of Technology within the Institute for Chemical Technology and Polymer Chemistry under the supervision of Prof. Dr. Olaf Deutschmann.

The introductory chapter of this dissertation discusses the importance of hydrogen in the global energy transition, which provides context on the relevance of the solid oxide cell technology which is the main focus of this work. Existing research on modeling solid oxide cell systems is summarized, gaps in the literature are identified and corresponding research objectives are formulated.

The subsequent chapter aims to provide some of the fundamental knowledge required to understand the work presented within this dissertation as well as a more thorough presentation of the methodologies employed in the published journal articles. Fundamental operating principles of solid oxide cells are introduced and followed by a discussion of the models used in this work.

The three journal articles published as a result of this research build the central chapters of this dissertation. They are briefly introduced in the main body of this document and their full contents can be found in the appendix. The publications are presented in the following order:

- **Chapter 3:** "Development and calibration of a fast flow model for solid oxide cell stack internal manifolds" published in the *Journal of Power Sources*.
- **Chapter 4:** "A Versatile Multi-Scale Framework for Transient Simulations of Solid Oxide Cells and Stack Modules Integrated in DETCHEM" published in the *Journal of The Electrochemical Society*.
- **Chapter 5:** "Modeling, optimization and comparative assessment of power-to-methane and carbon capture technologies for renewable fuel production" published in *Applied Energy*.

The dissertation is concluded by a summary of the contributions offered by this project to the body of research on solid oxide cell modeling as well as perspectives on future avenues of research.

Abstract

The current shift towards renewable energy systems relies heavily on the efficient production and utilization of hydrogen. Solid Oxide Cells (SOCs) have emerged as a pivotal technology in this domain, offering high efficiency in both power generation (SOFC) and electrolysis (SOEC) modes.

The transition of the SOC technology from laboratory research to industrial deployment also shifts the focus of SOC modeling methods from mechanistic investigations towards the engineering tasks of system development and process optimization. This dissertation aims at accelerating the deployment of the SOC technology by providing new modeling tools intended to aid the performance optimization of SOC modules and the systems surrounding them. By improving upon existing modeling efforts, more accurate simulations of the physical processes within SOC stacks are enabled without compromising on the computation speed required for engineering tasks.

The research identifies a critical gap in existing modeling frameworks: the trade-off between computational speed and physical fidelity when simulating gas flow in stack manifolds. One of the most prominent issue in this subject area was found to be the lack of reliable data required to parametrize simplified modeling approaches. To resolve this, detailed three-dimensional computational fluid dynamics (CFD) simulations are performed on representative U-type internal manifold geometries using OpenFOAM. These simulations reveal that standard friction factors are inadequate to describe the pressure losses in SOC stack manifolds. Consequently, a set of improved closed-form expressions for pressure loss coefficients and Darcy friction factors are developed through analysis of the detailed CFD simulation results. These expressions are integrated into a network model of the flow, enabling the prediction of flow distribution with deviations of less than 5% compared to high-fidelity CFD, but at a fraction of the computational cost.

Utilizing the newly developed expressions for pressure losses throughout the stack and building upon previous multi-scale SOC modeling works, a comprehensive SOC stack model is developed. The model accounts for electrochemical kinetics, thermocatalytic chemistry, charge transport, as well as different mechanisms of mass and heat transport. In addition to the stack flow model, other improvements such as a conservative set of equations for mass transport in gas channels and an iterative scheme for the computation of the cell potential distribution in SOC stacks are introduced. Initially, the model is parametrized and validated through the comparison of button cell simulations and experimental button cell data. High accuracy across various temperatures and gas compositions is demonstrated. The model is subsequently employed to investigate the impact of the manifold on the flow distribution of an SOEC stack operated at elevated current density. Results reveal significant air channel inlet flow velocity variations of 11% around the average having negligible impact on the stack performance compared to a reference case with homogeneous influx.

Finally, the improved modeling framework is applied to a system-level optimization study of multiple power-to-methane (PtM) processes. This last study performs a comparison of PtM processes built from a combination of different electrolysis, methanation and carbon oxide supply technologies. A major focus of this study is to quantify the advantage reaped from integrating different carbon oxide supply technologies to the PtM process. Therefore, the biomass gasification, amine gas treatment and direct air capture processes are coupled to different SOEC stack architectures (electrolyte-supported and cathode-supported) as well as different methanation processes (fixed-bed and three-phase methanation reactors). The results demonstrate that integrating the carbon supply process into a

PtM plant provides a significant advantage for all combinations of technologies. The analysis further highlights a strategic trade-off where capital costs of electrolyzers may be significantly reduced by the synergistic interaction between exothermically operated SOECs and the strongly endothermic carbon capture processes.

Overall, this dissertation provides useful and novel tools for the simulations of SOCs which aid in bridging the gap between the detailed analysis of physical phenomena and the engineering of system-level applications. These tools, as well as the insights resulting from their application in dedicated case-studies, provide an improved foundation for the design and optimization of future energy conversion systems that utilize the SOC technology.

Kurzfassung

Der derzeitige Wandel hin zu erneuerbaren Energiesystemen hängt stark von der effizienten Erzeugung und Nutzung von Wasserstoff ab. Festoxidzellen (solid oxide cells, SOCs) haben sich als Schlüsseltechnologie in diesem Bereich etabliert und bieten hohe Effizienz sowohl in der Stromerzeugung (SOFC) als auch der Elektrolyse (SOEC).

Der Übergang der SOC-Technologie von der Laborforschung zur industriellen Anwendung verschiebt auch den Fokus der SOC-Modellierungsmethoden: weg von mechanistischen Untersuchungen hin zu ingenieurtechnischen Aufgaben der Systementwicklung und Prozessoptimierung. Diese Dissertation zielt darauf ab, den Einsatz der SOC-Technologie zu beschleunigen, indem neue Modellierungswerkzeuge bereitgestellt werden, welche die Leistungsoptimierung von SOC-Modulen und den sie umgebenden Systemen unterstützen. Durch die Verbesserung bestehender Modellierungsansätze werden genauere Simulationen der physikalischen Prozesse innerhalb von SOC-Stacks ermöglicht, ohne die für ingenieurtechnische Aufgaben erforderliche Rechengeschwindigkeit zu beeinträchtigen.

Diese Arbeit identifiziert eine kritische Lücke in bestehenden Modellierungsmethoden: den Zielkonflikt zwischen Rechengeschwindigkeit und physikalischer Genauigkeit bei der Simulation von Strömungen in Stack-Gasverteilern. Eines der größten Probleme in diesem Themenbereich ist der Mangel an zuverlässigen Daten zur Parametrierung vereinfachter Modellierungsansätze. Um dies zu beheben, werden detaillierte dreidimensionale numerische Strömungssimulationen (CFD) an repräsentativen U-Typ-Innenverteilergeometrien mit Hilfe von OpenFOAM durchgeführt. Diese Simulationen zeigen, dass herkömmliche Reibungszahlen unzureichend sind, um die Druckverluste in diesen Gasverteilern zu beschreiben. Folglich wird durch die Analyse der detaillierten CFD-Simulationsergebnisse ein Satz verbesserter geschlossener Ausdrücke für Druckverlustkoeffizienten und Rohrreibungszahlen entwickelt. Diese Ausdrücke werden in ein Netzwerkmodell der Strömung integriert, was die Vorhersage der Strömungsverteilung mit Abweichungen von weniger als 5% im Vergleich zu genauer CFD ermöglicht, jedoch zu einem Bruchteil der Rechenkosten.

Unter Verwendung der neu entwickelten Ausdrücke für Druckverluste im gesamten Stack und aufbauend auf früheren Arbeiten zur mehrskaligen SOC-Modellierung wird ein umfassendes SOC-Stack-Modell entwickelt. Das Modell berücksichtigt elektrochemische Kinetik, thermokatalytische Chemie, Ladungstransport sowie verschiedene Mechanismen des Stoff- und Wärmetransports. Zusätzlich zum Stack-Strömungsmodell werden weitere Verbesserungen eingeführt, wie ein konservativer Gleichungssatz für den Stofftransport in Gaskanälen und ein iteratives Schema zur Berechnung der Zellpotentialverteilung in SOC-Stacks. Zunächst wird das Modell durch den Vergleich von Knopfzellensimulationen mit experimentellen Knopfzellendaten parametriert und validiert, wobei eine hohe Genauigkeit über verschiedene Temperaturen und Gaszusammensetzungen hinweg nachgewiesen wird. Anschließend wird das Modell eingesetzt, um den Einfluss des Verteilers auf die Strömungsverteilung eines bei hoher Stromdichte betriebenen SOEC-Stacks zu untersuchen. Die Ergebnisse zeigen signifikante Variationen der Einlassströmungsgeschwindigkeit in den Luftkanälen von 11% um den Mittelwert, die jedoch im Vergleich zu einem Referenzfall mit homogenem Zustrom einen vernachlässigbaren Einfluss auf die Stack-Leistung haben.

Schließlich wird die verbesserte Modellierungsmethode auf eine Optimierungsstudie für mehrere Power-to-Methane (PtM)-Prozesse angewendet. Diese Studie vergleicht PtM-Prozesse, die aus einer Kombination verschiedener Elektrolyse-, Methanisierungs- und Kohlenstoffoxidbereitstellungstechnologien bestehen. Ein Hauptfokus dieser Studie liegt auf der Quantifizierung des Vorteils, der sich aus der Integration verschiedener Technologien zur Kohlenstoffoxidbereitstellung in den PtM-Prozess ergibt. Dazu werden Biomassevergasung, Amin-Gaswäsche und Direct Air Capture-Prozesse mit verschiedenen SOEC-Stack-Architekturen (elektrolytgestützt und kathodengestützt) sowie verschiedenen Methanisierungsprozessen (Festbett- und Dreiphasen-Methanisierungsreaktoren) gekoppelt. Die Ergebnisse zeigen, dass die Integration des Kohlenstoffbereitstellungsprozesses in einer PtM-Anlage für alle Technologiekombinationen einen signifikanten Vorteil bietet. Die Analyse hebt weitere strategische Kompromissmöglichkeiten hervor, bei denen die Investitionskosten von Elektrolyseuren durch die synergistische Wechselwirkung zwischen exotherm betriebenen SOECs und den stark endothermen Prozessen der Kohlenstoffabscheidung erheblich gesenkt werden können.

Insgesamt stellt diese Dissertation nützliche und neuartige Werkzeuge für die Simulation von SOCs bereit, die dazu beitragen, die Lücke zwischen der detaillierten Analyse physikalischer Phänomene und der technischen Entwicklung von Anwendungen auf Systemebene zu schließen. Diese Werkzeuge sowie die Erkenntnisse aus ihrer Anwendung in dedizierten Fallstudien bilden eine verbesserte Grundlage für die Auslegung und Optimierung zukünftiger Energieumwandlungssysteme, welche die SOC-Technologie nutzen.

Acknowledgments

First and foremost, I would like to express my sincere gratitude to Prof. Dr. Olaf Deutschmann for giving me the opportunity to pursue this academic project. I am grateful for the trust he placed in my ability to learn, contributing much to my growth over the past years. I am also thankful for his continuous support and guidance which have been an instrumental part of my research. In addition, his talent for bringing together such a skilled and friendly group of people is truly appreciated.

I owe a special thanks to my friend and colleague Dr. Lukas Wehrle who taught me much of what I know about electrochemistry and scientific writing. His mentorship was invaluable during the early stages of my work, and his insight has guided most of my research. Our close collaboration during the early stages of this project was instructive, productive and especially enjoyable.

I would like to thank Martin Spoo, Dr. Matthias Hettel, Ursula Schwald and Yvonne Dedececk for their continuous help in tackling the wide variety of tasks that accompany a research project. I have always enjoyed visiting them and appreciate that they have always made time for me.

I extend my appreciation to Dr. Julian Dailly and Daniel Schmider for their passionate commitment to multiple joint projects. Their hard work towards the orchestration and execution of collaborative research is truly inspiring.

It has been a privilege to work alongside my office mates Felix, Hendrick, Jakob, Johannes, Katya, Pallabi, Philipp and Rinu. Their presence made the office an enjoyable place and I appreciated the insights as much as the distractions. I am deeply appreciative of their willingness to listen and their ability to keep spirits high. My work was greatly enriched by all my colleagues of the Institute for Chemical Technology and Polymer Chemistry, whom I always enjoyed working with. To the daily lunch group, I am especially grateful for the humor and camaraderie that made my days so enjoyable.

My deepest gratitude belongs to my parents. Their unwavering belief in me and their unrelenting support have paved the way for every opportunity I have had. Their support of my curiosity has led me to this point. I am endlessly grateful to my paternal grandmother, who I believe has taught me the most important things I know. I am also grateful to my sister for being a constant inspiration. I thank the entirety of my family for their constant encouragement and for keeping me grounded throughout this long journey.

I would like to thank my dear friend Molly for being a steady presence in my life, a constant source of cheer and for providing me with much needed perspective.

Finally, I am deeply grateful to my dear partner Franziska for her patience, support and belief in me. Her continued encouragement was essential to the completion of this dissertation.

Contents

Nomenclature

Latin symbols

A_{cat}^{V}	Catalyst surface area per unit volume	m^{-1}
$A_{\text{el/io}}^{\text{V}}$	Interfacial area between electronic and ionic phases per unit volume	m^{-1}
B_{g}	Permeability coefficient of the dusty gas model	m^{2}
C	Concentration of species	$\text{mol}\,\text{m}^{-3}$
C_{DL}	Double-layer capacitance per unit surface area	$\text{F}\,\text{m}^{-2}$
c_p	Specific heat capacity	$\text{J}\,\text{kg}^{-1}\,\text{K}^{-1}$
d	Diameter	m
$D_{k,\text{Kn}}^{\text{eff}}$	Effective Knudsen diffusion coefficient	$\text{m}^{2}\,\text{s}^{-1}$
D_{kl}	Binary diffusion coefficient	$\text{m}^{2}\,\text{s}^{-1}$
D_{kl}^{eff}	Effective binary diffusion coefficient	$\text{m}^{2}\,\text{s}^{-1}$
E°	Reversible cell voltage at standard conditions	V
E_{cell}	Applied cell voltage	V
E_{rev}	Reversible cell voltage	V
E_{TNV}	Thermoneutral voltage	V
F	Faraday constant	$\text{C}\,\text{mol}^{-1}$
f_{D}	Darcy friction factor	-
F_{s}	Safety factor of the grid convergence index	-
h	Height or specific enthalpy	m or $\text{J}\,\text{kg}^{-1}$
h_{conv}	Heat transfer coefficient through forced convection	$\text{W}\,\text{m}^{-2}\,\text{K}^{-1}$
h_{free}	Heat transfer coefficient through free convection	$\text{W}\,\text{m}^{-2}\,\text{K}^{-1}$
I	Total current	A
i	Current density	$\text{A}\,\text{m}^{-2}$
i_0	Exchange current density	$\text{A}\,\text{m}^{-2}$ or $\text{A}\,\text{m}^{-1}$
i_{DL}^{V}	Volumetric charge transfer rate from double layer charging	$\text{A}\,\text{m}^{-3}$
i_{F}^{V}	Faradaic volumetric charge transfer rate	$\text{A}\,\text{m}^{-3}$

i_e^V	Total volumetric charge transfer rate	$\mathrm{A\,m^{-3}}$
J_m	Area-specific molar flux of species m	$\mathrm{mol\,m^{-2}\,s^{-1}}$
$k_{f,r}$	Forward reaction rate constant	Varies
L	Channel length	m
l_{char}	Characteristic length	m
n_{e}	Number of electrons transferred	-
n_{BS}^V	Number of particles per unit volume before sintering	$\mathrm{m^{-3}}$
$\dot{\omega}_m$	Molar production rate of species m through gas-phase reactions	$\mathrm{mol\,m^{-3}\,s^{-1}}$
$\mathbf{q}$	Heat flux vector field	$\mathrm{W\,m^{-2}}$
q_{conv}	Convective heat flux	$\mathrm{W\,m^{-2}}$
q_{rad}	Radiative heat flux	$\mathrm{W\,m^{-2}}$
$\dot{q}_{\mathrm{solid}}^V$	Total volumetric heat source term in the homogenized solid phase	$\mathrm{W\,m^{-3}}$
q_{surf}	Heat flux at the stack surface	$\mathrm{W\,m^{-2}}$
$\dot{q}_{\mathrm{act}}^V$	Volumetric heat source from activation losses	$\mathrm{W\,m^{-3}}$
$\dot{q}_{\mathrm{echem}}^V$	Volumetric reversible heat from charge transfer reactions	$\mathrm{W\,m^{-3}}$
$\dot{q}_{\mathrm{joule}}^V$	Volumetric heat source from Joule heating	$\mathrm{W\,m^{-3}}$
$\dot{q}_{\mathrm{schem}}^V$	Volumetric heat source from surface chemistry reaction enthalpy	$\mathrm{W\,m^{-3}}$
R	Ideal gas constant	$\mathrm{J\,mol^{-1}\,K^{-1}}$
$\mathbf{R}$	Set of all reactions	-
R_{cont}	Contact resistance	$\Omega\,\mathrm{m^2}$
$\mathbf{R}_{\mathrm{g}}$	Set of gas-phase reactions	-
R_{rad}	Thermal resistance through radiation	-
$\mathbf{R}_{\mathrm{s}}$	Set of surface reactions	-
$\mathbf{S}$	Set of all species	-
$\mathbf{S}_{\mathrm{g}}$	Set of gas-phase species	-
$\dot{s}_m$	Volumetric production rate of species m through thermocatalytic reactions	$\mathrm{mol\,m^{-3}\,s^{-1}}$
$\dot{s}_m^A$	Surface-specific production rate of species m through thermocatalytic reactions	$\mathrm{mol\,m^{-2}\,s^{-1}}$
$\mathbf{S}_{\mathrm{s}}$	Set of surface species	-

u	Average flow velocity	$\mathrm{m\,s^{-1}}$
$\mathbf{u}$	Velocity vector	$\mathrm{m\,s^{-1}}$
V	Volume	$\mathrm{m^3}$
W	Molecular mass of the gas mixture	$\mathrm{kg\,mol^{-1}}$
w	Channel width or weighting factor	m or -
Y_m	Mass fraction of species m	-
z	Spatial coordinate (MEA-normal direction)	m
$Z_{h,g}$	Average number of contacts between particle types h and g	-

Greek symbols

α_p	Volume fraction of phase p	-
$\alpha_{p,\mathrm{BS}}$	Volume fraction before sintering of phase p	-
β	Charge transfer coefficient	-
ΔG	Gibbs free energy change	$\mathrm{J\,mol^{-1}}$
ΔH	Enthalpy change	$\mathrm{J\,mol^{-1}}$
Δp	Pressure change	Pa
ΔS	Entropy change	$\mathrm{J\,K^{-1}}$
Δs_r	Molar reaction entropy	$\mathrm{J\,mol^{-1}\,K^{-1}}$
ϵ	Emissivity	-
ε	Porosity	-
η	Overpotential	V
η_{act}	Activation overpotential	V
η_{conc}	Concentration overpotential	V
γ_h	Percolation probability of phase h	-
Γ_{surf}	Surface site density of catalyst	$\mathrm{mol\,m^{-2}}$
κ_r	Temperature exponent of the reaction rate	-
λ	Thermal conductivity	$\mathrm{W\,m^{-1}\,K^{-1}}$
λ^V_{TPB}	TPB length per unit volume	$\mathrm{m^{-2}}$
μ	Dynamic viscosity	$\mathrm{Pa\,s}$

ν	Kinematic viscosity or stoichiometric coefficient	$\mathrm{m^2\,s^{-1}}$ or -
ϕ_{el}	Electrostatic potential of the electron conducting phase	V
ϕ_{io}	Electrostatic potential of the ion conducting phase	V
ρ	Density	$\mathrm{kg\,m^{-3}}$
σ_m	Conductivity of phase m	$\mathrm{S\,m^{-1}}$
σ_{SB}	Stefan-Boltzmann constant	$\mathrm{W\,m^{-2}\,K^{-4}}$
τ	Tortuosity	-
θ_m	Surface coverage of species m	-
ξ	Particle number ratio or lateral interaction factor	- or $\mathrm{J\,mol^{-1}}$
ζ	Pressure loss coefficient	-

Dimensionless numbers

Gz	Graetz number	-
Nu	Nusselt number	-
Pr	Prandtl number	-
Ra	Rayleigh number	-
Re	Reynolds number	-

Chemical species

CO_2	Carbon dioxide	-
CO	Carbon monoxide	-
H^+	Proton / Hydrogen ion	-
$LiBH_4$	Lithium borohydride	-
O^{2-}	Oxygen ion	-
OH^-	Hydroxyl ion	-

Abbreviations

ASR	Area-Specific Resistance
AWE	Alkaline Water Electrolysis
CFD	Computational Fluid Dynamics
COER	Carbon Monoxide Evolution Reaction

COOR Carbon Monoxide Oxidation Reaction

CSTR Constantly Stirred Tank Reactor

DAE Differential-Algebraic Equations

DFT Density Functional Theory

DGM Dusty Gas Model

FVM Finite Volume Method

GCI Grid Convergence Index

GDC Gadolinium-Doped Ceria

HER Hydrogen Evolution Reaction

HOR Hydrogen Oxidation Reaction

LSCF Lanthanum Strontium Cobalt Ferrite

LSM Lanthanum Strontium Manganite

MEA Membrane Electrode Assembly

MIEC Mixed Ionic Electronic Conductor

ODE Ordinary Differential Equations

OER Oxygen Evolution Reaction

ORR Oxygen Reduction Reaction

PCC Protonic Ceramic Cells

PEM Proton Exchange Membrane

PFM Plug Flow Model

PtM Power-to-Methane

RU Repeating Unit

ScSZ Scandia-Stabilized Zirconia

SIMPLE Semi-Implicit Method for Pressure-Linked Equations

SNG Synthetic Natural Gas

SOC Solid Oxide Cell

SOEC Solid Oxide Electrolysis Cell

SOFC Solid Oxide Fuel Cell

TPB Triple Phase Boundary

YSZ Yttria-Stabilized Zirconia

CHAPTER 1

Introduction

1.1. Background and context

Solid oxide cells (SOCs) are a class of electrochemical devices that can be used for the production of hydrogen and carbon monoxide as well as for the production of electricity from a variety of fuels. As energy conversion devices, their development is closely tied to the evolution of the energy sector. Since this dissertation focuses on the advancement and use of SOC modeling techniques, this introductory section will provide an overview of the role of SOCs in the current global energy transition, summarize the current challenges of this technology and show how numerical models have proven useful for overcoming such challenges. Finally, the objective and scope of this dissertation will be clarified.

1.1.1. The role of hydrogen in the energy transition

The transition from fossil energy sources to carbon-free power production is at the center of the fight against man-made climate change [1].

As a consequence, the proportion of renewable energy in power grids around the globe is in constant growth. In OECD countries alone, the primary energy supply from renewable sources has risen by 2.6% on average every year between 1990 and 2018, reaching 10.5% in 2018 [2]. Means of harnessing renewable energy include solar, wind and hydroelectric power plants as well as the combustion of biomass or their derived biofuels.

While all of these sources of electricity have become viable alternatives to fossil fuel based power plants, their growth is still restricted by essential limitations of these technologies. The fluctuating nature of the underlying sources of energy such as the wind, the sun or the flow of rivers leads to temporal fluctuations in power production capacities.

Storage of excess energy in chemical form is one crucial part of the solution to this issue. Hydrogen in particular has rapidly become one of the most promising forms of chemical energy storage, with a total of 60 countries having a dedicated hydrogen strategy as of 2024 [3].

The popularity of hydrogen as an energy carrier can be attributed to its versatility. While it can be used to produce electricity in storage plants meant to coordinate power supply and demand, it can be further processed into renewable fuels for mobile applications, serve as renewable feedstock for the chemical sector and substitute carbon monoxide as a reducing agent to decarbonize steel production.

Indeed, a significant part of industrial emissions are caused by chemical reactions producing CO_2 as a byproduct. Notably, the production of steel in blast furnaces uses carbon monoxide as a reducing agent, which is oxidized to CO_2 that is released into the atmosphere. Decarbonizing the process

itself therefore requires a different reducing agent, and hydrogen is an effective alternative. This process is currently being explored by the Salzgitter AG, which uses a solid oxide electrolysis unit capable of producing 200 Nm^3/h, which was the largest in the world when it was installed in 2022 [4]. Production of one ton of steel through the conventional blast furnace process leads to emissions of 1.8 to 2.3 tCO_2eq, while the process of direct reduction of iron can be nearly CO_2-neutral when it is performed with green hydrogen [5]. In 2020, the production of steel accounted for the emission of 2.6 gigatonnes of CO_2 [6].

Within the chemical sector, ammonia production is the largest contributor to global emissions. With an emission intensity of 2.4 tonnes of CO_2 per tonne of ammonia produced, it accounted for the emission of 450 megatonnes of CO_2 in 2020 [7]. These emissions stem almost entirely from the production of hydrogen required in the process which is most often produced through methane reforming or coal gasification [3]. Currently, ammonia production is responsible for the largest portion of the current hydrogen demand. The CO_2 emissions from ammonia production can be almost entirely negated by providing carbon-free hydrogen.

Hydrogen also provides convenience in the transition to carbon-neutral processes because it can be converted to hydrogen-carrying synthetic fuels. This allows the renewable production of synthetic fossil fuels and chemical feedstock. Synthetic fuels such as synthetic natural gas or synthetic aviation fuel are designed to seamlessly replace a fossil fuel for the end user, minimizing the amount of infrastructure change required during the transition to renewable fuels. Despite the global strive for emission mitigation, the global demand for natural gas is increasing steadily [8]. This means that new systems consuming natural gas are constantly being built, and it is not realistic to expect all of them to be electrified. Still, their emission could be mitigated by supplying them with synthetic fuels produced from green hydrogen.

In addition, the conversion of hydrogen into so-called hydrogen carriers alleviates the main issue of hydrogen as energy carrier: its low volumetric energy density, which makes its storage and transport costly. Hydrogen carriers are used to facilitate the storage and transport of hydrogen by providing better volumetric energy density and safety [9]. Many chemicals are being considered as potential hydrogen carriers, and all provide different compromises between efficiency, ease of transport and safety. Methane for example is being considered because it can be transported using the extensive existing natural gas transport infrastructure and doubles as a synthetic fuel when it fulfills the requirements for SNG [10]. Ammonia is also a promising hydrogen carrier because it is versatile, does not contain carbon and its production process is mature. Ammonia is a valuable chemical feedstock, but can also be used as a fuel by burning it directly. It has a good energy density, especially liquefied, and is stable, although toxic [11].

Hydrogen can also be stored in metals to reach high volumetric energy density. For example, a multitude of metal hydrides are being considered for hydrogen storage, with exceptional volumetric energy densities such as 14.7 GJ/m^3 for Lithium borohydride ($LiBH_4$) [12]. For reference, liquid ammonia has a volumetric energy density of 12.7 GJ/m^3 [7]. Alternatively, hydrogen can be stored indirectly in elementary metals such as iron through their oxidation state. Iron can be produced by reducing iron oxides in a hydrogen atmosphere, and in turn the produced iron can be used to reduce steam to hydrogen, effectively turning it into hydrogen storage without physically carrying the hydrogen atoms [13].

1.1.2. SOCs: a pivotal technology of the hydrogen economy

Due to its plethora of applications, it is no surprise that hydrogen is a desirable resource. The reason why hydrogen is expected to become an essential energy carrier is that it can be produced without greenhouse gas emissions through water electrolysis. Water electrolysis is the process that allows the production of hydrogen from water and electricity. It is performed by driving an electric current between two electron conductors, the electrodes, separated by an electrolyte. The electrolyte is the central component of an electrolysis system. It is a material that is conductive to ions such as oxygen or hydrogen ions, while not being conductive to electrons. The electrolyte allows for the spatial separation of two steps of the water splitting reaction, allowing the reaction to be driven by an external electric potential.

This fundamental principle can be implemented in a variety of ways, which is the reason why there are a multitude of electrolysis technologies. These technologies can be differentiated by the electrolyte they use.

Alkaline water electrolysis (AWE), which is currently the most widespread industrial electrolysis technology, uses liquid electrolytes in the form of potassium hydroxide (KOH) or sodium hydroxide (NaOH) solutions. In this case, the mobile charge carriers are hydroxyl ions OH^-. This technology is favored for its low capital investment cost [14].

Proton exchange membrane (PEM) electrolysis is another mature electrolysis technology which leverage solid polymer electrolytes which conduct protons H^+. The technology is generally more expensive than AWE, but boasts a range of benefits such as dynamic operation capability and high purity of the produced hydrogen [15].

Solid oxide electrolysis cells (SOECs) utilize the oxygen conductivity of certain ceramics at high temperatures, typically between 600 to 1000 °C [16]. Although costly to provide and maintain, these high operating temperatures provide a range of advantages. A variety of materials conducting oxygen ions O^{2-} in this temperature range have been developed, the most widely used being yttria-stabilized zirconia.

Protonic ceramic cells (PCC) are a similar technology, but use perovskite ceramics that conduct protons. They operate in a temperature range between 400 and 600 °C [17]. The slightly milder operating conditions are easier to handle while still reaping most of the same benefits from high operating temperatures as SOECs, although the achievable efficiency in such devices is slightly reduced by the undesired flow of multiple other charge carriers through the perovskite membranes.

In this dissertation, the focus lies on the SOECs for efficient hydrogen production and further processing into synthetic natural gas (SNG). Solid oxide fuel cells (SOFCs) which allow the reverse process, conversion of hydrogen to electricity, will be considered as well.

1.1.3. Benefits and challenges of the SOC technology

SOECs offer numerous advantages over other electrolysis technologies, primarily due to their high operating temperatures. The elevated operating temperature significantly enhances the kinetics of electrochemical reactions, thereby enabling sufficient reaction rates without the need for expensive catalytic materials. For instance, while low-temperature fuel cells often rely on costly platinum-based

catalysts to facilitate the electrochemical reactions, SOECs can utilize more affordable materials in their fuel electrodes, the most common being nickel.

High operating temperatures are also an advantage during the electrolysis process because it lowers the electrical energy consumption of the electrolysis reactions. Instead, a larger part of the reaction enthalpy is provided by heat, which is already produced as a byproduct of the electrolysis process [18]. Thermal integration with other heat-intensive processes allows to fully take advantage of the unparalleled electrical efficiency of SOECs while offsetting the cost of managing high-temperature gases [19].

For SOFC, the high operating temperatures allow for internal decomposition and reforming of hydrogen carriers such as methane or ammonia. Integrating these fuel processing steps directly into the fuel cell simplifies the design of the system and reduces the amount of system components. The high fuel flexibility of SOCs is also compounded by their resistance to poisoning by carbonated species, enabling operation with a variety of fuels, including natural gas and biogas [20].

The same resistance to carbon poisoning also enables the electrolysis of carbon dioxide into carbon monoxide in SOECs and the oxidation of carbon monoxide in SOFCs [21]. Furthermore, the ability of SOCs to function reversibly, switching between fuel cell and electrolysis modes, makes them highly versatile for energy storage and conversion applications [22]. These combined benefits position SOCs as a promising solution for advanced energy systems.

However, a number of technological challenges also inhibit the adoption of SOCs. The most obvious challenge is to manage their significant operating temperatures. Costly systems are required to heat up SOC modules during start-up, regulate their temperature during operation and manage manage water evaporation and condensation. System components surrounding the SOCs are exposed to uncharacteristically harsh conditions such as exposure to oxygen or steam at temperatures above 600 °C which is extremely corrosive [23]. Thermal insulation also becomes of utmost importance, as heat losses have a high impact on system efficiency [24]. Hence, the high temperatures have a major impact on system cost and maintenance. The same factors increase the volume and weight of systems based on SOCs, which is especially problematic for mobile applications.

Still, the deployment of SOCs in industrial applications is picking up, and the cost of manufacturing SOCs is deemed to be the most significant remaining issue before widespread adoption of the technology [25]. Although no noble metal catalysts are required, the ceramic materials are still costly and the manufacturing process is difficult. Maturing of the production processes is therefore essential to enable the widespread adoption of SOCs in industrial applications.

1.2. Importance of simulation in the development of SOCs

Numerical modeling and simulation of SOCs plays a major role in the development of the technology and its applications. The numerical simulation of SOCs has a large number of applications due to the wide variety of modeling methodologies. Since practical applications of SOCs in commercial systems are rather recent, the majority of research efforts have concentrated on developing models aimed at enhancing the community's understanding of the physics underlying SOCs. These models can be distinguished by the scale of the physical processes they consider.

At the smallest of scales, the understanding of the electrochemical reactions and ion transport in SOCs is enhanced through models at the scale of a few atoms by way of molecular dynamics and density functional theory (DFT). Molecular dynamics simulations are used in the literature to provide insights into material properties and reactions [26]. The understanding it provides is essential for the development of efficient and durable SOC materials. By simulating the interactions within these materials, optimized ceramic compositions and structures can be designed to enhance their performance [27]. In addition, the resulting information about the properties of the studied materials informs subsequent mesoscale modeling efforts.

DFT simulations have become a valuable tool in SOC research, offering insights into physical properties that govern electrochemical performance. This simulation method provides insights into formation energies of species and lattice defects participating in the chemical reactions under study, as well as energy barriers to the transport of charge carriers. Therefore, DFT is used to quantify the charge transport properties of ceramics by calculating defect (e.g., oxygen vacancies) formation and migration energies in electrolytes and mixed conductors, supporting the discorvery and design of materials [28]. DFT can also be used to study the catalytic activity of electrode materials and reaction pathways for both electrochemical and thermocatalytic reactions by estimating adsorption energies and activation energy barriers [29].

Mechanistic investigations of thermocatalytic and electrochemical reactions are also performed using models at the continuum scale that use the mean-field assumption [30]. This approach requires much less computational resources than atomistic models and can be used in mesoscale simulations. Goodwin et al. used such a model to compare two different hydrogen oxidation mechanisms in Ni-YSZ SOFC anodes [31]. They observed that their model of the hydrogen-spillover mechanism could match a larger range of polarization measurements than the oxygen-spillover mechanism. Based on the framework of Zhu et al. [32], Banerjee et al. [33] compared three hypothesized reaction mechanisms for the oxygen reduction reaction in a LSM-YSZ cermet and identified the one that is most likely to be true by fitting the mechanism parameters with experimental data, comparing the generality of the models against validation data and evaluating the plausibility fitted thermodynamic parameters.

Small-scale geometric structures are also under scrutiny in SOCs, because the exact geometry of a porous electrode has a great influence on the performance and durability a cell. Therefore, research is conducted on specialized stochastic models to predict the 3D structure of electrodes depending on their composition and manufacturing process [34]. Not only are these models useful during the design process of SOCs by providing helpful tools for the optimization of electrode microstructure, mathematical modeling of electrode geometry also serves as a basis for macroscopic modeling studies [35].

Detailed continuum models of cells, which comprise both electrodes, the electrolyte, and the gaseous phase in the porous electrodes, are generally used to supplement experimental investigations. Their purpose is to further the understanding of the physico-chemical processes in the cells. By purposefully including or excluding specific physical phenomena from the models and confirming how well the model is able to reproduce experiments, it is possible to elucidate which are the dominant phenomena in determining the behavior of cells. Bao et al. used such a method, comparing the Fickian, Stefan-Maxwell and dusty gas model for mass transport in SOFC electrodes under various conditions

of polarization and gas composition [36]. Thereby, they are able show the role of Knudsen diffusion in the generation of pressure gradients in the electrodes. This effect is demonstrated to be a result of the different molecular mass of reactant and product of the electrochemical reaction.

Detailed continuum models can also be used to predict the performance of cells. Although this can also be achieved by simpler models, models that aim to closely reproduce all relevant physical phenomena in a cell come with significant advantages. Such detailed models require less calibration data because they are grounded in established physical principles, such as electrochemical kinetics, mass transport, and heat transfer, which inherently capture the underlying behavior of the system. As a result, the calibration of such models consists of determining the physical properties of the cell and its components. The resulting model can be expected to be accurate beyond the operating conditions used for the calibration as long as the underlying physical models are still valid, as was shown by Weber et al. through a meta-analysis of various PEM fuel cell models [37]. This predictive power makes detailed continuum models especially useful for scale-up studies of SOCs for which stack-scale experimental data is impractical to collect [35, 38].

0D models trade accuracy and predictive power for simplicity and computational efficiency. While they can still be anchored in physical principles, these principles are often deeply simplified or replaced with empirical correlations to reduce complexity. Instead of solving partial differential equations for mass transport or electrochemical kinetics, 0D models may use scaling laws or simplified analytical solutions to approximate the behavior of the system. For example, good results are still obtained by simplifying mass transport with the assumption of constant concentration gradients and Fick's law, which is used to produce a fully algebraic cell model by Leonide et al. [39]. Simplified models are particularly useful for rapid performance estimations, which is valuable for optimization tasks, system level simulations or real time control applications where computational speed is critical [40, 41].

Surrogate models offer a different trade-off between accuracy and computational efficiency by approximating the behavior of detailed physical models. These models are typically constructed using data generated from high-fidelity simulations or experiments and employ techniques such as machine learning or polynomial regression to capture the underlying relationships between inputs and outputs without consideration of the underlying physical phenomena. While surrogate models sacrifice the physical insights provided by the aforementioned models, they excel in scenarios requiring rapid evaluations, such as parameter optimization or real-time control [42]. Their ability to deliver fast and reasonably accurate predictions makes them particularly valuable for system-level analyses and iterative design processes, where repeated simulations of complex models would be computationally prohibitive [43, 44]. The complete lack of physical basis, however, means that their accuracy is mostly determined by the amount of available calibration data. Overfitting is more likely and extrapolations beyond the operating conditions of the calibration data can not be expected to be reliable.

1.3. Current state of multi-scale SOC modeling

Multiscale modeling is an approach that integrates simulations of physical phenomena that take place at significantly different length and time scales. In the context of SOCs, multiscale modeling connects

phenomena occurring at the atomic level (e.g., electrochemical and thermocatalytic reactions), microscopic level (e.g., charge transport through the electrodes and electrolyte) with those at the cell level (e.g., mass transport along gas channels) and system level (balance of plant).

Overall, continuum scale modeling is the preferred approach for detailed simulations ranging between the millimeter scale of the membrane-electrode assembly (MEA) to the meter scale of full stack models [45]. At the scale of the MEA, the main processes to consider are the electrochemical reactions, charge transport, mass transport through the electrodes, and thermocatalytic reactions depending on the gas compositions.

For continuum scale mass transport through porous electrodes, the dusty gas model (DGM) is widely used by the SOC modeling community. In a comparative study, Bao et al. demonstrated that the DGM is a considerable improvement compared to the simpler Stefan-Maxwell and Fickian transport models [36].

Depending on the targeted application, charge transport in SOCs is modeled using either an interfacial or a distributed charge transfer model, the difference lying in where the electrochemical reactions are assumed to occur. Interfacial charge transfer models are based on the assumption that all significant charge transfer reactions are concentrated in a volume so small that they do not need to be resolved in space. Instead, all charge transfer reactions happen directly at the surface of the dense electrolyte [32]. This approach turns the charge transport problem into a set of algebraic equations which is easy to solve and sufficiently accurate for most purposes, which is why the approach is still used in contemporary continuum models [46].

For studies on the influence of the electrode microstructure or for models with a better degree of generality, distributed charge transfer models are used. Therein, the charge transfer rate across the full thickness of the electrodes is resolved, resulting in a charge transport problem formulated as a set for coupled Poisson equations for the electrostatic potential fields in the electron conducting phase and in the ion conducting phase [47].

Simulating electrochemical cells also requires mass transport models for the flow of gas that is supplied to the electrodes, and a heat transport model to compute the temperature of the cell. Button cells, which are predominantly used for the characterization of cell materials and manufacturing procedures, are typically operated under conditions in which the gases are well mixed, allowing the use of simple and well-established 0D constantly stirred tank reactor (CSTR) models [48]. Larger cells require flow models that accurately capture the spatial variations in gas concentration, pressure, and temperature across the surface of the cell. These models comprise transport equations of varying degrees of detail in 1D, 2D, or even 3D to account for convective and diffusive transport of mass and heat. Simple flow patterns such as the flow of gas through the channels of an interconnect can be modeled reasonably well using the simple plug flow model (PFM) [49]. When the flow field design of a full cell is of interest, such as to ensure uniform reactant distribution, efficient product removal and effective heat management, the models need to account for multidimensional flow patterns [50].

Special attention is required to prevent the numerical complexity of the problem to grow exponentially with each physical phenomenon being considered. The most straightforward approach to manage this complexity is to decompose the problem so that phenomena of different scales can be solved separately. This approach is central to multiscale model. Since the phenomena are still coupled, this generally results in a hierarchical problem structure, where problems are solved in order, from the

smallest to the largest scale. For each level, the discretization in time and space might be adapted to fit the scope of the current problem. In SOC models, the smallest scales are also greatly simplified by reducing the dimensionality of the physical problem. 1D models are considered to be sufficient for the simulation of button cells, while accurate simulations of SOC stacks require 3D models [38].

For the multi-scale simulation of transient processes, all but the longest time scale can be ignored and replaced with steady state simulations [51]. Ignoring transient phenomena altogether greatly lessens the computational cost of simulations, and is indeed a common strategy employed for the modeling of SOCs. However, the transient behavior of SOCs is essential to their most common characterization methods (electromagnetic impedance spectra, distribution of relaxation times) as well as current challenges of the technology. Indeed, the start-up behavior or SOC systems and their performance during dynamic operation is of great interest for applications linked to energy storage.

1.4. Identified challenges in SOC stack modeling

Despite the extensive body of research regarding SOC modeling, the technology's transition from laboratory scale to industrial deployment brings forth a multitude of challenges. These range from fundamental material science issues—such as long-term degradation mechanisms and electrode stability—to macroscopic engineering hurdles.

Within the context of SOC modeling, this dissertation identifies and addresses one specific computational barrier: the accurate representation of gas distribution in large stacks without excessive computational cost.

As SOC technology scales from single cells to stacks, the complexity of gas distribution increases significantly. In a stack, gases are distributed through manifolds into hundreds of individual channels. While the physics of this process are well-understood, accurately capturing them in a simulation model involves a difficult trade-off between fidelity and computational speed.

The difficulty in simulating the flow in an entire SOC stack is compounded by the vast differences in flow regimes present at any single point in time. As manifolds distribute gases to individual gas channels, the flow conditions in the manifolds differ significantly from those withing the cells. In the manifolds, the flow is generally three-dimensional, and often turbulent. Meanwhile, the flow inside of single cells has consistently low Reynolds numbers, but potentially large variations in fluid properties. This introduces challenges in accurately modeling flow distribution, pressure losses and species transport, which can critically impact stack performance and durability [52].

To address these challenges, computational fluid dynamics (CFD) simulations are often employed, incorporating three-dimensional Navier-Stokes equations with species transport to resolve complex flow behavior [50]. Turbulence models may be applied, though accurately simulating the transition between laminar and turbulent flow regimes remains an active research challenge [53]. However, the computational cost of resolving the 3D Navier-Stokes equations for a full stack is often prohibitive for iterative design and operating condition optimization.

To enable faster simulations, stack models might assume a perfect distribution of flow rates at the cell inlets or rely oversimplified physical models for the flow distribution [54, 55]. While efficient,

these approaches risk overlooking the impact of flow maldistribution, which can lead to local reactant starvation or thermal gradients [52].

The low accuracy of such simplified stack flow modeling approaches creates a specific gap in the modeling spectrum: there is a need for modeling approaches that can reliably predict the flow distribution throughout a stack, but with significantly lower computational overhead than full 3D CFD.

1.5. Objective and scope of this dissertation

The overarching objective of this dissertation is to improve the accuracy of computational models used to simulate SOC performance at the cell, stack and system levels. These tools are specifically intended to aid the performance optimization of SOC modules and the systems surrounding them in order accelerate the deployment of the technology. To this end, the work focuses on the development and validation of a set of custom models that improve upon existing modeling efforts, more accurately representing the physical processes occurring within SOC stacks and their integration into larger systems.

A particular emphasis is placed on the modeling of gas flow in stack manifolds. This part of the system is often oversimplified in conventional models due to its high complexity and comparatively low impact. As a consequence, most flow models whose computational load is small enough to be integrated in detailed continuum-models of SOC stacks are inadequate, as was highlighted in the previous section. In this context, this dissertation builds upon the established practice of hydraulic network modeling for the simulation of SOC stack manifolds and improves upon it by determining a set of accurate model parameters. High-fidelity CFD simulations are performed with OpenFOAM, from which the parameters are extracted and reintroduced in the simplified model.

Beyond flow modeling, this dissertation presents a comprehensive SOC stack model that incorporates key physical processes relevant to SOC operation, including charge transport, electrochemical reactions, and mass transport through porous media. The newly developed manifold flow model is integrated in this multi-scale model along with additional improvements upon the original modeling methodology. This model is parametrized and validated by comparing button cell simulations with experimental data. Scaling up the cell model to a full stack enables a case-study on the impact of flow maldistribution on stack performance.

The integration of the stack model into system-level simulations is demonstrated. This enables the evaluation of SOC performance in the context of complex thermally integrated systems, such as power-to-methane (PtM) plants. A design trade-off and parametric analysis of a multitude of PtM systems is performed, offering insights into optimal operating conditions and system configurations.

The scope of this dissertation is thus structured around three key contributions, each corresponding to a peer-reviewed publication:

- A simplified yet accurate manifold flow model for SOC stacks, validated with high-fidelity CFD simulations.
- A full multi-physics model for SOC stack simulation, validated against experimental data and suitable for predictive modeling.

- The integration of the stack model into system-level simulations to evaluate the efficiency of different PtM process configurations.

Together, these contributions offer improved tools for performance prediction, design optimization, and system integration.

CHAPTER 2

Fundamentals and methods

2.1. Operating principles of SOCs

SOFCs and SOECs, collectively referred to as SOCs, are electrochemical energy conversion devices operating at high temperatures (typically 600–1000°C [16]). SOFCs generate electricity through the electrochemical oxidation of a fuel, while SOECs convert electrical energy into chemical energy via the electrolysis of steam or carbon dioxide. Their high efficiency, fuel flexibility and potential for thermal integration in energy systems make SOCs an attractive technology for sustainable energy conversion applications.

A schematic representation of a planar SOC is provided in Figure 2.1. The core of any SOC is the membrane electrode assembly (MEA), which comprises two electrodes and an electrolyte between them.

While the term *electrolyte* commonly refers to materials with the property of ion conductor and electron insulator, it is generally used to refer to the central electrolyte layer specifically. In this manuscript, materials with such properties will be referred to as *electrolyte materials* instead. Similarly, this manuscript follows the naming convention of the SOC community with regards to the term *electrode*, which is used to refer to the porous structure combining electron conductor and ion conductor.

The electrolyte allows the passage of ionic charge carriers while preventing the passage of electrons. This separation of charge carriers allows to channel the electrons through an external circuit, which is the main advantage of an electrochemical cell.

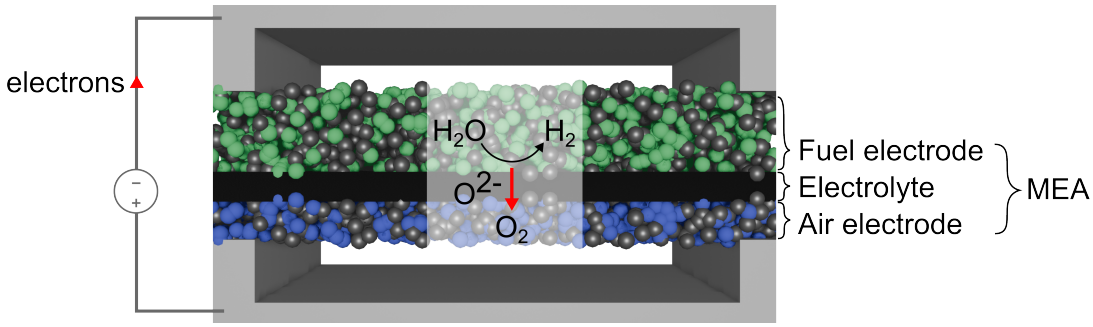

Figure 2.1.: Schematic of a planar SOEC.

The main role of the electrodes on both sides of the electrolyte is to conduct electrons produced in the electrochemical reactions. Since the electrochemical reactions comprise gaseous species, electrons and ions, they can only take place at the phase boundary between the gas phase, an electron conductor and an ion conductor. This phase boundary is optimized by manufacturing porous electrodes that

combine electron and ion conducting phases. Such mixed conducting behavior is either achieved by combining two materials with complementary conductivity, or the use of a single material with mixed conductive behavior.

The first method consists of manufacturing *cermet* electrodes, a composite material obtained by combining a metallic electron conductor with an oxygen ion conducting ceramic. These combinations can be achieved through different processes such as co-sintering of both phases or infiltration of the metallic phase in a ceramic backbone. All manufacturing methods share the common goal of maximizing the length of the triple phase boundary (TPB) between pores, metal and ceramic while ensuring all phases are also percolating to enable the transport of gases, electrons and ions.

The use of mixed ionic electronic conducting materials (MIECs) can simplify the electrode manufacturing since the electrochemical reactions can take place over the whole surface of the material [56]. Only one material has to be sintered and only two phases have to percolate. However, combining the function of an electron conductor, an ion conductor and a catalyst in a single material that needs to be durable and chemically compatible with adjacent materials is difficult. While non-composite air electrodes are common, mixed conducting fuel electrode materials are still complemented with metallic catalysts [57].

SOCs can be manufactured in two primary geometries: planar and tubular, each offering distinct advantages and challenges in terms of performance, scalability, and manufacturing complexity.

The flat geometry of planar SOCs allows for high power density and simple stack assembly by allowing multiple cells to be stacked to form compact modules. Planar designs also facilitate precise control over layer thicknesses and microstructure, which is beneficial for optimizing electrochemical performance. However, they are more susceptible to thermal stresses due to the rigid flat geometry, which can more easily lead to cracking or delamination during thermal cycling. Additionally, sealing between cells in a stack is more challenging, as it requires gas-tight seals that can withstand high temperatures and thermal cycling [58].

In contrast, tubular SOCs feature a cylindrical design where the electrolyte is formed into a tube, and the electrodes are deposited on its inner and outer surfaces. This geometry inherently provides better mechanical robustness and thermal shock resistance, as the curved structure distributes stress more evenly. Tubular cells also simplify sealing, since the closed-end tube naturally separates the fuel and oxidant streams. However, the longer diffusion paths and lower packing density compared to planar cells result in lower power density. Moreover, the manufacturing process for tubular cells is generally more complex and less scalable, often involving extrusion or dip-coating techniques that are harder to automate and control precisely [59].

The choice between planar and tubular configurations depends on the specific application requirements, such as desired power output, operating conditions, and system integration constraints. While planar cells dominate in stationary electrolysis due to their scalability and efficiency, tubular cells remain attractive for applications where mechanical durability is prioritized, such as mobile power production.

In this dissertation, the focus lies on planar SOCs because a study of a planar application is targeted, namely high temperature electrolysis for the production of synthetic natural gas. In stacks of planar SOCs, the MEAs are mounted between *interconnects*, metallic plates containing channels for the

passage of gas and ribs in contact with the MEA to collect electrons. The stacks are assembled by alternating between MEAs and interconnects while ensuring proper sealing between layers. The combination of a cell and its encompassing interconnects is called a repeating unit (RU).

By enabling researchers and engineers to understand and optimize SOCs across a large spectrum of spacial and temporal scales, from the elementary chemical reactions to the heat transport in stacks, modeling is a powerful tool for facilitating the deployment of the technology. This section presents an overview of the principal components of SOCs and the fundamental physical processes governing SOC operation. A solid understanding of these processes forms the basis for the subsequent modeling activities reported in the publications constituting this dissertation.

2.1.1. Electrochemical reactions in SOCs

In SOFCs and SOECs, the electrochemical reactions occur at the electrodes. In SOFCs, hydrogen and carbon monoxide are oxidized at the fuel electrode (anode)

$$\mathrm{H_2} + \mathrm{O^{2-}} \longrightarrow \mathrm{H_2O} + 2\,\mathrm{e^-}, \tag{2.1}$$

$$\mathrm{CO} + \mathrm{O^{2-}} \longrightarrow \mathrm{CO_2} + 2\,\mathrm{e^-} \tag{2.2}$$

through reactions that will be called the hydrogen oxidation reaction (HOR) and the carbon monoxide oxidation reaction (COOR).

At the air electrode (cathode), oxygen is reduced

$$\frac{1}{2}\,\mathrm{O_2} + 2\,\mathrm{e^-} \longrightarrow \mathrm{O^{2-}} \tag{2.3}$$

through the oxygen reduction reaction (ORR).

In sum, this results in the two following global hydrogen and carbon monoxide oxidation reactions:

$$\mathrm{H_2} + \frac{1}{2}\,\mathrm{O_2} \longrightarrow \mathrm{H_2O}, \tag{2.4}$$

$$\mathrm{CO} + \frac{1}{2}\,\mathrm{O_2} \longrightarrow \mathrm{CO_2}. \tag{2.5}$$

In SOECs, the reactions are reversed. At the fuel electrode (cathode), steam or carbon dioxide is reduced to hydrogen or carbon monoxide (HER and COER) respectively. At the air electrode (anode), oxide ions release electrons to form molecular oxygen (OER).

A single cell can be used both as an SOFC and SOEC as long as its material constituents are chemically stable under both operation modes [60]. While switching from the fuel cell to electrolyzer, the anode of the cell becomes the cathode and the cathode becomes the anode as the flow of electrons is reversed. Since this dissertation considers both modes of operation, a terminology that is not dependent on the mode of operation is used instead. The electrode that performs the reduction or evolution of oxygen is referred to as *air electrode*. The electrode that performs the oxidation or evolution of hydrogen and carbon monoxide is referred to as *fuel electrode*.

In SOCs, the direction of the reactions and their rate is dependent on the difference in electric potential between both electrodes, and more specifically, how it relates to the *equilibrium potential* of the cell.

2.1.1.1. Equilibrium potential

The thermodynamic favorability of chemical reactions is governed by the Gibbs free energy change ΔG. ΔG is the difference between the Gibbs free energy of the reactants and products of the reaction. It represents the work that can be extracted from a spontaneous reaction under constant pressure and temperature, or that needs to be supplied to a non-spontaneous reaction. For a given reaction,

$$\Delta G = \Delta H - T\Delta S, \tag{2.6}$$

where ΔH is the enthalpy change, T is the temperature, and ΔS is the entropy change. A negative ΔG indicates a spontaneous reaction (SOFC mode), while a positive ΔG requires energy input (SOEC mode) [61].

Electrochemical systems operate by capturing, or supplying, this work electrically. This is achieved by spacially separating two distinct steps of a reaction, which allows to lead the electrons exchanged during the reaction through an external circuit. These electrons are collected at the anode and transported to the cathode of the electrochemical device, and the electrostatic potential applied between these two electrodes by the external circuit determine the rate of the electrochemical reaction.

The electrostatic potential that needs to be applied between the electrodes to prevent both forward and backward reaction is called the equilibrium potential or reversible voltage E_{rev} and is directly related to the Gibbs free energy change of the reaction:

$$E_{\text{rev}} = -\frac{\Delta G}{n_{\text{e}}\, F}, \tag{2.7}$$

where n_{e} is the number of electrons transferred in the reaction, and F is Faraday's constant.

The equilibrium potential is central to the operation of electrochemical cells, because the difference between the equilibrium potential E_{rev} and the applied cell voltage by the external electrical circuit E_{cell} determines the rate of the reaction and the efficiency of the system. The equilibrium potential is usually computed using the Nernst equation:

$$E_{\text{rev}} = E^{\circ} - \frac{R\,T}{n_{\text{e}}\, F} \ln \frac{\prod\limits_{s \in \mathbf{S}_{\text{products}}} a_s^{\nu_s}}{\prod\limits_{s \in \mathbf{S}_{\text{reactants}}} a_s^{\nu_s}}, \tag{2.8}$$

where E° is the reversible voltage of the cell at standard conditions, R is the ideal gas constant, a is the chemical activity of the species participating in the reaction and ν is the stoichiometry of a species in the reaction.

2.1.1.2. Overpotentials

The term *overpotential* designates the difference between the equilibrium potential of an electrochemical cell E_{rev} and the actual potential between the electrodes applied by an external circuit E_{cell}. An overpotential is required to drive the electochemical reaction by overcoming energy losses, and it can be subdivided in three different contributions:

- The *activation overpotential* acts in conjunction with thermal energy to overcome the activation barrier of the electrochemical reaction, and its magnitude directly modulates the speed of the electrochemical reaction.
- Although the porous structure of SOC electrodes is designed to facilitate mass transport, gases inside of the electrodes are far from ideally mixed. While the equilibrium potential of a cell can be determined from the supplied reactant concentrations, the electrochemical reactions take place inside of the electrodes where the reactant concentration differs during operation. This modified reactant concentration results in a less advantageous equilibrium potential at the reaction sites. The difference between the equilibrium potential of the cell and the equilibrium potential computed from the gas concentrations at the reaction sites is called the *concentration overpotential*.
- The charged species produced by the electrochemical reactions during operation of a cell are driven by potential gradients to move through the conductive materials of the electrodes and electrolyte. The potential difference across the electrodes required to displace the charge carriers is called the *ohmic overpotential*, as it can often be estimated with Ohm's law.

While it is clear that the existence of an overpotential is required for the operation of a fuel or electrolysis cell, the relationship between the magnitude of the overpotential and the achieved current density can vary greatly and is a direct indicator for the effectiveness of the cell. A fuel cell achieving high currents for a low overpotential not only minimizes the electrical energy that is lost by dissipation as heat, but also facilitates the heat management of the system and allows to reach higher power densities. For electrolysis cells, such considerations are slightly skewed by the endothermic electrochemical reaction, but are identical at high current densities.

2.1.1.3. Thermodynamics of high temperature electrolysis

One of the main qualities of the SOEC technology are the consequences of high operating temperatures on the electrolysis process, which can be understood through the thermodynamic properties of the reaction.

Equation 2.6 indicates that the change in Gibbs free energy through a reaction ΔG is negatively proportional to the temperature of the system. As ΔG is the part of the reaction enthalpy that is supplied electrically, this means for the electrolysis process that the total reaction enthalpies of the endothermic H_2O and CO_2 splitting reactions need to be supplied with a decreasing amount of electrical energy and an increasing amount of thermal energy.

The magnitude of this phenomenon can be observed in Figure 2.2, which depicts the electrical energy demand and heat demand of the water and carbon dioxide electrolysis reactions, which add up to the total energy demand of the respective reactions. The figure shows a significant reduction of the Gibbs free energy change through the reactions between 0°C and 1000°C.

Thermal energy is generally cheaper to provide, especially considering that heat is released by the electrochemical device itself during operation. Indeed, as the electrolysis process is driven by an overpotential, the surplus electrical energy that is not directly stored in chemical form is dissipated as heat. However, this heat may also be utilized by the endothermic reaction, meaning that the provided electrical energy can be fully utilized.

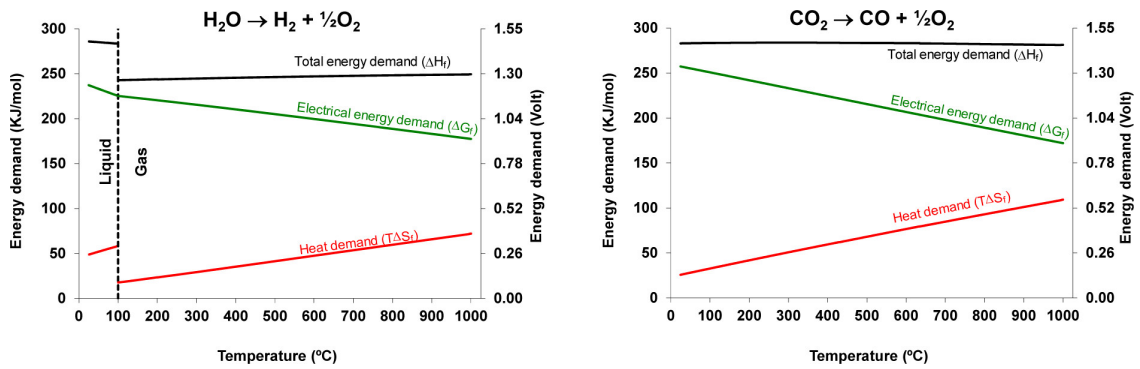

Figure 2.2.: Demand in electrical energy and heat of the water and carbon dioxide electrolysis reactions. Reproduced from Ebbesen et al. [17]. Copyright 2014 American Chemical Society.

Consequently, an exact balance can be struck between the heat required by the reaction $T\Delta S$ and the dissipated electrical energy $n\,F\ (E_{\text{cell}} - E_{\text{rev}})$, which is reached at the so-called thermoneutral voltage $E_{\text{TNV}} = {}^{\Delta H}/_{n_{\text{e}}\,F}$ [18].

Performing electrolysis at high temperatures is therefore exceptionally efficient. In addition, thermoneutral operation is also a great advantage from a heat management perspective. Since no heat needs to be transported to or from the electrolysis cell, there are close to no temperature gradients in the cell. In turn, mechanical strain caused by differences in thermal expansion is minimized.

2.1.1.4. Kinetics of electrochemical reactions

In electrochemical cells, the main parameter influencing the rate of the electrochemical reactions is the overpotential η, which is the difference between the equilibrium potential of the reaction and the actual cell potential:

$$\eta = E_{\text{cell}} - E_{\text{rev}}. \tag{2.9}$$

In addition, temperature, reactant concentrations and electrode materials also influence the reaction rates. All of these parameters are reflected in the Butler-Volmer equation, which is generally used to understand and estimate the rate of electrochemical reactions [62]:

$$i = i_0 \left[\exp\left(\frac{\beta_{\text{a}}\, n_{\text{e}}\, F\, \eta}{RT} \right) - \exp\left(-\frac{\beta_{\text{c}}\, n_{\text{e}}\, F\, \eta}{RT} \right) \right], \tag{2.10}$$

where i is the current density, i_0 is the exchange current density, β are the charge transfer coefficients, η is the overpotential, R is the gas constant and T is the temperature.

The exchange current density reflects the rate of simultaneous forward and backward reactions at equilibrium. It is mainly dependent on the electrode material and is influenced by temperature and reactant concentrations.

In the porous electrodes commonly employed in SOCs, the reaction sites are distributed over areas of the electrodes in which parameters such as reactant concentrations are not homogeneous, which complicates the use of the Butler-Volmer equation as a predictive tool for the full electrochemical cell. Local variations of the equation are still valid, as they consider the rates of half-cell reactions

under the local operating conditions. However, the computed local reaction rates need to be unified by considerations of the charge transport through the cell in order to predict achieved currents.

2.1.2. Thermocatalytic reactions in SOCs

While the operation of SOCs revolves around the electrochemical reactions, one key advantage of the technology is the ease of performing additional catalytic reactions in parallel. While electrochemical reactions are mostly driven by electrochemical potentials and occur at phase boundaries where ionic species, electrons and gaseous species meet, thermocatalytic reactions happen at the phase boundary between gas and catalyst. Their rate are a function of temperature and catalyst activity.

Reactions that reform energy carriers into hydrogen or carbon monoxide are of particular interest for the operation of SOFCs, since they allow the operation of the cells with a large variety of fuels. A fuel cell capable of performing internal steam reforming of methane and higher alkanes can be fueled directly with natural gas, enabling efficient electricity generation in a compact system [63]. Since ammonia gains increasing traction as an energy carrier, the ability to perform ammonia cracking in SOFC fuel electrodes allows direct utilization of the ammonia, foregoing the need for dedicated system components for this task [64].

Some processes are also enhanced by performing catalytic reactions inside SOEC fuel electrodes. While synthesis gas can be produced in SOECs only through electrochemical reactions, facilitating the reverse water gas shift reaction can enhance the overall system efficiency by utilizing excess heat [65].

What enables SOC electrodes to act as effective chemical reactors is their high operating temperatures. Since the activity of catalysts is generally improved at higher temperatures, sufficient reaction rates are achieved in SOCs with cost-effective catalyst materials. While ammonia cracking can be performed at reduced temperatures of 370 - 550°C with ruthenium-based catalysts [66], the nickel fuel electrodes of SOFCs are adequate for direct ammonia operation [67].

Such catalysts function by adsorbing reactants onto their surface, which weakens the bonds between atoms. The weakened bonds lower the activation energy for subsequent reactions of the adsorbed molecule such as its decomposition or interaction with other adsorbed species. Finally, adsorbed molecules can desorb from the surface of the catalyst, re-entering the gas phase and freeing up reaction sites.

2.1.3. Charge transport in SOCs

Since electrochemical cells operate by leading the electrons of the electrochemical reactions through an external circuit, the central component of an SOC is the electrolyte that blocks the passage of electrons but conducts oxygen ions. In SOCs, electrolyte materials are used in the dense membrane to prevent gas and electron flow, as well as in parts of the porous electrodes where both electron and ion conduction is required.

2.1.3.1. Ion conduction in solid oxide electrolytes

Oxygen ion (O^{2-}) conduction in SOC electrolyte materials is achieved through a crystal structure that supports the formation and migration of oxygen vacancies. In materials such as yttria-stabilized zirconia (YSZ), trivalent dopants (e.g., Y^{3+}) subtitute some of the tetravalent cations (Zr^{4+}), creating charge-compensating oxygen vacancies. In Kröger-Vink notation:

$$Y_2O_3 \xrightarrow{ZrO_2} 2\,Y'_{Zr} + 3\,O^{\times}_{O} + V^{\bullet\bullet}_{O}. \tag{2.11}$$

These oxygen vacancies enable oxide ions to hop from one lattice site to another when driven by a gradient in electrochemical potential. The mobility of oxygen ions increases with temperature, following an Arrhenius-type behavior. The ionic conductivity of electrolyte materials is typically described as [61]

$$\sigma_{\mathrm{io}} = \sigma_0 \exp\left(-\frac{E_{\mathrm{a}}}{RT}\right) \tag{2.12}$$

with the pre-exponential factor σ_0, the activation energy for ion migration E_{a}, the gas constant R and the temperature T.

This strong temperature dependence explains why SOCs operate at elevated temperatures. At lower temperatures, ionic transport becomes sluggish, leading to high ohmic losses.

2.1.3.2. Electron conduction in ceramic materials

SOC positrodes are exposed to highly oxidizing conditions due to the high concentration of oxygen at elevated temperatures. Most metals cannot be employed under such conditions, but some ceramic materials are viable and cost-effective alternative electron conductors.

Electron conduction through ceramics is achieved by creating mixed valence systems. The most common electron conducting ceramic in SOCs is Lanthanum Strontium Manganite (LSM). While pure $LaMnO_3$ contains manganese in a +3 oxidation state, the substitution of some La^{+3} with Sr^{+2} creates holes in the electronic structure that localize to form some manganese in a +4 oxidation state. At high temperatures, these electron holes hop between manganese ions which allows the conduction of electrons through LSM [68].

2.1.3.3. Mixed ionic-electronic conduction

In some ceramics such as GDC and LSCF, electronic conduction occurs in parallel to ion conduction depending on the surrounding atmosphere. Taking GDC as an example, in a reducing atmosphere, cerium polarons Ce'_{Ce} are thought to be produced when oxygen leaves the lattice [69]:

$$O^{\times}_{O} + 2\,Ce^{\times}_{Ce} \rightleftharpoons V^{\bullet\bullet}_{O} + 2\,Ce'_{Ce} + \frac{1}{2}\,O_2(g). \tag{2.13}$$

Cerium polarons allow for the transport of electrons through GDC while the production of additional oxygen vacancies also increases the oxygen ion conductivity.

MIECs can be excellent electrode materials because they enhance the reaction zone: since the MIEC accepts all charged species of the electrochemical reactions, the reaction can take place over the

entire surface of the electrode instead. This is a large advantage over the cermet electrodes which combine one ion conductor with an electron conductor. In cermets, the electrochemical reaction can only take place at the TPB between gas, electron conductor and ion conductor.

2.1.4. Materials used in SOCs

All components of SOC stacks are under considerable strain due to elevated temperatures, thermal cycling and exposition to corrosive gases. The development of materials capable of operating effectively under such conditions is a substantial part of the development of this technology. The materials most commonly found in core components of SOC stacks are presented in this section.

2.1.4.1. Dense electrolyte materials

The electrolytes in SOCs must exhibit high oxygen ion conductivity. In addition, they must be chemically stable under the reducing and/or oxidizing conditions they are exposed to, and chemically compatible with the neighboring materials in the cell in order to prevent the formation of isolating interlayers during operation. In addition, good mechanical stability is required to ensure the durability of the cell, especially under thermal cycling. Cracks or pinholes in the electrolyte layer provide a path for gas leakage which quickly leads to the failure of the cell.

The most widely used electrolyte material in SOCs is Yttria-Stabilized Zirconia (YSZ). It is stable under both reducing and oxidizing conditions, has a reasonable ionic conductivity in the range of 800-1000°C and does not conduct electrons. It is not only used in the dense electrolyte layer but also as electrolyte in composite electrodes. YSZ is found in two common compositions, either 8 mol% or 10 mol% Y_2O_3 in ZrO_2. While 8YSZ provides the highest ion conductivity, 10YSZ is sometimes preferred because its performance is more stable over time [70].

Scandia-Stabilized Zirconia (ScSZ), with a composition of 10 mol% Sc_2O_3 along with 1 mol% CeO_2 in ZrO_2, is also a common alternative electrolyte, with properties similar to YSZ but slightly superior conductivity at the cost of a more expensive base material [60].

Gadolinium-Doped Ceria (GDC) is also often used in the electrolyte layer because it boasts a very high oxygen ion conductivity, so high that it retains good performance at significantly lower operating temperatures of 500–700°C [71]. However, GDC also exhibits some electron conductivity in reducing atmospheres. In some applications where careful system design mitigates the electronic leakage, the high ion conductivity of GDC justifies its use as dense electrolyte despite the loss in faradaic efficiency. Lowering operating temperatures provides a range of benefits such as lower cost for balance-of-plant equipment, reduced strain from thermal cycling and improved start-up behavior, which is worth the loss in efficiency in certain systems. But because GDC also exhibits better chemical compatibility with positrode materials than YSZ, it is more commonly employed as a thin *barrier layer* between the positrode and the dense YSZ electrolyte, preventing the two from reacting.

2.1.4.2. Fuel electrode materials

In SOCs, fuel electrodes are most often manufactured from cermets: composite materials made of a ceramic and a metallic component. Therein, the metallic phase serves a dual purpose. It conducts the electrons to the electrochemical reaction sites, and catalyses both the thermocatalytic and the electrochemical reactions.

Due to the high operating temperatures of SOCs, sufficient catalytic activity is reached with cost-effective materials. For this reason, nickel is used in the vast majority of cermet fuel electrodes. In the temperature range of SOCs, its is a good catalyst for the HOR/HER and COOR/COER electrochemical reactions as well as for ammonia cracking and steam reforming of methane. In addition, its reasonable price allows for its use in sufficient quantities to serve as the main electron conductor in the porous electrodes. The manufacturing of the cells is greatly simplified since no additional catalyst has to be added to the electrode, and the performance of the cell benefits from a large TPB between gas, metal and ceramic being available for the electrochemical reaction.

The second, ion conducting component of cermet electrodes is often produced from the same material as the dense electrolyte. Therefore, YSZ is most commonly used, while ScSZ and GDC are not uncommon either. GDC is an especially interesting material for cermet electrodes because of its electric conductivity, but the degradation of Ni-GDC electrode poses a challenge [72].

However, nickel-based fuel electrodes are vulnerable to redox cycling, carbon deposition and sulfur poisoning in hydrocarbon fueled cells, which motivates ongoing research into alternative materials such as perovskite-based electrodes and infiltration-based approaches that improve redox tolerance and maintain catalytic activity [73].

2.1.4.3. Air electrode materials

In air electrodes, the highly oxidizing conditions prevent the use of most metals as electron conductors. Thus, ceramic materials are used instead.

For composite positrodes, the most common electron conducting material is LSM. LSM has a high electronic conductivity and is chemically compatible with YSZ. Therefore, LSM-YSZ composite air electrodes are widespread [74].

MIEC air electrodes are viable alternatives, of which Lanthanum Strontium Cobalt Ferrite (LSCF) is the most common. While the low compatibility of LSCF with YSZ or ScSZ is problematic, as these materials react during sintering to form insulating interlayers [75], LSCF is compatible with GDC. Therefore, LSCF electrodes may be used either with pure GDC electrolyte layers or with a GDC barrier between electrolyte and electrode. In addition, LSCF can also be combined with GDC to form a composite electrode with improved ionic conductivity.

Current efforts in electrode development also include microstructure optimization through architectures such as graded electrodes or electrospun electrodes. These aim at increasing phase boundary sizes and improving gas diffusion with the goal of reducing polarization resistances [76, 77].

2.1.4.4. Interconnects and seals

Interconnects link individual cells in a stack and must conduct electrons while preventing gas mixing. Chromium-containing ferritic stainless steels are common due to their stability, low cost and thermal expansion compatibility with ceramic layers. Although they are not chemically compatible with all electrode materials, surface coatings such as Mn-Co spinels [78] can be used to prevent chromium evaporation and subsequent poisoning of cathodes.

Sealing materials must resist high temperatures and accommodate thermal cycling without chemical degradation or loss of hermeticity. Glass-ceramic seals are often used for their ability to flow and seal during initial operation and solidify for long-term stability. Seal reliability is one of the major bottlenecks in large-scale SOC stack deployment, requiring careful thermal design and materials selection. Recent research in this area has focused on compliant glass systems, fiber-reinforced seals, and alternative metal-ceramic joining strategies. The development of robust and chemically stable sealants remains crucial for stack longevity and economic viability [79].

2.1.4.5. Degradation mechanisms

As was shown by the body of research concerning the development of materials able to withstand the harsh operating conditions of SOCs, the long-term performance and durability of cells is an omnipresent consideration. A variety of degradation phenomena can affect SOCs, usually in response to the highly reducing and oxidizing conditions, high temperatures, thermal cycling and pressure differences across the membrane. Most degradation phenomena are specific to the materials of a cell and its specific use-case. Thus, only the most frequent challenges will be mentioned in the following paragraphs.

A common degradation pathway of SOC stacks is chromium poisoning of air electrodes, which arises from the volatilization of interconnect materials. The resulting chromium species can migrate and deposit on the air electrode, significantly impairing the OER/ORR and causing a drop in electrochemical performance. Electrochemical cleaning has been shown to successfully reverse chromium deposition, and chromium resistant electrode materials are actively being researched. In addition, interconnect coatings can significantly slow down the poisoning process [80].

Nickel migration and coarsening within the fuel electrode is also a common cause for drops in cell performance. Performance losses have been shown to be both caused by the reduction in TPB density as well as the loss of electrical contact of parts of the nickel phase in the affected electrodes. Migration and coarsening occur at high temperatures and are accelerated at high overpotentials [81].

Interfacial delamination of the MEA is another common degradation mechanism which is most commonly observed in SOEC air electrodes. While mismatched thermal expansion coefficients are a common cause for delamination, it is more systematically observed in SOEC air electrodes because of the pressure buildup resulting from the OER. This phenomenon is compounded by different mechanisms of particle formation between electrode and electrolyte materials, which induce mechanical stains eventually resulting in delamination [82].

In fuel electrode supported cells, carbon deposition becomes a concern when hydrocarbons are used as fuel. Available reaction sites are reduced even by thin layers of deposited carbon, and in more

severe cases the access to the reaction sites is impeded through pore clogging. Due to this, both activation and concentration overpotentials of the cells are increased. Reverting carbon deposition requires re-oxidation of the electrode [83].

2.1.5. Gas flow in SOC systems

Since SOCs are continuously operated chemical reactors, a steady flux of reactants has to be transported to the reaction sites and the products need to be evacuated. This process happens at two different spacial scales, which are explained in this section.

2.1.5.1. Gas transport in the porous electrodes

Inside the SOCs, the electrochemical reactions happen close to the surface of the electrolyte layer. This means that the reactants and the products need to traverse the full thickness of the electrodes to reach the reaction site. Therefore, the structure of the electrodes needs to facilitate mass transport, as it is crucial to the performance of cells at high current densities. Indeed, a high current density means that a large flux of reactants is required, which is not easy to realize in a ceramic material that also needs to be optimized for electric and ionic conductivity and catalytic activity.

In the porous electrodes, mass transport mainly occurs over three concurrent mechanisms:

- Viscous flow arises from pressure gradients in the electrode. In SOC electrodes, the largest pressure gradients are caused by the depletion or production of species through chemical reactions, such as the consumption of oxygen in SOFC air electrodes.

- Diffusion allows the transport of reactants even without pressure gradients. It is driven by gradients in chemical potential, leading to a flux of species from regions of high concentration to regions of low concentrations. This allows the reactants to flow towards the reaction sites even where the stoichiometry of chemical reactions does not lead to a pressure gradient: in hydrogen electrodes of SOFCs, the electrochemical reaction consumes hydrogen and produces steam. The depletion of hydrogen and excess of water cause concentration gradients which drive a diffusive flux of these two species. Coincidentally, the diffusion coefficient of hydrogen is significantly higher than that of other gas species commonly found in SOCs, which accelerates significantly the diffusive mass transport though fuel electrodes compared to the slower diffusion processes in air electrodes.

- Knudsen diffusion is also promoted by concentration gradients, but describes a diffusion mechanism whose speed is dictated by molecule-to-wall interactions instead of molecule-to-molecule interactions. In SOC electrodes, Knudsen diffusion is significant because pore diameters are not much larger than the mean free path between molecules. In that case, molecule-to-molecule and molecule-to-wall interactions simultaneously impact the transport of species against their concentration gradients.

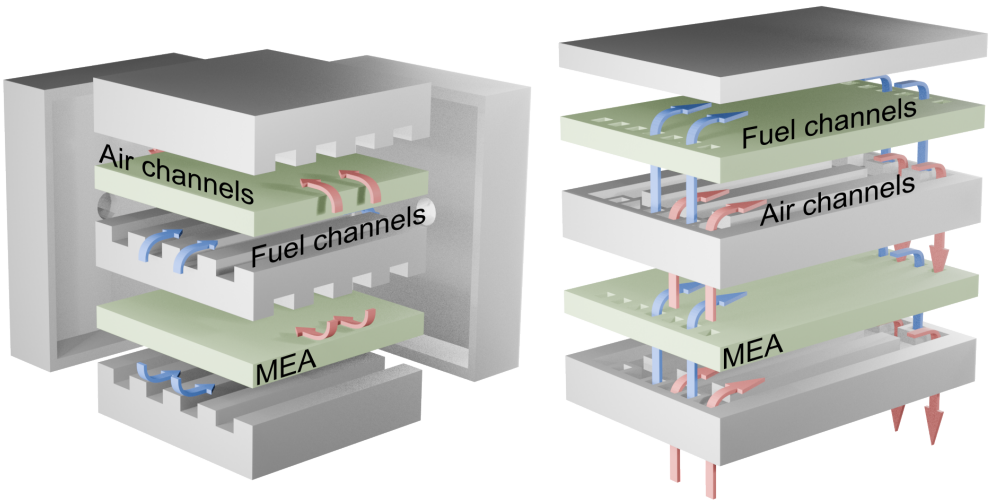

Figure 2.3.: Simplified schematic of stacks with external manifolds (left) and internal manifolds (right). The flow of air is depicted by red arrows while the flow of fuel is shown by blue arrows.

2.1.5.2. Gas transport in planar cell stacks

One of the main tasks during the scale-up of small solid oxide button cells to larger systems is ensuring optimal flow of reactants to the electrodes. Gas flow solutions differ a lot between planar and tubular cells, but for stacks of planar cells there are essentially two solutions: external manifolds and internal manifolds, both shown in Figure 2.3.

In both cases, channels are manufactured directly into the interconnects. The structure allows for enough contact with the MEA for electron transport while minimizing the friction losses of the flow along the cell. The difference is in how the gases are led into these channels, which need to be fed with two different gases while being separated by less than a millimeter.

If the separation between fuel inlet and air inlet is achieved through a cross-flow gas channel configuration, gases can simply be fed by manifolds, each of which covers an entire side of the stack. These are called external manifolds. However, the required cross-flow configuration is generally avoided, as it is known to lead to the highest thermal stresses of any flow configuration.

Instead, internal manifolds are made by integrating vertical channels directly into the interconnects and the cassettes that surround the MEA. By sealing every other vertical channel in an alternating pattern, gases can be separated adequately while achieving any desired channel configuration: co-flow, counter-flow or cross-flow. Internal manifolds have become the preferred solution because of this flexibility and the scalability of the design. Stacks of any number of cells can be manufactured from a single RU design. However, the design of internal manifolds can be more challenging as it involves a more complex geometry and carries the risk of uneven supply along the height of the stack.

It is worth noting that both concepts can also be combined, using an external manifold to provide an homogeneous air supply at high flow rates while using an internal manifold to channel the fuel in a co-flow or counter-flow configuration [84].

The design of these flow fields is critical to the overall performance and durability of the stack. Uneven gas distribution can lead to local fuel starvation, hot spots, or concentration polarization,

all of which degrade performance and accelerate degradation. Therefore, advanced stack designs may incorporate flow field optimization, such as tapered channels or flow distributors, to enhance uniformity [52].

Thermal effects also play a significant role in gas transport at the stack level. Temperature gradients affect gas viscosity and diffusivity, thereby influencing the overall transport behavior. Therefore, gas transport in planar cell stacks is a multi-physics problem involving fluid dynamics, mass transport, and thermal effects. Its proper management is essential for achieving high efficiency, uniform performance, and long-term stability in SOC systems.

2.2. Stack flow model order reduction methodology

CFD simulations are commonly employed to analyze and optimize the flow design of SOC stacks, providing insights into local flow velocities, concentration distributions, and temperature profiles [50]. Gas flow in planar stacks is typically governed by the principles of fluid dynamics in confined geometries. The flow regime is laminar inside of the channels, but often turbulent in parts of the manifolds due to the high flow rates required in large stacks. The Navier-Stokes equations can be used to describe mass and momentum transport, while species transport is modeled using convection-diffusion equations. For most applications however, simplifications are required due to the scale of the problem.

For the simulation of the flow inside single gas channels within a RU, approaches such as the plug flow or boundary layer model are often used to reduce computational complexity. These models have manageable computation times and are sufficiently accurate for the computation of species transport inside of SOC gas channels [85].

Simulation of the pressure drop across the stack and the associated flow maldistribution is a more complex problem to solve. While it is possible to solve the Navier-Stokes equations for the flow inside of a stack, computation times on such a scope are long. Such detailed flow simulations are only rarely combined with simulations of the electrochemical cells.

Instead, many reduced-order modeling approaches have been developed in order to allow for the combined computation of stack flow and chemical processes. One emergent modeling approach is the distributed resistance model which is an established method in the filed of heat exchanger design. The approach results in a great simplification of the flow model in the cells while still allowing reasonably detailed simulation of the flow in the manifolds [86].

Hydraulic network models are an alternative approach which consists of estimating the energy losses in a flow by relying on correlations derived from experiments or high fidelity simulation data. The advantage of such methods is that fluid flow can be accurately estimated by solving simple systems of algebraic equations. Their difficulty lies in finding accurate means of estimating energy losses in the fluid through various elements of a system.

As hydraulic network models are in widespread use in a variety of fields, there is a large body of literature dedicated to energy losses through various common system components under common operating conditions [87]. For example, the pressure drop Δp for the fully developed flow through an enclosed channel can be estimated using the Darcy-Weisbach equation $\Delta p = f_\mathrm{D} \cdot \frac{L}{D_h} \cdot \frac{\rho u^2}{2}$ where

f_D is the friction factor, L is the channel length, D_h is the hydraulic diameter, ρ is the gas density, and u is the average flow velocity. Therein, the friction factor is a function of the channel geometry and the flow conditions.

Unfortunately, parts of SOC manifold operate under flow conditions which have not been characterized extensively for such geometries. Still, the short computation time of hydraulic network models combined with their potential accuracy for the prediction of flow rates in SOC stack channels was deemed ideal for the purpose of full stack simulations.

In order to generate reliable data for the calibration and validation of a stack flow model relying on this methodology, 3D computational fluid dynamics simulations are performed using the open-source software package OpenFOAM as part of Chapter 3 [88]. The primary objective of these detailed simulations is to accurately capture the complex flow field within the stack's internal manifolds under various operating conditions in order to extract parameters required in a simplified flow model.

2.2.1. Governing equations

For the purposes of this dissertation, the fluid flow within the manifold is modeled as steady-state, incompressible and isothermal. The influence of the electrochemical reactions and the temperature changes is not directly considered in these simulations because the focus of the investigation lies on local flow phenomena, e.g., the magnitude of pressure drops at junctions and bends as a function of the flow parameters. At this scope, electrochemistry and heat transport only impact the Reynolds number of the flow. In the simulation campaign used for the parametrization of the flow model, the Reynolds number is varied through the flow velocity.

With these assumptions, the mass and momentum conservation equations to be solved can be formulated as follows [89]:

$$\nabla \cdot \mathbf{u} = 0, \tag{2.14}$$

$$\nabla \cdot (\mathbf{u} \otimes \mathbf{u}) = \nabla \cdot \mathbf{R} - \nabla \frac{p}{\rho}. \tag{2.15}$$

Here, $\mathbf{u}$ represents the velocity vector, $\mathbf{R}$ is the stress tensor, and $\frac{p}{\rho}$ is the kinematic pressure. According to the constitutive equation for incompressible Newtonian fluids, the stress tensor can be computed as follows:

$$\mathbf{R} = \nu \left(\nabla \mathbf{u} + (\nabla \mathbf{u})^\mathrm{T} \right), \tag{2.16}$$

where ν is the kinematic viscosity of the fluid.

The SimpleFOAM solver [90], an implementation of the SIMPLE algorithm for pressure-velocity coupling, is used to solve this set of equations. Linear numerical schemes with second order accuracy in space are used for the discretization of all terms of the equations. Aside from the upwind linear interpolation of face values used in the convective term, centered schemes are used.

All simulations were performed assuming the fluid properties of a 10% H_2 and 90% H_2O gas mixture at 650°C, corresponding to a kinematic viscosity of $\nu = 3.15 \cdot 10^{-4}$ $\mathrm{m^2\,s^{-1}}$ as computed using DETCHEM$^{\mathrm{SOC}}$ [91]. However, the simulations and the evaluation of their results were designed to fully take advantage of Reynolds similarity principle so that only the Reynolds number of the flow is of importance.

2.2.2. Grid convergence study

To ensure that the results of the numerical simulations are independent of the spatial discretization and to quantify the associated discretization error, a grid convergence study is performed.

The methodology follows the standardized procedure based on the Grid Convergence Index (GCI), as proposed by Roache [92]. The GCI provides a consistent, conservative error band on the calculated solution, offering a reliable measure of how close the solution is to the asymptotic value that would be obtained on an infinitely fine grid.

The study is conducted by systematically refining the computational mesh while keeping all other simulation parameters constant. A minimum of three grids with different resolutions are required: a coarse grid (grid 3), a medium grid (grid 2), and a fine grid (grid 1). A constant grid refinement ratio r needs to be maintained between the grids, defined as $r = h_{\text{coarse}}/h_{\text{fine}}$ where h is a characteristic cell size.

A representative value of the solution needs to be selected as a primary indicator for assessing the convergence. For the simulations performed in Chapter 3 [88], the total pressure drop across the stack was selected. The value of this variable is computed on each of the three grids, yielding the solutions ϕ_1, ϕ_2, and ϕ_3.

From these solutions, the effective order of convergence p can be determined. This value indicates how rapidly the solution converges as the mesh is refined and is calculated using the solutions from the three grids:

$$p = \frac{\ln\left(\frac{\phi_3 - \phi_2}{\phi_2 - \phi_1}\right)}{\ln(r)}. \tag{2.17}$$

When the asymptotic range of convergence is reached, p is expected to be reasonably close to the order of the numerical schemes used. For the second order schemes used in the detailed stack flow simulations, p should therefore approach 2.

Subsequently, the GCI for the grids can be calculated. The GCI represents an expected relative error compared to the solution on an infinitely fine mesh and serves as an error bar. It is computed from the error $\epsilon_{ab} = (\phi_a - \phi_b)/\phi_a$ between the solutions on grids a and b, and may be computed for the finer grid a from the following expression:

$$\text{GCI}_{ab} = \frac{F_\text{s}|\epsilon_{ab}|}{r^p - 1}, \tag{2.18}$$

where F_s is a factor of safety for which the recommended value of 3 is used in this dissertation. A small GCI value indicates that the solution is near the asymptotic value and that further refinement of the grid is unlikely to produce significant changes.

To further validate that the solution is in the asymptotic range, a consistency check of the GCI across different grid levels can be performed. This involves calculating the GCI for both the fine/medium grids (GCI_{12}) and the medium/coarse grids (GCI_{23}). If all simulations are in the asymptotic range of convergence, the following ratio should be approximately equal to 1.0, providing additional confidence in the convergence study [93]:

$$\frac{\text{GCI}_{23}}{r^p \cdot \text{GCI}_{12}} \approx 1.0\,. \tag{2.19}$$

2.2.3. Hydraulic network model

Hydraulic network modeling is a computational method that simplifies a complex 3D fluid system into a 1D network of interconnected branches (channels) and nodes (junctions). This approach yields a system of algebraic equations that can be solved with negligible computational cost, making it ideal for system-level engineering and optimization tasks.

The energy balance between two points of the network can be expressed with the Bernoulli equation, which is a statement of energy conservation along a single streamline. For an inviscid, incompressible and adiabatic flow, the equation states that the total energy, which comprises static pressure (p), dynamic pressure ($\frac{1}{2}\rho u^2$), and hydrostatic pressure ($\rho g h$), remains constant along a streamline:

$$p + \frac{1}{2}\rho u^2 + \rho g h = \text{constant}\,. \tag{2.20}$$

However, for the design of closed conduit flow systems, an energy balance across the full cross section of the fluid channels is more practical. Moreover, energy dissipation through viscous effects need to be considered in most systems. To account for this, practical models use the generalized Bernoulli equation, which considers the flow over the full channel cross section as well as energy sources and sinks. Removing the terms related to the potential gravitational energy which have negligible impact on gas flows of this scale, the extended Bernoulli equation can be expressed as [87]

$$(\bar{p}_1 + \alpha_1 \frac{1}{2}\bar{\rho}\bar{u}_1^2) - (\bar{p}_2 + \alpha_2 \frac{1}{2}\bar{\rho}\bar{u}_2^2) = \Delta p_{\text{loss}} \tag{2.21}$$

and deals with the properties of the flow averaged over the cross section.

The term Δp_{loss} represents the pressure change due primarily to energy dissipation from friction in straight channels and geometric features like bends and tees. In practice, these losses are quantified using Darcy friction factors f_D and pressure loss coefficients ζ, which are dimensionless coefficients determined for specific geometrical features and flow conditions through experimentation or high fidelity simulations.

The terms α are the kinetic energy correction factors and account for the fact that the velocity of the flow is not homogeneous across the channel cross-section. However, the velocity profile is often unknown in most practical cases. Thus, the kinetic energy correction terms are generally lumped into the pressure loss coefficients ζ so that the experimentally determined pressure change incorporates the combined effects of velocity profile reshaping and viscous losses. Therefore, Δp_{loss} also accounts for apparent energy changes related to reshaping the velocity profile while α_1 and α_2 are neglected.

A complete network model combines the extended Bernoulli equation for energy conservation along each branch with the principle of mass conservation at each node, where the total flow rate entering a junction must equal the total flow rate exiting. Solving this complete system of equations yields the pressure and flow rate distribution throughout the entire system.

2.3. SOC modeling methodology

Based on the understanding of the physical principles governing the operation of SOCs described in Section 2.1, it is possible to build models that capture all the relevant physical phenomena for the

targeted application. This dissertation aims at providing a consistent methodology for simulations from the scale of button cells up to stack modules so that the model may be calibrated based on button cell experiments and employed to predict the performance of stack modules. Transient models are prioritized, especially at the smallest scales, to enable the reproduction of transient experiments such as EIS which is crucial in the characterization of electrochemical systems.

In this section, all important components of the SOC model used in the publications constituting Chapters 4 [94] and 5 [95] are presented. The modeling framework is a continuation of previous modeling efforts by Deutschmann et al. [35, 38, 96, 97]. This section shares content with the methodology section of the publication presented in Chapter 4 [94], but provides more detail on the underlying assumptions of the equations and their derivation. It is structured according to the employed multi-scale modeling methodology, first presenting the models applied at the scale of the button cell, then along the length of a planar RU and finishing with the stack modeling methodology.

2.3.1. Gas transport in button cell gas compartments

Button cells are small circular cells usually manufactured for the sole purpose of testing. Due to their small diameter, button cells are easier to manufacture, convenient to experiment on and allow to assume homogeneous operating conditions across their surface. When designing a button cell model, this assumption leads to a model that is single-dimensional in space at most, as only gradients that are normal to the cell surface need to be considered.

The gas-filled volumes above and below a button cell, the gas compartments, are the outermost part of the present cell model. The gas composition in these volumes depend on the gas supply and the operation of the cell, which is why a model for the flow inside of the gas compartments is needed. As the change in gas composition in these compartments is noticeable in the results of EIS experiments, a transient flow model is required [98].

The typical operating conditions of button cells allow the application of the low Mach number assumption. This assumption is the broadest definition of incompressible flow, since its main implication is that pressure variations inside the flow are small enough to have a negligible impact on the density of the fluid, while still allowing changes in the fluid density through variations in temperature or composition [99]. In practice, low Mach number flow models are implemented by defining two different pressures. The *thermodynamic pressure* is a constant which is used to evaluate the constitutive equation, which in the present model is the ideal gas law. The *mechanical pressure*, conversely, is not constant and influences mass transport through the momentum conservation equation. This treatment of pressure is commonly referred to as *pressure filtering* [100].

For the simulation of chemically reacting flows, Day and Bell [101] developed a set of equations by simplifying the Navier-Stokes equations according to the low Mach number assumption. These equations serve as a base for the button cell gas compartment model derived in this section. Figure 2.4 shows a schematic of the control volume Ω representing the gas compartment in the model. For simplicity, it is represented as a cylinder, but since radial gradients in button cells will be neglected, the radial dimensions vanish from the equations.

The gas compartments of experimental setups designed for the characterization of button cells are engineered to create homogeneous gas properties over the electrode surface while minimizing gas

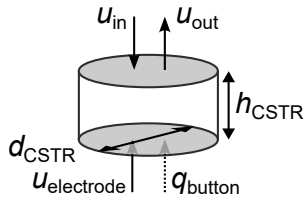

Figure 2.4.: Schematic of the assumed control volume for the button cell gas compartment model depicting gas velocities u and heat fluxes q.

diffusion between the gas compartments, the inlets and the outlets [102]. Back diffusion is usually eliminated by keeping elevated flow velocities through the gas compartment inlets and outlets. This results in increased Péclet numbers at the boundaries of the gas compartments, as is the case with $Pe > 20$ obtained with the recommended testing conditions of Klotz et al. [102] (referring to their reaction zone length of 1 cm, a diffusivity of $1.1 \cdot 10^{-3}$ $\mathrm{m^2\,s^{-1}}$ for hydrogen in a 40% H_2 / 60% H_2O mixture at 700°C and gas flow rates upwards of 250 sccm). Therefore, at the boundaries of the gas compartment Ω, diffusion phenomena are negligible compared to convection. This simplification leads to the following formulations for the incompressibility condition and the species conservation equations:

$$\nabla \cdot \mathbf{u} = \frac{1}{\rho c_p T} \nabla \cdot \mathbf{q} + \frac{1}{\rho} \sum_{m \in \mathbf{S}_\mathrm{g}} \left(\frac{W}{W_m} - \frac{h_m}{c_p T} \right) W_m \, \dot{\omega}_m, \tag{2.22}$$

$$\frac{\partial \, \rho \, Y_m}{\partial t} + \nabla \cdot \mathbf{u} \, \rho \, Y_m = W_m \, \dot{\omega}_m, \tag{2.23}$$

in which $\mathbf{u}$ is the velocity vector, ρ is the density of the gas mixture, T is the temperature, $\mathbf{q}$ is the heat flux vector field, W is the molecular mass of the gas mixture, W_m is the molecular mass of gas species m, c_p is the thermal capacity of the gas mixture, Y_m is the mass fraction of species m in the mixture and $\dot{\omega}_m$ is the molar production rate of species m through gas-phase reactions.

Conversely, inside of gas compartments, species diffusion can play an important role. However, the homogeneity of gas properties over the electrodes, which is an essential characteristic of optimized experimental setups, allows to avoid detailed considerations of the transport mechanisms within the gas compartments. Instead, the flow model is further simplified with the assumption that the properties of the gas inside Ω are constant, regardless of how this homogeneity is achieved. Therefore, the model is obtained by integrating Equations 2.22 and 2.23 over the volume of a gas compartment while assuming constant temperature and mass fractions for the gas inside the volume. Thereby, the divergence theorem allows to simplify the divergence terms and the volume integrals are simplified to multiplications with the volume due to the constant properties:

$$\oint_{\partial\Omega} \mathbf{u} \cdot \mathbf{n} \, dS = \frac{1}{\rho c_p T} \oint_{\partial\Omega} \mathbf{q} \cdot \mathbf{n} \, dS + \frac{V_\Omega}{\rho} \sum_{m \in \mathbf{S}_\mathrm{g}} \left(\frac{W}{W_m} - \frac{h_m}{c_p T} \right) W_m \, \dot{\omega}_m, \tag{2.24}$$

$$V_\Omega \frac{\partial \, \rho \, Y_m}{\partial t} + \oint_{\partial\Omega} \mathbf{u} \, \rho \, Y_m \cdot \mathbf{n} \, dS = V_\Omega W_m \, \dot{\omega}_m, \tag{2.25}$$

in which V_Ω is the volume of the gas compartment, $\partial\Omega$ is the boundary surface of the gas compartment and $\mathbf{n}$ is the field of normal vectors of $\partial\Omega$.

The surface integrals of the velocity can be substituted with the incoming volume flow rate $A_\mathrm{in} \, u_\mathrm{in}$, outgoing volume flow rate $A_\mathrm{out} \, u_\mathrm{out}$ and electrode volume flow rate $A_\mathrm{total} \, u_\mathrm{electrode}$. The surface

integrals of the mass flux $\mathbf{u}\,\rho\,Y_m$ can be substituted with the equivalent mass flow rates $A_{\text{in}}\,(u\,\rho\,Y_m)_{\text{in}}$, $A_{\text{out}}\,(u\,\rho\,Y_m)_{\text{out}}$ and $A_{\text{total}}\,(u\,\rho\,Y_m)_{\text{electrode}}$. The surface integral of the heat flux $\mathbf{q}$ is summarized as q_{button}, but no explicit formulation is provided because only isothermal button cell simulations were performed for this dissertation.

Simplifying A_{in} and A_{out} by averaging the incoming and outgoing flow over the full surface A_{total} leads to the final model [94]:

$$u_{\text{in}} + u_{\text{electrode}} - u_{\text{out}} = \frac{q_{\text{button}}}{\rho\,c_p\,T} + \frac{h_{\text{CSTR}}}{\rho} \sum_{m\,\in\,\mathbf{S}_{\text{g}}} \left(\frac{W}{W_m} - \frac{h_m}{c_p T} \right) W_m\,\dot{\omega}_m, \tag{2.26}$$

$$\frac{\partial\,\rho\,Y_m}{\partial t} + \frac{1}{h_{\text{CSTR}}} \left(u_{\text{in}} \rho_{\text{in}} Y_{m,\text{in}} - u_{\text{out}} \rho_{\text{out}} Y_{m,\text{out}} + J_m\,W_m \right) = W_m\,\dot{\omega}_m, \tag{2.27}$$

with u_{in} and u_{out} the velocity of the incoming and outgoing flow respectively (averaged over the full surface A_{total}), J_m the flux of species m through the electrode surface (see Equation 2.28) and h_{CSTR} the height of the gas compartment.

Due to the assumption of homogeneous gas composition in the gas compartments, this presented model corresponds to a transient CSTR model. For the same reason, no spacial gradients remain in the equations, which makes this model 0D. Still, the height of the gas compartment appears in the equations and has a significant impact on the transient behavior of the gas chamber.

2.3.2. Gas transport in porous electrodes

In the functional layer, diffusion layer, and current-collecting layer of each porous electrode, gas transport between the gas channel and the electrolyte is described using the dusty gas model (DGM). The DGM is well-suited to describe species transport in porous media because it accounts for the combined effect of multiple transport mechanisms acting simultaneously. Unlike simpler models such as Fickian diffusion or Stefan–Maxwell equations, the DGM can simultaneously capture multicomponent diffusion and pore-scale effects, making it particularly appropriate for SOC electrodes [36]. According to the DGM, the total molar flux of a species arises from three contributions: (i) viscous (Darcy) flow driven by pressure gradients, (ii) continuum (molecular) diffusion due to concentration gradients, and (iii) Knudsen diffusion caused by molecule–pore wall collisions when pore sizes are comparable to or smaller than the mean free path of gas molecules [103]. The balance of these mechanisms depends strongly on pore geometry, porosity, tortuosity, and operating conditions such as pressure and temperature.

Since gradients in all directions except across the MEA are neglected, the following transport equations are formulated in 1D. The expression for the area-specific molar flux J_m of gas-phase species $m \in \mathbf{S}_{\text{g}}$ is [32, 104]:

$$J_m = -\left[\sum_{k\,\in\,\mathbf{S}_{\text{g}}} D_{mk}^{\text{DGM}} \frac{\partial c_k}{\partial z} + \left(\sum_{k\,\in\,\mathbf{S}_{\text{g}}} \frac{D_{mk}^{\text{DGM}} c_k}{D_{k,\text{Kn}}^{\text{eff}}} \right) \frac{B_{\text{g}}}{\mu} \frac{\partial p}{\partial z} \right], \tag{2.28}$$

where the effective transport coefficients D_{mk}^{DGM}, $D_{k,\text{Kn}}^{\text{eff}}$ and B_{g}, which incorporate the influence of the porous microstructure, are defined as follows.

The generalized diffusion coefficients D_{kl}^{DGM} used in the DGM flux expression are obtained by inverting the resistance matrix $\mathbf{H}$:

$$D_{kl}^{\mathrm{DGM}} = (\mathbf{H}^{-1})_{kl}. \tag{2.29}$$

The entries H_{ab} of the transport matrix $\mathbf{H}$ describe the resistances to multicomponent diffusion in the porous medium. They combine the effects of Knudsen diffusion of species a and binary diffusion between a and the other species $k \in \mathbf{S}_{\mathrm{g}}$, weighted by their mole fractions X_k:

$$H_{ab} = \left[\frac{1}{D_{a,Kn}^{\mathrm{eff}}} + \sum_{k \in \mathbf{S}_{\mathrm{g}} \setminus a} \frac{X_k}{D_{ak}^{\mathrm{eff}}} \right] \delta_{ab} + (\delta_{ab} - 1) \frac{X_a}{D_{ab}^{\mathrm{eff}}}. \tag{2.30}$$

The coefficient B_{g} represents the permeability of the porous electrode to viscous flow. It depends on the porosity ε, mean pore diameter d_{pore}, and tortuosity factor τ_{pore}:

$$B_{\mathrm{g}} = \frac{\varepsilon^3 d_{\mathrm{pore}}^2}{72\, \tau_{\mathrm{pore}} \left(1 - \varepsilon\right)^2}. \tag{2.31}$$

The effective Knudsen diffusion coefficient $D_{k,Kn}^{\mathrm{eff}}$ accounts for molecular transport limited by collisions with pore walls. It scales with the mean pore diameter and decreases with tortuosity:

$$D_{k,Kn}^{\mathrm{eff}} = \frac{\varepsilon}{\tau_{\mathrm{pore}}} \frac{d_{\mathrm{pore}}}{3} \sqrt{\frac{8\, R\, T}{\pi\, W_k}}. \tag{2.32}$$

The effective binary diffusion coefficient D_{kl}^{eff} describes continuum diffusion between species k and l in the porous medium. Like the Knudsen coefficient, it is reduced relative to the bulk value D_{kl} due to porosity and tortuosity

$$D_{kl}^{\mathrm{eff}} = \frac{\varepsilon}{\tau_{\mathrm{pore}}} D_{kl}, \tag{2.33}$$

while the binary diffusion coefficients D_{kl} are computed by the DETCHEM software library [91] according to the kinetic theory of dilute gases [105].

Finally, the factor τ_{pore} is the tortuosity factor. It represents the elongation of gas transport paths caused by the complex pore geometry, thereby reducing the effective diffusivity. In the absence of measurements, it is estimated using Equation 2.62.

Based on the flux expression, a species conservation equation can be established for the density $\rho_m = Y_m\, \rho$ of species $m \in \mathbf{S}_{\mathrm{g}}$ in the porous electrode layers. Besides transport, this balance includes sources and sinks associated with electrochemical charge transfer reactions at phase boundaries and with thermocatalytic surface reactions [32, 104]:

$$\varepsilon \frac{\partial\, Y_m\, \rho}{\partial t} = -\frac{\partial\, J_m\, W_m}{\partial z} + \sum_{r \in \mathbf{R}_{\mathrm{CT}}} \frac{\nu_{m,r} i_{F,r}^{V} W_m}{n_{e,r} F} + W_m\, \dot{s}_m. \tag{2.34}$$

Here z is the spatial coordinate in the MEA-normal direction, $\dot{s}_m$ the production rate of species m by thermocatalytic reactions (Equation 2.37), $i_{F,r}^{V}$ the Faradaic charge transfer rate of reaction $r \in \mathbf{R}_{\mathrm{CT}}$ (Equation 2.41), $n_{e,r}$ the number of electrons transferred per reaction, and $\nu_{m,r}$ the stoichiometric coefficient of species m in reaction r. The pressure used in the flux definition (Equation 2.28) is evaluated from the ideal gas law, which is reasonable at typical SOC operating pressures and

temperatures. Summing Equation 2.34 over all gas species gives the conservation equation for the total gas density ρ. This results in a surplus of differential equations which is utilized to mitigate numerical errors. The conservation equation for the total gas density is solved in addition to the equations for all partial densities. The partial densities are renormalized to ensure that they sum up to the total density, and thereby numerical errors are compensated proportionally to the species mass fractions. This method is preferred to the conventional approach of computing the dominant species mass fraction as unity minus all other mass fractions because there is no universally dominant species in SOC systems.

At the channel/electrode boundary, the gas composition in the porous electrode is assumed to be identical to that in the channel, affirming the continuity of species concentrations. The flux J_m computed at this interface provides the coupling between the bulk gas transport in the channel and the porous media transport in the electrode. At the opposite side, the electrode/electrolyte interface is treated as impermeable to gases, enforcing a zero-flux boundary condition.

2.3.3. Thermocatalytic heterogeneous chemistry

When fuels other than pure hydrogen are supplied to the SOC, heterogeneous chemistry on the catalytically active electrode materials, most commonly nickel, must be taken into account. Typical examples include direct ammonia-fed fuel cells where internal ammonia decomposition occurs [67, 106], internal reforming of methane in natural-gas-fueled cells [32, 107], and internal methanation during co-electrolysis of H_2O and CO_2 [108].

Microkinetic modeling can be used to systematically understand and predict the behavior of thermocatalytic reactions in SOC electrodes. This approach involves constructing a detailed reaction mechanism consisting of elementary reaction steps such as adsorption, surface reactions, and desorption, each governed by temperature-dependent rate expressions [109]. By solving the coupled rate equations under steady-state or transient conditions, microkinetic models yield surface species coverages and overall reaction rates while reducing the amount of simplifying assumptions of rate-determining steps and quasi-equilibrium approximations.

This mechanistic rigor makes microkinetic modeling a powerful tool for exploring how operating conditions, catalyst properties, or gas compositions influence SOC performance. Reactions such as methane reforming, ammonia cracking or the reverse water-gas shift involve species that also take part in the electrochemical reactions. Considering all significant reaction steps as well as the the influence of surface coverages on reaction rates allows microkinetic models to better capture the interplay between thermocatalysis and electrocatalysis compared to methods using global kinetic expressions.

Incorporating surface reactions requires the introduction of additional state variables: the surface coverages θ_m of catalyst sites by surface species $m \in \mathbf{S}_{\text{surf}}$. The temporal evolution of these coverages is described by a conservation equation that depends on the site density Γ_{surf} and the surface-specific production rate $\dot{s}_m^A$ [38, 100, 110, 111]:

$$\frac{\partial \theta_m}{\partial t} = \frac{\psi_m \dot{s}_m^A}{\Gamma_{\text{surf}}}, \tag{2.35}$$

where ψ_m denotes the number of adsorption sites occupied by species m.

The bridge between the chemistry model and the mass transport models is made by computing the surface-specific production rates $\dot{s}_m^A$, which account for both gas-phase and surface species. They are obtained as the sum of contributions from all considered reactions $r \in \mathbf{R}_{\text{surf}}$ [111]:

$$\dot{s}_m^A = \sum_{r \in \mathbf{R}_{\text{surf}}} \left(\nu''_{m,r} - \nu'_{m,r}\right) k_{f,r} \prod_{k \in \mathbf{S}_{\text{g}} \cup \mathbf{S}_{\text{surf}}} c_k^{\nu'_{k,r}}, \tag{2.36}$$

where $\nu'_{m,r}$ and $\nu''_{m,r}$ are the stoichiometric coefficients of species m as reactant and product in reaction r. Therein, c_k denotes the concentration of species k, expressed in $[\text{mol}\,\text{m}^{-3}]$ for gas-phase species and $[\text{mol}\,\text{m}^{-2}]$ for surface species. The dimension of the rate constant $k_{f,r}$ therefore vary depending on the stoichiometry of the specific reaction. This expression is evaluated using the DETCHEM software library [91].

The production rates of surface species enter the source term of Equation 2.35. For gas-phase species, the model requires volumetric production rates. These are obtained by multiplying the surface-specific production rate with the catalyst surface area per unit volume A_{cat}^V, typically associated with the metallic phase:

$$\dot{s}_m = \dot{s}_m^A A_{\text{cat}}^V. \tag{2.37}$$

The forward reaction rate constants $k_{f,r}$ are expressed through a modified Arrhenius relation [111]

$$k_{f,r} = A_r T^{\kappa_r} \exp\left(-\frac{E_{a,r}}{RT}\right) \prod_{k \in \mathbf{S}_{\text{surf}}} \exp\left(\frac{\xi_{k,r}\theta_k}{RT}\right), \tag{2.38}$$

where A_r is the pre-exponential factor, κ_r introduces additional temperature dependence, $E_{a,r}$ is the activation energy, and $\xi_{k,r}$ represents the influence of lateral interactions with surface species k on the activation energy of reaction r.

These kinetic parameters are defined for each elementary step of the reaction mechanism. In the case study of Chapter 4, a mechanism for methane reforming and water-gas shift on nickel consisting of 42 elementary reactions is applied [112]. Nevertheless, other mechanisms may be substituted for different fuels or electrode compositions [113].

Thermodynamic consistency of such mechanism can be ensured using the approach of Maier et al. [111]. This procedure enforces that the ratio of forward and backward reaction rates reproduces the correct equilibrium constant. Backward reactions are introduced solely for this adjustment; in all other respects, the reaction set is treated as a collection of forward reactions in Equations 2.36 and 2.38.

2.3.4. Electrochemistry

The electrochemical model forms the core of a fuel cell simulation, since it establishes the relationship between the cell potential E_{cell} and the current density i.

In this dissertation, local electrochemical reaction rates are described using a modified Butler–Volmer equation. This relation connects the local half-cell activation overpotential η_{act} with the corresponding local charge transfer rate $i_r^{A/\lambda}$ of the electrochemical reaction r:

$$i_r^{A/\lambda} = i_{0,r} \left[\exp\left(\frac{\beta_{\text{a}} F n_{e,r} \eta_{\text{act}}}{RT} \right) - \exp\left(-\frac{\beta_{\text{c}} F n_{\text{e},r} \eta_{\text{act}}}{RT} \right) \right]. \tag{2.39}$$

Here, $i_{0,r}$ is the exchange current density, and $n_{\text{e},r}$ denotes the number of electrons transferred in reaction r. The parameters β_{a} and β_{c} are the anodic and cathodic charge transfer coefficients. They reflect how the activation barrier is split between the forward and backward directions of the reaction and therefore depend on the underlying elementary steps.

The exchange current density itself depends strongly on the electrode material and local gas composition. It is generally expressed in the following Arrhenius-type form:

$$i_{0,r} = A_r \exp\left(-\frac{E_r}{RT} \right) f(p_s), \tag{2.40}$$

where A_r is a pre-exponential factor, E_r is an apparent activation energy, and $f(p_s)$ is a function of the partial pressures of the reacting gases. The resulting exchange current density has different dimensions depending on the electrode type: A/cm in a cermet electrode (where reactions occur along a line at the TPB), and A/cm^2 in a mixed ionic–electronic conductor electrode (where reactions occur on the two phase boundary).

Strictly speaking, the Butler–Volmer equation is derived for single-step, single-electron transfer reactions. Nevertheless, it provides an accurate approximation for multistep reactions with multiple electron transfers by adjusting the values of $i_{0,r}$, β_a, and β_c to match experimental data [61]. As such, it is widely used as a phenomenological correlation even when the mechanistic details are unknown. In reversible SOC models, the same kinetic parameters can often be applied to both oxidation and reduction reactions, such as the oxygen evolution and oxygen reduction reactions [114–116]. Despite the fundamental differences in the elementary charge transfer reactions occurring depending on the mode of operation of the reversible cell, the approach of fitting a single set of representative kinetic parameters $i_{0,r}$, β_a, and β_c to experimental data can yield sufficient accuracy for engineering applications.

In the case study considered in Chapter 4 [94], both the LSM–YSZ air electrode and the Ni–YSZ fuel electrode are cermet electrodes. Charge transfer thus occurs at the triple phase boundary (TPB), where gas, ionic, and electronic conducting phases meet. The volumetric Faradaic charge transfer rate $i_{F,r}^V$ for reaction r is obtained as

$$i_{F,r}^V = i_r^\lambda \, \lambda_{\text{TPB}}^V, \tag{2.41}$$

where λ_{TPB}^V denotes the TPB length per unit volume. This expression effectively scales the local reaction rate at the TPB by the amount of electrochemically active interface present in the electrode microstructure.

The activation overpotential η_{act} is defined as the deviation between the actual electric potential difference and the corresponding reversible potential of the reaction. It depends on the electronic phase potential ϕ_{el}, the ionic phase potential ϕ_{io}, and the reversible half-cell potential $E_{\text{rev},r}$:

$$\eta_{\text{act}} = \phi_{\text{el}} - \phi_{\text{io}} - E_{\text{rev},r}. \tag{2.42}$$

The reversible potential $E_{\text{rev},r}$ for each reaction pathway is determined from the Gibbs free energies of formation and the local gas composition. For example [47],

$$E_{\text{rev,H}_2} = E^{\circ}_{\text{H}_2} + \frac{RT}{2\,F} \ln\left(\frac{p_{\text{H}_2\text{O}}}{p_{\text{H}_2}}\right), \tag{2.43}$$

$$E_{\text{rev,CO}} = E^{\circ}_{\text{CO}} + \frac{RT}{2\,F} \ln\left(\frac{p_{\text{CO}_2}}{p_{\text{CO}}}\right), \tag{2.44}$$

$$E_{\text{rev,O}_2} = E^{\circ}_{\text{O}_2} + \frac{RT}{4\,F} \ln\left[\left(\frac{p_{\text{O}_2}}{p_{\text{atm}}}\right)^{0.5}\right], \tag{2.45}$$

where $p_{\text{atm}} = 101325$ Pa. These expressions are essentially Nernst equations adapted to each electrochemical pathway.

If the fuel gas mixture allows both H_2/H_2O and CO/CO_2 electrochemical pathways, then reaction rates are computed for both mechanisms. However, both reactions occur at the same TPB and therefore compete for reactants and reaction sites. This competition effect is approximated by weighting the computed electrochemical reaction rates with the local mole fractions of the oxidized products H_2O and CO_2 [117]:

$$i^{\lambda}_{\text{total}} = w\, i^{\lambda}_{\text{H}_2/\text{H}_2\text{O}} + (1-w)\, i^{\lambda}_{\text{CO}/\text{CO}_2} \tag{2.46}$$

$$w = \frac{X_{\text{H}_2\text{O}}}{X_{\text{H}_2\text{O}} + X_{\text{CO}_2}}. \tag{2.47}$$

This ensures that the effective current density reflects the relative availability of each pathway according to the local gas composition, which itself varies across the electrode due to transport limitations and surface reaction site availability.

2.3.5. Charge transport

The electrochemical model presented above computes the charge transfer rate over the full thickness of both electrodes, rather than only at the porous electrode/bulk electrolyte interface as is often assumed in simplified approaches. As a result, the local overpotential η must be resolved at every position inside the electrode. This requires knowledge of the potential fields throughout the electron-conducting phase ϕ_{el} and the ion-conducting phase ϕ_{io}, which in turn depend on the corresponding current density fields i_{el} and i_{io}.

These quantities are determined by the charge transport model, which describes the motion of charge carriers generated throughout the porous electrodes by electrochemical reactions. Typically, these charge carriers are electrons e' in the electron-conducting phases and oxygen vacancies $\text{V}_{\text{O}}^{\bullet\bullet}$ in the ion-conducting phases. It is worth recalling that in this work, the term *electrode* refers to the the combined ion and electron conducting components of the porous solid phases on either side of the

central dense electrolyte membrane. The term *electrolyte* is reserved for the impermeable membrane itself.

In the present cell model, the distributed transport model developed by Zhu et al. [47] is applied. It originates from the Nernst–Planck formulation, but is simplified for materials with single charge-carrying species by neglecting charge transport driven by concentration gradients. With this assumption, the current density in a given phase $m \in \{\mathrm{el}, \mathrm{io}\}$ becomes directly proportional to its effective conductivity σ_m^{eff} (see Equation 2.60) and the gradient of the local potential:

$$i_m = \sigma_m^{\mathrm{eff}} \frac{\partial \phi_m}{\partial z}. \tag{2.48}$$

With the assumption of electroneutrality in the bulk of charge conducting materials, the divergence of the current densities in the electronic and ionic phases corresponds to the production (or consumption) of charge carriers, i.e. the volumetric charge transfer rate i_e^V. The charge transfer rates in the two phases are equal in magnitude and opposite in sign:

$$\frac{\partial i_{\mathrm{el}}}{\partial z} = i_e^V \tag{2.49}$$

$$\frac{\partial i_{\mathrm{io}}}{\partial z} = -i_e^V. \tag{2.50}$$

To close the system of equations, expressions for i_e^V together with appropriate boundary conditions are required. Here, the total charge transfer rate is assumed to consist of two contributions: the Faradaic charge transfer rate i_F^V and the charging of the electrical double layer i_{DL}^V:

$$i_e^V = i_F^V + i_{\mathrm{DL}}^V. \tag{2.51}$$

The Faradaic contribution is obtained from Equation 2.41, while the double-layer charging is described using a simple plate-capacitor model [33]:

$$\frac{\partial}{\partial t}\left(\phi_{\mathrm{el}} - \phi_{\mathrm{io}}\right) = \frac{i_{\mathrm{DL}}^V}{C_{\mathrm{DL}}\, A_{\mathrm{el/io}}^{\mathrm{V}}}, \tag{2.52}$$

where C_{DL} denotes the double-layer capacitance per unit surface area, and $A_{\mathrm{el/io}}^{\mathrm{V}}$ is the interfacial area between the electron- and ion-conducting phases per unit electrode volume.

The only transient term in the charge transport model is the charging of the double layer. This effect is primarily relevant for impedance spectroscopy simulations, where the short time scales of double-layer charging become significant. For steady-state or quasi-steady simulations, i_{DL}^V can safely be neglected. In such cases, the discretized form of Equations 2.49 and 2.50 becomes a set of algebraic equations that is solved numerically using the secant method.

Boundary conditions complete the problem specification. For the electron-conducting phase, the potential is fixed to E_{cell} at the air electrode/air-channel interface and to 0 V at the fuel electrode/fuel-channel interface. If the electrolyte is assumed to be a pure ionic conductor, the electronic current must vanish at both electrode/electrolyte boundaries. For the ionic phase, which extends through the cathode, electrolyte, and anode, the ionic current must vanish at the gas-channel boundaries.

Finally, contact resistances may be included at any phase interface. Contact resistances in cells are difficult to measure directly. They do however appear as part of the total ohmic resistance of a cell as can be measured for example as the high frequency intercept of EIS. The sum of contact

resistances may therefore be computed by subtracting the resistance of the bulk, determined through conductivity measurements of the individual materials, from the total ohmic resistance of a cell.

2.3.6. Microstructure

To describe gas transport, charge conduction, and electrochemical reactions in porous electrodes, a number of morphological parameters must be specified. These include porosity, tortuosity, characteristic pore sizes, interfacial surface areas, and TPB lengths.

While some of these characteristics can be measured directly, or inferred from microstructural simulations of sintering, it is more convenient for the purpose of modeling if they can be predicted reliably with analytical relations.

Electrode preparation routes impact the resulting morphologies significantly, so the microstructure model needs to be adapted to the considered electrodes. In this work, only cermet electrodes and single phase electrodes sintered in a single manufacturing step are considered. Therefore, the analytical framework proposed by Bertei and Nicolella is employed [118, 119], which considers a three-phase system consisting of pore formers f, an electron conductor k and an ion conductor l which form the set of materials $\mathbf{S}_p = \{k, l, f\}$. Herein, their equations are simplified by assuming that the powders for k, l and f are monodisperse. Differences in particle sizes between materials are still considered. In percolation theory, the key parameter is the percolation probability γ_h of each phase $h \in \mathbf{S}_p$. The percolation probability reflects the likelihood of a continuous network of the phase forming across the electrode, and is the basis of the microstructure model. It is calculated as [119]

$$\gamma_h = 1 - \left(\frac{4.236 - Z_{h,h}}{2.472} \right)^{3.7}, \tag{2.53}$$

with $Z_{h,h}$ the average number of contacts per particle of phase h.

The average number of contacts between any two particle types $h, g \in \mathbf{S}_p$ is computed as follows [119]:

$$Z_{h,g} = \frac{\xi_g r_g^2}{\sum_{p \in \mathbf{S}_p} \xi_p r_p^2} \begin{cases} \frac{3\left(2-\sqrt{3}\right)\left(P_{h,g}+1\right)}{1+P_{h,g}-\left(P_{h,g}\left(P_{h,g}+2\right)\right)^{0.5}} & \text{if} P_{h,g} \geq 1 \\ \frac{3\left(2-\sqrt{3}\right)\left(P_{h,g}^{-1}+1\right)}{\left[1+P_{h,g}^{-1}-\left(P_{h,g}^{-1}\left(P_{h,g}^{-1}+2\right)\right)^{0.5}\right]P_{h,g}^{-2}} & \text{if} P_{h,g} < 1 \end{cases} \tag{2.54}$$

$$\text{with} \quad P_{h,g} = \frac{d_h}{d_g} \tag{2.55}$$

and with the particle diameters d and the particle number ratios (before sintering) ξ.

Assuming a contact angle of particles after sintering of 15°, the expression for the TPB density λ_{TPB}^V which is required by the electrochemical model follows as [119]

$$\lambda_{\text{TPB}}^V = \gamma_k \gamma_l Z_{k,l} \pi \min\left(d_k, d_l\right) \sin \tfrac{\pi}{12} \xi_k n_{\text{BS}}^V, \tag{2.56}$$

where n_{BS}^V is the number of particles per unit volume before sintering. It is computed as [119]

$$n_{\text{BS}}^V = \frac{6}{\pi} \frac{(1 - \varepsilon_{\text{BS}})}{\sum_{p \in \mathbf{S}_p} \xi_p d_p^3}, \tag{2.57}$$

with $\varepsilon_{\mathrm{BS}}$ the porosity before sintering. Since porosity before sintering and pore former particle diameter are seldom provided in the literature, the porosity before sintering is generally assumed to be 0.36 (the densest packing for monodisperse hard spheres) and the pore former particle diameter is assumed to be the same as the electron conductor particle diameter.

The area of contact between k and l is required by the plate capacitor model of the charge transport model. It is computed as [119]

$$A_{k/l}^{V} = \gamma_k \gamma_l Z_{k,l} \frac{\pi}{4} \left(\min\left(d_k, d_l\right) \sin \tfrac{\pi}{12}\right)^2 \xi_k n_{\mathrm{BS}}^{V}. \tag{2.58}$$

The total surface area of a particle k exposed to the gas phase after sintering $A_{k/\mathrm{g}}^{V}$ also needs to be determined for the thermocatalytic model, as the electron conductor is often catalytically active. It is estimated as [119]:

$$A_{k/\mathrm{g}}^{V} = \pi n_{\mathrm{BS}}^{V} \xi_k d_k^2. \tag{2.59}$$

In a single-phase MIEC electrode, n_{BS}^{V} can be computed with $\xi_l = 0$ and the value of $A_{k/\mathrm{g}}^{V}$ is also used in the electrochemical model and as the surface area of the plate capacitor model.

Knowing the percolation probabilities of k and l, it is possible to estimate the effective conductivity of each phase $p \in \{k, l\}$ by scaling the bulk material conductivity σ_p^{mat} [120]:

$$\sigma_p^{\mathrm{eff}} = \sigma_p^{\mathrm{mat}} \left[\left(1 - \varepsilon\right) \alpha_p \gamma_p\right]^{1.5} \tag{2.60}$$

in which $\alpha_p = \frac{\xi_p d_p^3}{\xi_k d_k^3 + \xi_l d_l^3}$ is the solid volume fraction and ε is the porosity after sintering which includes the pore former phase.

The average pore diameter d_{pore} and pore phase tortuosity τ_{pore} remain to be determined for the gas transport model in the electrodes. The average pore diameter is estimated as [97]

$$d_{\mathrm{pore}} = \frac{2}{3} \frac{\varepsilon}{1 - \varepsilon_{\mathrm{BS}}} \frac{d_k d_l}{\alpha_{k,\mathrm{BS}}\, d_l + \alpha_{l,\mathrm{BS}}\, d_k}, \tag{2.61}$$

with the solid volume fraction before sintering $\alpha_{p,\mathrm{BS}} = \frac{\xi_p d_p^3}{\sum_{i \in S_p} \xi_i d_i^3}$ while the tortuosity is estimated as [121]

$$\tau_{\mathrm{pore}} = \left(1.23 \frac{(1 - \varepsilon)^{4/3}}{\varepsilon}\right)^2. \tag{2.62}$$

2.3.7. Gas transport in planar RU gas channels

All of the models presented up to this point can be combined in order to form a 1D button cell model. For the simulation of 2D planar RUs, the assumption that species diffusion and charge transport along the length of the MEA are negligible allows to use the same model equations for the MEA itself. By introducing a flow model for the gas channels, the second dimension of the problem is added. The flow model is already sufficient to finalize a model for a combination of gas channel, MEA and fuel channel under isothermal conditions. Assuming homogeneous operating conditions in the third dimension, this constitutes a model for planar RUs. The heat transport model of the subsequent section will complete this RU model.

The treatment of bulk gas flow in planar RU channels builds on similar considerations as introduced for button cells in Section 2.3.1. Both approaches rely on the low Mach number assumption, which allows pressure variations to be neglected in the equation of state while still accounting for density changes due to composition and temperature.

The main difference lies in the geometry and characteristic flow behavior. While button cells are small enough that gas compartments can be assumed to be perfectly mixed, planar RUs involve narrow, elongated channels. These channels require a spatially resolved description of the flow along their length. Figure 2.5 illustrates a segment of such a gas channel considered in this section.

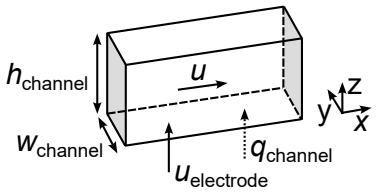

Figure 2.5.: Schematic of a differential element of the SOC gas channel model depicting gas velocities u and heat fluxes q. While illustrated in 3D, dimensions y and z are eliminated from the final system of equations through assumptions of homogeneity.

In order to shorten computation times, the plug flow model was considered. However, in order to enable transient simulations of the flow in planar RUs, a transient model with similar assumptions was developed as part of this dissertation. The three following assumptions are applied: (i) the low Mach number assumption, (ii) negligible diffusion in the flow compared to convection [85], and (iii) cross-section homogeneity in the channel due to the narrow channel geometry [100].

The initial set of equations is obtained from the low Mach number reacting flow transport equations of Day and Bell [101]. After removing the diffusion terms according to the second assumption, they are as follows:

$$\nabla \cdot \mathbf{u} = \frac{1}{\rho c_p T} \nabla \cdot \mathbf{q} + \frac{1}{\rho} \sum_{m \in \mathbf{S}_\mathrm{g}} \left(\frac{W}{W_m} - \frac{h_m}{c_p T} \right) W_m \dot{\omega}_m, \tag{2.63}$$

$$\frac{\partial \rho Y_m}{\partial t} + \nabla \cdot \mathbf{u} \rho Y_m = W_m \dot{\omega}_m, \tag{2.64}$$

where $\mathbf{u}$ is the velocity vector field, W the molecular weight of the gas mixture, h_m the specific enthalpy of species m, $\dot{\omega}_m$ the volume-specific production rate, and Y_m the mass fraction of species m in the set of gas species $\mathbf{S}_\mathrm{g}$. $\mathbf{q}$ is the heat flux vector field, and since diffusion inside the flow is negligible, it is only relevant at the boundary.

The first equation corresponds to the conservation of mass under low Mach number conditions. Therein, the divergence of the velocity field $\nabla \cdot \mathbf{u}$ is driven by heat fluxes $\mathbf{q}$ and by local species production terms $\dot{\omega}_m$. The second equation describes the conservation of species.

The absence of the momentum conservation equation is notable. Under the assumptions of an incompressible flow that is homogeneous over the channel cross-section, the velocity field can already be fully determined from Equation 2.63.

Due to the assumption of cross-sectional homogeneity, all gradients in two directions (chosen to be y and z) inside of the channel can be negated. However, some fluxes through the lateral channel boundaries need to be considered. These fluxes can be accounted for during the integration of

Equations 2.63 and 2.64 over the cross section of the channel. Integrating the equations over the channel cross section is simplified by the constant flow properties in the two concerned dimensions. When the properties are constant and there are no fluxes through the boundaries, the integration is simply a multiplication with the cross section area. If fluxes through the boundaries are present, they appear as additional terms that may be considered source terms in the final 1D differential equation.

Integration of Equation 2.63 over the cross section produces two source terms. The first results from the gas flux across the channel/electrode boundary and is given by

$$w_{\text{channel}}\, u_{\text{electrode}} = w_{\text{channel}} \frac{RT}{p} \sum_{m \in \mathbf{S}_\text{g}} J_m, \tag{2.65}$$

where w_{channel} is the width of the gas channel, $u_{\text{electrode}}$ is the velocity of the flow coming from the porous electrode and J_m is computed according to Equation 2.28. The second term is a result of the heat flux between the gas and the channel boundaries and is given by

$$\frac{1}{\rho\, c_p T}\, q_{\text{channel}} = \frac{w_{\text{channel}} \left(q^N_{\text{conv}} - q^S_{\text{conv}}\right) + h_{\text{channel}} \left(q^T_{\text{conv}} - q^B_{\text{conv}}\right)}{\rho\, c_p T}, \tag{2.66}$$

where q^N_{conv}, q^S_{conv}, q^T_{conv} and q^B_{conv} represent the wall-normal heat flux at the north, south, top and bottom boundaries of the rectangular channel. They are computed according to Equation 2.74 presented as part of the heat transport model.

Integration of the species concentration Equation 2.64 over the cross section produces a single source term $w_{\text{channel}}\, W_m\, J_m$ due to the species flux across the channel/electrode boundary.

Dividing the partially integrated set of equations by the cross section area produces the final 1D model equations [94]:

$$\frac{\partial u}{\partial x} = \frac{u_{\text{electrode}}}{h_{\text{channel}}} + \frac{1}{\rho\, c_p T} \frac{q_{\text{channel}}}{h_{\text{channel}}\, w_{\text{channel}}} + \frac{1}{\rho} \sum_{m \in \mathbf{S}_\text{g}} \left(\frac{W}{W_m} - \frac{h_m}{c_p T}\right) W_m\, \dot{\omega}_m, \tag{2.67}$$

$$\frac{\partial\, \rho\, Y_m}{\partial t} = -\frac{\partial\, u\, \rho\, Y_m}{\partial x} + W_m\, \dot{\omega}_m + \frac{W_m\, J_m}{h_{\text{channel}}}. \tag{2.68}$$

These equations are closely coupled to the heat transport equations presented in Section 2.3.8 through the temperature, the temperature-dependent gas properties and the heat source term q_{channel}.

Finally, the boundary conditions at the inlet consist of prescribing an inlet flux with a specified velocity, temperature, and composition. Since the velocity profile across the channel is not resolved, entrance effects are not considered.

2.3.8. Heat transport in planar RU gas channels

While button cells can generally be assumed to be operated isothermally due to their small dimensions and the typically high gas flow rates, the performance of larger planar SOCs is significantly impacted by temperature gradients along the MEA. Therefore, a heat transport model that takes into account all significant heat sources and sinks is critical for the accuracy of planar RU simulations. This section presents the model for heat transport through the gas channels of planar RUs, while the two following sections present the two different models for the transport of heat through the solid phase used in planar RUs and stack simulations respectively.

Heat transport through the gas channels is computed using an energy conservation equation derived from the model of Day and Bell [101] in the same fashion as the mass transport model presented in the previous section. The final transport equation in 1D is given by

$$\frac{\partial \rho\, h}{\partial t} = -\frac{\partial\, \mathbf{u}\, \rho\, h}{\partial x} + \frac{q_{\text{channel}}}{h_{\text{channel}} w_{\text{channel}}} \tag{2.69}$$

Since the specific enthalpy h is a nonlinear function of the gas temperature T, the temperature is determined iteratively using the Newton method. q_{channel} is defined as in Equation 2.66.

The source term q_{channel} represents the heat exchanged between the gas phase and the channel walls. Since the flow and temperature profile inside the channel are not resolved, the heat flux needs to be estimated using an empirical correlations for forced convection through a channel.

The following set of expressions is used in order to estimate the convective heat transfer coefficient h_{conv} using an empirical expression for the Nusselt number Nu in fully developed laminar flow in catalytic monolith channels [122]:

$$h_{\text{conv}} = \frac{Nu\, \lambda_{\text{g}}}{d_{\text{h}}}, \tag{2.70}$$

$$Nu = 3.095 + 8.933 \left(\frac{1000}{Gz}\right)^{-0.5386} exp\left(-\frac{6.7275}{Gz}\right), \tag{2.71}$$

$$Gz = \frac{d_{\text{h}}}{x} Re\, Pr, \tag{2.72}$$

$$d_{\text{h}} = \frac{2\, w_{\text{channel}}\, h_{\text{channel}}}{w_{\text{channel}} + h_{\text{channel}}}, \tag{2.73}$$

where λ_g is the heat conductivity of the gas, d_{h} is the hydraulic diameter of the channel, x is the distance to the channel inlet, Re is the Reynolds number of the flow and Pr is the Prandtl number of the fluid.

The heat transfer coefficient h_{conv} allows to compute the heat flux through the lateral boundaries of the channels:

$$q_{\text{conv}} = h_{\text{conv}}\, (T_{\text{solid}} - T)\,. \tag{2.74}$$

Since the convective heat flux depends on the gas temperature T, the solid surface temperatures T_{solid} and the gas flow, it varies along the length of the gas channel and may even vary along its perimeter. However, as the 1D flow model is coupled to a 1D MEA model, the temperature of every channel side varies only along its length.

2.3.9. Heat transport through the solid phase of planar RUs

For the solid phase of planar RUs, the following heat diffusion equation is solved in 2D [38]:

$$\rho^{\text{eff}} c_p^{\text{eff}} \frac{\partial T}{\partial t} = \nabla \cdot \lambda^{\text{eff}} \nabla T + \dot{q}^{V}_{\text{solid}} \tag{2.75}$$

where ρ^{eff} is the effective density, c_p^{eff} is the effective specific heat capacity and λ^{eff} is the effective thermal conductivity of the solid phase.

The material properties are expressed as effective properties because SOC electrodes are porous and composite. Instead of resolving the heat transport through their complex mircrostructure, the

properties of the electrodes are homogenized by averaging the thermal properties of their constituents according to their volume fractions. These effective properties are computed as follows [38]:

$$\rho_l^{\text{eff}} = \sum_{m \in \mathbf{M}_l} \alpha_{m,l}\, \rho_m \tag{2.76}$$

$$c_{p,l}^{\text{eff}} = \sum_{m \in \mathbf{M}_l} \alpha_{m,l}\, c_{p,m} \tag{2.77}$$

$$\lambda_l^{\text{eff}} = \prod_{m \in \mathbf{M}_l} {\lambda_m}^{\alpha_{m,l}} \tag{2.78}$$

with $\alpha_{m,l}$ being the volume fraction of the material m from the set of all materials $\mathbf{M}_l$ in the layer l. $\mathbf{M}_l$ typically contains an electrode material, and electrolyte material and a gas phase. The volume fractions should sum up to unity: $\sum_{m \in \mathbf{M}_l} \alpha_{m,l} = 1$.

In Equation 2.75, $\dot{q}^V_{\text{solid}}$ represents the sum of all volumetric heat source terms, which is different depending on the location in the cell. In electrodes where thermocatalytic reactions take place, typically the fuel electrode, $\dot{q}^V_{\text{solid}}$ includes reaction enthalpy:

$$\dot{q}^V_{\text{schem}} = - \sum_{k \in \mathbf{S}_{\text{g}}} h_k \dot{s}_k W_k. \tag{2.79}$$

The reversible reaction heat $\dot{q}^V_{\text{echem}}$ from the charge transfer reactions

$$\dot{q}^V_{\text{echem}} = - \sum_{r \in \mathbf{R}_{\text{CT}}} \frac{i^V_{F,r}}{n_{e,r}\, F} T \Delta s_r \tag{2.80}$$

with the molar reaction entropy Δs_r is also assumed to be entirely released in the fuel electrode, since computing the reaction heat from half-cell reaction would require thermodynamic properties of charge carriers which are difficult to determine. The activation losses $\dot{q}^V_{\text{act}}$ from the charge transfer reactions are considered in both electrodes and computed as

$$\dot{q}^V_{\text{act}} = \eta_{\text{act},r} i^V_{F,r}. \tag{2.81}$$

Due to the transport of electrons and ions through materials with finite conductivity, Joule heating $\dot{q}^V_{\text{joule}}$ also needs to be included in $\dot{q}^V_{\text{solid}}$. It is computed as

$$\dot{q}^V_{\text{joule}} = \frac{i^2_{\text{el}}}{\sigma^{\text{eff}}_{\text{el}}} + \frac{i^2_{\text{io}}}{\sigma^{\text{eff}}_{\text{io}}} \tag{2.82}$$

with the effective conductivities of the electron and ion conducting phases σ^{eff} and the current densities i. Additionally, contact resistances R_{cont} must often be taken into account due to the numerous phase interfaces in SOCs. The joule heating from contact resistances is computed as

$$q_{\text{joule,cont}} = i^2 R_{\text{cont}}. \tag{2.83}$$

While Joule heating through contact resistance is area specific, its implementation is simplified by considering it as a volumetric heat source in the adjacent discretized volume of the neighboring electrode.

Since the present heat transport model is 2D, the combination of the interconnect and the gas channels requires special consideration. In such a model, the ribs of the interconnect occupy the same space as the gas channels. At these points in space, a solid phase and gas phase temperature

need to be distinguished and the surfaces relevant to the following heat transport mechanisms need to be carefully considered. Therefore, the diffusive heat transport term $\nabla \cdot \lambda^{\text{eff}} \nabla T$ of Equation 2.75, which also applies to the interface between electrode and ribs, needs to be amended in order to account for the reduced contact area between the two.

In addition, at the high operating temperature of SOCs, heat transport through radiation may become significant. In the present model, heat transport across the gas channel through radiation is considered and computed according to the following heat flux [38]:

$$q_{\text{rad}} = \frac{\sigma_{\text{SB}} \left(T_{\text{ede}}^4 - T_{\text{ic}}^4\right)}{R_{\text{rad,ede}\to\text{ic}}} \tag{2.84}$$

with the electrode surface temperature T_{ede}, the interconnect surface temperature T_{ic} and the Stefan-Boltzmann constant σ_{SB}. Like Joule heating through contact resistances, the heat flux is implemented as a volumetric source term applied to the concerned discretized volumes.

$R_{\text{rad,ede}\to\text{ic}}$ is the thermal resistance to radiation, and includes the dimensions of the channel w_{channel} and h_{channel}, the view factors F between these areas and their total emissivities ϵ [38]:

$$R_{\text{rad,ede}\to\text{ic}} = \frac{1-\epsilon_{\text{ede}}}{\epsilon_{\text{ede}}} + \frac{1}{F_{\text{ede}\to\text{ic}}} + \frac{1-\epsilon_{\text{ic}}}{\epsilon_{\text{ic}}\left(1 + 2\,h_{\text{channel}}/w_{\text{channel}}\right)} \tag{2.85}$$

in which $F_{\text{ede}\to\text{ic}} = F_{\text{ede}\to\text{ic,plate}} + F_{\text{ede}\to\text{ic,rib}}$.

Finally, every surface of the channel also produces a convective heat transport term q_{conv}, as discussed in the previous section (see Equation 2.74).

Because of the high thermal conductivity of metallic interconnects compared to ceramic MEA materials, the temperature of the interconnect is assumed to be homogeneous inside of its cross section.

2.3.10. Heat transport through the solid phase of stacks

For the simulation of SOC stacks, a 3D heat transport model is used instead of the previous 2D model in order to observe the effects of heat loss through all sides of the stack on the performance of different regions of the stack.

In order to limit the growth in numerical complexity despite the increased problem scope, the thermal model of the stack is homogenized. Instead of considering the individual layers of the MEA, the interconnect and the gas channels, the full RU is assimilated to a porous monolithic material with anisotropic effective thermal properties. Information about temperature differences between individual layers of a RU is lost, but the macroscopic behavior of the stack is approximated. This simplification allows the same heat transport equation as before to be solved in 3D, but using a much coarser discretization:

$$\rho^{\text{eff}} c_p^{\text{eff}} \frac{\partial T}{\partial t} = \nabla \cdot \lambda^{\text{eff}} \nabla T + \dot{q}_{\text{solid}}^{V}. \tag{2.86}$$

The effective properties ρ^{eff} and c_p^{eff} are still computed according to Equations 2.76 and 2.77, but the averaging is performed at the scale of a RU. In order to accurately model the anisotropic thermal conductivity that results from the layered structure of RUs, the computation of λ^{eff} is adjusted according to the method of Banerjee et al. [38] which consists of modeling the heat transfer resistance

of a RU as a combination of series and parallel heat transfer resistances of its individual components. The exact arrangement of the resistance network depends on the cell structure and the considered direction, which is where the anisotropy arises.

Since the layers of the RUs are homogenized, $\dot{q}^V_{\text{solid}}$ needs to include all the heat source terms from every layer of the RU, averaged over the RU height. However, these can only be computed as part of the 2D planar RU presented above, which requires a fine discretization of the MEA. Therefore, the 2D RU model is nested within the 3D heat transport model by solving it in a different space with a different discretization and homogenizing the resulting heat sources over the RU height. This principle is illustrated in Figure 2.6 and further discussed as part of the numerical methods in Section 2.4.2.

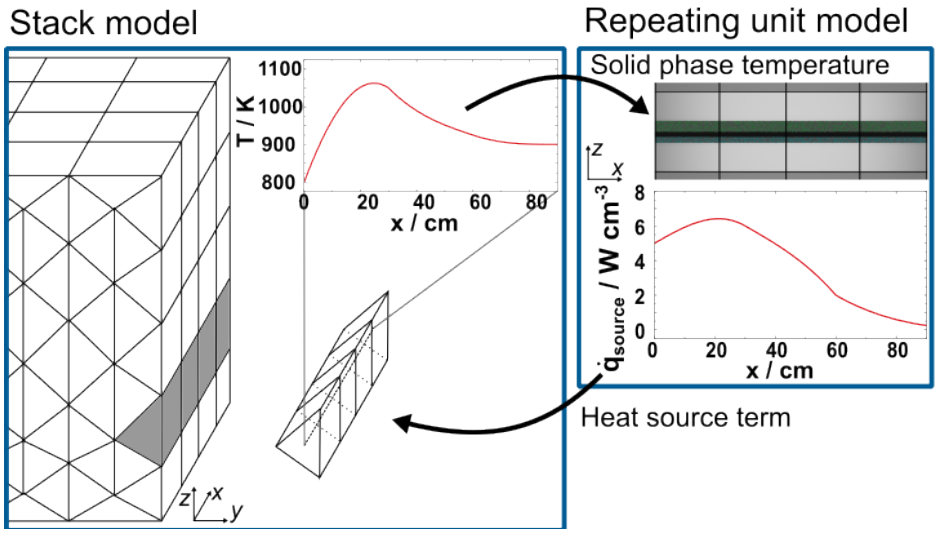

Figure 2.6.: Illustration of the homogenization of the stack heat transport model and its interaction with the RU model. Reproduced from Furst et al. [94], licensed under CC BY 4.0.

In the stack simulations performed in this study, SOC stacks were assumed to be insulated by a thick layer of inert material with low thermal conductivity and resting in air at ambient temperature. In such conditions, the heat is conducted from the insulation layer to the ambient air, but the heat transfer rate is strongly influenced by the free convection of air that arises from the heat transfer. Therefore, the boundary flux around the stack is computed from empirical expressions for the heat transfer coefficient of planes under free convection.

As the heat transfer rate across a given plane also depends on its orientation, three different coefficients are required. In all cases, the heat transfer rate h_{free} is computed from the Nusselt number Nu, the characteristic length of the surface l_{char} and the thermal conductivity of the gas λ_{env}:

$$h_{\text{free}} = \frac{Nu}{l_{\text{char}}} \lambda_{\text{env}}. \tag{2.87}$$

The differences arise in the computation of the Nusselt number, which is itself a function of the Prandtl number $Pr = \mu/\rho\,\alpha$ and the Rayleigh number $Ra = \rho\,\beta\,\Delta T\,l^3_{\text{char}}\,g/\mu\,\alpha$ with the thermal expansion coefficient β, the acceleration due to gravity g, the dynamic viscosity μ and the thermal diffusivity α.

For the vertical planes around the sides of the stack, Nu_{vertical} is computed as

$$Nu_{\text{vertical}} = (0.825 + 0.387\, Ra^{\frac{1}{6}} f_1)^2 \tag{2.88}$$

$$\text{with } f_1 = (1 + 0.671\, Pr^{-\frac{9}{16}})^{-\frac{8}{27}}. \tag{2.89}$$

For the horizontal plane at the top of the stack, Nu_{upper} is computed as

$$Nu_{\text{upper}} = \begin{cases} 0.766\,(Ra \cdot f_2)^{\frac{1}{5}}, & \text{if } Ra \cdot f_2 \leq 70000 \\ 0.15\,(Ra \cdot f_2)^{\frac{1}{3}}, & \text{otherwise} \end{cases} \tag{2.90}$$

$$\text{with } f_2 = (1 + 0.536\, Pr^{-\frac{11}{20}})^{-\frac{20}{11}}. \tag{2.91}$$

For the horizontal plane at the bottom of the stack, Nu_{lower} is computed as

$$Nu_{\text{lower}} = 0.27\, Ra^{\frac{1}{4}}. \tag{2.92}$$

In the interest of thoroughness, losses to the environment through radiation are also considered. The final expression for the heat flux at the stack surface is therefore

$$q_{\text{surf}} = h_{\text{free}}(T - T_{\text{env}}) + \epsilon_{\text{surf}}\, \sigma_{\text{SB}}\, (T^4 - T_{\text{env}}^4) \tag{2.93}$$

with the emissivity of the surface of the insulation layer ϵ_{surf} and the Stefan–Boltzmann constant σ_{SB}.

2.3.11. Flow through the stack

For the simulation of stacks in which differences in flow rates between different channels are suspected to significantly impact performance, a model for the flow through the entire stack is required.

In this dissertation, the flow through SOC stacks, specifically those with internal manifolds, is modeled using a hydraulic network model. With this method, the flow through channels is considered to be 1D and the relationship between pressure, velocity and the properties of the fluid is computed using the Bernoulli equation, with added terms for pressure losses through friction. Flow features which disperse energy through friction, such as the junctions and bends, are reflected in the model equations by pressure loss terms that depend on the local geometry and properties of the flow.

Herein, this methodology was selected because it is computationally inexpensive compared to the other common methodologies considered for the simulation of the flow in SOC stacks, which consist of adding partial differential equations. The network model implemented in this dissertation consists of $(8 + 2\, n_{\text{RU}})\, n_{\text{cells}}$ equations for the full flow through the stack, with n_{RU} the number of gas channels for a single gas type in a single RU and n_{cells} the number of cells in the stack. Naturally, this computational efficiency is only possible because the mechanics of the flow are greatly simplified. Still, good accuracy can be reached, as is shown in Chapter 3 and the corresponding publication [88].

The accuracy of this model mostly depends on the accuracy of the expressions used to estimate the energy dissipation through friction in the system components. The flow network and the energy losses considered in this model, expressed as drop in total pressure Δp, are depicted in Figure 2.7.

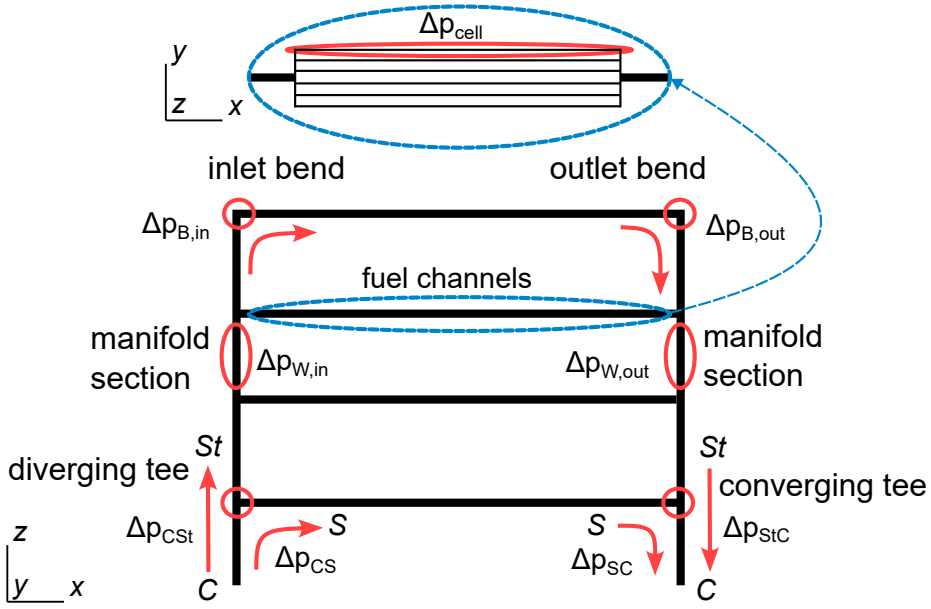

Figure 2.7.: Schematic of the flow within a stack with internal manifold. The pressure losses identified and included in the hydraulic network model are marked in red. The nomenclature used to differentiate the common channel (C), side channel (S) and straight passage (St) of the diverging and converging tee junctions is shown. Reproduced from Furst et al. [94], licensed under CC BY 4.0.

By formulating equations for the conservation of mass and energy at intersections of the flow and across the gas channels for a stack with U-type manifold, the following set of equations is obtained for each gas type (fuel and sweep gas) of each cell $k \in [1, n_{\text{cells}}]$ [94]:

$$\begin{cases} Q^k_{\text{in}} - \sum_j^{n_{\text{RU}}} Q^k_{\text{RU}\,j} = 0 & k = n_{\text{cells}} \\ Q^k_{\text{in}} - Q^{k+1}_{\text{in}} - \sum_j^{n_{\text{RU}}} Q^k_{\text{RU}\,j} = 0 & k \neq n_{\text{cells}} \end{cases} \tag{2.94}$$

$$\begin{cases} Q^k_{\text{out}} - \sum_j^{n_{\text{RU}}} Q^k_{\text{RU}\,j} = 0 & k = n_{\text{cells}} \\ Q^k_{\text{out}} - Q^{k+1}_{\text{out}} - \sum_j^{n_{\text{RU}}} Q^k_{\text{RU}\,j} = 0 & k \neq n_{\text{cells}} \end{cases} \tag{2.95}$$

$$\begin{cases} Q^k_{\text{in}} - Q_{\text{tot}} = 0 & k = 1 \\ p^{k-1}_{\text{tot,in}} + \Delta p^{k-1}_{\text{W,in}} + \Delta p^{k-1}_{\text{CSt}} - p^k_{\text{tot,in}} = 0 & k \neq 1 \end{cases} \tag{2.96}$$

$$\begin{cases} p^k_{\text{out}} - P_0 = 0 & k = 1 \\ p^k_{\text{tot,out}} - p^{k-1}_{\text{tot,out}} + \Delta p^{k-1}_{\text{W,out}} + \Delta p^{k-1}_{\text{StC}} = 0 & k \neq 1 \end{cases} \tag{2.97}$$

and for $j \in [1, n_{\text{RU}}]$

$$\begin{cases} p^k_{\text{tot,in}} + \Delta p^k_{\text{RU}\,j} + \Delta p_{\text{B,in}} + \Delta p_{\text{B,out}} - p^k_{\text{tot,out}} = 0 & k = n_{\text{cells}} \\ p^k_{\text{tot,in}} + \Delta p^k_{\text{RU}\,j} + \Delta p^k_{\text{CS}} + \Delta p^k_{\text{SC}} - p^k_{\text{tot,out}} = 0 & k \neq n_{\text{cells}} \end{cases} \tag{2.98}$$

where $p_{\text{tot}} = p + \rho\, u^2/2$, $p^k_{\text{tot,in}}$ and $p^k_{\text{tot,out}}$ are the total pressures before and after the k-th cell, $Q^k_{\text{RU}\,j}$ is the flow rate through the j-th channel of the k-th cell, $\Delta p^k_{\text{RU j}}$ is the pressure loss across the j-th channel of the k-th cell, Δp_{CS} and Δp_{SC} are the turning losses in T-junctions at the inlet and outlet of the stack, Δp_{CSt} and Δp_{StC} are straight passage losses in T-junction at the inlet and outlet of the stack, $\Delta p_{\text{B,in}}$ and $\Delta p_{\text{B,out}}$ are turning losses at the top of the stack, Δp_{W} are the wall friction

losses in a straight section of the inlet or outlet manifold, P_0 is the static pressure at the outlet of the stack and Q_{tot} is the total flow rate fed to the stack. This system of algebraic equations is solved iteratively using the secant method.

This model considers not only the flow maldistribution along the height of the stack which is predominantly caused by the pressure losses in the manifold, it also considers the difference in flow rates between different channels of a same cell which is caused by the change in fluid properties with temperature. In this dissertation, all pressure losses are computed according the expressions determined in Chapter 3 [88]. It should also be noted that the present manifold model does not account for dynamic behavior. As such, it is only used for simulations of the steady-state flow.

Since the present network model considers the flow rates through individual gas channels, it is not inherently compatible with the homogenized stack model. Therefore, the temperature and gas composition are interpolated from the discretized volumes of the discretized stack model onto the flow model. In turn, the flow rates are interpolated from the flow model onto the discretized volumes of the stack model.

2.4. Computational procedure for SOC simulation

While Section 2.3 presented the set of differential-algebraic equations that are used for the simulation of SOC, their solution is only possible using suitable numerical methods. In this section, the numerical methods used to implement a numerical solver for the previously defined set of equations is presented.

2.4.1. Finite volume method

All the partial differential equations of Section 2.3 are discretized in space using the finite volume method (FVM). The FVM starts by integrating the differential equations over a small discretized volume and subsequently simplifying some of the resulting volume integrals to surface integrals by means of the divergence theorem. For example, in the volume integral of Equation 2.99 over a small volume Ω

$$\iiint_{\Omega} \rho^{\text{eff}} c_p^{\text{eff}} \frac{\partial T}{\partial t} dV = \iiint_{\Omega} \nabla \cdot \lambda^{\text{eff}} \nabla T \, dV + \iiint_{\Omega} \dot{q}^{V}_{\text{solid}} dV \tag{2.99}$$

the second term may be simplified to an integral over the surface $\partial\Omega$ using the divergence theorem

$$\iiint_{\Omega} \nabla \cdot \lambda^{\text{eff}} \nabla T \, dV = \iint_{\partial\Omega} \lambda^{\text{eff}} \nabla T \cdot \mathbf{n} \, dS, \tag{2.100}$$

where $\mathbf{n}$ is the normal vector of the surface, pointing outward of the volume.

Only then, the equation is discretized by approximating the integrals numerically. Defining a node P at the centroid of the control volume, the volume integrals may be simplified as the value of the integrand at the point P multiplied by the volume V_Ω of Ω

$$\iiint_{\Omega} \rho^{\text{eff}} c_p^{\text{eff}} \frac{\partial T}{\partial t} dV = V_\Omega \left(\rho^{\text{eff}} c_p^{\text{eff}} \frac{\partial T}{\partial t} \right)_P . \tag{2.101}$$

This simplification is exactly accurate when the integrand is constant or linear within the cell. P is the discrete point for which the properties (the temperature in the present case) are computed.

Similarly, a surface integral over a face f may be simplified as the value at the face centroid P_f times the surface of the face S_f:

$$\iint_{\partial\Omega} \lambda^{\text{eff}} \nabla T \cdot \mathbf{n} \, dS = \sum_{f \in \partial\Omega} S_f \left(\lambda^{\text{eff}} \nabla T \cdot \mathbf{n} \right)_{P_f} . \tag{2.102}$$

In order to express this equation in terms of values at cell centroids, properties such as the thermal conductivity λ^{eff} at the points P_f are interpolated from the values at the cell centroid P and the neighboring cell centroid N. In addition, gradients such as ∇T also need to be approximated numerically.

While linear interpolation and central difference schemes are used for diffusion terms, the full model is only first order accurate due to the use of first order upwind schemes for the convective terms. Low order schemes are used to improve the numerical stability of the solution procedure, which is problematic for this very stiff set of differential equations. This needs to be compensated with a fine discretization. For example, the simulations performed to create the stack performance maps presented in Chapter 5 [95] use a discretization of 85 cells across the thickness of the MEA. The mesh is refined to cell heights of 0.5 µm close to the electrolyte where nonlinear phenomena are concentrated. Along the length of a RU, an axial discretization of 140 cells is used, leading to a cell length of 0.6 mm.

The spatial discretization via the FVM transforms the original set of partial differential equations into a large system of coupled ordinary differential equations (ODE) in time. This partially discretized system can be expressed in the general form $\mathbf{M}\frac{\partial \mathbf{y}}{\partial t} = f(\mathbf{y}, t)$ where $\mathbf{y}$ is the vector of all unknown variables at the cell centroids. This system of ODE is integrated in time using the specialized solver package LIMEX [123]. Typical simulation times on a single processor are of the order of one second for button cell simulations, five minutes for RU simulations and two hours for stack simulations. Considering thermocatalytic reactions in the fuel electrode increases computation times up to tenfold depending on the complexity of the mechanism and speed of the reactions in the simulated operating conditions.

The LIMEX solver was chosen for its numerical stability, which is granted by the linearly implicit extrapolation method combined with adaptive time-stepping. The instability of SOC simulations can be attributed to the coupling of nonlinear physical phenomena with large differences in time scales. Notably, the electrochemical reactions are driven by the exponential term of the Butler-Volmer equation (Equation 2.10) and couples source terms of the mass transport model with the charge transport model. The formulation of the equilibrium potential (Equations 2.43–2.45) is a further example of nonlinearity and is especially problematic when any active gas species concentration is low. Therefore, small changes in gas phase concentrations can have a drastic impact on electrochemical source terms. As the source terms lead to gas concentration changes in turn, this interaction can quickly lead to oscillations or nonphysical gas concentrations if explicit numerical schemes are used.

2.4.2. Separation of scales

While all model equations were presented in Section 2.3 in their transient formulation, it is not practical to consider the dynamic behavior of all phenomena at the same time. For example, when simulations are performed at the scale of a planar RU, the heat-up of the solid phase is significantly slower than all other considered phenomena. In such a case, the computation may be greatly accelerated by considering that only the slowest phenomenon is transient, while all the others are instantaneous and do not need to be resolved in time [51].

While many configurations might be useful to consider, the following cases where studied during this dissertation:

- **Transient button cell simulations** need to consider transient phenomena of different time scales because they are performed in order to replicate EIS experiments which are specifically designed to characterize the behavior of electrochemical cells at different time scales. Such simulations must therefore consider the dynamic behavior of the flow and the significantly faster charge transport.
- **Isothermal button cell and RU simulations** are performed in order to study the polarization behavior of the cells and do not need to consider any transient behavior. Still, for the sake of numerical stability and ease of implementation, mass transport is resolved in time while charge transport is considered instantaneous.
- **Transient RU simulations** are performed in order to study the start-up behavior of the cells, which is determined by the evolution of the solid phase temperature. Therefore, only the solid phase heat transport is considered to be transient in this case.
- **Stack simulations** are performed in this dissertation in order to predict the steady-state performance of stacks. While the transient formulation of the heat transport model is used, the simulations are not time-accurate because the cell potentials are computed using the relaxation scheme presented in Section 2.4.4. Therefore, only the steady-state results are expected to be accurate.

Two different methods are used in order to simulate the instantaneous processes. For the charge transport model and the stack flow model, the set of algebraic equations (obtained after the discretization of the partial differential equations in the case of charge transport) is solved iteratively using the secant method within every time step of the encompassing transient solver. Alternatively, the transient set of equations of the fast processes may simply be solved until the steady state is reached within every time step of the encompassing transient solver. This methodology creates the hierarchical solver architecture illustrated in Figure 2.8.

In the case of stack simulations, heat transport is considered to be the slowest phenomenon. All fast physical processes are summarized into a submodel. In practice, this submodel is the RU model described in Sections 2.3.2 through 2.3.8, homogenized over the RU height as described in Section 2.3.10. This RU submodel can be thought as a single slice of a RU in flow direction, normalized to be applicable to every computational cell in the stack heat transport model. During the transient solution of the heat transport model, this RU submodel can be solved until its own steady state is reached for each time step and in each computational cell of the temperature solver. This yields identical results to using a steady-state formulation of the RU model equations. Although

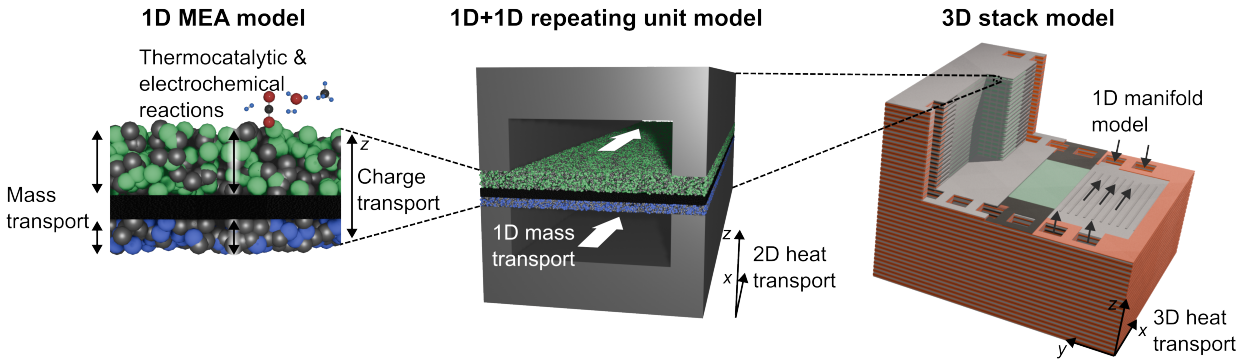

Figure 2.8.: Illustration of the spacial scales that are separated and solved independently during a soc stack stimulation. Reproduced from Furst et al. [94], licensed under CC BY 4.0.

this solution method still involves solving the transient formulation of the equations, it requires significantly less computation time because the systems of equations are much easier to solve independently.

2.4.3. Clustering

The hierarchical solver architecture described previously, which groups the fast processes into a RU submodel solved at each time step of the slower thermal model, streamlines the simulation. However, isolating these fast processes of the simulation into a discrete model that takes solid temperature distribution, cell potential and inlet gas flow rate as parameters and returns the heat source terms required by the temperature solver presents an additional opportunity for optimization.

Indeed, identical conditions may be found at different points of the stack. In such a case, it is not necessary to solve the submodel multiple times as its results may simply be reused. This idea can be pushed further by reusing submodel results when the input parameters are only marginally different. Some accuracy is lost in the process, but computations are accelerated.

Redundant calculations are avoided by grouping computational cells that operate under similar, though not necessarily identical, conditions. This grouping is achieved through a clustering algorithm [124, 125]. For each resulting cluster, a single, representative RU simulation is performed using a characteristic set of operating conditions derived from that cluster. The results of this single simulation are then assumed to be valid for all computational cells belonging to that cluster.

The clustering itself is performed based on the key operating parameters of the cells that vary throughout the stack: the local solid temperature, the cell potential, and the inlet gas flow rates. The decision is governed by predefined thresholds for maximum absolute and relative deviations between cell parameters and the representative values of a cluster. Within this dissertation, the clustering algorithm was used to significantly accelerate the convergence of stack simulations towards the steady state. Once reached, computations were refined by clustering only cells under identical operating conditions.

2.4.4. Cell potential computation in stacks

In a stack of series-connected cells, Kirchhoff's law dictates that the total electrical current must be uniform throughout the vertical stack coordinate z. Therefore, for a given target current I_{target} to flow through the stack, a fitting electrical potential must be established in each cell. This section outlines the numerical procedure used to determine the potential field that satisfies this condition.

The problem is solved using an iterative approach based on the Newton method. Since the polarization resistance is the derivative of cell potential with respect to current, it can be used to iteratively correct the potential until the desired current is achieved. However, the homogenized model used in this work does not resolve individual cells. Instead, it computes continuous fields.

Consequently, the potential difference across cells is also introduced as a homogeneous field E. Assuming the potential drop within interconnects to be negligible, E is homogeneous within the x-y plane. Hence, the iterative scheme is applied at each discretized vertical coordinate. An updated estimate for the homogenized potential difference field $E_{n+1}(t, z)$ is computed from the previous iteration's guess $E_n(t, z)$ as follows:

$$E_{n+1}(t, z) = E_n(t, z) + R_n(t, z) \cdot (I_n(t, z) - I_{\text{target}})\, k_{\text{relax}} \tag{2.103}$$

with the total current $I_n(t, z)$ and the total polarization resistance $R_n(t, z)$ integrated over the horizontal x-y plane at height z for the n-th iteration. An optional relaxation factor k_{relax} is included to enhance numerical stability in sensitive cases.

To obtain the parameters of this iterative step, the local current density i and area-specific resistance (ASR) fields must be determined for the current potential guess $E_n(t, z)$. This is accomplished by solving the RU submodel to a steady state for every computational cell in the domain. The resulting fields are then interpolated and integrated over the horizontal planes to yield the necessary values of $I_n(t, z)$ and $R_n(t, z)$.

Within each RU submodel, the local ASR is estimated as the sum of its ohmic, activation, and concentration components:

$$ASR = ASR_{\Omega} + \frac{\eta_{\text{conc}}}{i} + \frac{\eta_{\text{act,elyt,fuel}} + \eta_{\text{act,elyt,air}}}{i}. \tag{2.104}$$

The concentration overpotential η_{conc} arises from partial pressure gradients between the gas channels p_{chan} and the electrolyte surface p_{elyt}:

$$\eta_{\text{conc}} = \frac{R\,T}{2\,F} \log\left(\frac{p_{\text{H}_2\text{,chan}}\, p_{\text{H}_2\text{O,elyt}}}{p_{\text{H}_2\text{,elyt}}\, p_{\text{H}_2\text{O,chan}}}\right) + \frac{R\,T}{4\,F} \log\left(\frac{p_{\text{O2,chan}}}{p_{\text{O2,elyt}}}\right). \tag{2.105}$$

The activation overpotentials $\eta_{\text{act,elyt,fuel}}$ and $\eta_{\text{act,elyt,air}}$ are calculated at the electrolyte surface using Equation 2.42. The final component, ASR_{Ω}, represents the ohmic resistance of the cell. It can, for the most part, be computed from the conductivity of the cell materials, but contains a contribution from contact resistances which depend on the cell manufacturing process and is therefore determined during model calibration.

The iterative process described by Equation 2.103 continues until the calculated current $I_n(t, z)$ converges to the target current I_{target} within a predefined tolerance. For simulations where only the final steady state is of interest, computations can be significantly accelerated by performing only a single iteration per time step.

CHAPTER 3

Enabling fast and accurate stack flow simulations

The accelerated commercialization of the SOC technology has created a pressing need for simulation tools that are both accurate and computationally efficient. Such tools are essential for the iterative design and system-level optimization of large-scale SOC stacks. A factor that may critically impact the performance and long-term durability of compact SOC systems is the uniformity of the gas flow rates through different cells of a stack. Non-uniform flow, also called maldistribution, caused by the design of the internal gas flow can lead to localized fuel starvation and increased thermal gradients, which in turn accelerates degradation [52]. Therefore, the gas flow in SOC stacks needs be considered to ensure robust system design.

Conventional CFD solutions which solve the Navier-Stokes equations are invaluable tools for designing the flow in SOC systems. They provide insight into the flow patterns inside stacks and allow preliminary testing of cell and stack flow designs [50].

However, the computational cost of detailed CFD is too prohibitive for simultaneously performing detailed simulations of the MEA. Stack simulations require large meshes with a fine discretization due to the presence of numerous small channels. In addition, the flow in large SOC systems may contain transitions between turbulent and laminar flow regimes, which are still difficult to resolve with turbulence models [53].

Network models offer an extremely fast alternative flow computation method, reducing the problem to a set of algebraic equations that can be solved quickly. These models are ideally suited for system-level analysis, but their accuracy is entirely dependent on the availability of correct pressure loss coefficients ζ and Darcy friction factors f_{D} for the studied geometry and flow regime.

This dependency represents a significant gap in the literature, particularly for the laminar flow conditions characteristic of SOC manifolds. The literature on pressure losses in flow features such as T-junctions focuses heavily on turbulent flow condition and no suitable data for the conditions found in the laminar region of SOC stacks have been found in the literature. Consequently, simplified SOC stack flow modeling studies have either neglected these losses or used inappropriate coefficients, compromising their predictive accuracy [55, 126].

The research presented in this chapter directly addresses this challenge by developing and calibrating a computationally inexpensive and accurate algebraic flow model for a representative U-type SOC stack manifold. The methodology is centered on an approach combining high-fidelity CFD simulation with machine learning. First, a series of detailed 3D flow simulations were performed to generate a reliable dataset for stacks of 20 to 40 cells across a range of laminar flow conditions. From these results, the pressure losses across key geometric features (tees, bends, and straight channels) were systematically extracted. Then, symbolic regression was employed to derive closed-form expressions

for the pressure loss coefficients and the Darcy friction factors as functions of local flow conditions like Reynolds numbers and flow rate ratios.

This work contains three key contributions to SOC modeling. First, it demonstrates that commonly assumed friction factors for fully developed channel flow are inaccurate in SOC manifolds, where the successive branching of the flow creates highly skewed velocity profiles that significantly alter wall friction. Second, it provides a new set of validated, closed-form expressions for pressure loss coefficients and friction factors for a reasonable flow geometry and laminar flow conditions. Finally, the resulting algebraic network model is shown to accurately predict the flow distribution with negligible computation time, demonstrating the value of the modeling approach and laying a foundation for future modeling work.

This study is published in the Journal of Power Sources in the article titled "Development and calibration of a fast flow model for solid oxide cell stack internal manifolds" [88]. The complete publication is attached in Appendix A. Its cover sheet is showcased in Figure 3.1.

Journal of Power Sources 613 (2024) 234857

Contents lists available at ScienceDirect

Journal of Power Sources

journal homepage: www.elsevier.com/locate/jpowsour

Development and calibration of a fast flow model for solid oxide cell stack internal manifolds

Oscar Furst, Olaf Deutschmann *

Karlsruhe Institute of Technology, Kaiserstraße 12, Karlsruhe, 76131, Baden-Württemberg, Germany

HIGHLIGHTS

- Commonly used Darcy–Weisbach friction factor shown to be inaccurate in SOC manifolds.
- Pressure loss coefficient expressions for junctions in SOC manifolds are provided.
- Fast and accurate algebraic model of the flow distribution in SOC stacks is presented.

GRAPHICAL ABSTRACT

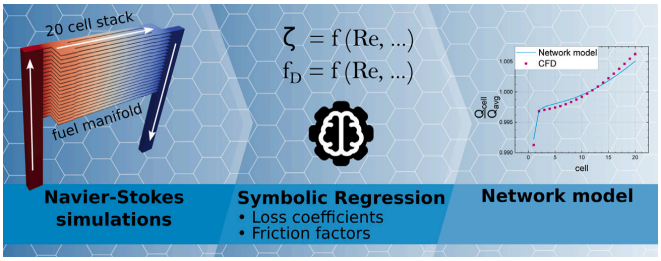

ARTICLE INFO

Keywords:
Solid oxide cell stack internal manifold
Flow network model
Pressure loss coefficients

ABSTRACT

Due to the commercialization of solid oxide cells (SOC) progressing at an accelerated pace, computationally inexpensive SOC models adapted to the iterative nature of the engineering process are in increasing demand. Flow simulation in the stack is especially challenging in this regard because detailed computational fluid mechanic models are computationally demanding, while simplified models rely on pressure loss coefficients and friction factors not readily available in the literature. In this study, a computationally inexpensive algebraic model of an SOC stack internal manifold is developed and calibrated for laminar flow conditions. Thereby, pressure loss coefficients and Darcy friction factors are determined for a broad range of operating conditions through symbolic regression of Navier–Stokes flow simulation results of stacks of 20 to 40 cells. The derived Darcy friction factors for the inlet and outlet manifolds prove to be of particular importance, as they deviate strongly from the expressions assumed in similar modeling studies. The predictive power of the developed model is demonstrated by providing accurate predictions of the flow distribution in the stack, even outside of the calibration window.

Figure 3.1.: Cover sheet of the publication "Development and calibration of a fast flow model for solid oxide cell stack internal manifolds" [88]. The complete publication is attached in Appendix A.

CHAPTER 4

A versatile framework for SOC stack simulations

The publication presented in the preceding chapter addressed the critical challenge of modeling fluid dynamics in SOC stack manifolds, providing a validated, fast-running model for predicting flow distribution. The strength of the presented method is its computational speed, which is needed to allow simulations of the full set of physical phenomena required for accurate prediction of SOC stack performances. The overall behavior of an SOC stack is governed by the interplay between chemistry, mass and heat transport occurring across a vast range of scales.

In order to provide predictive tools despite the complexity of the physical problem, the SOC modeling community has found a number of methods to simplify model equations and accelerate simulation tools. The work presented in this dissertation builds upon a hierarchical multi-scale simulation methodology developed by Deutschmann et al. [35, 38, 96, 97], which leverages the difference in spacial and temporal scale of the physical processes occurring inside SOC stacks to minimize the dimensionality and coupling of all processes. The methodology was outlined in sections 2.3 and 2.4 and is the main topic of the publication presented in this chapter: "A Versatile Multi-Scale Framework for Transient Simulations of Solid Oxide Cells and Stack Modules Integrated in DETCHEM" published in the *Journal of The Electrochemical Society* [94].

In addition to expediting the simulations, this hierarchical methodology provides the flexibility to perform targeted simulations of only parts of the system. While this may be used for optimization studies targeting specific physical processes, its main use herein is to progressively increase the scope of the simulations in order to replicate experiments performed on small button cells and extrapolate their performance up to full stacks.

The corresponding publication demonstrates the possibilities provided by this integrated workflow through a series of case studies that bridge the gap from laboratory-scale validation to stack-level application. The workflow begins with the parameterization of a co-electrolysis cell model by reproducing experimental EIS and polarization curves from Ebbesen et al. [21]. Thereby, the co-electrolysis data is kept for validation and showcases the predictive accuracy of the approach. The utility of the calibrated model is then demonstrated through two distinct applications: a transient simulation of an ammonia-fed RU to analyze its thermal dynamics during start-up, and a 40-cell stack simulation to evaluate the impact of flow maldistribution on SOEC stack performance and temperature gradients.

Simulations of the electrolysis stack of 40 cells are performed at an elevated current density of $-2.11\ \mathrm{A\,cm^{-2}}$ and a steam conversion rate of 72.5%. For temperature management, a high sweep gas flow rate is used, with an average air channel inlet velocity of 3.2 m/s. The simulation shows a significant maldistribution of the sweep gas, with the inlet velocity of air channels close the the stack inlet of 11% above the average channel velocity. Fuel maldistribution is noticeable but small in comparison, with variations within only 2% of the average fuel channel inlet velocity.

The influence of the flow maldistribution on stack performance is estimated by the difference in potential distribution and temperatures throughout the stack between the aforementioned simulation and a reference case with ideal flow distribution. Even at high current density, the studied manifold geometry is not found to significantly impact the stack performance. Moreover, the potential distribution along the height of the SOEC stack is found to be skewed in such a way that compensates performance losses in the bottom cells with improved performance in the upper cells.

By showcasing the workflow from experimental calibration to predictive stack simulation, the value of the provided methodology for the scale-up of the technology is demonstrated. Incorporating this work into the established detailed chemistry software package DETCHEM renders it available to a larger audience, which is meant to accelerate the deployment of the SOC technology as a whole.

The peer-reviewed publication presented in this chapter, "A Versatile Multi-Scale Framework for Transient Simulations of Solid Oxide Cells and Stack Modules Integrated in DETCHEM", is published in the *Journal of The Electrochemical Society* [94]. The complete publication is attached in Appendix B. Its cover sheet and graphical abstract is showcased in Figure 4.1.

Journal of The Electrochemical Society, 2025 **172** 074508

A Versatile Multi-Scale Framework for Transient Simulations of Solid Oxide Cells and Stack Modules Integrated in DETCHEM

Oscar Furst and Olaf Deutschmann[z]

Institute for Chemical Technology and Polymer Chemistry (ITCP), Karlsruhe Institute of Technology, 76131 Karlsruhe, Germany

This paper presents the comprehensive multi-scale modeling framework integrated in the DETCHEM detailed chemistry software package, designed for the transient simulation of solid oxide cells (SOC), including button cells, planar repeating units, and stack modules. The framework uses a hierarchical approach, enabling calibration with button cell experiments and subsequent application to larger systems. Key features of the model include transient 1D simulations for generating electrochemical impedance spectra (EIS), spatially resolved mass and charge transport models for microstructure optimization, 2D mass and heat transport for planar cell simulations and a 3D homogenized model for performance analysis of SOC stack modules. Additionally, the model incorporates a thermocatalytic chemistry module to simulate the decomposition of a variety of fuels and an internal manifold model to study flow maldistribution in SOC stacks. The framework's versatility is demonstrated through case studies, including the calibration and validation of a co-electrolysis cell model using experimental EIS and polarization curves, transient simulations of ammonia-fed repeating units, and the evaluation of flow maldistribution effects in a stack module.

 [DOI: 10.1149/1945-7111/ade56d]

Manuscript submitted February 19, 2025; revised manuscript received May 6, 2025. Published July 9, 2025.

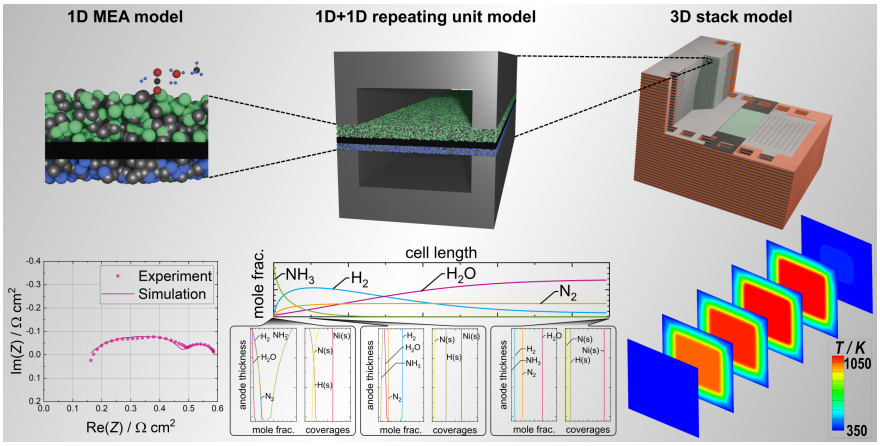

Figure 4.1.: Cover sheet and graphical abstract of publication "A Versatile Multi-Scale Framework for Transient Simulations of Solid Oxide Cells and Stack Modules Integrated in DETCHEM". The complete publication is attached in Appendix B.

CHAPTER 5

Efficiency optimization of power-to-methane systems utilizing SOEC

While accurately simulating the performance of SOC stacks is useful in itself for the purpose of cell and stack design, it is of even greater interest to use such a model to inform the design of larger, integrated energy systems in which the stack is a central component, as SOC stacks can never operate without at least a system to supply reactants and manage its temperature. As the logical continuation of the SOC stack modeling activities presented in the preceding chapters, this chapter deals with the simulation of full systems that utilize SOEC. In the associated publication, "Modeling, optimization and comparative assessment of power-to-methane and carbon capture technologies for renewable fuel production", a comparative study of PtM systems is performed which builds upon the detailed SOC stack model.

PtM plants are energy conversion systems which use electricity, water and carbon dioxide to produce methane. The process revolves around the combination of electrolysis and methanation technologies, the produced hydrogen reacting with carbon oxides to methane. The PtM pathway is an attempt to addresses the issue posed by the ever-increasing demand for natural gas despite the global ambition of reducing CO_2 emissions [8]. However, it competes against an abundant natural resource, and therefore the process needs to be extremely cost-effective to be economically viable. As energy costs constitute the majority of the levelized cost of methane production through the PtM process, this translates to a very high efficiency requirement.

However, the design of efficient PtM systems is a significant engineering challenge, involving the complex thermal and material integration of multiple technologies, including electrolysis, methanation, and optionally carbon capture. Simultaneously, the opportunities for thermal integration that the technology offers might be the key to its viability: the heat produced by the exothermic methanation reaction can be utilized by a high temperature electrolysis technology such as SOCs for the production of steam, which is a significant energy sink of the process [19]. This allows the combined process to reach a high total efficiency.

With the goal of increasing the viability of the PtM technology, this study focuses on uncovering possible efficiency optimizations of PtM processes offered by advantageous combinations of processes and operating points. As this task requires the ability to reasonably predict the performance of the electrolyzer to changes in a multitude of operating parameters, the detailed stack model previously introduced is an invaluable tool for such a study.

The present study considers twelve different combinations of methanation, electrolysis and carbon supply technologies. The integration of the carbon supply into the PtM process chain is considered in order to evaluate if it can also substantially benefit from the reaction heat of the methanation process, despite the considerable heat requirements of the high temperature electrolysis process.

For this purpose, direct air capture (DAC), amine gas treatment (AGT) of flue gases and biomass gasification (BG) are considered. Implemented correctly, each of these technologies has the potential to operate the PtM technology with a closed-loop carbon cycle. These processes are complemented by either cathode-supported (CSC) or electrode-supported (ESC) solid oxide electrolysis units and methanation units comprised of either fixed-bed methanation (FBM) reactors or three-phase methanation (TPM) reactors.

While numerous studies have investigated PtM systems, a comprehensive comparative assessment that systematically optimizes operating conditions across a wide array of integrated carbon capture technologies, particularly AGT and DAC coupled with SOEC, remains scarce in the literature. Furthermore, many system-level optimization studies rely on simplified electrolyzer models, potentially overlooking crucial performance trade-offs. This study addresses these gaps by employing a robust methodology combining process simulation with pinch analysis and a derivative-free optimization algorithm to asses the highest achievable efficiency of multiple combinations of technologies. Ultimately, the optimized operating conditions are examined in order to understand the trade-offs and synergies that increase the system efficiencies.

It should be noted that this system study utilizes an earlier iteration of the SOC model presented in the previous section: the inlet flow throughout the stack is assumed to be distributed evenly. The stack flow model of Koh et al. [55] is used for the computation of the pressure drop across a stack, but has no bearing on the stack performance.

The analysis detailed in the appended publication quantifies the efficiency improvements achievable through thermal integration of the carbon supply, particularly demonstrating efficiency gains of more than 10% when integrating DAC or AGT processes. The discussion of the optimal operating conditions for SOECs within these integrated systems highlights the benefit of endothermic operation for maximizing efficiency while also exploring the potential economic advantage of exothermic SOEC operation.

The peer-reviewed publication presented in this chapter, "Modeling, optimization and comparative assessment of power-to-methane and carbon capture technologies for renewable fuel production", is published in *Applied Energy* [95]. The complete publication is attached in Appendix C. Its cover sheet and graphical abstract is showcased in Figure 5.1.

Applied Energy 375 (2024) 123972

Contents lists available at ScienceDirect

Applied Energy

journal homepage: www.elsevier.com/locate/apenergy

Modeling, optimization and comparative assessment of power-to-methane and carbon capture technologies for renewable fuel production

Oscar Furst [a], Lukas Wehrle [a], Daniel Schmider [b], Julian Dailly [b], Olaf Deutschmann [a,*]

[a] Karlsruhe Institute of Technology, Kaiserstraße 12, Karlsruhe, 76131, Baden-Württemberg, Germany
[b] European Institute for Energy Research, Emmy-Noether-Straße 11, Karlsruhe, 76131, Baden-Württemberg, Germany

GRAPHICAL ABSTRACT

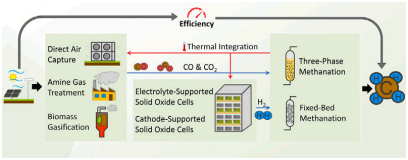

ARTICLE INFO

Keywords:
Power-to-methane
Solid oxide electrolysis cells
Catalytic methanation
Direct air capture
Amine gas treatment
Biomass gasification

ABSTRACT

Power-to-X systems which convert electrical energy into stable chemical energy carriers are a promising solution to the long-term energy storage challenge posed by the increasing market penetration of intermittent renewable power sources. In this paper, a systematic and flexible method for optimizing the steady-state operating conditions of Power-to-Methane (PtM) plant concepts is showcased and applied to perform a comparative assessment of a multitude of PtM process chains. As opposed to existing studies, a large number of comprehensive PtM system models integrating multiple carbon capture technologies and Solid Oxide Electrolysis Cell (SOEC) stacks are optimized. Using detailed 3D SOEC stack simulations and interpolation-based model reduction, the performance of electrolyte-supported (ESC) and cathode-supported cells (CSC) integrated in a variety of PtM systems with air and pure oxygen sweep gas concepts is compared. A total of 20 plant concepts using different combinations of carbon capture (biomass gasification, amine gas treatment, direct air capture) and methanation (fixed-bed, slurry bubble column) technologies are investigated using the pinch method. The results demonstrate that thermal integration of the carbon capture process in PtM systems can raise the total efficiency of the process chains by up to 10.9% for direct air capture and 10.4% for amine gas treatment, with the plants reaching high heating value efficiencies of 70.2% and 84.6% respectively. Endothermic, high temperature operation of SOECs is shown to consistently yield the highest PtM efficiencies due to the minimization of cell overpotentials and power inverter losses. Conversely, exothermic operation of SOECs thermally integrated with energy-intensive carbon capture processes is shown to significantly lower capital expenditures (CAPEX) while incurring an efficiency loss lower than 1% compared to thermoneutral operation.

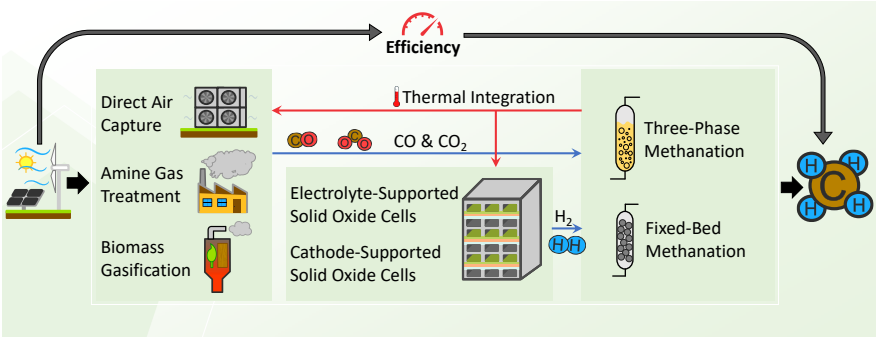

Figure 5.1.: Cover sheet and graphical abstract of the publication "Modeling, optimization and comparative assessment of power-to-methane and carbon capture technologies for renewable fuel production". The complete publication is attached in appendix C.

CHAPTER 6

Conclusion and outlook

The core challenge addressed throughout this work lies in managing the inherent complexity of SOC systems during modeling efforts, with the purpose of readying the technology for its adoption in sustainable energy conversion applications. Methods were developed to enable or improve the simulation of multiple physical phenomena in SOC modules, such as gas distribution through internal manifolds, gas transport along RU channels and the cell potential profile along the height of SOC stacks. These model components were subsequently integrated in an existing SOC modeling framework which allows the simulations of SOFC and SOEC stacks. The improved modeling framework was used in order to perform a study on the efficiency of PtM systems.

The first publication focused on addressing a long-standing bottleneck in stack simulation: the accurate and efficient modeling of reactant flow distribution within internal manifolds. Flow maldistribution may significantly impact stack performance and longevity, yet existing models are hampered by either the computational cost of CFD or the lack of reliable pressure loss parameters for the characteristic laminar flow conditions in SOC manifolds.

This study employed 3D CFD simulations with OpenFOAM to analyze the flow patterns within a representative U-type manifold geometry across various stack sizes and Reynolds numbers relevant to SOC operation. A key finding from these simulations was the significant deviation of the flow profiles from the idealized, fully developed channel flow often assumed in simplified models. The successive branching in the manifold leads to highly skewed velocity profiles, particularly in the inlet manifold, with significant impact on the wall friction characteristics. This observation confirmed that standard Darcy friction factors derived from the Darcy-Weisbach equation are fundamentally inaccurate for predicting pressure gradients along the length of SOC internal manifolds.

To address the lack of literature data suitable for the parametrization of hydraulic network models of the flow in SOC stacks, a set of parameters was determined for the computation of pressure losses in the studied geometry. Pressure losses across distinct geometric features (tee junctions, bends, straight sections) under varying flow conditions were extracted from the CFD results. Subsequently, a machine learning technique was utilized to derive closed-form algebraic expressions for both the pressure loss coefficients ζ in junctions and bends, and for the Darcy friction factors f_D in the straight manifold sections. These new expressions allow the computation of pressure losses as a function of the local flow conditions (Reynolds numbers in different branches, flow rate ratios).

Finally, these closed-form expressions were integrated into a computationally inexpensive network model of the flow. Validation against the full CFD data demonstrated that this simplified model, parameterized with the new correlations, could predict the flow distribution across the stack with good accuracy (NRMSD typically below 5%) and sub-second computation time. This work not only demonstrates the necessity for further efforts to determine loss coefficients for a wider variety of

SOC manifold geometries, it also provides an initial validated set of correlations an model equations that allows incorporating realistic flow distribution effects into comprehensive stack simulations.

The second publication contained a comprehensive description of the model equations of a SOC model built upon previous modeling efforts by Deutschmann et al. [35, 38, 96, 97] and incrementally improved to include the stack flow model developed in this work as well as smaller improvements such as a conservative numerical scheme for the transient simulation of one-dimensional flow along cell channels and the computation of the potential profile along the height of SOC stacks. The complete modeling framework allows the simulative scale-up of an experimental button cell design up to the scale of an SOC stack.

In this work, the model was set up to mirror a cell design published by Ebbesen et al. [21]. Unknown cell properties were obtained through fitting the model to the published EIS data and successfully validated using the polarization measurements of the same cell. The polarization behavior of the cells was closely matched by the model for different temperatures and gas compositions, both in electrolysis and fuel cell operation and including the water-gas shift reaction on the Nickel electrode.

An SOEC stack model was subsequently designed based on the obtained cell model, and used to perform a study on the impact of flow maldistribution on the performance of the stack. The flow in the stack was simulated using a network model that considers maldistribution in the vertical and horizontal dimensions of the stack. The pressure losses throughout the considered internal manifold could be computed using the expressions for pressure loss coefficients and Darcy friction factors developed in the preceding publication.

Simulations of the electrolysis stack of 40 cells were performed at an elevated current density of $-2.11\ \mathrm{A\,cm^{-2}}$ and a steam conversion rate of 72.5%. For temperature management, a high sweep gas flow rate was selected with an average air channel inlet velocity of 3.2 m/s. Results showed a significant maldistribution of the sweep gas, with inlet velocity peaks close the the manifold inlet of 11% above the average. Fuel maldistribution was noticeable, but small in comparison, with variations within only 2% of the average inlet velocity.

A reference case with ideal flow distribution was simulated in order to evaluate the impact of the flow maldistribution on the performance of the stack. No significant difference in stack efficiency was observed despite the elevated current density. Closer observation of the potential distribution along the height of the SOEC stack revealed the performance losses in the bottom cells were compensated by improved performance in the upper cells.

The final publication of this dissertation applied an intermediary iteration of the developed SOC stack model to address a major challenge of the energy transition: the study of the viability of different energy conversion systems, specifically PtM processes. Through maximal process integration and optimization of operating conditions, this study provides a systematic, quantitative comparison of the achievable efficiency of diverse PtM plant concepts.

A flexible system simulation framework was constructed, capable of integrating various technology options for the three core PtM components: (i) an electrolysis module built either with electrolyte-supported or cathode-supported SOECs, (ii) sources of carbon oxides, namely the BG, AGT or DAC technologies, (iii) and a catalytic methanation unit using either FBM or 3PM reactor types.

Pinch analysis was employed to mimic ideal thermal integration and a derivative-free optimization algorithm (combining Monte Carlo sampling with the Nelder-Mead method) was employed to find the operating conditions maximizing the HHV efficiency for each of the 20 distinct plant configurations studied. While system optimization necessitated the use of a reduced-order SOEC model, the use of the multi-scale SOEC model for the generation of an interpolation-based surrogate model was pivotal for ensuring reliable SOEC module performance prediction.

The comparison between the achievable efficiencies of the PtM processes showed that the source of carbon oxides has the highest impact on the system efficiency. Of the plant concepts considered in this study, those utilizing the pressurized BG process reach the highest HHV efficiencies with 87.0%. Plant concepts utilizing AGT achieve similar efficiencies with 84.6%, and the DAC process still reached efficiencies of up to 74.8%. Integration of the carbon oxide source in the PtM processes proved highly beneficial in all cases. Despite the high amount of heat required for steam production, enough waste heat remains to be used in the AGT and DAC process, leading to potential increased HHV efficiencies of more than 10% compared to separated systems. The BG process also benefits from the integration with an SOEC unit due to the supply of pure oxygen, which enables autothermal operation.

Further analysis of the optimized operating conditions yielded significant insights into PtM system design. The gas temperatures at the inlet of the electrolyzer was found to have a very high impact on the full system efficiency, as endothermic stack operation maximizes the electrical efficiency of the electrolyzer. Still, a bi-objective optimization of the plant efficiency and the required number of electrolysis stacks was performed, as SOEC stacks have a significant cost. This optimization revealed that exothermic electrolyzer operation provides additional opportunities for thermal integration with carbon capture technologies such as AGT and DAC, allowing for a significant reduction of the necessary number of SOEC stack with only small losses in overall plant efficiencies compared to thermoneutral operation.

Overall, the research presented in this dissertation progresses from the detailed modeling of sub-components to the improvement of a comprehensive multi-scale SOC modeling framework and its application in system-level analysis and optimization. The accurate and fast manifold flow model developed in the first study enables new avenues of studies with the multi-scale framework, allowing it to realistically incorporate flow distribution effects and evaluate their impact on stack performance. In turn, the versatile multi-scale framework provided the high-fidelity SOEC stack model necessary for the meaningful optimization of integrated PtM systems in the third study.

While this dissertation makes valuable contributions to the field of SOC modeling, certain limitations should be acknowledged, which also point towards promising avenues for future research.

The manifold flow model developed in this study is sufficient to yield some insight into the magnitude and effect of flow maldistribution in SOC stacks, but practical application of the model during design process of SOC stacks requires it to be adaptable to various manifold geometries. Therefore, further work determining pressure loss coefficients as a function of not only flow conditions, but also manifold geometry, would be of great interest for such applications. In addition, appropriate pressure loss coefficients for turbulent operating conditions need to be researched in order to enable the simulation of large SOC stacks and high flow rate conditions.

Still, possible avenues of research regarding the impact of flow maldistribution on the performance of SOC stacks using the model developed during this dissertation were not exhausted. While simulations performed on exothermically operated SOEC stacks revealed stabilizing interactions between the cell performance and the flow distribution (low flow rates lead to temperature increases, which improve the efficiency of the cell, thereby reducing heat production locally), the impact of flow maldistribution in SOFC stacks can be expected to be more critical. However, such simulation campaigns on SOFC stacks are complicated by the significantly increased computation times resulting from the interaction between flow rates and electrochemistry, related issues of numerical stability and the possibility of thermal runaway.

In addition, even though the presented SOC modeling methodology is meant to be as versatile as possible, there are a number of applications to which it is not suited.

One major drawback is that the morphologies of cells and stacks that may be studied is limited. Studying tubular cells with the current set of equations is possible only under very specific conditions of the flow and only for cells with sufficiently large diameters to justify neglecting the curvature of the MEA. For the simulation of tubular cell bundles, a different heat transport and flow models would be necessary. Even some less common planar SOC stacks can not be studied with the present methodology, such as cross-flow stack designs which are incompatible with the 1D RU model. Similarly, the assumptions surrounding operating conditions during button cell experiments were found to not be universally applicable. Notably, low gas flow rates are favored in some experimental studies that aim at maximizing the conversion rates of SOCs. Under such conditions, the cell temperature is suspected to differ significantly from the gas temperature depending on the experimental setup. The assumption of homogeneity of the gas phase above the electrodes is also likely to be inaccurate under low gas flow rates, for larger cells or large gas compartment volumes. Heat transport, as well as more complex flow models, should be considered in such cases.

More simplifications lie in the electrochemical model, in which the elementary reaction mechanism is not considered and the coefficients of the Butler-Volmer kinetic expression are determined empirically. These simplification reduce the complexity of the model and accelerate simulations, but prevent studies of the underlying reaction mechanisms. The information granted by elementary electrochemical reaction mechanisms is also likely to be necessary for accurate modeling of the cell degradation phenomena related to catalyst poisoning and may enable simulations of the cell operation strategies that mitigate such degradation.

However, it is also worth mentioning that striving for a more versatile modeling methodology is not necessarily desirable, as versatility comes with important compromises, particularly with regard to numerical performance and optimization of the numerical model. Notably, the transient formulation of some model equations is necessary for some of the studies performed herein, but simulations of steady state operation are sufficient for a great number of application. In such cases, much time is lost accurately computing every time step until the steady state is reached. In addition, the complexity of a modeling methodology that combines a multitude of physical phenomena impedes the optimization of the numerical schemes, which takes an additional toll on computation times.

Finally, extending the perspective from the component to the system level, the synergistic interactions identified in the Power-to-Methane study merit further investigation using metrics that accurately reflect the economic viability of the solution. The optimization results presented in this dissertation

highlighted two potentially advantageous operating modes for the SOEC: maximizing the system efficiency by favoring the supply of thermal energy to an endothermic electrolysis process, or minimizing the required active cell area through exothermic operation in the range in which the produced heat can be utilized by a carbon capture process. Since both approaches have a significant impact on the amount of electrolysis units and their degradation rates, the viability of such operating strategies can only be assessed by explicitly accounting for capital expenditures. A comprehensive techno-economic analysis aimed at determining the levelized cost of methane under such operating conditions can therefore assert if the identified physical synergies translate into economically viable industrial solutions.

In summary, this dissertation comprises works that improve upon multiple aspects of the current state of multi-scale SOC modeling. The developed models are meant to provide tools that may expedite the development of systems based around the SOC technology. Likewise, the studies on SOC systems performed in this work provide helpful insights into the intricate physical phenomena that govern the operation of such systems. Ultimately, these contributions aim to accelerate the deployment of the SOC technology as a whole so that it may assist in the transition to sustainable energy systems.

As the market surrounding the production and conversion of renewable energy is rendered volatile by uncertainties in the technological development and constantly shifting policies, the improvement of predictive modeling capabilities is certain to aid by reducing the risks associated with the application of emerging technologies. Since hydrogen has been widely accepted as a cornerstone of tomorrows energy market, SOC are likely to become a pivotal technology for the future. Consequently, work towards advancing the modeling capabilities of SOC systems constitutes a valuable contribution toward realizing a sustainable energy infrastructure.

References

[1] United Nations Environment Programme. *Emissions Gap Report 2024: No more hot air ... please!* Nairobi: United Nations Environment Programme, **2024**. DOI: 10.59117/20.500.11822/46404.

[2] International Energy Agency. *Renewables Information 2019*. Renewables Information. Paris: OECD, **2019**. DOI: 10.1787/fa89fd56-en.

[3] International Energy Agency. *Global Hydrogen Review 2024*. Paris: IEA, **2024**.

[4] *Sunfire - World's largest high-temperature electrolyzer achieves record efficiency*. **2022**. URL: https://www.sunfire.de/en/news/detail/worlds-largest-high-temperature-electrolyzer-achieves-record-efficiency (visited on Mar. 6, 2023).

[5] P. Shukla, J. Skea, R. Slade, A. Al Khourdajie, R. van Diemen, D. McCollum, M. Pathak, S. Some, P. Vyas, R. Fradera, M. Belkacemi, A. Hasija, G. Lisboa, S. Luz, J. Malley. *IPCC, 2022: Climate Change 2022: Mitigation of Climate Change. Contribution of Working Group III to the Sixth Assessment Report of the Intergovernmental Panel on Climate Change*. **2023**.

[6] International Energy Agency. *Iron and Steel Technology Roadmap - Towards more sustainable steelmaking*. Paris: IEA, **2020**.

[7] International Energy Agency. *Ammonia Technology Roadmap: Towards more sustainable nitrogen fertiliser production*. Paris: OECD, **2021**. DOI: 10.1787/f6daa4a0-en.

[8] *Imports of natural gas by partner country | Eurostat*. **2023**. URL: https://ec.europa.eu/eurostat/databrowser/view/nrg_ti_gas/default/table?lang=en (visited on Feb. 20, 2023).

[9] International Energy Agency. *The Future of Hydrogen*. Paris: IEA, **2019**.

[10] M. Götz, J. Lefebvre, F. Mörs, A. McDaniel Koch, F. Graf, S. Bajohr, R. Reimert, T. Kolb. "Renewable Power-to-Gas: A technological and economic review". *Renewable Energy* **2016**, 85, 1371–1390. DOI: 10.1016/j.renene.2015.07.066.

[11] M. Aziz, A. T. Wijayanta, A. B. D. Nandiyanto. "Ammonia as Effective Hydrogen Storage: A Review on Production, Storage and Utilization". *Energies* **2020**, 13 (12), 3062. DOI: 10.3390/en13123062.

[12] N. Klopčič, I. Grimmer, F. Winkler, M. Sartory, A. Trattner. "A review on metal hydride materials for hydrogen storage". *Journal of Energy Storage* **2023**, 72, 108456. DOI: 10.1016/j.est.2023.108456.

[13] M. Thaler, V. Hacker. "Storage and separation of hydrogen with the metal steam process". *International Journal of Hydrogen Energy*. 2010 AIChE Annual Meeting Topical Conference on Hydrogen Production and Storage Special Issue **2012**, 37 (3), 2800–2806. DOI: 10.1016/j.ijhydene.2011.06.119.

[14] J. Brauns, T. Turek. "Alkaline Water Electrolysis Powered by Renewable Energy: A Review". *Processes* **2020**, 8 (2), 248. DOI: 10.3390/pr8020248.

[15] R.-T. Liu, Z.-L. Xu, F.-M. Li, F.-Y. Chen, J.-Y. Yu, Y. Yan, Y. Chen, B. Yu Xia. "Recent advances in proton exchange membrane water electrolysis". *Chemical Society Reviews* **2023**, 52 (16), 5652–5683. DOI: 10.1039/D2CS00681B.

[16] M. Singh, D. Zappa, E. Comini. "Solid oxide fuel cell: Decade of progress, future perspectives and challenges". *International Journal of Hydrogen Energy* **2021**, 46 (54), 27643–27674. DOI: 10.1016/j.ijhydene.2021.06.020.

[17] S. D. Ebbesen, S. H. Jensen, A. Hauch, M. B. Mogensen. "High Temperature Electrolysis in Alkaline Cells, Solid Proton Conducting Cells, and Solid Oxide Cells". *Chemical Reviews* **2014**, 114 (21), 10697–10734. DOI: 10.1021/cr5000865.

[18] M. B. Mogensen. "Thermodynamics of high temperature H2O and CO2 electrolysis". *figshare* **2020**. DOI: 10.6084/M9.FIGSHARE.12652322.V1.

[19] R. Anghilante, C. Müller, M. Schmid, D. Colomar, F. Ortloff, R. Spörl, A. Brisse, F. Graf. "Innovative power-to-gas plant concepts for upgrading of gasification bio-syngas through steam electrolysis and catalytic methanation". *Energy Conversion and Management* **2019**, 183, 462–473. DOI: 10.1016/j.enconman.2018.12.101.

[20] A. Hagen, H. Langnickel, X. Sun. "Operation of solid oxide fuel cells with alternative hydrogen carriers". *International Journal of Hydrogen Energy* **2019**, 44 (33), 18382–18392. DOI: 10.1016/j.ijhydene.2019.05.065.

[21] S. D. Ebbesen, R. Knibbe, M. Mogensen. "Co-Electrolysis of Steam and Carbon Dioxide in Solid Oxide Cells". *Journal of The Electrochemical Society* **2012**, 159 (8), F482. DOI: 10.1149/2.076208jes.

[22] M. B. Mogensen, M. Chen, H. L. Frandsen, C. Graves, J. B. Hansen, K. V. Hansen, A. Hauch, T. Jacobsen, S. H. Jensen, T. L. Skafte, X. Sun. "Reversible solid-oxide cells for clean and sustainable energy". *Clean Energy* **2019**, 3 (3), 175–201. DOI: 10.1093/ce/zkz023.

[23] K. Zhang, A. El-Kharouf, T. Caykara, R. Steinberger-Wilckens. "Effect of Temperature and Water Content on the Oxidation Behaviour and Cr Evaporation of High-Cr Alloys for SOFC Cathode Air Preheaters". *High Temperature Corrosion of Materials* **2023**, 100 (1), 21–45. DOI: 10.1007/s11085-023-10167-1.

[24] G. Schiller, M. Lang, P. Szabo, N. Monnerie, H. von Storch, J. Reinhold, P. Sundarraj. "Solar heat integrated solid oxide steam electrolysis for highly efficient hydrogen production". *Journal of Power Sources* **2019**, 416, 72–78. DOI: 10.1016/j.jpowsour.2019.01.059.

[25] A. Hauch, R. Küngas, P. Blennow, A. B. Hansen, J. B. Hansen, B. V. Mathiesen, M. B. Mogensen. "Recent advances in solid oxide cell technology for electrolysis". *Science* **2020**, 370 (6513), eaba6118. DOI: 10.1126/science.aba6118.

[26] H. Lu, D. Hua, T. Iqabl, X. Zhang, G. Li, D. Zhang. "Molecular dynamics simulations of the coke formation progress on the nickel-based anode of solid oxide fuel cells". *International Communications in Heat and Mass Transfer* **2018**, 91, 40–47. DOI: 10.1016/j.icheatmasstransfer.2017.11.009.

[27] Y.-F. Wang, J. Yuan, B. Sundén, Y.-L. Hu. "Coarse-grained molecular dynamics investigation of nanostructures and thermal properties of porous anode for solid oxide fuel cell". *Journal of Power Sources* **2014**, 254, 209–217. DOI: 10.1016/j.jpowsour.2013.12.079.

[28] R. Pornprasertsuk, P. Ramanarayanan, C. B. Musgrave, F. B. Prinz. "Predicting ionic conductivity of solid oxide fuel cell electrolyte from first principles". *Journal of Applied Physics* **2005**, 98 (10), 103513. DOI: 10.1063/1.2135889.

[29] S.-G. Wang, X.-Y. Liao, J. Hu, D.-B. Cao, Y.-W. Li, J. Wang, H. Jiao. "Kinetic aspect of CO2 reforming of CH4 on Ni(1 1 1): A density functional theory calculation". *Surface Science* **2007**, 601 (5), 1271–1284. DOI: 10.1016/j.susc.2006.12.059.

[30] S. B. Adler, W. G. Bessler. "Elementary kinetic modeling of solid oxide fuel cell electrode reactions". *Handbook of Fuel Cells*. Ed. by W. Vielstich, A. Lamm, H. A. Gasteiger, H. Yokokawa. 1st ed. Wiley, **2010**. DOI: 10.1002/9780470974001.f500031.

[31] D. G. Goodwin, H. Zhu, A. M. Colclasure, R. J. Kee. "Modeling Electrochemical Oxidation of Hydrogen on Ni–YSZ Pattern Anodes". *Journal of The Electrochemical Society* **2009**, 156 (9), B1004. DOI: 10.1149/1.3148331.

[32] H. Zhu, R. J. Kee, V. M. Janardhanan, O. Deutschmann, D. G. Goodwin. "Modeling Elementary Heterogeneous Chemistry and Electrochemistry in Solid-Oxide Fuel Cells". *Journal of The Electrochemical Society* **2005**, 152 (12), A2427. DOI: 10.1149/1.2116607.

[33] A. Banerjee, O. Deutschmann. "Elementary kinetics of the oxygen reduction reaction on LSM-YSZ composite cathodes". *Journal of Catalysis* **2017**, 346, 30–49. DOI: 10.1016/j.jcat.2016.11.035.

[34] H. Moussaoui, J. Laurencin, Y. Gavet, G. Delette, M. Hubert, P. Cloetens, T. Le Bihan, J. Debayle. "Stochastic geometrical modeling of solid oxide cells electrodes validated on 3D

reconstructions". *Computational Materials Science* **2018**, 143, 262–276. DOI: 10.1016/j.commatsci.2017.11.015.

[35] L. Wehrle, D. Schmider, J. Dailly, A. Banerjee, O. Deutschmann. "Benchmarking solid oxide electrolysis cell-stacks for industrial Power-to-Methane systems via hierarchical multi-scale modelling". *Applied Energy* **2022**, 317, 119143. DOI: 10.1016/j.apenergy.2022.119143.

[36] C. Bao, Z. Jiang, X. Zhang. "Modeling mass transfer in solid oxide fuel cell anode: I. Comparison between Fickian, Stefan-Maxwell and dusty-gas models". *Journal of Power Sources* **2016**, 310, 32–40. DOI: 10.1016/j.jpowsour.2016.01.099.

[37] A. Z. Weber, J. Newman. "Modeling Transport in Polymer-Electrolyte Fuel Cells". *Chemical Reviews* **2004**, 104 (10), 4679–4726. DOI: 10.1021/cr020729l.

[38] A. Banerjee, Y. Wang, J. Diercks, O. Deutschmann. "Hierarchical modeling of solid oxide cells and stacks producing syngas via H2O/CO2 Co-electrolysis for industrial applications". *Applied Energy* **2018**, 230, 996–1013. DOI: 10.1016/j.apenergy.2018.08.122.

[39] A. Leonide, Y. Apel, E. Ivers-Tiffee. "SOFC Modeling and Parameter Identification by Means of Impedance Spectroscopy". *ECS Transactions* **2009**, 19 (20), 81–109. DOI: 10.1149/1.3247567.

[40] T. Cui, J. Zhu, Z. Lyu, M. Han, K. Sun, Y. Liu, M. Ni. "Efficiency analysis and operating condition optimization of solid oxide electrolysis system coupled with different external heat sources". *Energy Conversion and Management* **2023**, 279, 116727. DOI: 10.1016/j.enconman.2023.116727.

[41] R. Styn, H. J. Reichelt, R. Peters, T. E. Müller. "Techno-economic assessment of hythane-fueled industrial SOFC systems". *Energy* **2025**, 340, 139273. DOI: 10.1016/j.energy.2025.139273.

[42] J. Li, T. Yu. "A novel data-driven controller for solid oxide fuel cell via deep reinforcement learning". *Journal of Cleaner Production* **2021**, 321, 128929. DOI: 10.1016/j.jclepro.2021.128929.

[43] J. Bao, C. Wang, Z. Xu, B. J. Koeppel. *Physics-Informed Machine Learning with Application to Solid Oxide Fuel Cell System Modeling and Optimization*. PNNL–29124. Pacific Northwest National Laboratory (PNNL), Richland, WA (United States), **2019**. DOI: 10.2172/1569289.

[44] A. Syauqi, V. M. Nagulapati, Y. D. Chaniago, J. A. Ningtyas, R. Andika, H. Lim. "Advancement in power-to-methanol integration with steel industry waste gas utilization through solid oxide electrolyzer cells: Surrogate model-based approach for optimization". *Sustainable Energy Technologies and Assessments* **2025**, 73, 104160. DOI: 10.1016/j.seta.2024.104160.

[45] S. B. Beale, M. Andersson, C. Boigues-Muñoz, H. L. Frandsen, Z. Lin, S. J. McPhail, M. Ni, B. Sundén, A. Weber, A. Z. Weber. "Continuum scale modelling and complementary experimentation of solid oxide cells". *Progress in Energy and Combustion Science* **2021**, 85, 100902. DOI: 10.1016/j.pecs.2020.100902.

[46] F. R. Bianchi, B. Bosio. "Performance modelling of intermediate temperature solid oxide cells applied as electrochemical air separation unit". *Chemical Engineering Journal Advances* **2025**, 22, 100728. DOI: 10.1016/j.ceja.2025.100728.

[47] H. Zhu, R. J. Kee. "Modeling Distributed Charge-Transfer Processes in SOFC Membrane Electrode Assemblies". *Journal of The Electrochemical Society* **2008**, 155 (7), B715. DOI: 10.1149/1.2913152.

[48] S. Primdahl, M. Mogensen. "Gas Conversion Impedance: A Test Geometry Effect in Characterization of Solid Oxide Fuel Cell Anodes". *Journal of The Electrochemical Society* **1998**, 145 (7), 2431–2438. DOI: 10.1149/1.1838654.

[49] S. Srikanth, M. P. Heddrich, S. Gupta, K. A. Friedrich. "Transient reversible solid oxide cell reactor operation – Experimentally validated modeling and analysis". *Applied Energy* **2018**, 232, 473–488. DOI: 10.1016/j.apenergy.2018.09.186.

[50] R. T. Nishida, S. B. Beale, J. G. Pharoah, L. G. J. de Haart, L. Blum. "Three-dimensional computational fluid dynamics modelling and experimental validation of the Jülich Mark-F

solid oxide fuel cell stack". *Journal of Power Sources* **2018**, 373, 203–210. DOI: 10.1016/j.jpowsour.2017.10.030.

[51] D. Bhattacharyya, R. Rengaswamy. "A Review of Solid Oxide Fuel Cell (SOFC) Dynamic Models". *Industrial & Engineering Chemistry Research* **2009**, 48 (13), 6068–6086. DOI: 10.1021/ie801664j.

[52] M. Mortada, H. S. Ramadan, J. Faraj, A. Faraj, H. El Hage, M. Khaled. "Impacts of reactant flow nonuniformity on fuel cell performance and scaling-up: Comprehensive review, critical analysis and potential recommendations". *International Journal of Hydrogen Energy* **2021**, 46 (63), 32161–32191. DOI: 10.1016/j.ijhydene.2020.06.013.

[53] R. B. Langtry, F. R. Menter. "Correlation-Based Transition Modeling for Unstructured Parallelized Computational Fluid Dynamics Codes". *AIAA Journal* **2009**, 47 (12), 2894–2906. DOI: 10.2514/1.42362.

[54] J. Wang, Z. Gao, G. Gan, D. Wu. "Analytical solution of flow coefficients for a uniformly distributed porous channel". *Chemical Engineering Journal* **2001**, 84 (1), 1–6. DOI: 10.1016/S1385-8947(00)00263-1.

[55] J.-H. Koh, H.-K. Seo, C. G. Lee, Y.-S. Yoo, H. C. Lim. "Pressure and flow distribution in internal gas manifolds of a fuel-cell stack". *Journal of Power Sources* **2003**, 115 (1), 54–65. DOI: 10.1016/S0378-7753(02)00615-8.

[56] N. H. Menzler, F. Tietz, S. Uhlenbruck, H. P. Buchkremer, D. Stöver. "Materials and manufacturing technologies for solid oxide fuel cells". *Journal of Materials Science* **2010**, 45 (12), 3109–3135. DOI: 10.1007/s10853-010-4279-9.

[57] A. Nechache, S. Hody. "Alternative and innovative solid oxide electrolysis cell materials: A short review". *Renewable and Sustainable Energy Reviews* **2021**, 149, 111322. DOI: 10.1016/j.rser.2021.111322.

[58] N. Minh. "Cell and stack design, fabrication and performance". *High-Temperature Solid Oxide Fuel Cells for the 21st Century*. Ed. by K. Kendall, M. Kendall. Second Edition. Boston: Academic Press, **2016**, 255–282. DOI: 10.1016/B978-0-12-410453-2.00008-7.

[59] R. Chen, Y. Gao, J. Gao, H. Zhang, M. Motola, M. B. Hanif, C.-X. Li. "From concept to commercialization: A review of tubular solid oxide fuel cell technology". *Journal of Energy Chemistry* **2024**, 97, 79–109. DOI: 10.1016/j.jechem.2024.05.026.

[60] M. B. Mogensen. "Materials for reversible solid oxide cells". *Current Opinion in Electrochemistry*. Energy Storage - Energy Transformation **2020**, 21, 265–273. DOI: 10.1016/j.coelec.2020.03.014.

[61] R. P. O'Hayre, S.-W. Cha, W. G. Colella, F. B. Prinz. *Fuel cell fundamentals*. Third edition. Hoboken, NJ: Wiley, **2016**.

[62] M. A. Laguna-Bercero, ed. *High Temperature Electrolysis*. Vol. 95. Lecture Notes in Energy. Cham: Springer International Publishing, **2023**. DOI: 10.1007/978-3-031-22508-6.

[63] M. M. Welander, B. Hu, S. Belko, K. X. Lee, P. K. Dubey, I. Robinson, P. Singh, M. C. Tucker. "Direct utilization of gaseous fuels in metal supported solid oxide fuel cells". *International Journal of Hydrogen Energy* **2023**, 48 (4), 1533–1539. DOI: 10.1016/j.ijhydene.2022.10.008.

[64] M. Kishimoto, H. Muroyama, S. Suzuki, M. Saito, T. Koide, Y. Takahashi, T. Horiuchi, H. Yamasaki, S. Matsumoto, H. Kubo, N. Takahashi, A. Okabe, S. Ueguchi, M. Jun, A. Tateno, T. Matsuo, T. Matsui, H. Iwai, H. Yoshida, K. Eguchi. "Development of 1 kW-class Ammonia-fueled Solid Oxide Fuel Cell Stack". *Fuel Cells* **2020**, 20 (1), 80–88. DOI: 10.1002/fuce.201900131.

[65] K. Zhao, Q. Bkour, X. Hou, S. W. Kang, J. C. Park, M. G. Norton, J.-I. Yang, S. Ha. "Reverse water gas shift reaction over CuFe/Al2O3 catalyst in solid oxide electrolysis cell". *Chemical Engineering Journal* **2018**, 336, 20–27. DOI: 10.1016/j.cej.2017.11.028.

[66] *Ammonia cracking*. URL: https://www.clariant.com/en/Business-Units/Catalysts/Energy-Transition/Ammonia-cracking (visited on Aug. 6, 2025).

[67] S. S. Rathore, S. Biswas, D. Fini, A. P. Kulkarni, S. Giddey. "Direct ammonia solid-oxide fuel cells: A review of progress and prospects". *International Journal of Hydrogen Energy* **2021**, 46 (71), 35365–35384. DOI: 10.1016/j.ijhydene.2021.08.092.

[68] M. Pavone, A. B. Muñoz-García, A. M. Ritzmann, E. A. Carter. "First-Principles Study of Lanthanum Strontium Manganite: Insights into Electronic Structure and Oxygen Vacancy Formation". *The Journal of Physical Chemistry C* **2014**, 118 (25), 13346–13356. DOI: 10.1021/jp500352h.

[69] H. Zhu, A. Ashar, R. J. Kee, R. J. Braun, G. S. Jackson. "Physics-Based Model to Represent Membrane-Electrode Assemblies of Solid-Oxide Fuel Cells Based on Gadolinium-Doped Ceria". *Journal of The Electrochemical Society* **2023**, 170 (10), 104506. DOI: 10.1149/1945-7111/acfff6.

[70] S. Kyun Kim, H. Jin Lee, J. Young Moon, Y.-R. Jo, J. Lee, J.-H. Park, S.-D. Kim, J. Hoon Joo. "Understanding the phase stability of yttria stabilized zirconia electrolyte under solid oxide electrolysis cell operation conditions". *Journal of Materials Chemistry A* **2024**, 12 (14), 8319–8330. DOI: 10.1039/D3TA06652E.

[71] Y. Leng, S. H. Chan, Q. Liu. "Development of LSCF–GDC composite cathodes for low-temperature solid oxide fuel cells with thin film GDC electrolyte". *International Journal of Hydrogen Energy*. TMS07: Symposium on Materials in Clean Power Systems **2008**, 33 (14), 3808–3817. DOI: 10.1016/j.ijhydene.2008.04.034.

[72] A. Sciazko, T. Shimura, Y. Komatsu, N. Shikazono. "Ni-GDC and Ni-YSZ electrodes operated in solid oxide electrolysis and fuel cell modes". *Journal of Thermal Science and Technology* **2021**.

[73] A. N. Zainon, M. R. Somalu, A. M. Kamarul Bahrain, A. Muchtar, N. A. Baharuddin, M. A. S.a, N. Osman, A. Abdul Samat, A. K. Azad, N. P. Brandon. "Challenges in using perovskite-based anode materials for solid oxide fuel cells with various fuels: a review". *International Journal of Hydrogen Energy* **2023**, 48 (53), 20441–20464. DOI: 10.1016/j.ijhydene.2022.12.192.

[74] M. J. Jørgensen, M. Mogensen. "Impedance of Solid Oxide Fuel Cell LSM/YSZ Composite Cathodes". *Journal of The Electrochemical Society* **2001**, 148 (5), A433. DOI: 10.1149/1.1360203.

[75] Y. Lim, J. Park, H. Lee, M. Ku, Y.-B. Kim. "Rapid fabrication of lanthanum strontium cobalt ferrite (LSCF) with suppression of LSCF/YSZ chemical side reaction via flash light sintering for SOFCs". *Nano Energy* **2021**, 90, 106524. DOI: 10.1016/j.nanoen.2021.106524.

[76] N. T. Hart, N. P. Brandon, M. J. Day, J. E. Shemilt. "Functionally graded cathodes for solid oxide fuel cells". *Journal of Materials Science* **2001**, 36 (5), 1077–1085. DOI: 10.1023/A:1004857104328.

[77] S. T. Aruna, L. S. Balaji, S. S. Kumar, B. S. Prakash. "Electrospinning in solid oxide fuel cells – A review". *Renewable and Sustainable Energy Reviews* **2017**, 67, 673–682. DOI: 10.1016/j.rser.2016.09.003.

[78] J. H. Zhu, D. A. Chesson, Y. T. Yu. "Review—(Mn,Co)3O4-Based Spinels for SOFC Interconnect Coating Application". *Journal of The Electrochemical Society* **2021**, 168 (11), 114519. DOI: 10.1149/1945-7111/ac3a29.

[79] M. K. Mahapatra, K. Lu. "Glass-based seals for solid oxide fuel and electrolyzer cells – A review". *Materials Science and Engineering: R: Reports* **2010**, 67 (5), 65–85. DOI: 10.1016/j.mser.2009.12.002.

[80] A. Kalu, X. Li, L. Zhou, S. Liu, S. Chen, Q. Li, X. Zhu, X. Liu, W. Li. "Strategies to Counter Cr poisoning on air electrodes of solid oxide cells". *International Journal of Hydrogen Energy* **2025**, 101, 85–104. DOI: 10.1016/j.ijhydene.2024.12.189.

[81] M. B. Mogensen, M. Chen, H. L. Frandsen, C. Graves, A. Hauch, P. V. Hendriksen, T. Jacobsen, S. H. Jensen, T. L. Skafte, X. Sun. "Ni migration in solid oxide cell electrodes: Review and revised hypothesis". *Fuel Cells* **2021**, 21 (5), 415–429. DOI: 10.1002/fuce.202100072.

[82] Z. Pan, Q. Liu, Z. Yan, Z. Jiao, L. Bi, S. H. Chan, Z. Zhong. "On the delamination of air electrodes of solid oxide electrolysis cells: A mini-review". *Electrochemistry Communications* **2022**, 137, 107267. DOI: 10.1016/j.elecom.2022.107267.

[83] V. Subotić, C. Schluckner, H. Schroettner, C. Hochenauer. "Analysis of possibilities for carbon removal from porous anode of solid oxide fuel cells after different failure modes". *Journal of Power Sources* **2016**, 302, 378–386. DOI: 10.1016/j.jpowsour.2015.10.071.

[84] A. Léon, A. Micero, B. Ludwig, A. Brisse. "Effect of scaling-up on the performance and degradation of long-term operated electrolyte supported solid oxide cell, stack and module in electrolysis mode". *Journal of Power Sources* **2021**, 510, 230346. DOI: 10.1016/j.jpowsour.2021.230346.

[85] L. L. Raja, R. J. Kee, O. Deutschmann, J. Warnatz, L. D. Schmidt. "A critical evaluation of Navier–Stokes, boundary-layer, and plug-flow models of the flow and chemistry in a catalytic-combustion monolith". *Catalysis Today* **2000**, 59 (1-2), 47–60. DOI: 10.1016/S0920-5861(00)00271-6.

[86] S. B. Beale, S. V. Zhubrin. "A Distributed Resistance Analogy for Solid Oxide Fuel Cells". *Numerical Heat Transfer, Part B: Fundamentals* **2005**, 47 (6), 573–591. DOI: 10.1080/10407790590907930.

[87] I. E. Idelchik. *Handbook of Hydraulic Resistance, 4th Edition Revised and Augmented*. Begell House Inc., **2008**. DOI: 10.1615/978-1-56700-251-5.0.

[88] O. Furst, O. Deutschmann. "Development and calibration of a fast flow model for solid oxide cell stack internal manifolds". *Journal of Power Sources* **2024**, 613, 234857. DOI: 10.1016/j.jpowsour.2024.234857.

[89] G. K. Batchelor. *An introduction to fluid dynamics*. Cambridge Mathematical Library ed. Cambridge: Cambridge University Press, **2000**.

[90] *OpenFOAM: User Guide: simpleFoam*. URL: https://www.openfoam.com/documentation/guides/latest/doc/guide-applications-solvers-incompressible-simpleFoam.html (visited on May 23, 2024).

[91] O. Deutschmann, S. Tischer, K. S, V. Janardhanan, C. Correa, D. Chatterjee, N. Mladenov, H. D. Minh, H. Karadeniz, M. Hettel, V. Menon, A. Banerjee, H. Gossler, A. Shirsath, D. E. *DETCHEM*. **2022**. URL: https://www.detchem.com.

[92] P. J. Roache. "Perspective: A Method for Uniform Reporting of Grid Refinement Studies". *Journal of Fluids Engineering* **1994**, 116 (3), 405–413. DOI: 10.1115/1.2910291.

[93] *Examining Spatial (Grid) Convergence*. URL: https://www.grc.nasa.gov/www/wind/valid/tutorial/spatconv.html (visited on Oct. 29, 2023).

[94] O. Furst, O. Deutschmann. "A Versatile Multi-Scale Framework for Transient Simulations of Solid Oxide Cells and Stack Modules Integrated in DETCHEM". *Journal of The Electrochemical Society* **2025**, 172 (7), 074508. DOI: 10.1149/1945-7111/ade56d.

[95] O. Furst, L. Wehrle, D. Schmider, J. Dailly, O. Deutschmann. "Modeling, optimization and comparative assessment of power-to-methane and carbon capture technologies for renewable fuel production". *Applied Energy* **2024**, 375, 123972. DOI: 10.1016/j.apenergy.2024.123972.

[96] V. Menon, Q. Fu, V. M. Janardhanan, O. Deutschmann. "A model-based understanding of solid-oxide electrolysis cells (SOECs) for syngas production by H2O/CO2 co-electrolysis". *Journal of Power Sources* **2015**, 274, 768–781. DOI: 10.1016/j.jpowsour.2014.09.158.

[97] L. Wehrle, Y. Wang, P. Boldrin, N. P. Brandon, O. Deutschmann, A. Banerjee. "Optimizing Solid Oxide Fuel Cell Performance to Re-evaluate Its Role in the Mobility Sector". *ACS Environmental Au* **2022**, 2 (1), 42–64. DOI: 10.1021/acsenvironau.1c00014.

[98] H. Zhu, R. J. Kee. "Modeling Electrochemical Impedance Spectra in SOFC Button Cells with Internal Methane Reforming". *Journal of The Electrochemical Society* **2006**, 153 (9), A1765. DOI: 10.1149/1.2220065.

[99] S. E. Bechtel, R. L. Lowe. *Fundamentals of continuum mechanics: with applications to mechanical, thermomechanical, and smart materials*. Amsterdam Boston: Academic Press, an imprint of Elsevier, **2015**.

[100] R. J. Kee, M. E. Coltrin, P. Glarborg, H. Zhu. *Chemically Reacting Flow: Theory, Modeling, and Simulation*. 1st ed. Hoboken, NJ: Wiley, **2017**. DOI: 10.1002/9781119186304.

[101] M. S. Day, J. B. Bell. "Numerical simulation of laminar reacting flows with complex chemistry". *Combustion Theory and Modelling* **2000**, 4 (4), 535–556. DOI: 10.1088/1364-7830/4/4/309.

[102] D. Klotz, A. Weber, E. Ivers-Tiffée. "Practical Guidelines for Reliable Electrochemical Characterization of Solid Oxide Fuel Cells". *Electrochimica Acta* **2017**, 227, 110–126. DOI: 10.1016/j.electacta.2016.12.148.

[103] E. A. Mason, A. P. Malinauskas. *Gas transport in porous media: the dusty-gas model*. Chemical engineering monographs 17. Amsterdam: Elsevier, **1983**.

[104] V. M. Janardhanan, O. Deutschmann. "Numerical study of mass and heat transport in solid-oxide fuel cells running on humidified methane". *Chemical Engineering Science* **2007**, 62 (18), 5473–5486. DOI: 10.1016/j.ces.2007.01.043.

[105] J. O. Hirschfelder, C. F. Curtiss, R. B. Bird. *Molecular theory of gases and liquids*. Corrected ed., with notes added. Hoboken, NJ: Wiley, **1964**.

[106] L. Wehrle, A. Ashar, O. Deutschmann, R. J. Braun. "Evaluating high power density, direct-ammonia SOFC stacks for decarbonizing heavy-duty transportation applications". *Applied Energy* **2024**, 372, 123646. DOI: 10.1016/j.apenergy.2024.123646.

[107] Y. Lin, Z. Zhan, J. Liu, S. A. Barnett. "Direct operation of solid oxide fuel cells with methane fuel". *Solid State Ionics* **2005**, 176 (23), 1827–1835. DOI: 10.1016/j.ssi.2005.05.008.

[108] L. Wang, M. Rao, S. Diethelm, T. E. Lin, H. Zhang, A. Hagen, F. Maréchal, J. Van herle. "Power-to-methane via co-electrolysis of H2O and CO2: The effects of pressurized operation and internal methanation". *Applied Energy* **2019**, 250, 1432–1445. DOI: 10.1016/j.apenergy.2019.05.098.

[109] L. Kunz, L. Maier, S. Tischer, O. Deutschmann. "Modeling the Rate of Heterogeneous Reactions". *Modeling and Simulation of Heterogeneous Catalytic Reactions*. Ed. by O. Deutschmann. Weinheim: Wiley-VCH, **2011**, 113–148. DOI: 10.1002/9783527639878.ch4.

[110] M. Coltrin, R. Kee, F. Rupley. *Surface CHEMKIN (Version 4. 0): A Fortran package for analyzing heterogeneous chemical kinetics at a solid-surface—gas-phase interface*. SAND-90-8003B, 6128661. **1991**. DOI: 10.2172/6128661.

[111] L. Maier, B. Schädel, K. Herrera Delgado, S. Tischer, O. Deutschmann. "Steam Reforming of Methane Over Nickel: Development of a Multi-Step Surface Reaction Mechanism". *Topics in Catalysis* **2011**, 54 (13), 845. DOI: 10.1007/s11244-011-9702-1.

[112] V. M. Janardhanan, O. Deutschmann. "CFD analysis of a solid oxide fuel cell with internal reforming: Coupled interactions of transport, heterogeneous catalysis and electrochemical processes". *Journal of Power Sources* **2006**, 162 (2), 1192–1202. DOI: 10.1016/j.jpowsour.2006.08.017.

[113] *DETCHEM-Mechanisms*. URL: https://www.detchem.com/mechanisms (visited on Nov. 22, 2024).

[114] C. H. Wendel, Z. Gao, S. A. Barnett, R. J. Braun. "Modeling and experimental performance of an intermediate temperature reversible solid oxide cell for high-efficiency, distributed-scale electrical energy storage". *Journal of Power Sources* **2015**, 283, 329–342. DOI: 10.1016/j.jpowsour.2015.02.113.

[115] D. Ferrero, A. Lanzini, P. Leone, M. Santarelli. "Reversible operation of solid oxide cells under electrolysis and fuel cell modes: Experimental study and model validation". *Chemical Engineering Journal* **2015**, 274, 143–155. DOI: 10.1016/j.cej.2015.03.096.

[116] Y. Wang, A. Banerjee, L. Wehrle, Y. Shi, N. Brandon, O. Deutschmann. "Performance analysis of a reversible solid oxide cell system based on multi-scale hierarchical solid oxide

cell modelling". *Energy Conversion and Management* **2019**, 196, 484–496. DOI: 10.1016/j.enconman.2019.05.099.

[117] V. Menon, V. M. Janardhanan, O. Deutschmann. "Modeling of Solid-Oxide Electrolyser Cells: From H2, CO Electrolysis to Co-Electrolysis". *ECS Transactions* **2013**, 57 (1), 3207. DOI: 10.1149/05701.3207ecst.

[118] A. Bertei, C. Nicolella. "A comparative study and an extended theory of percolation for random packings of rigid spheres". *Powder Technology* **2011**, 213 (1), 100–108. DOI: 10.1016/j.powtec.2011.07.011.

[119] A. Bertei, C. Nicolella. "Percolation theory in SOFC composite electrodes: Effects of porosity and particle size distribution on effective properties". *Journal of Power Sources* **2011**, 196 (22), 9429–9436. DOI: 10.1016/j.jpowsour.2011.06.087.

[120] J. H. Nam, D. H. Jeon. "A comprehensive micro-scale model for transport and reaction in intermediate temperature solid oxide fuel cells". *Electrochimica Acta* **2006**, 51 (17), 3446–3460. DOI: 10.1016/j.electacta.2005.09.041.

[121] P.-Y. Lanfrey, Z. V. Kuzeljevic, M. P. Dudukovic. "Tortuosity model for fixed beds randomly packed with identical particles". *Chemical Engineering Science* **2010**, 65 (5), 1891–1896. DOI: 10.1016/j.ces.2009.11.011.

[122] R. E. Hayes, S. T. Kolaczkowski. *Introduction to catalytic combustion*. Amsterdam: Gordon and Breach, **1997**.

[123] P. Deuflhard, E. Hairer, J. Zugck. "One-step and extrapolation methods for differential-algebraic systems". *Numerische Mathematik* **1987**, 51 (5), 501–516. DOI: 10.1007/BF01400352.

[124] S. Tischer, O. Deutschmann. "Recent advances in numerical modeling of catalytic monolith reactors". *Catalysis Today* **2005**, 105 (3), 407–413. DOI: 10.1016/j.cattod.2005.06.061.

[125] V. Menon, V. M. Janardhanan, S. Tischer, O. Deutschmann. "A novel approach to model the transient behavior of solid-oxide fuel cell stacks". *Journal of Power Sources* **2012**, 214, 227–238. DOI: 10.1016/j.jpowsour.2012.03.114.

[126] J. J. Baschuk, X. Li. "Modelling of polymer electrolyte membrane fuel cell stacks based on a hydraulic network approach". *International Journal of Energy Research* **2004**, 28 (8), 697–724. DOI: 10.1002/er.993.

APPENDIX A

Attached publication of Furst et al. [88]

Title: Development and calibration of a fast flow model for solid oxide cell stack internal manifolds
Journal: Journal of Power Sources
Authors: Oscar Furst, Olaf Deutschmann

Journal of Power Sources 613 (2024) 234857

Contents lists available at ScienceDirect

Journal of Power Sources

journal homepage: www.elsevier.com/locate/jpowsour

Development and calibration of a fast flow model for solid oxide cell stack internal manifolds

Oscar Furst, Olaf Deutschmann *

Karlsruhe Institute of Technology, Kaiserstraße 12, Karlsruhe, 76131, Baden-Württemberg, Germany

HIGHLIGHTS

- Commonly used Darcy–Weisbach friction factor shown to be inaccurate in SOC manifolds.
- Pressure loss coefficient expressions for junctions in SOC manifolds are provided.
- Fast and accurate algebraic model of the flow distribution in SOC stacks is presented.

GRAPHICAL ABSTRACT

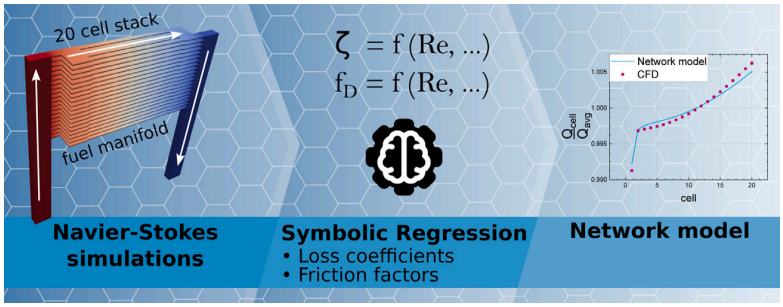

ARTICLE INFO

Keywords:
Solid oxide cell stack internal manifold
Flow network model
Pressure loss coefficients

ABSTRACT

Due to the commercialization of solid oxide cells (SOC) progressing at an accelerated pace, computationally inexpensive SOC models adapted to the iterative nature of the engineering process are in increasing demand. Flow simulation in the stack is especially challenging in this regard because detailed computational fluid mechanic models are computationally demanding, while simplified models rely on pressure loss coefficients and friction factors not readily available in the literature. In this study, a computationally inexpensive algebraic model of an SOC stack internal manifold is developed and calibrated for laminar flow conditions. Thereby, pressure loss coefficients and Darcy friction factors are determined for a broad range of operating conditions through symbolic regression of Navier–Stokes flow simulation results of stacks of 20 to 40 cells. The derived Darcy friction factors for the inlet and outlet manifolds prove to be of particular importance, as they deviate strongly from the expressions assumed in similar modeling studies. The predictive power of the developed model is demonstrated by providing accurate predictions of the flow distribution in the stack, even outside of the calibration window.

1. Introduction

In recent years, the commercialization of solid oxide cells (SOC) has experienced an unprecedented surge, with the production capabilities of commercial manufacturers being scaled up to meet the anticipated global demand [1]. Concurrently, the planning of industrial applications of large quantities of integrated SOC stacks [2,3] drives the demand for simulation tools adapted to the optimization tasks performed during the system engineering process [4]. While SOC models have traditionally served as valuable academic tools for comprehending the intricate physico-chemical dynamics within cells and stacks, this change necessitates the development of faster simulation tools tailored to the iterative nature of the engineering process.

* Corresponding author.
E-mail addresses: oscar.furst@kit.edu (O. Furst), deutschmann@kit.edu (O. Deutschmann).
URL: https://www.itcp.kit.edu/deutschmann/ (O. Deutschmann).

https://doi.org/10.1016/j.jpowsour.2024.234857
Received 10 April 2024; Received in revised form 27 May 2024; Accepted 3 June 2024
Available online 26 June 2024

Nomenclature

Abbreviations

BC	Boundary condition
GCI	Grid convergence index
MEA	Membrane electrode assembly
NRMSD	Normalized root mean square deviation
SOC	Solid oxide cell

Sub- and superscripts

i	i^{th} cell (counting from the top)
n	n^{th} cell (counting from the top)
avg	Average
B	Bend
C	Common branch (of a tee junction)
in	Inlet
M	Manifold
out	Outlet
S	Side branch (of a tee junction)
St	Straight passage (of a tee junction)
tot	Total

Variables

μ	[Pa s]	Dynamic viscosity
ν	[$m^2\,s^{-1}$]	Kinematic viscosity
ρ	[$kg\,m^{-3}$]	Density
ζ	[–]	Pressure loss coefficient
a		Slope of a linear function
b		Intersect of a linear function
D_H	[m]	Hydraulic diameter
f_D	[–]	Darcy friction factor
h	[m]	Height
k	[m^2]	Permeability
L	[m]	Length
n	[–]	Number of cells in the stack
p	[Pa]	Pressure
Q	[$m^3\,s^{-1}$]	Flow rate
Re	[–]	Reynolds number
u	[$m\,s^{-1}$]	Velocity
x, y, z	[m]	Spacial coordinates

Models used to optimize cell and stack designs need to simulate the system performance as a function of various design parameters such as cell materials, electrode microstructure and operating conditions. By nature, the cell models used for such tasks need to be extrapolatable with reasonable accuracy beyond the operating points used for calibration, which is achieved through detailed but computationally expensive modeling of the underlying physical processes. Fortunately, such simulations can be expedited through the use of space-marching [5] and clustering algorithms [6]. The computational efficiency of flow simulation within the stack, however, emerges as a critical factor. The intricacies of computational fluid mechanic models that encompass both inertial and viscous flow patterns, along with their impact on flow distribution in the stack, pose a significant computational challenge. Simultaneously, flow maldistribution caused by the stack manifold can have a significant effect on stack operating conditions, especially regarding degradation rates [7]. Such effects are especially relevant whenever a limited amount of space can be allotted to the manifold system, as is the case for mobile applications [8]. In light of this, there is a growing imperative to develop stack manifold models that strike a balance between accuracy and computation time, facilitating the swift progression of the design and optimization processes.

The flow distribution in stacks can be studied with high accuracy using 3-dimensional stack models resolving the flow-field with the Navier–Stokes equation [9]. Compared to the experimental approach, detailed simulations have the added advantage of providing access to the entire flow-field. However, such models suffer from long computation times, especially when the electrochemistry is also simulated.

In order to reduce computational costs, Beale et al. [10–12] introduced the distributed resistance analogy for solid oxide fuel cell manifold modeling. With this method, the full momentum conservation equation is still solved in the manifold, but simplified inside the active region of the stack, which allows the use of a coarser mesh. In exchange for a minimal loss in precision, computation times can be reduced by roughly an order of magnitude.

The most computationally efficient models are flow network models [13–15], because they only require the solution of a set of algebraic equations. While the loss of accuracy is greater, sub-second computation times can be achieved, which is a reduction by more than four orders of magnitude compared to the detailed simulation. However, their accuracy relies heavily on the availability of pressure loss coefficients for the geometric features of the studied manifold, such as junctions and bends. This is especially challenging for stack manifolds because the literature on pressure loss coefficients in tee junctions focuses heavily on turbulent operation [16], leading scientists to use ill-suited coefficients or neglect them altogether [13,17]. In any stack, the final portion of the inlet manifold and the initial portion of the outlet manifold operate in the laminar regime due to the low flow rate. In stacks with low flow rates at the inlet (e.g., due to a low number of cells), and therefore low Reynolds number, the flow can be fully laminar.

In this study, a network model is developed for the manifold design of interest, for which pressure loss coefficients are computed using 3-dimensional Navier–Stokes flow simulation results obtained from stacks comprising 20 to 40 cells under laminar flow conditions. The use of symbolic regression is showcased for the development of closed-form expressions used for the computation of loss coefficients in the simplified model.

Expressions for the evaluation of the Darcy friction factor in the inlet and outlet manifolds are also developed, and the result is shown to differ from the friction factors often used in similar modeling studies.

The resulting model is shown to predict flow maldistribution in the studied manifold geometry with good accuracy and negligible computation times. Crucially, the model demonstrates its efficacy beyond the confines of the calibration window, underlining its potential as a valuable tool for engineers and researchers engaged in the design and optimization of SOC systems. Compared to detailed, three-dimensional computational fluid dynamics (CFD) investigations, this approach can be leveraged to expedite the simulations of full SOC stacks with internal manifolds.

2. Methodology

2.1. Manifold geometry

For the purpose of this study, a U-type stack manifold design was developed for the stacks of 9 cm × 14.2 cm fuel electrode-supported cells under co-flow operation studied by Wehrle et al. [18]. Literature on current commercial stack manifold designs is very scarce, with the notable exception of the Jülich Mark-F which is a counter-flow design [10,19,20]. Therefore, the design produced herein resulted from the aggregation of geometric data from similar modeling studies [21,22] and educated guesses based on published images of commercial stacks [23,24]. In this study, the modeling efforts are focused on the

Table 1
Fuel manifold geometry parameters.

Parameter	Value	Unit
Manifold channel width	17	mm
Manifold channel depth	17	mm
Fuel channel width	4.75	mm
Fuel channel height	1	mm
Fuel channel length	90	mm
Inlet & outlet header length	17	mm
Sealing width	8	mm
Interconnect rib width	1.5	mm
Interconnect total height	3.5	mm
MEA height	0.4103	mm

(a) Schematic of the flow paths through the fuel channels of a cell.

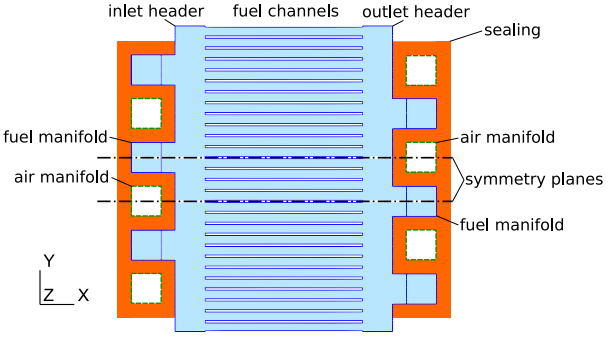

(b) Simulated flow domain for a 20 cell stack, corresponding to the region demarcated by symmetry planes. Annotations in italic correspond to boundary conditions listed in Table 2.

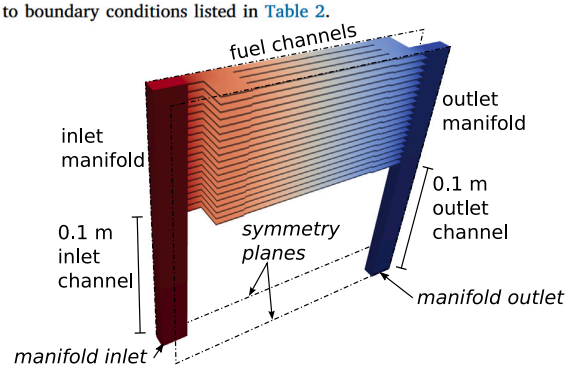

Fig. 1. Visualizations of the geometry of the simulated manifold.

fuel manifold, as the symmetrical design allows to apply the results to the air manifold as well. A schematic of the resulting fuel manifold for a single cell is shown in Fig. 1(a) and a detailed list of measurements is provided in Table 1.

Due to the repetitive structure of the flow domain, the computational cost of detailed simulations can be greatly reduced by simulating a slice of the manifold with symmetry boundary conditions on each side, as shown in Fig. 1(b). Due to the large width of the stack (142 mm) compared to the slice (25 mm), the incurred loss of accuracy is expected to be small.

2.2. Navier–Stokes flow model

The flow in the manifold was studied through simulations using the SimpleFOAM solver of OpenFOAM [25], which solves the steady-state incompressible Navier–Stokes equations using the SIMPLE algorithm. In this case, the following set of the equations is solved [26]:

$$\nabla \cdot u = 0 \tag{1}$$

Table 2
Boundary conditions used to solve the Navier–Stokes equation.

Boundary	Velocity BC	Pressure BC
Manifold inlet	parabolic profile, $\bar{u} = u_{\text{in}}$	$\frac{\partial p}{\partial n} = 0$
Manifold outlet	$\frac{\partial u}{\partial n} = 0$	$p = 0$
Symmetry plane	symmetry	symmetry
Walls	$u = 0$	$\frac{\partial p}{\partial n} = 0$

Table 3
List of simulations, each characterized by the number of cells in the stack and the average flow velocity in the fuel channels $\bar{u}_{\text{cells}}$, leading to a Reynolds number Re_{in} at the inlet.

n°	Number of cells	$\bar{u}_{\text{cells}}$	Re_{in}	Function
1	40	$1\,\text{m}\,\text{s}^{-1}$	284	Training data
2	20	$1\,\text{m}\,\text{s}^{-1}$	142	Training data
3	20	$2\,\text{m}\,\text{s}^{-1}$	248	Training data
4	20	$0.5\,\text{m}\,\text{s}^{-1}$	71	Training data
5	20	$3\,\text{m}\,\text{s}^{-1}$	426	Test data
6	20	$0.25\,\text{m}\,\text{s}^{-1}$	47	Validation data

$$\nabla \cdot (u \otimes u) = \nabla \cdot R - \nabla \frac{p}{\rho} \tag{2}$$

with the velocity vector u, the stress tensor R and the kinematic pressure $\frac{p}{\rho}$.

The boundary conditions (BC) used for the simulations are listed in Table 2. Inlet and outlet channels with a length of 0.1 m were added to the geometry in order to guarantee a fully developed flow at the inlet of the manifold and reduce the influence of the outlet boundary conditions on the flow in the outlet manifold.

In order to analyze the flow over a broad range of parameters, the flow was simulated for stacks with a different number of cells (20 to 40) and for a range of Reynolds numbers ($Re_{\text{in}} \in \{47, 71, 142, 284, 426\}$). At a Reynolds number of 568 achieved with an average fuel channel velocity $\bar{u}_{\text{cells}} = 4\,\text{m}\,\text{s}^{-1}$ in the 20 cell stack, transient behavior was observed which cannot be resolved using the SimpleFOAM solver. Solving the transient Navier–Stokes equation for stacks of 20 cells and the level of accuracy targeted by this study is not practically feasible due to computation times increasing by several orders of magnitude. Therefore, the start of this transient flow regime represents an upper bound for the range of Reynolds numbers at the inlet that can be studied with the present methodology. Simulations were performed using the fluid properties of a 90% H_2O, 10% H_2 mixture at 650 °C, leading to a kinematic viscosity of $\nu = 3.15 \cdot 10^{-4}\,\text{m}^2\,\text{s}^{-1}$. An exhaustive list of investigated flow conditions is provided in Table 3.

In order to ensure that the flow model resulting from this study is not only applicable to the fitted flow conditions, the simulation with the highest Reynolds number was kept as test data and the simulation with the lowest Reynolds number was kept as validation data. The test data was not used to fit the loss coefficients developed in this study, but was consulted during their development in order to ensure accurate extrapolation beyond the calibration window. The validation data was used only to test the accuracy of the resulting model at the very end of the study.

The applicability of Reynolds' law of similarity to all quantities of interest in this study (pressure loss coefficients, Darcy friction factors, permeabilities and flow distribution) was confirmed by performing an additional simulation at $Re_{\text{in}} = 142$ with a kinematic viscosity of $\nu = 6.30 \cdot 10^{-4}\,\text{m}^2\,\text{s}^{-1}$, which led to discrepancies in the results well below 0.1% in magnitude. As a result, the findings of this study are not only applicable to flows with the simulated gas properties, but to any flow of similar Reynolds number.

A grid convergence study according to Roache [27] was performed on the 20 cells, $Re_{\text{in}} = 284$ case using 3 grids with respectively 18, 50 and 142 million hexahedral cells (grid refinement ratio $r \approx 1.4$). The difference in the average pressure in the inlet manifold and the outlet manifold Δp_{stack}, measured 1 mm below the first cell, was used as a

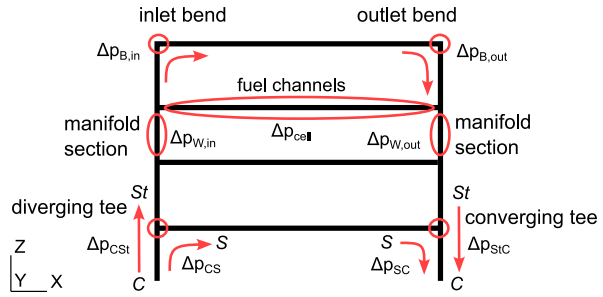

Fig. 2. Schematic of the manifold geometry with a visualization of flow features with significant influence on the total pressure in the flow. The nomenclature used to differentiate the common channel *C*, side channel *S* and straight passage *St* of converging and diverging tees is annotated in italic.

criterion for the computation of the relative error between two meshes

$$\epsilon_{12} = \frac{\Delta p_{\text{stack}}^{\text{grid 2}} - \Delta p_{\text{stack}}^{\text{grid 1}}}{\Delta p_{\text{stack}}^{\text{grid 1}}}. \tag{3}$$

Using second order interpolation and integration schemes in OpenFOAM, an order of convergence

$$p = \ln\left(\frac{\Delta p_{\text{stack}}^{\text{grid 1}} - \Delta p_{\text{stack}}^{\text{grid 2}}}{\Delta p_{\text{stack}}^{\text{grid 2}} - \Delta p_{\text{stack}}^{\text{grid 3}}}\right) / \ln(r) = 1.75 \tag{4}$$

and a grid convergence index

$$GCI = \frac{3\,|\epsilon_{12}|\,r^p}{(r^p - 1)} = 3.8\% \tag{5}$$

was computed for the intermediate mesh, which provides a reasonable error band for the solution. As the grid convergence study was performed over three meshes, the results could be verified to be in the asymptotic range of convergence. Results reported herein were all obtained using the intermediate grid spacing.

2.3. Computation of pressure losses

The following significant flow features in which total pressure $p_{\text{tot}} = p + \rho\,\vec{u}^2/2$ is lost or recovered are isolated in the simulated geometry (see Fig. 2):

- Diverging tees in the inlet manifold
- Converging tees in the outlet manifold
- Straight channel sections between tees
- Bends at the upper end of the manifolds
- Fuel channels, including inlet and outlet headers

The methodology used to compute the pressure gradients and loss coefficients in the manifolds is visualized in Fig. 3(a):

In order to assimilate the simulated results to a one-dimensional network model, the dimensionality of the results is reduced by averaging the static pressure $p(x, y, z)$, axial velocity $u_z(x, y, z)$ and total pressure $p_{\text{tot}}(x, y, z)$ across the cross-section of the manifolds in order to obtain $\overline{p}(z)$, $\overline{u}_z(z)$ and $\overline{p}_{\text{tot}}(z)$ which are only functions of the height coordinate.

For every manifold section located between the fuel channels of two cells, a linear regression is performed to express the total pressure in the i^{th} manifold section as a linear function of the manifold height

$$\overline{p}_{\text{tot}}(z) \approx a_i\, z + b_i \qquad z \in \left[z_{i,1/4}, z_{i,3/4}\right] \tag{6}$$

with the total pressure averaged over the cross section of the manifold $\overline{p}_{\text{tot}}$ expressed as a function of the height coordinate z, the slope a_i and intercept b_i determined through linear regression, knowing that the slope $a_i = \partial\overline{p}_{\text{tot}}^{\,i}/\partial z$ is the pressure gradient in the i^{th} manifold section.

Since the adjacent tee junctions causes a disturbance of the pressure in the nearby regions of the manifold sections (seen in the plot of $\overline{p}_{\text{tot}}(z)$ in Fig. 3(a)), the regression is only performed over half of the length of every section, from the coordinate $z = z_{i,1/4}$ to the coordinate $z = z_{i,3/4}$ which exclude the first and last quarter of the manifold sections.

At the inlet and outlet of the headers in the cells, the pressure is undisturbed by the adjacent junctions. Therefore, the total pressures at the start of the inlet header $\overline{p}^{\,i}_{\text{tot,cell,in}}$ and the end of the outlet header $\overline{p}^{\,i}_{\text{tot,cell,out}}$ are simply averaged over their cross-section:

$$\overline{p}^{\,i}_{\text{tot,cell,pos}} = \frac{1}{h_{\text{cell}}\,w_{\text{M}}} \int_{z_{i,\text{begin}}}^{z_{i,\text{end}}} \int_{y_{\text{begin}}}^{y_{\text{end}}} \overline{p}_{\text{tot}}(x_{\text{pos}}, y, z)\,dy\,dz$$
$$\text{with pos} \in \{\text{in}, \text{out}\} \tag{7}$$

with h_{cell} the height of a fuel channel, w_{M} the width of the manifold and its outlet towards the fuel channels, y_{begin} and $y_{\text{end}} = y_{\text{begin}} + w_{\text{M}}$ the y-coordinates of the sides of the manifold and $z_{i,\text{begin}}$ and $z_{i,\text{end}} = z_{i,\text{begin}} + h_{\text{cell}}$ the heights at which the ith fuel channel begins and ends. They are used to compute the pressure losses along the cells and the pressure loss coefficients of the tees and bends.

Herein, the nomenclature of Idelchik [16] was adopted to differentiate between the three branches of converging and diverging tees. The branch with the highest flow rate, which is the source of the flow in diverging tees and the sink of the flow in converging tees, is called the *common channel* and the subscript *C* is used. The branch opposite of the common channel is called the *straight passage* and the subscript *St* is used. The remaining branch is called the *side branch* and the subscript *S* is used.

Diverging tees have two flow paths: turning from the common channel to the side branch, and the straight passage from the common channel (see Fig. 2). Pressure loss due to friction is observed for the turning flow, while pressure recovery is observed for the straight passage (see Fig. 3(a)). The rise in total pressure across the junctions is due to low-speed gas from the boundary layer which exits the flow, which leaves the gas with a higher specific energy in the main channel [16]. The corresponding pressure loss coefficients are computed as follows [16]:

$$\zeta_{\text{CS}} = \frac{\overline{p}_{\text{tot,S}} - \overline{p}_{\text{tot,C}}}{\rho\overline{u}^2_{z,C}/2} \tag{8}$$

$$\zeta_{\text{CSt}} = \frac{\overline{p}_{\text{tot,St}} - \overline{p}_{\text{tot,C}}}{\rho\overline{u}^2_{z,C}/2}. \tag{9}$$

As previously mentioned and seen in Fig. 3(a), changes in total pressure due to this geometrical feature can already be observed in the manifold sections before and after the tees. In order to separate the effects of the wall friction from the effect of the tee, the total pressure drop is computed using the results of the linear regression:

$$\Delta p^i_{\text{CSt}} = \overline{p}^{\,i}_{\text{tot,St}} - \overline{p}^{\,i}_{\text{tot,C}}$$
$$= a_{i-1}\, z_{\text{i-1,begin}} + b_{i-1} - \left(a_i\, z_{\text{i,end}} + b_i\right). \tag{10}$$

The linear regression is not needed in the fuel channels, so that the turning pressure drop is computed as:

$$\Delta p^i_{\text{CS}} = \overline{p}^{\,i}_{\text{tot,cell,in}} - \overline{p}^{\,i}_{\text{tot,C}}$$
$$= \overline{p}^{\,i}_{\text{tot,cell,in}} - \left(a_i\, z_{\text{i,end}} + b_i\right). \tag{11}$$

In the converging tees of the outlet manifold, the two flow paths go from the side branch to the common branch and from the straight channel to the common branch (see Fig. 2). The same methodology as above is employed, with the pressure drops being computed in the direction of the flow:

$$\zeta_{\text{SC}} = \frac{\overline{p}_{\text{tot,C}} - \overline{p}_{\text{tot,S}}}{\rho\overline{u}^2_{z,C}/2} \tag{12}$$

$$\zeta_{\text{StC}} = \frac{\overline{p}_{\text{tot,C}} - \overline{p}_{\text{tot,St}}}{\rho\overline{u}^2_{z,C}/2}. \tag{13}$$

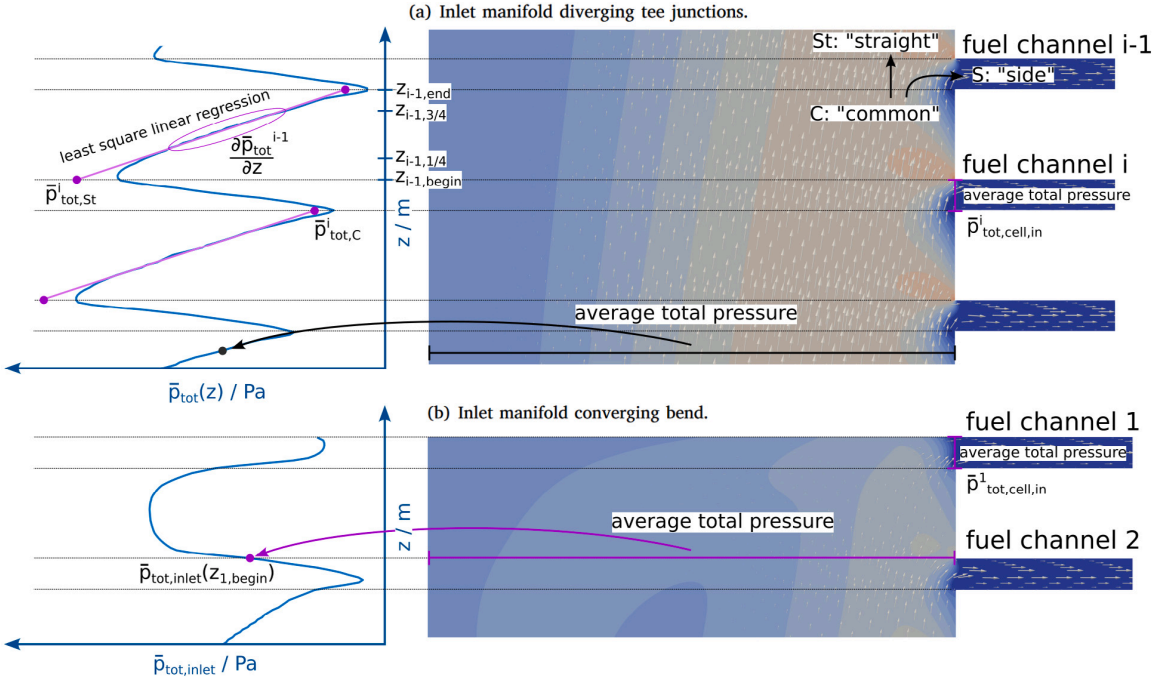

Fig. 3. Visualization of methodology used to compute (a) the pressure gradient along sections of the inlet manifold, pressure drops across tees and (b) the pressure drop across bends.

At the top of the stack, there is a converging bend from the inlet manifold to the uppermost cell and a diverging bend from the cell to the outlet manifold. These bends also have a significant influence on the total pressure profile in the uppermost manifold sections, as is shown in Fig. 3(b). Especially at the end of the inlet manifold, the stagnation of the flow causes an increase of the static pressure. The increased pressure causes a reversal of the flow direction in the low velocity parts of the manifold cross section, which leads to a large eddy. The eddy continually transports higher-energy gas, which is entrained by the relatively fast bulk flow, past the second fuel channel. Simultaneously, the other side of the eddy transports very slowly moving gas in the opposite direction over a much larger area. Due to the nonlinearity of the contribution of velocity to the kinetic energy, the eddy leads to an increase of the total pressure up to the middle of the final manifold section. After this point, the vertical motion of the eddy stops gradually, as its motion is mostly lateral in the uppermost part of the manifold. The increase in total pressure is further accentuated by the reversed flow outside of the symmetry plane (not visible on the figure), close to the lateral manifold walls, which leaves the manifold through the second fuel channel. This further removes slowly-moving portions of the flow, thereby increasing the energy of the flow per unit volume [16]. In order to capture this effect, the uppermost manifold section is included in the bend loss coefficients:

$$\zeta_{\mathrm{B,in}} = \frac{\overline{p}^{1}_{\mathrm{tot,cell,in}} - \overline{p}_{\mathrm{tot,inlet}}\left(z_{1,\mathrm{begin}}\right)}{\rho\left(\overline{u}_{z,\mathrm{inlet}}\left(z_{1,\mathrm{begin}}\right)\right)^{2}/2} \tag{14}$$

$$\zeta_{\mathrm{B,out}} = \frac{\overline{p}_{\mathrm{tot,outlet}}\left(z_{1,\mathrm{begin}}\right) - \overline{p}^{1}_{\mathrm{tot,cell,out}}}{\rho\left(\overline{u}_{z,\mathrm{outlet}}\left(z_{1,\mathrm{begin}}\right)\right)^{2}/2}. \tag{15}$$

Despite the complexity of the encountered flow patterns, the reduction of such complex, intrinsically 3-dimensional flows to 0-dimensional pressure loss equations is common practice and has been shown to work for a large variety of problems [16]. Through rigorous application of such a methodology to all flow features in the stack, the pressure at these strategically selected positions of the stack can be reconstructed with enough precision to provide a satisfactory prediction of the flow maldistribution, which is shown in Section 3.3.

2.4. Closed-form expressions for pressure losses

In order to compute flow distribution in a manifold with the geometry defined in Section 2.1 using a network model based on the Bernoulli equation, the total pressure losses identified in the previous section need to be estimated as functions of the local flow conditions and geometry. In this study, the number of relevant geometrical factors is minimized by only allowing changes to the number of cells in the stack (and consequently its total height), all other geometric parameters being kept constant.

With the assumption that the loss coefficients in converging and diverging tee junctions can be formulated as a function of the Reynolds number in the common branch Re_C and side branch Re_S as well as the ratio of flow rates between branches (ϱ_{St}/ϱ_C and ϱ_S/ϱ_C), an open source symbolic regression package [28,29] is used to develop expressions for every loss coefficient ζ. Symbolic regression is an application of machine learning which develop analytic functions that model a dataset. In the present case, the loss coefficients ζ_{CS}, ζ_{CSt}, ζ_{SC} and ζ_{StC} determined for the first four simulations listed in Table 3 are used as training data. The aim is to obtain expressions for the loss coefficients that are applicable to a wide range of flow conditions (see Reynolds' law of similarity in Section 2.2) in stacks with a varying amount of cells, provided that the manifold channel width and depth, fuel channel height, inlet and outlet header length, distance between manifold channels and distance between fuel channels is identical. The result of the symbolic regression process is a pareto front composed of a multitude of analytic functions, each representing a different optimum between accuracy of the fit to the training data and complexity of the function. In order to alleviate issues related to overfitting, the fifth simulation case is not used as training data but instead as test data to select an expression that extrapolates correctly beyond the training data. The sixth simulation was not consulted at this stage of the process in order to preserve an unbiased set of validation data.

The same methodology is used to develop analytic expressions for the loss coefficients in the bends at the top of the manifold, although

they are assumed to be only functions of the Reynolds number in the manifold Re_M.

The pressure loss from the inlet to the outlet of a cell was found to be an almost perfectly linear function of the average flow velocity, and therefore the pressure loss can be estimated using Darcy's law for which only the permeability k needs to be determined:

$$\Delta p = \bar{u}\,\frac{\mu\,L}{k}. \tag{16}$$

Herein, this information is used to compute the pressure drop across the cells for the validation of the model which is done by reproducing the flow distribution using the simplified model in Section 3.3. In a full SOC stack model, the difference in pressure across the cells will be influenced by the production and consumption of gas species, which may be computed using adapted flow models [14].

The pressure loss along a straight segment of the manifold (between two gas channels) is commonly computed by evaluating the pressure gradient $\frac{\partial p}{\partial z}$ in a channel using the Darcy–Weisbach equation with conventional Darcy friction factors f_D [13,30–32]:

$$\Delta p = f_D\,L\,\frac{\rho}{2}\,\frac{\bar{u}^2}{D_H}. \tag{17}$$

However, since the flow is not fully developed in any region inside the manifold, the observed pressure gradients deviate strongly from those computed this way (see Section 3.2). So, in order to be able to evaluate the pressure losses in straight segments of the manifold, the pressure gradient is computed using an expression for the Darcy friction factor f_D that is developed using the symbolic regression methodology. The Reynolds numbers in the manifolds and cells (Re_M and Re_{cell}), the ratio of flow rates between branches (Q_{St}/Q_C and Q_S/Q_C) and relative position along the manifold height z/h_{tot} are used as possible variables in the symbolic regression process.

The developed expressions for the pressure loss coefficients and the Darcy friction factors can be found in Section 3.2.

2.5. Network model of the stack flow

The network model developed in this study is an extension of the algorithm of Koh et al. [13] in which five equations are established for each cell in the stack in order to compute the static pressure at the inlet of the diverging tees p^i_{in}, the mass flow rate at the inlet of the diverging tees Q^i_{in}, the mass flow rate through the channels of the cell Q^i_{cell}, the static pressure at the outlet of the converging tees p^i_{out} and the mass flow rate at the outlet of the converging tees Q^i_{out}. The set of $5\,n$ equations for a stack of n cells is formulated as follows:

$$\begin{cases} Q^i_{in} - Q^i_{cell} = 0 & i = 1 \\ Q^i_{in} - Q^{i-1}_{in} - Q^i_{cell} = 0 & i \neq 1 \end{cases} \tag{18}$$

$$\begin{cases} Q^i_{out} - Q^i_{cell} = 0 & i = 1 \\ Q^i_{out} - Q^{i-1}_{out} - Q^i_{cell} = 0 & i \neq 1 \end{cases} \tag{19}$$

$$\begin{cases} p^i_{tot,in} + \Delta p^i_{cell} + \Delta p^i_{B,in} + \Delta p^i_{B,out} - p^i_{tot,out} = 0 & i = 1 \\ p^i_{tot,in} + \Delta p^i_{cell} + \Delta p^i_{CS} + \Delta p^i_{SC} - p^i_{tot,out} = 0 & i \neq 1 \end{cases} \tag{20}$$

$$\begin{cases} Q^i_{in} - Q_{tot} = 0 & i = n \\ p^{i+1}_{tot,in} + \Delta p^{i+1}_{W,in} + \Delta p^{i+1}_{CSt} - p^i_{tot,in} = 0 & i \neq n \end{cases} \tag{21}$$

$$\begin{cases} p^i_{tot,out} - P_0 = 0 & i = n \\ p^i_{tot,out} - p^{i+1}_{tot,out} + \Delta p^{i+1}_{W,out} + \Delta p^{i+1}_{StC} = 0 & i \neq n \end{cases} \tag{22}$$

with $p_{tot} = p + \rho\,u^2/2$.

For the purposes of this study, the inlet and outlet of the U-type manifold is assumed to be at the bottom, and the cells are numbered from the top to the bottom. The pressure loss terms Δp are defined as in Sections 2.3–2.4 and computed using the expressions provided in Section 3.2.

The result is a set of nonlinear algebraic equations which can be solved from a reasonable first guess using a damped Newton method.

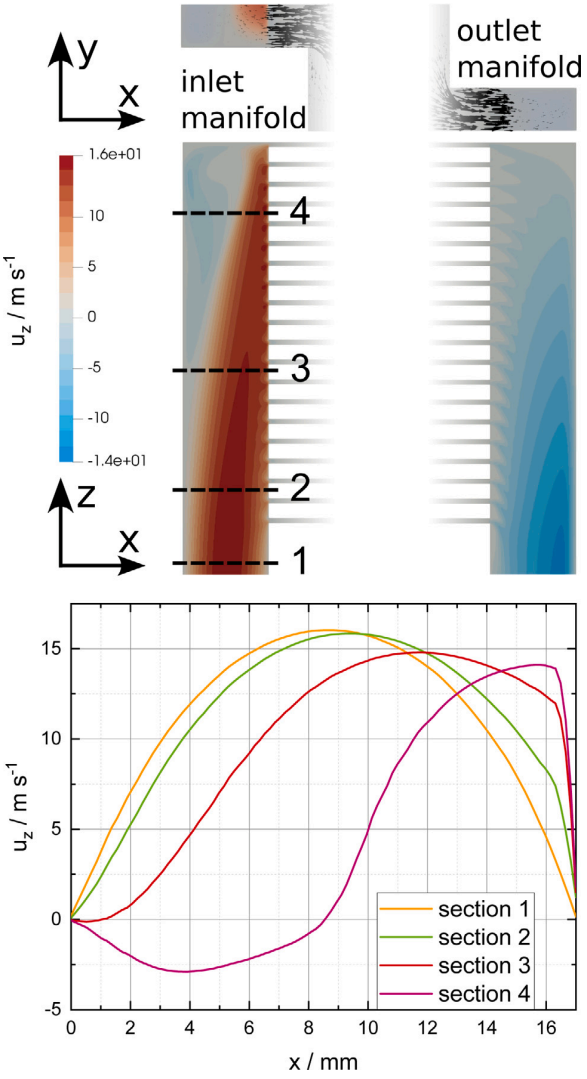

Fig. 4. Axial velocity u_z in the symmetry planes of the inlet and outlet manifolds in the 20 cells Re_{in} = 426 case and profiles of the axial velocity at 4 locations of the inlet manifold. Above the side view of the manifold, a cross-section of the fourth cell is depicted with black arrows showing the velocity vectors in the xy-plane.

3. Results

3.1. Navier–Stokes simulation results

Fig. 4 shows a contour plot of the axial velocity u_z distribution in the symmetry planes of the inlet and outlet manifolds for the simulation with 20 cells and Re_{in} = 426. Additionally, the velocity profiles along four sections of the inlet manifold are depicted.

This visualization shows clearly that the maximum flow velocity in every cross-section of the inlet manifold does not decrease significantly along the length of the manifold, despite the flow rate diminishing greatly between the inlet and the top of the stack. Although the flow rate through Section 4 is 80% lower than the flow rate through Section 1, the maximum velocity decreases by only 12%. At the inlet, the velocity profile is parabolic, as is typical for fully developed channel flows. However, the successive branching of the flow towards the cell channels causes the velocity profile to shift towards one side of the manifold, while a large eddy forms towards the other side.

As a consequence, the velocity gradient at the right side of the channel increases steadily towards the top of the stack, despite the lowering average flow velocity. Since velocity gradients lead to a shearing motion in the flow, the shear stresses (R in Eq. (2)) increase due to the viscosity of the fluid, which is the cause for friction losses. This local increase of the shear stress at the wall is therefore expected to lead to an unusual relationship between flow rate and wall friction losses, which is detailed in the following section.

The flow in the outlet manifold appears to be slightly more homogeneous, although the axial velocity profile is also shifted towards the right. While the wall friction losses are impacted by the skewed velocity profile, the absence of large recirculation zone should facilitate the prediction of pressure losses in the outlet manifold.

3.2. Expressions for the pressure losses

Using the methodology described in Section 2.4, the following expressions were developed for the pressure loss coefficients in the tees and bends:

$$\zeta_{\mathrm{CSt}} = \frac{\overline{p}_{\mathrm{tot,St}} - \overline{p}_{\mathrm{tot,C}}}{\rho \overline{u}_{z,\mathrm{C}}^2/2} \approx 39.67 \left(\frac{Q_{\mathrm{S}}}{Q_{\mathrm{C}}}\right)^2 \frac{Q_{\mathrm{St}}}{Q_{\mathrm{C}}} - 0.4069 \tag{23}$$

$$\zeta_{\mathrm{CS}} = \frac{\overline{p}_{\mathrm{tot,S}} - \overline{p}_{\mathrm{tot,C}}}{\rho \overline{u}_{z,\mathrm{C}}^2/2} \approx -\frac{Q_{\mathrm{S}}/Q_{\mathrm{C}}}{Re_{\mathrm{C}}} \left(226\, Re_{\mathrm{S}} + 3574\right) - 0.9842 \tag{24}$$

$$\zeta_{\mathrm{StC}} = \frac{\overline{p}_{\mathrm{tot,C}} - \overline{p}_{\mathrm{tot,St}}}{\rho \overline{u}_{z,\mathrm{C}}^2/2} \approx \frac{Re_{\mathrm{S}}\, Q_{\mathrm{C}}/Q_{\mathrm{St}} + {}^{15.59}/_{Re_{\mathrm{S}}} - 14.79}{Re_{\mathrm{C}}\, Q_{\mathrm{St}}/Q_{\mathrm{C}}} \tag{25}$$

$$\zeta_{\mathrm{SC}} = \frac{\overline{p}_{\mathrm{tot,C}} - \overline{p}_{\mathrm{tot,S}}}{\rho \overline{u}_{z,\mathrm{C}}^2/2} \approx \frac{2845\, Q_{\mathrm{S}}/Q_{\mathrm{C}}}{1.01 - Re_{\mathrm{C}}} + 0.7872 \tag{26}$$

$$\zeta_{\mathrm{B,in}} = \frac{\overline{p}_{\mathrm{tot,cell,in}} - \overline{p}_{\mathrm{tot,M_{in}}}}{\rho \overline{u}_{z,\mathrm{M_{in}}}^2/2} \approx {}^{-5727}/_{Re_{\mathrm{M_{in}}}} \tag{27}$$

$$\zeta_{\mathrm{B,out}} = \frac{\overline{p}_{\mathrm{tot,M_{out}}} - \overline{p}_{\mathrm{tot,cell,out}}}{\rho \overline{u}_{z,\mathrm{M_{out}}}^2/2} \approx {}^{-4702}/_{Re_{\mathrm{M_{out}}}}. \tag{28}$$

The data points extracted from the first converging and diverging tee from every stack were not used in the symbolic regression of ζ_{CSt}, ζ_{CS}, ζ_{StC} and ζ_{SC}, since a slightly irregular behavior can be expected due to the proximity to the bend at the first cell. In Fig. 5, the selected expressions for converging and diverging tee loss coefficients are plotted against the loss coefficients computed from the OpenFOAM simulation results. The orange markers represent the simulation data that was used to develop the loss coefficients expressions and the magenta markers represent the test data, which was used to verify that the selected expressions extrapolate correctly outside of the calibration range. The green markers represent the validation data, which was only evaluated at the end of the study to provide an unbiased validation case.

Similarly, the selected expressions for inlet and outlet bend loss coefficients are plotted against the loss coefficients computed from the OpenFOAM simulation results in Fig. 6. Contrary to the tees, few data points can be provided since there is only one bend of each type in each simulated case. Fortunately, the close proximity of the data points with similar local Reynolds numbers $\mathrm{Re_M}$ indicates that the pressure loss coefficients in the bends is solely a function of the local Reynolds number and does not depend on the Reynolds number at the inlet of the manifold or the number of cells in the stack.

Normalized root mean square deviations (NRMSD) between the equations and the simulated data, normalized using the range of the simulated data, were computed and listed in Table 4. The NRMSD was selected as a criterion because it emphasizes a good match of every data point by penalizing large errors in single data points (compared, e.g., to an arithmetic average error), while still encouraging a better fit for every data point than using the maximum error as a criterium. The error is normalized to allow for meaningful comparison of the quality of the regression between pressure loss coefficients with large differences in magnitude. The NRMSD is computed by comparing every simulated data point with its counterpart which is computed from the empirical expression by inserting values of Re_{C}, Re_{S}, $Q_{\mathrm{S}}/Q_{\mathrm{C}}$ and $Q_{\mathrm{St}}/Q_{\mathrm{C}}$ found in the simulation for this data point:

Table 4
Normalized root mean square deviation between the empirical expressions and the simulated data.

Empirical expression	NRMSD/%		
	Training data	Test data	Validation data
ζ_{CSt}	6.2	7.3	17
ζ_{CS}	0.12	0.18	0.11
ζ_{StC}	2.1	2.2	7.9
ζ_{SC}	0.25	0.79	0.91
$\zeta_{\mathrm{B,in}}$	1.8	13	1.7
$\zeta_{\mathrm{B,out}}$	1.2	1.7	5.2

$$\mathrm{NRMDS} = \frac{\sqrt{\frac{1}{n_{\mathrm{data}}} \sum_{i=1}^{n_{\mathrm{data}}} \left(\zeta_{\mathrm{sim},i} - \zeta\left(Re_{\mathrm{C}}^i, Re_{\mathrm{S}}^i, \frac{Q_{\mathrm{S}}}{Q_{\mathrm{C}}}^i, \frac{Q_{\mathrm{St}}}{Q_{\mathrm{C}}}^i\right)\right)^2}}{\zeta_{\mathrm{sim,max}} - \zeta_{\mathrm{sim,min}}} \tag{29}$$

Excellent agreement is reached for both of the turning loss coefficients ζ_{CS} and ζ_{SC} (NRMSD < 1%), which is of utmost importance as their large magnitude imply a large influence on the flow distribution.

Despite the very simple expressions chosen for $\zeta_{\mathrm{B,in}}$ and $\zeta_{\mathrm{B,out}}$, which is due to the lack of fit data, the agreement of the bend loss coefficients is satisfactory. The impact of this uncertainty on the flow distribution is expected to be moderate because the high magnitude of these loss coefficient is counteracted by the low flow velocities in the corresponding regions. Solely the loss coefficient for the case with the high Reynolds number $Re_{\mathrm{in}} = 426$ is inaccurately predicted, with a NRMSD of 13%.

The expressions obtained for the straight passage loss coefficients ζ_{CSt} and ζ_{StC} are the least accurate, especially ζ_{CSt} for the diverging tees at low Reynolds numbers (see Fig. 5) where the NRMSD reaches 17%. Although the fit could be improved by using expressions with a higher complexity, simplicity is prioritized due to the risk of overfitting and very low magnitude of the corresponding pressure loss and recovery (pressure increase). Since the straight passage pressure loss coefficients are small, the influence on the flow distribution can be expected to be small.

The fact that the fit obtained for pressure losses in the turning flow is more accurate than the fit obtained for the straight passage (considering expressions of similar complexity) is likely due to the fact that pressure losses during flow redirection is mostly caused by friction losses. While the difference in total pressure can be attributed to a single phenomenon in this case, the friction losses for the straight passage are anticipated to be of similar magnitude as the increase in pressure due to the transfer of momentum from the turning flow to the bulk flow, the increase in specific energy due to entrainment of the boundary layer by the turning flow and the disturbance caused by the eddy in the inlet manifold. The straight passage pressure losses being positive or negative depending on the simulated case is likely due to such competing effects.

The expressions developed to compute the Darcy friction factors f_D in straight sections of the inlet and outlet manifolds are listed below:

$$f_{D,\mathrm{in}} \approx \frac{63.13}{Re_{\mathrm{M}}} \left(Re_{\mathrm{cell}} \frac{z}{h_{\mathrm{tot}}} + 0.3544 - \frac{z}{h_{\mathrm{tot}}}\right) \tag{30}$$

$$f_{D,\mathrm{out}} \approx \frac{31.47}{Re_{\mathrm{M}}} \left(Re_{\mathrm{cell}} + 1.4735\right). \tag{31}$$

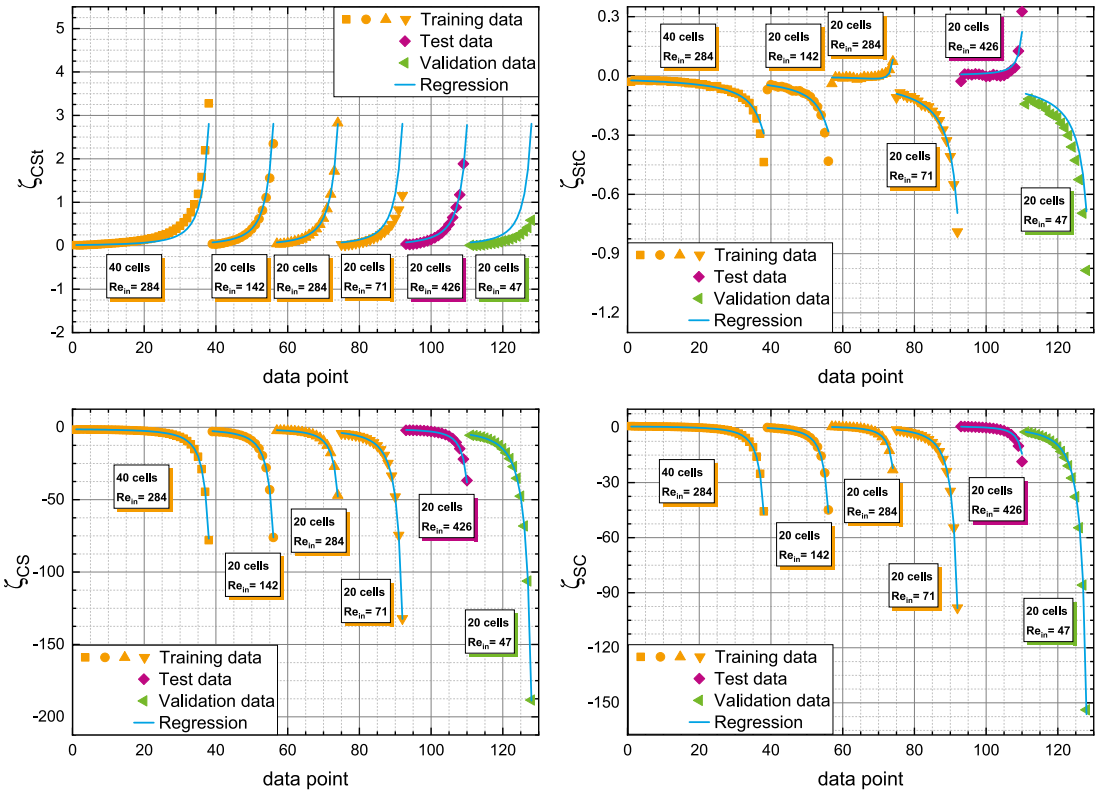

Fig. 5. Pressure loss coefficients in tees computed from detailed simulations (points) plotted against empirical expressions determined through symbolic regression (lines). Each data point corresponds to a single tee, each with a unique combination of Re_C, Re_S, ϱ_s/ϱ_c and ϱ_s/ϱ_c. Data points closer to the top of their respective manifolds feature lower Re_C and ϱ_s/ϱ_c while ϱ_s/ϱ_c grows and Re_S fully depends on the flow distribution. Data points extracted from the same detailed simulations are plotted next to each other. The detailed simulations are described by the number of cells simulated and the Reynolds number at the manifold inlet $\mathrm{Re_{in}}$ (see Table 3).

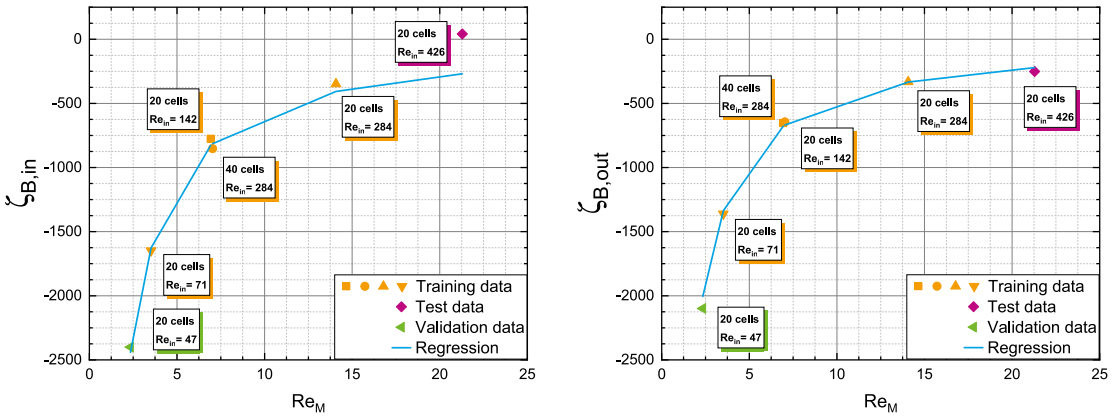

Fig. 6. Pressure loss coefficients in bends computed from detailed simulations (points) plotted against empirical expressions determined through symbolic regression (lines). The abscissa represent the Reynolds numbers $\mathrm{Re_M}$ found at the inlet of the converging bend in the inlet manifold (left) and at the outlet of the diverging bend in the outlet manifold (right). Each data point corresponds to a single bend and is labeled with the simulation it was extracted from (see Table 3).

The pressure gradient in the outlet manifold was observed to be a mostly linear function of the product of the Reynolds number in the manifold Re_{M} and the Reynolds number in the adjacent cell Re_{cell}, which results in the friction factor $f_{D,\mathrm{out}}$ being a linear function of Re_{cell}.

As the considered flow in the manifold channels is laminar, it relates more closely to Darcy's law (Eq. (16)), which predicts a linear growth of the pressure gradient with the velocity. In the present case, the permeability factor k of Darcy's law relates to the aforementioned Darcy friction factors as follows, with D_H being the hydraulic diameter of the manifold:

$$k = \frac{2\,D_H^2}{f_D\,Re_M}. \tag{32}$$

This allows a more straightforward visualization of the parameters influencing the flow in the manifold in Fig. 7. The figure shows that the outlet permeability k_{out} is practically constant for most cases, although

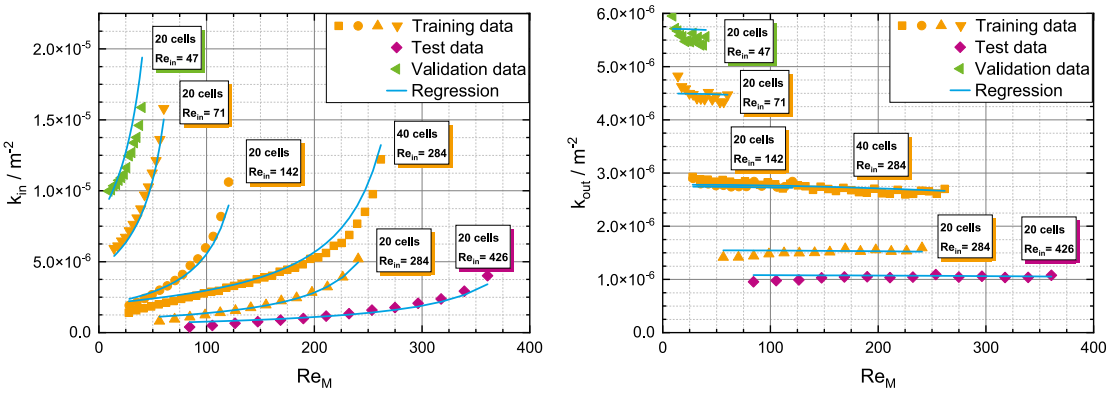

Fig. 7. Permeabilities k of straight sections of the inlet (left) and outlet (right) manifold channels computed from detailed simulations plotted against expressions determined through symbolic regression. The data points are grouped by the simulations they were extracted from, inside of which each point corresponds to a different section of the manifold. The abscissa represent the Reynolds numbers $\mathrm{Re_M}$ found in these sections of the manifold, which is higher close to the inlet of the inlet manifold and close to the outlet of the outlet manifold.

its value changes between the cases. This behavior is a clear contradiction of the commonly assumed Darcy friction factor which is solely proportional to Re_M^{-1} which would manifest as a single horizontal line at $k \approx 1.0 \cdot 10^{-5}$ in these diagrams [33]. Instead, the same permeability is observed for the two cases which feature an identical average flow velocity in the cells of $\bar{u}_\mathrm{cells} = 1\,\mathrm{m\,s^{-1}}$, the Reynolds number in the adjacent cells Re_cell can be assumed to be a major factor influencing the permeability in the outlet manifold.

The cases with $\mathrm{Re_{in}} = 47$ and $\mathrm{Re_{in}} = 71$ follow a similar trend, although they exhibit an increased permeability by up to 12% at low Reynolds numbers $\mathrm{Re_M}$. In these regions of the flow, the bulk flow in the outlet manifold has very low inertia, resulting in smoother velocity profiles more similar to the fully developed flow which results in lower friction losses. Although the regression does not capture this phenomenon accurately, the low flow velocity relative to the remaining manifold and the small magnitude of the phenomenon implies that the error in the computed pressure difference will be small.

The pressure gradient in the inlet manifold was found to be a non-monotonic function of the Reynolds number in the manifold Re_M, with the pressure gradient increasing from the bottom of the inlet manifold up to half the height of the stack, at which point the maximal pressure gradient is encountered and after which the pressure gradient decreases towards the top of the manifold. This is counter-intuitive, as the highest wall friction losses are expected to be found in the regions with the highest flow rates, which implies that the actual flow maldistribution is greater than might be estimated using pressure gradients for fully developed flow. This behavior is explained by the shape of the velocity profile, which transitions from a parabolic profile at the inlet, to a highly skewed profile in the upper parts of the stack (see Section 3.1). The skewed profile produces high velocity gradients in close proximity to the channel wall adjacent to the inlet headers, which increases the friction losses dramatically. Therefore, the permeability k_out attributable to the flow is higher close to the inlet, which is the region with the highest Reynolds number Re_M.

Inside of the cells, in the inlet header, fuel channels and outlet header, the pressure gradient was found to be a perfectly linear function of the flow rate. Sharp total pressure drops occur between those regions due to the sudden change in cross-sectional area, which are located at the inlet and outlet of the headers. These pressure drops are also perfectly linear functions of the flow rate through the cell. Therefore, the pressure drop across a cell can be simplified to a single linear function of the flow rate such as Darcy's law (Eq. (16)), for which the parameter $k = 6.326 \cdot 10^{-8}\,\mathrm{m^2}$ was fitted with a least square method.

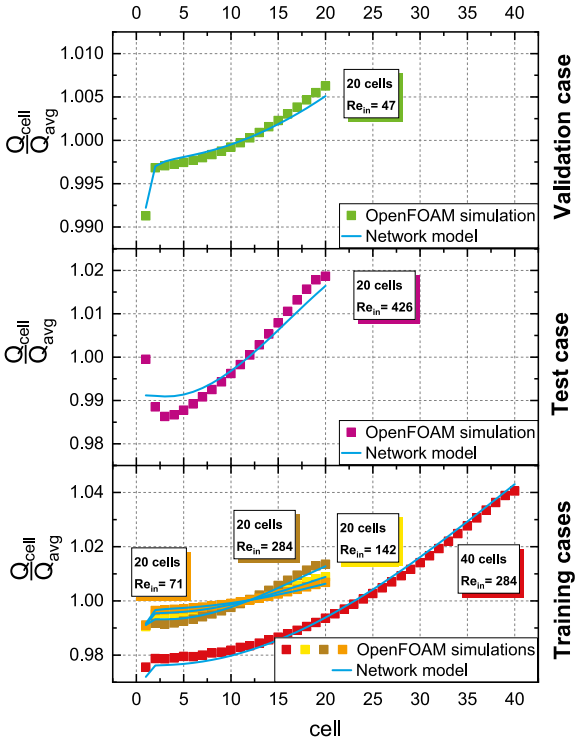

Fig. 8. Flow distribution, represented by the flow rate in every cell normalized by the average flow rate, computed via 3D simulation compared to the network model.

3.3. Flow network model validation

With the expressions for the pressure loss coefficients and pressure gradients listed in the previous section, all pressure losses required in the network model presented in Section 2.5 can be computed. Thereby, the ability of the determined expressions for loss coefficients to predict the flow distribution in the manifold is asserted. The flow distribution computed using the network model are compared to the results of the OpenFOAM simulations in Fig. 8.

Good agreement is reached with every simulation. The largest error is observed for the test case, with $Re_\mathrm{in} = 426$, which has a NRMSD for $Q_\mathrm{cell}/Q_\mathrm{avg}$ of 9.5%. This is due to the relatively high velocity of

the flow which provokes a different flow behavior close to the top of the stack. As the flow stagnates when it reaches the wall at the top of the inlet manifold, the dynamic pressure of the gas, which is its kinetic energy per unit volume, transforms into static pressure. This increases the difference in pressure between the inlet and the outlet of the uppermost cell of the stack, which results in an increased flow rate. While cases with low inlet Reynolds numbers Re_{in} have very sharp drops in flow rates in the uppermost cells due to the increased friction losses in the bend, the effect gradually reverses with increasing Reynolds numbers. In the $Re_{in} = 426$ case, the increased static pressure even reaches the second cell. The overestimated loss coefficient leads to an inability to predict the increased flow rate in the uppermost cell of the stack. Consequently, the accuracy of the predicted flow rates in the remaining cells also suffers, as the local flow conditions are not accurately predicted. Due to the important change in flow distribution caused by this phenomenon, in future model calibrations, the training data should contain a case in which it appears.

The agreement of the model with the remaining simulations, the training cases and the validation case, is excellent, with a NRMSD below 5%. Most of the model inaccuracy is expected to stem from the difficulty in predicting the pressure gradient in the manifold sections close to the inlet, which was explained in the previous section. However, the sudden change in flow rate between the uppermost cells of the stack is predicted with great accuracy in the cases with Reynolds numbers ranging from 47 to 284.

The model developed in this study can therefore be assumed to be accurate inside of this range of Reynolds numbers $Re_{in} \in [47, 284]$. With the considered fuel channel dimensions and fluid properties, in stacks of 20 to 40 cells, this corresponds to average flow velocities in the fuel channels $\bar{u}_{cells}$ of $0.25\,m\,s^{-1}$ to $2\,m\,s^{-1}$, which are commonly encountered. As Reynolds' law of similarity applies, this range can be expressed as $1.3 < Re_{cells} < 10.5$ so that it applies to any Newtonian fluid independently of its density and viscosity.

4. Conclusion

A methodology for the determination of closed-form expressions for the pressure loss coefficients and Darcy friction factors for tee junctions, bends and channels found in SOC stack internal manifolds under laminar flow conditions was presented and used to develop a computationally inexpensive but accurate stack flow model.

Six detailed simulations of the three-dimensional, incompressible flow in a U-Type manifold were performed on a fine mesh for various laminar flow conditions in stacks of 20 to 40 cells. Pressure losses across tees, bends and channels were extracted from all simulations and the pressure loss coefficients and Darcy friction factors corresponding to these losses were evaluated. Pressure losses in the manifold channels were shown to not depend only on the flow velocity, as a linear dependence on the adjacent side channel flow velocity was observed. Additionally, local wall friction losses in the inlet manifold were also shown to change as the parabolic velocity profile found at the manifold inlet transitions to a skewed profile.

After identifying the flow parameters which are most likely to impact the pressure losses in each flow feature, a symbolic regression machine learning algorithm was used to determine functions of those flow parameters which can be used to compute pressure loss coefficients and friction factors for a wide range of flow conditions.

The resulting expressions for the loss coefficients and friction factors were validated by developing a network model of the manifold flow. The system of energy and mass conservation equations supplemented by pressure losses computed with the aforementioned expressions allowed to predict with satisfactory accuracy the flow distribution for two cases which were not used in the development of the model.

The resulting model is fast, with computation times well below one second, and has been designed to be valid for stacks with an arbitrary number of cells and a large range of flow conditions, provided the flow is laminar. The similarity of flows with identical Reynolds numbers also leads the model to be valid for different fluids at different temperatures. Although the loss coefficient and friction factor expressions were developed using simulations of U-type manifolds, the local flow conditions in tees and bends of Z-type manifolds are identical and the newly established expressions can be used to model the flow in such manifolds.

CRediT authorship contribution statement

Oscar Furst: Writing – original draft, Visualization, Validation, Software, Methodology, Investigation. **Olaf Deutschmann:** Writing – review & editing, Supervision, Funding acquisition, Conceptualization.

Declaration of competing interest

The authors declare that they have no known competing financial interests or personal relationships that could have appeared to influence the work reported in this paper.

Data availability

Data will be made available on request.

Acknowledgment

The authors acknowledge support by the state of Baden-Württemberg, Germany through bwHPC. Olaf Deutschmann acknowledges support from Deutsche Forschungsgemeinschaft (DFG) though project DE 659/14-1, project number 460038541. The authors appreciate very fruitful discussions with R.J. Kee (Colorado School of Mines) and J. Daily (EIfER, Karlsuhe).

References

[1] Topsoe to build large-scale SOEC electrolyzer manufacturing facility to meet customer needs for green hydrogen production and SOEC efficiency | Large scale electrolysis, 2021, URL https://www.topsoe.com/press-releases/haldor-topsoe-to-build-soec-electrolyzer-manufacturing-facility. (Accessed 29 November 2023).

[2] Sunfire, Renewable Hydrogen Project "MultiPLHY": World's Largest High-temperature Electrolyzer from Sunfire Successfully Installed, 2023, Sunfire. URL https://www.sunfire.de/en/news/detail/renewable-hydrogen-project-multiplhy-worlds-largest-high-temperature-electrolyzer-from-sunfire-successfully-installed. (Accessed 24 April 2023).

[3] Bloom energy demonstrates hydrogen production with the World's most efficient electrolyzer and largest solid oxide system, 2023, Bloom Energy. URL https://newsroom.bloomenergy.com/news/bloom-energy-demonstrates-hydrogen-production-with-the-worlds-largest-and-most-efficient-solid-oxide-electrolyzer. (Accessed 6 February 2024).

[4] G. Floerchinger, C. Cadigan, N.P. Sullivan, R.J. Braun, Characterizing the performance of kW-scale multi-stack solid oxide fuel cell modules through modeling, ECS Trans. 111 (6) (2023) 803–808, http://dx.doi.org/10.1149/11106.0803ecst, URL https://iopscience.iop.org/article/10.1149/11106.0803ecst.

[5] H. Zhu, R.J. Kee, V.M. Janardhanan, O. Deutschmann, D.G. Goodwin, Modeling Elementary Heterogeneous Chemistry and Electrochemistry in Solid-Oxide Fuel Cells, J. Electrochem. Soc. 152 (12) (2005) A2427, http://dx.doi.org/10.1149/1.2116607, URL https://iopscience.iop.org/article/10.1149/1.2116607.

[6] V. Menon, V.M. Janardhanan, S. Tischer, O. Deutschmann, A novel approach to model the transient behavior of solid-oxide fuel cell stacks, J. Power Sources 214 (2012) 227–238, http://dx.doi.org/10.1016/j.jpowsour.2012.03.114, URL https://www.sciencedirect.com/science/article/pii/S0378775312007902.

[7] M. Mortada, H.S. Ramadan, J. Faraj, A. Faraj, H. El Hage, M. Khaled, Impacts of reactant flow nonuniformity on fuel cell performance and scaling-up: Comprehensive review, critical analysis and potential recommendations, Int. J. Hydrog. Energy 46 (63) (2021) 32161–32191, http://dx.doi.org/10.1016/j.ijhydene.2020.06.013, URL https://linkinghub.elsevier.com/retrieve/pii/S0360319920321492.

[8] Y. Wang, J. Shi, X. Gu, O. Deutschmann, Y. Shi, N. Cai, Toward mobility of solid oxide fuel cells, Prog. Energy Combust. Sci. 102 (2024) 101141, http://dx.doi.org/10.1016/j.pecs.2023.101141, URL https://www.sciencedirect.com/science/article/pii/S0360128523000710.

[9] D.H. Kim, Y. Bae, S. Lee, J.-W. Son, J.H. Shim, J. Hong, Thermal analysis of a 1-kW hydrogen-fueled solid oxide fuel cell stack by three-dimensional numerical simulation, Energy Convers. Manage. 222 (2020) 113213, http://dx.doi.org/10.1016/j.enconman.2020.113213, URL https://linkinghub.elsevier.com/retrieve/pii/S0196890420307573.

[10] R.T. Nishida, S.B. Beale, J.G. Pharoah, L.G.J. de Haart, L. Blum, Three-dimensional computational fluid dynamics modelling and experimental validation of the Jülich Mark-F solid oxide fuel cell stack, J. Power Sources 373 (2018) 203–210, http://dx.doi.org/10.1016/j.jpowsour.2017.10.030, URL https://www.sciencedirect.com/science/article/pii/S0378775317313629.

[11] R.T. Nishida, S.B. Beale, J.G. Pharoah, Comprehensive computational fluid dynamics model of solid oxide fuel cell stacks, Int. J. Hydrog. Energy 41 (45) (2016) 20592–20605, http://dx.doi.org/10.1016/j.ijhydene.2016.05.103, URL https://www.sciencedirect.com/science/article/pii/S036031991530999X.

[12] S.B. Beale, S.V. Zhubrin, A distributed resistance analogy for solid oxide fuel cells, Numer. Heat Transfer B 47 (6) (2005) 573–591, http://dx.doi.org/10.1080/10407790590907930, URL https://www.tandfonline.com/doi/full/10.1080/10407790590907930.

[13] J.-H. Koh, H.-K. Seo, C.G. Lee, Y.-S. Yoo, H.C. Lim, Pressure and flow distribution in internal gas manifolds of a fuel-cell stack, J. Power Sources 115 (1) (2003) 54–65, http://dx.doi.org/10.1016/S0378-7753(02)00615-8, URL https://www.sciencedirect.com/science/article/pii/S0378775302006158.

[14] R.J. Kee, P. Korada, K. Walters, M. Pavol, A generalized model of the flow distribution in channel networks of planar fuel cells, J. Power Sources 109 (1) (2002) 148–159, http://dx.doi.org/10.1016/S0378-7753(02)00090-3, URL https://www.sciencedirect.com/science/article/pii/S037877530200903.

[15] R. Boersma, N. Sammes, Distribution of gas flow in internally manifolded solid oxide fuel-cell stacks, J. Power Sources 66 (1–2) (1997) 41–45, http://dx.doi.org/10.1016/S0378-7753(96)02469-X, URL https://linkinghub.elsevier.com/retrieve/pii/S037877539602469X.

[16] I.E. Idelchik, Handbook of Hydraulic Resistance, 4th Edition Revised and Augmented, Begell House Inc., 2008, http://dx.doi.org/10.1615/978-1-56700-251-5.0, URL https://www.begellhouse.com/ebook_platform/monograph/book/5877598576b05c67.html.

[17] J.J. Baschuk, X. Li, Modelling of polymer electrolyte membrane fuel cell stacks based on a hydraulic network approach, Int. J. Energy Res. 28 (8) (2004) 697–724, http://dx.doi.org/10.1002/er.993, URL https://onlinelibrary.wiley.com/doi/10.1002/er.993.

[18] L. Wehrle, D. Schmider, J. Dailly, A. Banerjee, O. Deutschmann, Benchmarking solid oxide electrolysis cell-stacks for industrial Power-to-Methane systems via hierarchical multi-scale modelling, Appl. Energy 317 (2022) 119143, http://dx.doi.org/10.1016/j.apenergy.2022.119143, URL https://www.sciencedirect.com/science/article/pii/S0306261922005190.

[19] S.B. Beale, M. Andersson, C. Boigues-Muñoz, H.L. Frandsen, Z. Lin, S.J. McPhail, M. Ni, B. Sundén, A. Weber, A.Z. Weber, Continuum scale modelling and complementary experimentation of solid oxide cells, Prog. Energy Combust. Sci. 85 (2021) 100902, http://dx.doi.org/10.1016/j.pecs.2020.100902, URL https://www.sciencedirect.com/science/article/pii/S036012852030112X.

[20] L. Blum, S.M. Groß, J. Malzbender, U. Pabst, M. Peksen, R. Peters, I.C. Vinke, Investigation of solid oxide fuel cell sealing behavior under stack relevant conditions at Forschungszentrum Jülich, J. Power Sources 196 (17) (2011) 7175–7181, http://dx.doi.org/10.1016/j.jpowsour.2010.09.041, URL https://www.sciencedirect.com/science/article/pii/S0378775310016472.

[21] M. Guo, G. Xiao, J.-q. Wang, Z. Lin, Parametric study of kW-class solid oxide fuel cell stacks fueled by hydrogen and methane with fully multiphysical coupling model, Int. J. Hydrog. Energy 46 (14) (2021) 9488–9502, http://dx.doi.org/10.1016/j.ijhydene.2020.12.092, URL https://linkinghub.elsevier.com/retrieve/pii/S0360319920346577.

[22] L. van Biert, M. Godjevac, K. Visser, P.V. Aravind, Dynamic modelling of a direct internal reforming solid oxide fuel cell stack based on single cell experiments, Appl. Energy 250 (2019) 976–990, http://dx.doi.org/10.1016/j.apenergy.2019.05.053, URL https://www.sciencedirect.com/science/article/pii/S0306261919309079.

[23] M. Preininger, B. Stoeckl, V. Subotic, R. Schauperl, C. Hochenauer, Electrochemical characterization and performance assessment of SOC stacks in electrolysis mode, ECS Trans. 91 (1) (2019) 2589–2600, http://dx.doi.org/10.1149/09101.2589ecst, URL https://iopscience.iop.org/article/10.1149/09101.2589ecst.

[24] K. Kendall, M. Kendall, High-Temperature Solid Oxide Fuel Cells for the 21st Century: Fundamentals, Design and Applications, Academic Press is an imprint of Elsevier, London, 2016.

[25] OpenFOAM | Free CFD Software | The OpenFOAM Foundation, 2024, URL https://openfoam.org/. (Accessed 26 February 2024).

[26] OpenFOAM: User Guide: simpleFoam. URL https://www.openfoam.com/documentation/guides/latest/doc/guide-applications-solvers-incompressible-simpleFoam.html.

[27] P.J. Roache, Perspective: A method for uniform reporting of grid refinement studies, J. Fluids Eng. 116 (3) (1994) 405–413, http://dx.doi.org/10.1115/1.2910291, URL https://asmedigitalcollection.asme.org/fluidsengineering/article/116/3/405/411554/Perspective-A-Method-for-Uniform-Reporting-of-Grid.

[28] D. Segal, SymbolicRegression Julia Package, 2023, URL https://juliapackages.com/p/symbolicregression. (Accessed 4 December 2023).

[29] M. Cranmer, Interpretable Machine Learning for Science with PySR and SymbolicRegression.jl, 2023, http://dx.doi.org/10.48550/arXiv.2305.01582, arXiv [astro-ph, physics:physics] URL http://arxiv.org/abs/2305.01582.

[30] Y. Qin, G. Liu, Y. Chang, Q. Du, Modeling and design of PEM fuel cell stack based on a flow network method, Appl. Therm. Eng. 144 (2018) 411–423, http://dx.doi.org/10.1016/j.applthermaleng.2018.08.050, URL https://www.sciencedirect.com/science/article/pii/S1359431118306070.

[31] J. Wang, Theory of flow distribution in manifolds, Chem. Eng. J. 168 (3) (2011) 1331–1345, http://dx.doi.org/10.1016/j.cej.2011.02.050, URL https://www.sciencedirect.com/science/article/pii/S1385894711002300.

[32] G. Karimi, J.J. Baschuk, X. Li, Performance analysis and optimization of PEM fuel cell stacks using flow network approach, J. Power Sources 147 (1) (2005) 162–177, http://dx.doi.org/10.1016/j.jpowsour.2005.01.023, URL https://www.sciencedirect.com/science/article/pii/S0378775305001539.

[33] H. Bruus, Theoretical microfluidics, Oxford Master Series in Physics, (18) Oxford University Press, Oxford ; New York, 2008, oCLC: ocn156817008.

APPENDIX B

Attached publication of Furst et al. [94]

Title: A Versatile Multi-Scale Framework for Transient Simulations of Solid Oxide Cells and Stack Modules Integrated in DETCHEM
Journal: Journal of The Electrochemical Society
Authors: Oscar Furst, Olaf Deutschmann

Journal of The Electrochemical Society, 2025 **172** 074508

A Versatile Multi-Scale Framework for Transient Simulations of Solid Oxide Cells and Stack Modules Integrated in DETCHEM

Oscar Furst and Olaf Deutschmann[z]

Institute for Chemical Technology and Polymer Chemistry (ITCP), Karlsruhe Institute of Technology, 76131 Karlsruhe, Germany

This paper presents the comprehensive multi-scale modeling framework integrated in the DETCHEM detailed chemistry software package, designed for the transient simulation of solid oxide cells (SOC), including button cells, planar repeating units, and stack modules. The framework uses a hierarchical approach, enabling calibration with button cell experiments and subsequent application to larger systems. Key features of the model include transient 1D simulations for generating electrochemical impedance spectra (EIS), spatially resolved mass and charge transport models for microstructure optimization, 2D mass and heat transport for planar cell simulations and a 3D homogenized model for performance analysis of SOC stack modules. Additionally, the model incorporates a thermocatalytic chemistry module to simulate the decomposition of a variety of fuels and an internal manifold model to study flow maldistribution in SOC stacks. The framework's versatility is demonstrated through case studies, including the calibration and validation of a co-electrolysis cell model using experimental EIS and polarization curves, transient simulations of ammonia-fed repeating units, and the evaluation of flow maldistribution effects in a stack module.

 [DOI: 10.1149/1945-7111/ade56d]

Manuscript submitted February 19, 2025; revised manuscript received May 6, 2025. Published July 9, 2025.

Nomenclature

Greek

α	[-]	Volume fraction
ϵ	[-]	Emissivity
Γ_{surf}	$[mol/m^2]$	Density of active sites on a catalyst
λ	$[W/m/K]$	Thermal conductivity
λ^V_{TPB}	$[1/m^2]$	Volumetric triple phase boundary length
μ	$[Pa\ s]$	Dynamic viscosity
ν	[-]	Stoichiometric coefficient
$\dot{\omega}$	$[mol/m^3/s]$	Species production rate (gas-phase reactions)
ϕ	$[V]$	Electric potential
ψ	[-]	Number of adsorption sites occupied
ρ	$[kg/m^3]$	Density
σ	$[S\ /\ m]$	Conductivity
θ	[-]	Surface coverage
ζ	[-]	Pressure loss coefficient

Latin

A^V_{DPB}	$[1/m]$	Volumetric double phase boundary area
C	$[F]$	Capacitance
c	$[mol/m^3]$	Concentration
c_p	$[J/kg/K]$	Specific heat capacity
E	$[V]$	Electric potential difference
E_a	$[J\ /\ mol]$	Activation energy
F	$[s\ A/mol]$	Faraday constant
G	$[J\ /\ mol]$	Gibbs energy
Gz	[-]	Grashof number
h	$[J\ /\ kg]$	Specific enthalpy
h_{conv}	$[W/m^2/K]$	Convective heat transfer coefficient
i^V_e	$[A/m^3]$	Charge transfer rate
I	$[A]$	Current
i	$[A/m^2]$	Current density
J	$[mol/m^2/s]$	Molar flux
k	Variable	Reaction rate constant
Nu	[-]	Nusselt number
p	$[Pa]$	Pressure
Pr	[-]	Prandtl number
q	$[W/m^2]$	Heat flux
$\dot{Q}$	$[W]$	Heat flow rate

[z]E-mail: deutschmann@kit.edu

(Continued).

$\dot{q}^V$	$[W/m^3]$	Volumetric heat production rate
Q	$[m^3/s]$	Flow rate
R	$[J/mol/K]$	Gas constant
Ra	[-]	Rayleigh number
$\mathbf{R}_{CT}$	[-]	Set of charge transfer reactions
Re	[-]	Reynolds number
$\mathbf{R}_{surf}$	[-]	Set of surface reactions
$\dot{s}$	$[mol/m^3/s]$	Species production rate (surface reactions)
$\mathbf{S}_g$	[-]	Set of gas species
$\mathbf{S}_{surf}$	[-]	Set of surface species
T	$[K]$	Temperature
u	$[m\ /\ s]$	Velocity
W	$[kg\ /\ mol]$	Molecular weight
X	[-]	Mole fraction
x, y, z	$[m]$	Spacial coordinates
Y	[-]	Mass fraction
Z	$[\Omega/m^2]$	Area specific impedance

In a future with a strong market penetration of renewable energy, chemical energy carriers will provide stable long-term energy storage and transportability. Hydrogen is predicted to be a cornerstone of this future energy market because it can be used as-is for power generation, or as chemical feedstock to be further processed into commodities and high value energy carriers.[1]

Solid Oxide Cells (SOCs) shape up to be a key technology in this scenario, as they boast high efficiencies utilized as both fuel cells and electrolyzers, and can be manufactured using more abundant catalyst materials than low-temperature electrochemical devices.[2] The SOC technology is undergoing its scale-up phase, with large manufacturing plants under construction[3] and multiple megawatt-scale SOC modules under operation.[4,5]

As interest in SOCs continues to grow, the modeling of Solid Oxide Electrolysis Cells (SOECs) and Solid Oxide Fuel Cells (SOFCs) becomes increasingly pertinent. Modeling is crucial throughout the entire life cycle of the cells, enhancing the effectiveness of their manufacture and optimizing the efficiency of their applications. The methodologies for simulating SOCs are as diverse as their applications, each tailored to meet specific requirements.

In systems modeling, when a performance prediction of a SOC integrated in a larger system is required, simulation speed is often as important as accuracy. In such applications, fast 0D models, which

Journal of The Electrochemical Society, 2025 172 074508

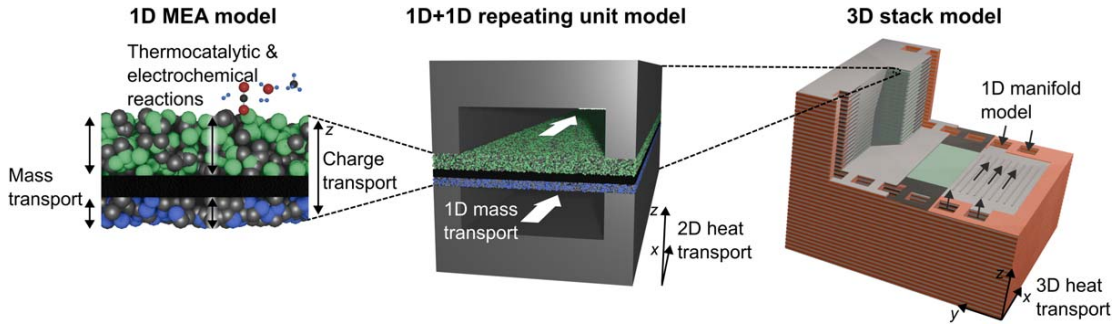

Figure 1. Illustration of the multi-scale modeling methodology. The 1D membrane electrode assembly (MEA) model is used for button cell simulations. It is complemented by a 1D channel model and 2D heat transport model to form a planar repeating unit (RU) model. The RU model can then be leveraged for 3D stack simulations.

are fitted to a specific cell design in a limited range of operating conditions using many experiments, are often the most appropriate ones.[6,7] These simple models serve the same purpose as surrogate models,[8,9] which circumvent modeling the physical phenomena altogether. Alternatively, some system models strike a balance between speed and accuracy by simulating a single cell representative for the performance of the whole stack.[10]

SOC models are also employed to optimize the design of the cells themselves, or the design of SOC stack modules.[11–13] In such cases, more detailed modeling approaches are warranted in order to ensure that all relevant physical processes are considered, especially when parameter variations are performed for which no experimental validation is available.[14] Such models also provide performance metrics inaccessible through experimentation alone, providing valuable information for the better design and operation of SOC.[15,16]

The most detailed simulation methodologies are used to enhance the understanding of the physical processes occurring within the cells. For example, simulating the electrochemical reaction using an elementary kinetic model may help to uncover the reaction pathways.[17,18] Modeling the chemical reactions responsible for the production of charge-carrying defects in ceramic conductors helps to understand the factors responsible for changes in the conductivity of ionic conductors.[19,20]

In this work, we present a flexible, multi-scale model designed for the transient simulation of button cells, planar repeating units and SOC stacks. The hierarchical approach, illustrated in Fig. 1, allows the calibration of the model to be performed with button cell experiments, which are the cheapest and fastest to perform, and to subsequently simulate repeating units and stacks.

The featured model, which is part of the DETCHEM[21] software package, includes the following capabilities:

- Transient 1D isothermal button cell simulations for the production of electrochemical impedance spectra (EIS) and polarization curves.
- Performance analysis of SOC modules through 2D repeating unit and 3D stack simulations considering transient heat transport.
- Microstructure optimization owing to the mass and charge transport models spacially resolved across the thickness of the membrane electrode assembly (MEA).
- A thermocatalytic chemistry model based on elementary reaction mechanisms compatible with a large database of mechanisms for the decomposition and production of hydrogen carriers.[22]
- Study of the influence of flow maldistribution in SOC stacks using an internal manifold model.

Compared to similar studies and previous versions of the software, the present modeling framework stands out with a fast and accurate internal manifold flow model, stack potential field computation algorithm and a conservative, transient 1D channel flow model.

A detailed exposition of the modeling framework is provided in the following Sections and concluded with a case-study of a Ni-YSZ/YSZ/LSM-YSZ cell for which experimental data were taken from literature in order to demonstrate the model's capability to predict SOC performance under various operating conditions, providing valuable insights for the design and optimization of SOC systems.

Methods

In the following sections, we present a comprehensive exposition of the DETCHEM^{SOC} model equations and solution algorithms. The first main Section pertains to the simulation of button cells and repeating units (1D MEA model and 1D+1D repeating unit model seen in Fig. 1), while the second main Section deals with the simulation of SOC stacks (3D stack model seen in Fig. 1).

This SOC model processes user-input parameters encompassing cell geometry, material properties, and physical characteristics to calculate the spatial distribution of species, temperatures, and current densities within the cells under the desired operating conditions.

Previous iterations of the modeling framework were described in our former studies[14,23–25] and a description of its current capabilities is provided herein. The parts of the modeling framework published before are briefly reiterated, while improvements and additions such as the improved channel flow model, stack potential field computation algorithm and the internal manifold model are given a more thorough description.

Planar solid oxide cell model.— *Mass and momentum transport.*—In order to be able to simulate transient phenomena in SOCs, such as the start-up, fluctuating inlet conditions and shut-down, a time-accurate model for the gas flow through the repeating unit gas channels and the button cell gas compartments was developed.

Bulk flow in planar repeating units: Since transient simulations are computationally intensive, computation times are kept reasonable through some simplifying assumptions which lead to a transient formulation of the plug flow model commonly used in chemical engineering. First, (i) a flow with a low Mach number is assumed. The low Mach number assumption is the broadest definition of incompressible flow, since its main implication is that pressure variations inside the flow are small enough to have a negligible impact on the density of the fluid, while still allowing changes in the fluid density through variations in temperature or composition.[26] Secondly, two of the main assumptions of the plug flow model are used, which are that (ii) diffusive mass transport along the channel is negligible compared to convective mass transport,[27] and that (iii) the flow can be assumed to be homogeneous across the channel cross-section due to its narrow geometry.[28]

An appropriate set of equations is obtained from the transport equations for low Mach number reacting laminar flows of Day and Bell[29] and removing diffusion terms:

$$\nabla\cdot\mathbf{u} = \frac{1}{\rho c_p T}\,\nabla\cdot\mathbf{q} + \frac{1}{\rho}\sum_{m\,\in\,\mathbf{S}_g}\left(\frac{W}{W_m} - \frac{h_m}{c_p T}\right)W_m\,\dot{\omega}_m \qquad [1]$$

$$\frac{\partial\,\rho\,Y_m}{\partial t} + \nabla\cdot\mathbf{u}\,\rho\,Y_m = W_m\,\dot{\omega}_m. \qquad [2]$$

with the velocity vector field $\mathbf{u}$, the heat flux vector field $\mathbf{q}$, molecular weight of the gas mixture W, specific enthalpy h_m, volume-specific production rate $\dot{\omega}_m$ and mass fraction Y_m of the species m which is part of the set of gas species $\mathbf{S}_g$.

These equations are then reduced to 1D (thereby satisfying the assumption of cross-section homogeneity) and discretized in space according to the finite volume method on a collocated grid using first order upwind interpolation of face values to yield a set of equations for the flow velocity, density and mass fractions. These equations are coupled to the heat transport equations presented later (Eq. 47) through the specific enthalpy h, the heat source term $\dot{Q}_{\text{channel}}$ (see Eq. 52) which appears as the surface integral of $\mathbf{q}$ and the enthalpy-dependent variables T and c_p.

The absence of momentum conservation equation is noteworthy. It is due to the assumption of 1D flow, resulting in a flow field that can be fully determined from Eq. 1. The momentum conservation equation becomes redundant unless the pressure gradient along the channel is of interest. Note that despite the low Mach number assumption, the pressure still varies throughout the flow due to viscous losses and variations in the density that are caused by changes in temperature and composition. However, the magnitude of these pressure changes are small enough to allow using a constant, homogeneous pressure field (commonly referred to as *thermodynamic pressure*) to evaluate the equation of state, while computing a variable, non-homogeneous pressure field (called the *mechanical pressure*) through the momentum equation and Eq. 1. This concept is sometimes referred to as *pressure filtering*.[28]

The boundary conditions at the inlet are straightforward, consisting of an inlet flux with specified velocity, temperature and mass fractions. Since the velocity profile across the channel cross-section is not resolved, entrance effects are not considered. Boundary conditions along the surface of the porous electrode, which, in the 1D model, manifest as source terms, need to be formulated carefully in order to yield a conservative set of equations. In the species conservation equation, the area-specific mass flux through the channel/electrode interface is expressed as $W_m J_m$, with the area-specific molar flux through the interface J_m computed according to the dusty gas model (DGM) (see Eq. 8). The bulk gas velocity across the electrode/channel interface, which results in a source term $u_{\text{electrode}}$ for the 1D discretization of Eq. 1, is computed as

$$u_{\text{electrode}} = \frac{RT}{p}\sum_{m\,\in\,\mathbf{S}_g} J_m. \qquad [3]$$

Thus, the final set of equations can be reformulated in 1D along the x axis with additional source terms:

$$\begin{aligned}\frac{\partial u}{\partial x} = {} & \frac{1}{h_{\text{channel}}}u_{\text{electrode}} \\ & + \frac{1}{\rho c_p T}\frac{\partial}{\partial x}\left(\frac{\dot{Q}_{\text{channel}}}{h_{\text{channel}}\,w_{\text{channel}}}\right) \\ & + \frac{1}{\rho}\sum_{m\,\in\,\mathbf{S}_g}\left(\frac{W}{W_m} - \frac{h_m}{c_p T}\right)W_m\,\dot{\omega}_m\end{aligned} \qquad [4]$$

$$\frac{\partial\,\rho\,Y_m}{\partial t} = -\frac{\partial\,u\,\rho\,Y_m}{\partial x} + W_m\,\dot{\omega}_m + \frac{1}{h_{\text{channel}}}W_m\,J_m \qquad [5]$$

with h_{channel} and w_{channel} the height and width of the channel.

Bulk flow in button cells: Since button cells are mainly used for the electrochemical characterization of cells, they are operated with a high mass flow rate of reactant in order to minimize the influence of mass transport in the gas compartments. Hence, the gas compartments can be assumed to be perfectly mixed and are simulated with a transient continuous stirred tank reactor model. Such a model was developed by Zhu and Kee and shown to accurately replicate the low frequency behavior of the system observed in EIS.[30] The aforementioned model uses a convective formulation of the mass conservation equation, which may lead to an accumulation of numerical errors in the density and mass fractions but perfect satisfaction of the equation of state. In order to conserve mass with a high accuracy throughout the computation, a transient CSTR model was developed by integrating the conservative Eqs. 1 and 2 over the volume of a gas compartment, assuming perfect mixing of the gas within and reformulating volume integral of divergence terms to surface integrals. The result is a set of equations very similar to the discretized formulation of Eqs. 1 and 2:

$$\begin{aligned}u_{\text{in}} + u_{\text{electrode}} - u_{\text{out}} = {} & \frac{q_{\text{channel}}}{\rho c_p T} + \frac{h_{\text{CSTR}}}{\rho} \\ & \times \sum_{m\,\in\,\mathbf{S}_g}\left(\frac{W}{W_m} - \frac{h_m}{c_p T}\right)W_m\,\dot{\omega}_m\end{aligned} \qquad [6]$$

$$\frac{\partial\,\rho\,Y_m}{\partial t} + \frac{1}{h_{\text{CSTR}}}(u_{\text{in}}\rho_{\text{in}}Y_{m,\text{in}} - u_{\text{out}}\rho_{\text{out}}Y_{m,\text{out}}) = W_m\,\dot{\omega}_m \qquad [7]$$

with u_{in} and u_{out} the velocity of the incoming and outgoing flow respectively and h_{CSTR} the height of the gas compartment. $u_{\text{electrode}}$ is the velocity of the flow of gas from the porous electrode into the gas compartment, and q_{channel} is the heat flux from the electrode into the gas compartment.

Due to the mostly homogeneous gas composition on both sides of the MEA, coplanar gradients inside the button cell are small. Therefore, the cell is assumed to be infinitely wide, leading to a purely 1D button cell model. Note that, in Eqs. 6 and 7, the infinitely wide surface facing the MEA is assumed to serve both as inlet and outlet in its entirety, since the subdivision of the surface in an inlet and outlet portion would only increase the inlet and outlet velocities by an arbitrary geometrical parameter without influencing the physical behavior of the gas compartment.

Compared to the model of Zhu and Kee,[30] this set of equations is conservative, but accumulates numerical errors in the equation of state (ideal gas law) as a trade-off.

Gas in the porous electrodes: Inside the MEA, mass transport in the normal direction is dominant. Consequently, it is assumed that gradients in coplanar directions can be neglected, allowing simulation of the mass trasport in the MEA through a 1D model. In the functional layer, diffusion layers and current-collecting layers of the porous electrodes, mass transport between the gas channel and the electrolyte is simulated in 1D using the dusty gas model (DGM). In the DGM, mass transport in a porous medium is assumed to be the result of three independent transport mechanisms: viscous flow driven by a pressure gradient, continuum diffusion and Knudsen diffusion.[31] In a 1D case, this results in the following expression for the area specific molar flux J_m of species $m \in \mathbf{S}_g$:[17,32]

$$J_{\text{m}} = -\left[\sum_{k\,\in\,\mathbf{S}_g} D_{mk}^{\text{DGM}}\frac{\partial c_k}{\partial z} + \left(\sum_{k\,\in\,\mathbf{S}_g}\frac{D_{mk}^{\text{DGM}}c_k}{D_{k,\text{Kn}}^{\text{eff}}}\right)\frac{B_g}{\mu}\frac{\partial p}{\partial z}\right] \qquad [8]$$

with

$$H_{ab} = \left[\frac{1}{D^{\text{eff}}_{a,Kn}} + \sum_{k \in \mathbf{S}_g \setminus a} \frac{X_k}{D^{\text{eff}}_{ak}}\right]\delta_{ab} + (\delta_{ab} - 1)\frac{X_a}{D^{\text{eff}}_{ab}} \quad [9]$$

$$D^{\text{DGM}}_{kl} = (\mathbf{H}^{-1})_{kl} \quad [10]$$

$$B_g = \frac{\alpha^3_{\text{pore}} d^2_{\text{pore}}}{72\,\tau_{\text{fac,pore}}(1-\alpha_{\text{pore}})^2} \quad [11]$$

$$D^{\text{eff}}_{k,Kn} = \frac{\alpha_{\text{pore}}}{\tau_{\text{fac,pore}}}\frac{d_{\text{pore}}}{3}\sqrt{\frac{8RT}{\pi W_k}} \quad [12]$$

$$D^{\text{eff}}_{kl} = \frac{\alpha_{\text{pore}}}{\tau_{\text{fac,pore}}} D_{kl} \quad [13]$$

$$\tau_{\text{fac,pore}} = \left(1.23\frac{(1-\alpha_{\text{pore}})^{4/3}}{\alpha_{\text{pore}}}\right)^2. \quad [14]$$

where H_{ab} are the components of the matrix $\mathbf{H}$ for every combination of gas species a, $b \in [1, n(\mathbf{S}_g)]$, δ_{ab} is the Kronecker delta, α_{pore} is the porosity of the electrode, D_{kl} is the binary diffusion coefficient for gases k and l, μ is the dynamic viscosity of the gas mixture, p is the gas pressure, d_{pore} is the mean pore diameter, X_k is the mole fraction of species k in the gas mixture and c_k is its concentration.

A species conservation equation for the density $\rho_m = Y_m \rho$ of species $m \in \mathbf{S}_g$ in porous layers can subsequently be established, additionally considering source terms due to charge transfer reactions and thermocatalytic chemistry:[17,32]

$$\alpha_{\text{pore}}\frac{\partial Y_m \rho}{\partial t} = -\frac{\partial J_m W_m}{\partial z} + \sum_{r \in \mathbf{R}_{\text{CT}}} \frac{\nu_{m,r} i^V_{F,r} W_m}{n_{e,r} F} + W_m \dot{s}_m \quad [15]$$

where z is the spacial coordinate in MEA-normal direction, $\dot{s}_m$ is the production rate of species m through thermocatalytic reactions (see Eq. 18), $i^V_{F,r}$ is the Faradaic charge transfer rate in the chare transfer reaction $r \in \mathbf{R}_{\text{CT}}$ (see Eq. 22), $n_{e,r}$ is the number of electrons transferred in the charge transfer reaction and $\nu_{m,r}$ is the stoichiometric coefficient of species m in reaction r. The mass conservation equation for the total gas density ρ can be obtained as the sum of conservation equations for all species in $\mathbf{S}_g$. The pressure used in the computation of the flux J_m in Eq. 8 is computed using the ideal gas law.

At the channel/electrode boundary, the gas composition is assumed to be identical to the gas in the channel. The flux J_m computed at this interface using Eq. 8 couples the transport model of the porous layers to the bulk gas transport model. The electrode/electrolyte interface is assumed to be impermeable, the flux J_m therefore vanishing.

Thermocatalytic heterogeneous chemistry.—Depending on the type of fuel fed to the SOC, the heterogeneous chemistry on the catalytically active cell materials, typically nickel, needs to be considered. Common use-cases are direct ammonia fuel cells with internal ammonia cracking,[33,34] internal methane reforming in fuel cells fed with natural gas[17,35] and internal methanation during co-electrolysis of H_2O and CO_2.[36]

Considering surface chemistry in an electrode requires an additional set of variables, which are the surface coverage θ_m of the catalyst with the surface species $m \in \mathbf{S}_{\text{surf}}$. It is computed in a conservation equation as a function of the density of available active sites Γ_{surf} and the surface species production rate per catalyst surface area $\dot{s}^A_m$ as[24,28,37,38]

$$\frac{\partial \theta_m}{\partial t} = \frac{\psi_m \dot{s}^A_m}{\Gamma_{\text{surf}}} \quad [16]$$

where ψ_m is the number of adsorption sites covered by species $m \in \mathbf{S}_{\text{surf}}$.

The surface specific production rates $\dot{s}^A_m$ of gas-phase and surface species $m \in \mathbf{S}_g \cup \mathbf{S}_{\text{surf}}$, in turn, are computed from a set of elementary kinetic reactions $r \in \mathbf{R}_{\text{surf}}$ as follows:

$$\dot{s}^A_m = \sum_{r \in \mathbf{R}_{\text{surf}}} (\nu''_{m,r} - \nu'_{m,r})\, k_{f,r} \prod_{k \in \mathbf{S}_g \cup \mathbf{S}_{\text{surf}}} c_k^{\nu'_{k,r}} \quad [17]$$

where $\nu'_{m,r}$ and $\nu''_{m,r}$ are the stoichiometric coefficients of species m as reactant and product in reaction r and $k_{f,r}$ is the forward reaction rate constant. c_k is the concentration of species k, which has a dimension of [mol m^{-3}] for a gas species and [mol m^{-2}] for a surface species. Accordingly, the dimension of $k_{f,r}$ varies with the dimensions of c_k and the stoichiometric coefficients $\nu''_{k,r}$. The production rates for surface species enter the source term of Eq. 16. The volumetric gas species m production rates $\dot{s}_m$ used in Eq. 15 is obtained by multiplying the surface specific production rate $\dot{s}^A_m$ with the catalyst surface area per unit volume, which is usually the surface area of the metallic phase:

$$\dot{s}_m = \dot{s}^A_m A^V_{\text{cat}}. \quad [18]$$

The reaction rate constants k_f are computed as:[38]

$$k_{f,r} = A_r T^{\kappa_r} \exp\left(-\frac{E_{a,r}}{RT}\right) \prod_{k \in \mathbf{S}_{\text{surf}}} \exp\left(-\frac{\xi_{k,r}\theta_k}{RT}\right). \quad [19]$$

where A is the pre-exponential factor, κ introduces a temperature dependence on the pre-exponential factor, E_a is the activation energy of the reaction and $\xi_{k,r}$ regulates the influence of surface coverages of species k on the activation energy of the reaction r in order to account for lateral interactions. These variables are unique to each reaction and are determined along with the reaction mechanism itself. In the case-study performed herein, a reaction mechanism of methane reforming and water-gas shift on nickel consisting of 42 elementary steps is used,[39] but other mechanisms may be used to model other fuel or electrode compositions.[22]

The thermodynamic consistency of these mechanism is guaranteed using the method outlined by Maier et al.[38] which ensures that the ratio of forward and backward reaction rate constants correspond to the thermodynamic equilibriums. Reactions are only paired as forward and backward reactions for the purpose of adjusting thermodynamic consistency. Otherwise, all reaction equations of a given mechanism are considered forward reactions for the purpose of Eqs. 17 and 19.

Electrochemical model.—In a fuel cell model, the electrochemical model is the central component which determines the relationship between the cell potential E_{cell} and the achieved current density i.

In DETCHEM$^{\text{SOC}}$, the electrochemical reaction rates are modeled using a modified Butler-Volmer equation, which links the local half-cell activation overpotential η_{act} to the resulting local charge transfer rate per unit length or area $i^{A/\lambda}_r$ of the charge transfer reaction r:

$$i^{A/\lambda}_r = i_{0,r}\left[\exp\left(\frac{\beta_a F n_{e,r}\eta_{\text{act}}}{RT}\right) - \exp\left(-\frac{\beta_c F n_{e,r}\eta_{\text{act}}}{RT}\right)\right] \quad [20]$$

where $i_{0,r}$ is the exchange current density and $n_{e,r}$ is the number of elementary charges transferred. β_a and β_c are the anodic and

cathodic charge transfer coefficients, which depend on the elementary reactions involved in the charge transfer mechanism.

The exact expressions used to compute the exchange current densities $i_{0,r}$ depend on the electrode materials,[17,40] but take the following general form:

$$i_{0,r} = A_r \exp\left(-\frac{E_r}{RT}\right) f(p_s) \quad [21]$$

with a pre-factor A_r, an activation energy E_r and a function of the gas partial pressures $f(p_s)$. The exchange current density is expressed in A/cm in a cermet electrode and in A/cm^2 in a mixed ionic-electronic conductor electrode.

While the Butler-Volmer equation is derived from transition state theory strictly for single-step, single-electron transfer reactions, it remains an excellent approximation even for multistep reactions involving multiple electron transfers.[41] In such cases, the charge transfer coefficients and the exchange current densities are treated as fitting parameters adjusted to experimental data. Thus, it is used as an empirical correlation with only loose connection to the reaction mechanism. In modeling studies of reversible SOCs, the same kinetic rate equation is often successfully applied to pairs of oxidation and reduction equations, e.g., the oxygen evolution reaction and the oxygen reduction reaction.[42–44] While this may suggest similar electrocatalytic activity of the electrode for both reactions, such empirical modeling approaches are not suited for drawing precise conclusions about the underlying reaction mechanisms.

Table III shows the expressions used to compute the exchange current densities in the case-study performed herein. In this study, the LSM-YSZ air electrode and the Ni-YSZ fuel electrode are both cermet electrodes, which results in the reactions taking place over the triples phase boundary between the gas, the metallic phase and the ceramic phase λ^V_{TPB}. Therefore, the local Faradaic charge transfer rate $i^V_{F,r}$ for reaction r is obtained as follows:

$$i^V_{F,r} = i^\lambda_r \, \lambda^V_{\mathrm{TPB}} \quad [22]$$

The superscript V indicates volumetric quantities, i.e., triple phase boundary (TPB) length per unit volume.

The activation overpotential η_{act} is determined from the local potential of the electron- and ion-conducting phases ϕ_{el} and ϕ_{io} and the local reversible half-cell reaction potential $E_{\mathrm{rev},r}$ depending on the considered reaction r:[45]

$$E_{\mathrm{rev,H_2}} = \frac{\Delta G^{0,\mathrm{f}}_{\mathrm{H_2O}} - \Delta G^{0,\mathrm{f}}_{\mathrm{H_2}}}{n_{e,r}F} + \frac{RT}{n_{e,r}F} \ln\left(\frac{p_{\mathrm{H_2O}}}{p_{\mathrm{H_2}}}\right) \quad [23]$$

$$E_{\mathrm{rev,CO}} = \frac{\Delta G^{0,\mathrm{f}}_{\mathrm{CO_2}} - \Delta G^{0,\mathrm{f}}_{\mathrm{CO}}}{n_{e,r}F} + \frac{RT}{n_{e,r}F} \ln\left(\frac{p_{\mathrm{CO_2}}}{p_{\mathrm{CO}}}\right) \quad [24]$$

$$E_{\mathrm{rev,O_2}} = \frac{\Delta G^{0,\mathrm{f}}_{\mathrm{O_2}}}{n_{e,r}F} + \frac{RT}{n_{e,r}F} \ln\left(\left(\frac{p_{\mathrm{O_2}}}{p_{\mathrm{atm}}}\right)^{0.5}\right) \quad [25]$$

$$\eta_{\mathrm{act}} = \phi_{\mathrm{el}} - \phi_{\mathrm{io}} - E_{\mathrm{rev}} \quad [26]$$

where $p_{\mathrm{atm}} = 101325$ Pa and $\Delta G^{0,\mathrm{f}}_m$ is the Gibbs free energy of formation of species m at temperature T.

In cases where the fuel composition allows both H_2 and CO reaction pathways, charge transfer rates $i^\lambda_{\mathrm{H_2/H_2O}}$ and $i^\lambda_{\mathrm{CO/CO_2}}$ are computed for both half-cell reactions. However, as the reaction sites are shared by both reaction pathways, the actual charge transfer rate in the fuel electrode is computed as the sum of both half cell reaction charge transfer rates weighted by the mole fractions of H_2O and CO_2:[24]

$$i^\lambda_{\mathrm{total}} = w \, i^\lambda_{\mathrm{H_2/H_2O}} + (1 - w) \, i^\lambda_{\mathrm{CO/CO_2}} \quad [27]$$

with

$$w = \frac{X_{\mathrm{H_2O}}}{X_{\mathrm{H_2O}} + X_{\mathrm{CO_2}}} \quad [28]$$

where the mole fractions correspond to the local composition of the gas phase, which changes across the thickness of the electrode according to the mass transport model.

Charge transport.—Since the electrochemical model computes the charge transfer rate over the full height of both electrodes (as opposed to just the porous electrode/bulk electrolyte interface, which is often assumed in simplified models), the overpotential η needs to be known at every point of the electrode. The potential fields ϕ_{el} and ϕ_{io} (electron-conducting and ion-conducting phase), which in term depend on the current density fields i_{el} and i_{io}, therefore need to be computed using a charge transport model.

The present distributed charge transport model considers the movement of charged particles, usually electrons e' in the electron-conducting phases and oxygen vacancies $V_{\dot{O}}$ in the ion-conducting phases, produced throughout the porous electrodes by charge transfer reactions. As is common in SOC literature, the terms *anode*, *cathode* and *electrode* are used herein to refer to all the solid phases of the porous structures on either sides of the impermeable bulk electrolyte, and *electrolyte* refers to the impermeable membrane.

In the present cell model, a simplified implementation of the distributed charge transfer model developed by Zhu et al.[46] is used, which is a Nernst-Planck equation simplified with the assumption that the charge transport due to species concentration gradients can be neglected. Therefore, the current density in the phase $m \in \{\mathrm{el}, \mathrm{io}\}$ is proportional to its effective conductivity σ^{eff}_m (see Eq. 45) and the local potential gradient:

$$i_m = \sigma^{\mathrm{eff}}_m \frac{\partial \phi_m}{\partial z} \quad [29]$$

The divergence of the electronic and ionic current density describes the amount of charge carriers produced in their respective phases, which is the charge transfer rate i^V_e. Under the assumption of electroneutrality, the accumulation of charge in both phases is equilibrated so that the charge transfer rates for the electronic and ionic phases are complementary:

$$\frac{\partial i_{\mathrm{el}}}{\partial z} = i^V_e \quad [30]$$

$$\frac{\partial i_{\mathrm{io}}}{\partial z} = -i^V_e. \quad [31]$$

Boundary conditions and the ability to evaluate the charge transfer rate i^V_e as a function of known variables close the system of equations and allows the computation of the potential fields ϕ_{el} and ϕ_{io}.

Herein, the charge transfer rate is assumed to be composed of the Faradaic charge transfer rate i^V_F and the double layer charge transfer rate i^V_{DL}:

$$i^V_e = i^V_F + i^V_{\mathrm{DL}} \quad [32]$$

The former is computed according to Eq. 22 while the latter is computed according to a plate capacitor model[18]

$$\frac{\partial}{\partial t}(\phi_{el} - \phi_{io}) = \frac{i_{DL}^{V}}{C_{DL} \cdot A_{el/io}^{V}} \quad [33]$$

where C_{DL} is the double-layer capacitance of the phase boundary between the ion-conducting phase and the electron-conducting phase per double-layer surface area and $A_{el/io}^{V}$ is the phase boundary per unit volume.

The only transient component of the charge transport model is the charging of the double layer, which is relevant for the simulation of impedance spectra. Since double-layer charging has a very short time-scale, i_{DL}^{V} can be assumed to vanish for all other types of simulations. In such cases, the discretized form of Eqs. 30 and 31 are integrated with the secant method.

As boundary conditions for the electron-conducting phase, a reference potential of E_{cell} is set at the cathode/air channel boundary and a reference potential of 0 V is set at the anode/fuel channel boundary. If the bulk electrolyte is a pure ion conductor, the electron flux must also vanish at the cathode/electrolyte and anode/electrolyte boundaries. In the ion-conducting phase, which exists in the cathode, electrolyte and anode, the ion flux must vanish at the cathode/air channel and anode/fuel channel boundaries.

Contact resistances can also be considered at such interfaces. As contact resistance is difficult to measure or predict, in this study the contact resistances are assumed to be the difference between measured ohmic resistance of the SOC (measured through EIS) and computed resistance of the electrolyte (determined from its geometry and conductivity measurements from literature), concentrated at the fuel electrode/electrolyte boundary.

Microstructure model.—In order to simulate the gas transport in the electrodes using the dusty gas model, charge transport through the porous conductors and electrochemical kinetics at the double and triple phase boundaries, it is of paramount importance to know a number of morphological characteristics of the electrodes such as its porosity, tortuosity, pore diameters, phase boundary areas and triple phase boundary lengths.

While a number of such properties can be determined experimentally or through numerical simulation of the sintering process, it is generally more economical to approximate these properties using analytical expressions derived from percolation theory. Since the fabrication process has a great influence on the morphology of the electrode, the set of expressions used to evaluate most parameters differs between cermet electrodes and infiltrated electrodes.

To evaluate the properties of cermet electrodes, the percolation model developed by Bertei and Nicolella is used.[14,47,48] Assuming an electrode composed of three phases, comprising pores and two solid phases m and n, a central component of the model is the percolation probability γ_k of the phase $k \in \{n, m\}$, which is computed using the following empirical correlation:[14,47]

$$\gamma_k = 1 - \left(\frac{4.236 - Z_{k,k}}{2.472}\right)^{3.7} \quad [34]$$

where $Z_{k,k}$ is the average contact number between k-particles.

The volume-specific length of the triple phase boundary λ_{TPB}^{V} can then be computed as:[14,48]

$$\lambda_{TPB}^{V} = 1.92\pi\left(\min(r_{p,m},\ r_{p,n}) \sin\frac{\pi}{12}\right) n_m^V\, Z_{m,n}\, \gamma_m \gamma_n \quad [35]$$

where $r_{p,k}$ is the mean radius of particles of the solid phase $k \in \{n, m\}$, n_k^V is the volume-specific number of particles in the electrode after sintering and $Z_{m,n}$ is the average contact number between m-particles and n-particles. Therein, an initial porosity before sintering of 0.36 is assumed.[48]

n_m^V and $Z_{m,n}$ can, in turn, be evaluated from the particle diameters and phase volume fractions through a series of expressions derived by Bertei and Nicolella[48] and not repeated here for the sake of clarity.

The volume-specific area $A_{m/n}^{V}$ of the boundary between solid phases m and n can be computed in a similar fashion:[48]

$$A_{m/n}^{V} = 0.96\,\pi\left(\min(r_{p,m},\ r_{p,n}) \sin\frac{\pi}{12}\right)^2 n_m^V\, Z_{m,n}\, \gamma_m \gamma_n \quad [36]$$

The volume-specific area of the boundary between phase $k \in \{n, m\}$ and the gas is computed as[45]

$$A_{k/gas}^{V} = 4\pi r_{p,k}^2 n_k^V \quad [37]$$

and the mean pore diameter d_{pore} as[14]

$$d_{pore} = \frac{2}{3}\frac{\alpha_{pore}}{1 - \alpha_{pore,BS}}\frac{d_m d_n}{\alpha_{m,BS} d_n + \alpha_{n,BS} d_m} \quad [38]$$

where d_k is the mean particle diameter of the phase $k \in \{n, m\}$ and $\alpha_{k,BS}$ is the volume fraction of the phase k before sintering.

To evaluate the properties of infiltrated electrodes, the percolation model developed by Vijay et al.[49] is used. By nature, the backbone of infiltrated electrodes is necessarily percolating, leaving only the percolation probabilities of the infiltrated nanoparticles n and the pores to be determined using the following empirical relations[14,49]

$$\gamma_n = \left(1 - \left(\frac{0.75 - S_n}{0.25}\right)^{0.52}\right)^{0.097} \quad [39]$$

$$\gamma_{pore} = \left(1 - \left(\frac{0.2 - \alpha_{pore}}{0.15}\right)^{2.68}\right)^{0.25} \quad [40]$$

where S_n is the surface area fraction of nanoparticles n computed as

$$S_n = \frac{\alpha_n \pi d_n^2}{\alpha_n \pi d_n^2 + \alpha_m \pi d_m^2}. \quad [41]$$

The volume-specific length of the triple phase boundary λ_{TPB}^{V} is computed as:[14,49]

$$\lambda_{TPB}^{V} = 2\pi r_{p,n} n_n^V\, Z_{n,m}\, \gamma_n \gamma_{pore} \quad [42]$$

in which phase n is the infiltrated nanoparticle phase while m is the backbone phase. In the case of infiltrated electrodes, the coordination number $Z_{n,m}$ can be computed from the lengthy but straightforward process detailed by Vijay et al.[49]

The volume-specific interfacial area $A_{m/n}^{V}$ is computed as

$$A_{m/n}^{V} = \pi r_{p,n}^2 n_n^V\, Z_{n,m}\, \gamma_n \quad [43]$$

and the mean pore diameter d_{pore} as

$$d_{pore} = \frac{2}{3}\frac{\alpha_{pore}}{1 - \alpha_{pore}} d_m. \quad [44]$$

In both infiltrated and cermet electrodes, the effective conductivity σ_k^{eff} of phase $k \in \{n, m\}$ is estimated from the conductivity of the dense material $\sigma_{mat,k}$:[14,50]

$$\sigma_k^{eff} = \sigma_{mat,k}[(1 - \alpha_{pore})\alpha_k \gamma_k]^{1.5}. \quad [45]$$

The tortuosity of the pores, when it cannot be measured, is approximated using the following expression developed by Lanfrey

et al. for random packings of identical particles:[51]

$$\tau_{\text{pore}} = \left(1.23\ \frac{(1-\epsilon)^{4/3}}{\epsilon}\right)^2 \quad [46]$$

Heat transport.—While button cells can generally be assumed to be operated isothermally due to their small dimensions and the typically high gas flow rates, the performance of larger planar SOCs is significantly impacted by temperature gradients along the MEA. Therefore, a heat transport model that takes into account all significant heat sources and sinks is critical for the accuracy of planar SOC simulations.

Experimental data which can be used to validate such models are rare, but the present heat transport model has been validated in the past by Wehrle et al.[25]

Bulk gas in planar cells: Heat transport through the gas channels is computed using an energy conservation equation derived from the model of Day and Bell[29] in the same fashion as the mass transport model presented in Eqs. 4–5:

$$\frac{\partial \rho\ h}{\partial t} = -\nabla\cdot\mathbf{u}\ \rho\ h \quad [47]$$

where h is the specific enthalpy of the gas mixture. Therein, heat transfer between the gas and the neighboring solid phase manifests as a boundary condition. When the equations are discretized and reduced to a single dimension along the gas channel length, the heat transfer can be treated as a source term $\dot{Q}_{\text{channel}}$. This source term is evaluated from an empirical expression for the Nusselt number Nu in the fully developed laminar flow of catalytic monolith channels,[52] which allows the computation of the heat transfer coefficient h_{conv}:

$$h_{\text{conv}} = \frac{Nu\ \lambda_{\text{g}}}{d_{\text{h}}} \quad [48]$$

$$Nu = 3.095 + 8.933\left(\frac{1000}{Gz}\right)^{-0.5386}\exp\left(-\frac{6.7275}{Gz}\right) \quad [49]$$

$$Gz = \frac{d_{\text{h}}}{x}\,Re\ Pr \quad [50]$$

$$d_{\text{h}} = \frac{2\ w_{\text{channel}}\ h_{\text{channel}}}{w_{\text{channel}} + h_{\text{channel}}} \quad [51]$$

where λ_g is the heat conductivity of the gas, d_{h} is the hydraulic diameter of the channel, x is the distance to the channel inlet, w_{channel} is the width of the channel, h_{channel} is the height of the channel, Re is the Reynolds number of the flow and Pr is the Prandtl number of the fluid.

The heat transfer coefficient h_{conv} allows to compute the heat flux through the lateral boundaries of the channels, which can be different on every side depending on the solid surface temperatures T_{solid}:

$$q_{\text{conv}} = h_{\text{conv}}\ (T_{\text{solid}} - T). \quad [52]$$

$\dot{Q}_{\text{channel}}$ is the surface integral of boundary fluxes q_{conv} over the gas/solid interface. Discretized with a first order method, the integral is simply the sum of all boundary fluxes q_{conv} at the four side of the channel multiplied by their corresponding surface areas.

Since the specific enthalpy h is a nonlinear function of the gas temperature T, the temperature is determined iteratively using the Newton method.

Solid phase: For the solid phase, the following 2D heat diffusion equation is solved:[24]

$$\rho^{\text{eff}} c_p^{\text{eff}} \frac{\partial T}{\partial t} = \nabla\cdot\lambda^{\text{eff}}\ \nabla T + \dot{q}^V_{\text{solid}} \quad [53]$$

The density ρ^{eff}, specific heat capacity c_p^{eff} and thermal conductivity λ^{eff} are expressed as effective homogenized properties of the considered layers (e.g., porous support layer, cermet electrode, bulk electrolyte), taking into account their porosities and compositions:

$$\rho_l^{\text{eff}} = \sum_{m\,\in\,\mathbf{M}_l} \alpha_{m,l}\rho_m \quad [54]$$

$$c_{p,l}^{\text{eff}} = \sum_{m\,\in\,\mathbf{M}_l} \alpha_{m,l}c_{p,m} \quad [55]$$

$$\lambda_l^{\text{eff}} = \sum_{m\,\in\,\mathbf{M}_l} \alpha_{m,l}\lambda_m \quad [56]$$

with $\alpha_{m,l}$ being the volume fraction of the material m from the set of solid materials $\mathbf{M}_l$ in the layer l.

In the heat diffusion equation, $\dot{q}^V_{\text{solid}}$ represents the sum heat source terms per unit volume, which differ depending on the location in the cell. In the fuel electrode, it includes endothermic or exothermic thermocatalytic reactions:

$$\dot{q}^V_{\text{schem}} = -\sum_{k\,\in\,\mathbf{S}_{\text{g}}} h_k\,\dot{s}_k\,W_k. \quad [57]$$

The reversible reaction heat $\dot{q}^V_{\text{echem}}$ from the charge transfer reactions

$$\dot{q}^V_{\text{echem}} = -\sum_{r\,\in\,\mathbf{R}_{\text{CT}}} \frac{i^V_{F,r}}{n_{e,r}\,F} T\Delta s_r \quad [58]$$

with the molar reaction entropy Δs_r is also assumed to be entirely released in the fuel electrode, since computing the reaction heat from half-cell reaction would require thermodynamic properties of charge carriers which are difficult to determine. In both electrodes, $\dot{q}^V_{\text{solid}}$ also includes activation losses $\dot{q}^V_{\text{act}}$ from the charge transfer reactions:

$$\dot{q}^V_{\text{act}} = \eta_{\text{act},r} i^V_{F,r} \quad [59]$$

Since all layers conduct charge carriers, $\dot{q}^V_{\text{solid}}$ also includes joule heating $\dot{q}^V_{\text{joule}}$, computes as

$$\dot{q}^V_{\text{joule}} = \frac{i^2_{\text{el}}}{\sigma^{\text{eff}}_{\text{el}}} + \frac{i^2_{\text{io}}}{\sigma^{\text{eff}}_{\text{io}}} \quad [60]$$

with the effective conductivities of the electron and ion conducting phases σ^{eff} and the current densities i. Additionally, contact resistances R_{cont} between all layers (current collectors, electrodes, barrier layers, electrolyte) are taken into account, which induce additional joule heating:

$$q_{\text{joule,cont}} = i^2 R_{\text{cont}}. \quad [61]$$

Joule heating through contact resistance is area specific, but is implemented as a volumetric heat source in the adjacent discretized volume of the neighboring electrode.

The surface of the electrode, where the electrode/channel interface is located, requires special consideration because it is simultaneously in contact with the ribs of the interconnect. Although the cell model is 2D, these ribs are still considered and can be imagined to form a porous layer connecting the electrode with the bulk of the interconnect. However, these layers are treated differently than the

porous electrode layers because the heat transfer mechanisms are different.

First, the diffusive heat transport term of Eq. 53 applies to the interface between electrode and ribs, only that it needs to be adjusted for the reduced contact area between the two. Then, due to the high temperatures in SOC, heat transport between interconnect and electrode through radiation at the channel surfaces also needs to be considered. It is modeled as the following heat flux:[24]

$$q_{\mathrm{rad}} = \frac{\sigma_{\mathrm{SB}}(T_{\mathrm{ede}}^4 - T_{\mathrm{ic}}^4)}{R_{\mathrm{rad,ede}\rightarrow\mathrm{ic}}} \quad [62]$$

with the electrode surface temperature T_{ede}, the interconnect surface temperature T_{ic} and the Stefan-Boltzmann constant σ_{SB}. Since the metallic interconnect typically has a much higher thermal conductivity than the MEA, and the interconnect is very long compared to its height, its temperature is assumed to be homogeneous across its height. Like Joule heating through contact resistances, the heat flux is implemented as volumetric source term applied to the concerned discretized volumes.

$R_{\mathrm{rad,ede}\rightarrow\mathrm{ic}}$ is the thermal resistance to radiation, and includes the dimensions of the channel w_{channel} and h_{channel}, the view factors F between these areas and their total emissivities ϵ:[24]

$$R_{\mathrm{rad,ede}\rightarrow\mathrm{ic}} = \frac{1-\epsilon_{\mathrm{ede}}}{\epsilon_{\mathrm{ede}}} + \frac{1}{F_{\mathrm{ede}\rightarrow\mathrm{ic}}} + \frac{1-\epsilon_{\mathrm{ic}}}{\epsilon_{\mathrm{ic}}(1+2\,h_{\mathrm{channel}}/w_{\mathrm{channel}})} \quad [63]$$

in which $F_{\mathrm{ede}\rightarrow\mathrm{ic}} = F_{\mathrm{ede}\rightarrow\mathrm{ic,plate}} + F_{\mathrm{ede}\rightarrow\mathrm{ic,rib}}$.

Finally, every surface of the channel also produces a convective heat transport term q_{conv}, as discussed in the previous Section (see Eq. 52).

Computational procedure.—In order to strike a profitable balance between model accuracy and computation speed, the model equations presented in the previous Sections are solved more efficiently through the use of two specific methods.

Decoupling time-scales: First, the physical processes are assumed to proceed in three significantly different time scales. Heat transport in the solid phase is the slowest of all considered processes, and can therefore be assumed to be the only transient process when it is considered. During the solution of the heat transport problem, it can be assumed that all other processes are so fast in comparison that they can be considered to be in the steady state at any time.

Therefore, mass and energy transport in the gas phase as well as charge transport are simulated transiently only for isothermal simulations. Since charge transport is the fastest of all considered processes by orders of magnitudes, it is usually decoupled by assuming that it is always in steady state, save for the computation of EIS.

Decoupling the equations in such a way greatly reduces the computational cost of the solution procedure without significant loss in accuracy, as long as the assumptions on time-scales hold true for the computed cases.

Space-marching: Assuming a plug shape of the flow in the channel also renders the energy and mass transport in the gas flow 1D along the length of the cell (see Eqs. 4–5). In such incompressible flows with no axial diffusion, no information needs to be propagated upstream, which allows to solve this partial differential equation through space-marching. All other significant transport equations, namely mass and charge transport in the MEA, were also formulated in 1D, but in flow-normal direction: the concentration and potential gradients in the MEA are orders of magnitudes greater in this direction. Therefore, the only information needed to simulate any cross-section of the MEA is the state of the flow in upstream direction, as long as the direction of the flow is identical in both channels (co-flow configurations).

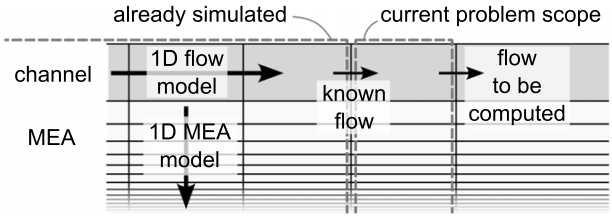

Figure 2. Illustration of the space-marching methodology.

Consequently, the problem can be solved numerically through space-marching. The partial differential equations in time and space are simplified to ordinary differential equations in time which are then solved using the semi-implicit differential-algebraic equation solver LIMEX.[53] The first discretized Section of the MEA can be solved over the full simulated time span before moving on to the next Section in flow direction. The method is illustrated in Fig. 2. It greatly reduces both simulation time and memory requirements.

This method cannot apply to the heat transport in the solid phase, since the problem is considered in 2D. However, since heat transport is decoupled from the other phenomena due to its time-scale, the space-marching algorithm can be used to compute the steady state of all other model components during each iteration of the thermal model.

Stack model.—With a functional repeating unit model, little is missing in order to be able to simulate a full SOC stack. Most importantly, SOC stack simulations require a 3D heat transport model, since significant temperature gradients can be observed in every direction. In addition, it is advantageous to be able to simulate the flow through the stack manifolds, since maldistribution of the flow to the individual cells can have a significant impact on the stack performance.[54] Flow maldistribution is an especially relevant topic in SOC stacks optimized for compactness, such as for mobile applications.[55] Finally, the potential difference under which individual cells operate is not homogeneous throughout the stack and need to be computed to accurately represent cells connected in series.

Computation procedure.—Similarly to the cell model, the stack model is accelerated by leveraging three different methods presented in this section. The resulting set of ordinary differential equations in time are also solved using the semi-implicit differential-algebraic equation solver LIMEX.[53]

Decoupling time-scales: To construct a computationally efficient SOC stack model, it is advantageous to decouple the relatively rapid chemical reactions and gas transport processes occurring within the cells from the considerably slower heat transport process taking place within the stack, just as it is done on the RU scale. In the case of stack simulations, only steady state simulations of the RUs and the flow need to be performed. These steady state simulations are performed under the assumption of a constant solid-phase temperature.

Homogenization: A SOC stack can be composed of hundreds of cells, each cell also being divided in dozens of RUs. Using a discretization as detailed as the cell model, with a matching discretization in the third dimension, would lead to impractical computation times, especially considering that the RU model has to be solved a great number of times for each iteration of the heat transport model.

Resolving the temperatures of the individual solid phases of the RUs requires a discretization in the μm scale of the MEA, while the stack's scale is oders of magnitudes larger. At the cost of losing information about the temperature differences between layers of the RUs, the cell can be homogenized and treated as a single porous material with anisotropic heat transport properties for the sake of the heat transport model at the stack scale.

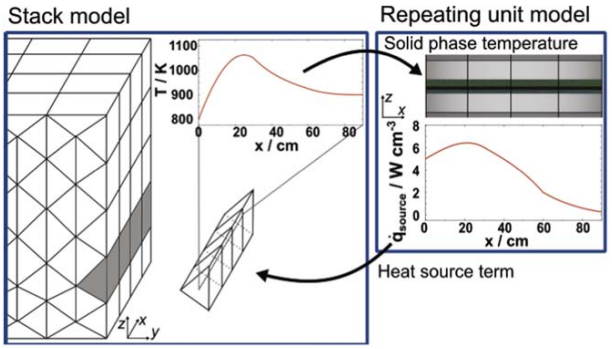

Figure 3. Schematic of the coupling between the homogenized stack heat transport model and the 1D+1D repeating unit model. A contiguous set of prismatic cells is isolated, its temperature profile extracted and passed to the RU model. In turn, the RU model is simulated and returns the spacial distribution of heat production along the RU.

The density $\rho^{\text{eff}}_{\text{stack}}$ and specific heat capacity $c^{\text{eff}}_{p,\text{stack}}$ of the lumped solid phase of the stack are computed as follows:[24]

$$\rho^{\text{eff}}_{\text{stack}} = \sum_{m \in \mathbf{M}} \alpha_{m,\text{tot}}\, \rho_m \qquad [64]$$

$$c^{\text{eff}}_{p,\text{stack}} = \sum_{m \in \mathbf{M}} \alpha_{m,\text{tot}}\, c_{p,m}. \qquad [65]$$

where $\mathbf{M}$ is the set containing all the solid phases in the stack and $\alpha_{m,\text{tot}}$ is the total volume fraction of material m.

Due to the layered geometry of planar SOCs, the spacially averaged thermal conductivity λ^{eff} needs to be anisotropic, since heat transport across the cells is slowed down by the low conductivity of the porous layers, while it is accelerated along the length and width of the cells by the interconnects. The thermal conductivity is computed according to the method elaborated by Banerjee et al.,[24] which consists of determining the total heat transfer resistance of a network of resistors each representing a separate component of the repeating units. In directions coplanar to the MEA, the resistors are arranged in parallel, while in the normal direction, the resistors are mainly arranged in series.

Using this method, the discretization does not need to take the individual RUs into account, greatly simplifying the meshing procedure. The only practical limitation is that computational cells should preferably be right prisms aligned in the same direction as the RUs. This way, a contiguous set of prismatic cells running from the inlet of the stack to the outlet can be assimilated to a RU, so that the temperature along the centerline of this set of cells can be used as constant solid-phase temperature in the RU model and the heat source terms resulting from the RU simulation can be applied to these prismatic cells in turn. This procedure is illustrated in Fig. 3, which shows how a contiguous set of prismatic cells is isolated, its temperature profile extracted and passed to the RU model. In turn, the RU model return the spacial distribution of heat production along the RU $\dot{q}^{V}_{\text{source}}(x)$.

Clustering: Each RU having their own temperature profile, gas flow rates and cell potential, it is necessary to evaluate the performance of each of them. Although the RU model may be computed for each set of contiguous computational cells, better computation speeds may be reached by re-using RU simulation results for multiple computational cells that operate under the same conditions. Such cases are very common, since stacks are usually symmetrical.

To reduce the computational load even further, a clustering algorithm is employed to group computational cells with similar, but not necessarily identical, operating conditions. For each cluster, a single RU is simulated, and its performance is assumed to be representative of every RU within the cluster.[56,57]

Of all operating parameters of RUs, the temperatures, potentials, and inlet flow rates can vary within the stack. Therefore, RUs are clustered according to these parameters after defining a maximum absolute and relative deviation between RUs of the cluster and the representative RU.

Heat transport.—Heat transport in the stack is simulated by solving a 3D heat diffusion equation which can be formulated identically to Eq. 53:[56]

$$\rho^{\text{eff}} c_p^{\text{eff}} \frac{\partial T}{\partial t} = \nabla \cdot \lambda^{\text{eff}} \nabla T + \dot{q}^{V}_{\text{source}} \qquad [66]$$

In addition to the equation now being solved in the third dimension, its implementation also differs. Since the stack thermal model is homogenized, the source term $\dot{q}^{V}_{\text{source}}$ represents the sum of all the heat sources identified at the RU scale, averaged over the volume of the RU.

A variety of boundary conditions are supported, comprising fixed temperature, fixed or temperature-dependent heat flux and free convection in a gas. They can be applied selectively to the six outer surfaces of the stack. Free convection in a gas is modeled using empirical correlations to compute the heat transfer coefficient h_{free}.[58,59] Three different coefficients are needed, all computed from Eq. 67 but different Nusselt numbers Nu: one for vertical surfaces, one for the upper horizontal surface and one for the lower horizontal surface:

$$h_{\text{free}} = \frac{Nu}{l_{\text{char}}} \lambda_{\text{env}} \qquad [67]$$

$$f_1 = (1 + 0.671\, Pr^{-\frac{9}{16}})^{-\frac{8}{27}} \qquad [68]$$

$$Nu_{\text{vertical}} = (0.825 + 0.387\, Ra^{\frac{1}{6}} f_1)^2 \qquad [69]$$

$$f_2 = (1 + 0.536\, Pr^{-\frac{11}{20}})^{-\frac{20}{11}} \qquad [70]$$

$$Nu_{\text{upper}} = \begin{cases} 0.766\, (Ra \cdot f_2)^{\frac{1}{5}}, & \text{if } Ra \cdot f_2 \leqslant 70000 \\ 0.15\, (Ra \cdot f_2)^{\frac{1}{3}}, & \text{otherwise} \end{cases} \qquad [71]$$

$$Nu_{\text{lower}} = 0.27\, Ra^{\frac{1}{4}} \qquad [72]$$

with λ_{env} the thermal conductivity of the fluid surrounding the stack module and l_{char} the characteristic length, which is the height of the vertical surfaces for the sides of the stack and the surface area divided by the perimeter of the horizontal surfaces for the top and bottom of the stack.

In this study, losses to the environment through free convection and radiation is considered, resulting to a heat flux at the stack surfaces q_{surf} of

$$q_{\text{surf}} = h_{\text{free}}(T - T_{\text{env}}) + \epsilon_{\text{surf}}\, \sigma_{\text{SB}}\, (T^4 - T^4_{\text{env}}) \qquad [73]$$

with the emissivity of the surface of the stack module ϵ_{surf} and the Stefan–Boltzmann constant σ_{SB}.

Potential computation.—In a series connection of cells, the electrical current through every cell must be equal according to Kirschoff's law. For a given current running through the stack, the potential of every cell needs to be determined so that it results in the required current. This is realized using the Newton method, taking advantage of the fact that the polarization resistance is the derivative

of the cell potential with respect to the current:

$$E_{n+1}(t,\, m) = E_n(t,\, m) + R_n(t,\, m)\cdot(I_n(t,\, m) - I_{\text{target}})\, k_{\text{relax}} \qquad [74]$$

with $E_n(t, m)$ the n-th iteration of the potential difference across the m-th cell at time t, R the polarization resistance of the cell, I the total current flowing through the cell and k_{relax} a relaxation factor used to stabilize the scheme in difficult cases.

However, Eq. 74 is formulated for a full cell of the stack, which are not discretized as such in the homogenized model. Instead, the integral values of current $I_n(t, z)$ and resistance $R_n(t, z)$ are obtained for any vertical coordinate z by integrating the current density and area-specific resistance (ASR) over a horizontal x–y plane of the homogenized stack. This integration is performed at every vertical coordinate at which a computational cell center can be found, so that a new estimation of the homogenized potential difference field $E_{n+1}(t, z)$ can be computed:

$$E_{n+1}(t,\, z) = E_n(t,\, z) + R_n(t,\, z)\cdot(I_n(t,\, z) - I_{\text{target}})\, k_{\text{relax}} \qquad [75]$$

The current density and ASR fields, which are integrated over the x–y planes in order to obtain the current $I_n(t, z)$ and resistance $R_n(t, z)$, are obtained by solving the RU model for every computational cell (potentially accelerated through clustering) into the steady state for the current guess of $E_n(t, z)$ and interpolating the RU simulation results for every relevant x–y plane. The ASR is estimated in every computational cell by the RU model with the following equations:

$$ASR = ASR_\Omega + \frac{\eta_{\text{conc}}}{i} + \frac{\eta_{\text{act,elyt,fuel}} + \eta_{\text{act,elyt,air}}}{i} \qquad [76]$$

$$\eta_{\text{conc}} = \frac{RT}{2\,F}\log\left(\frac{p_{\text{H}_2,\text{chan}}\, p_{\text{H}_2\text{O,elyt}}}{p_{\text{H}_2,\text{elyt}}\, p_{\text{H}_2\text{O,chan}}}\right) + \frac{RT}{4\,F}\log\left(\frac{p_{\text{O}_2,\text{chan}}}{p_{\text{O}_2,\text{elyt}}}\right). \qquad [77]$$

$\eta_{\text{act,elyt,fuel}}$ and $\eta_{\text{act,elyt,air}}$ are the activation overpotentials computed with Eq. 26 directly on the surface of the electrolyte. η_{conc} is the concentration overpotential estimated from the ratios of partial pressures of the reactants in the gas channels p_{chan} and in the corresponding electrode on the surface of the electrolyte p_{elyt}. ASR_Ω is the ohmic overpotential containing the resistance of the electrolyte obtained from material properties and contact resistances which are dependent on the construction of the cell. The contact resistances are obtained while calibrating the cell model.

Equation 75 is iterated until the achieved current is within a provided tolerance of the target I_{target}. If only the steady state solution is of interest, the solution procedure can be accelerated significantly by iterating only once per time step.

Internal manifold model.—The flow through the internal manifolds of SOC stacks is modeled using a hydraulic network model based on the Bernoulli equation. With this method, the flow through channels is considered to be 1D and the relationship between pressure, velocity and the properties of the fluid is computed using the Bernoulli equation, with added terms for pressure losses through friction. Geometric features of the flow, such as the junctions between straight channels, are simply represented by pressure losses that depend on the local geometry and properties of the flow.

Such a model is comparatively fast because it consists of a limited number of algebraic equations. In its present formulation, only $4 + n_{\text{RU}}$ equations have to be solved per side of the cell (fuel and air) to compute the pressure in the inlet manifold, flow rate in the inlet manifold, flow rate through all the n_{RU} channels, pressure in the outlet manifold and flow rate in the outlet manifold. In addition, it is able to model both laminar and turbulent flow. However its accuracy relies on the quality of the expressions used to compute the pressure losses. The pressure losses considered in this model are depicted in Fig. 4.

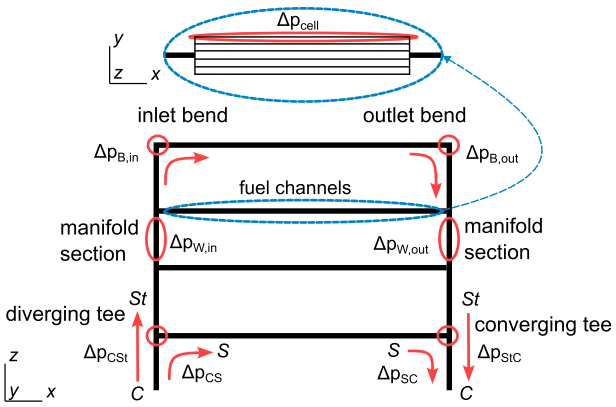

Figure 4. Schematic of the stack flow with a visualization of flow features for which the pressure losses are considered in the manifold model. The labels C, S and St are used to differentiate the common channel, side channel and straight passage of tee junctions. Adapted from Furst et al.[60]

The system of algebraic equations for a U-type manifold in a stack of n_{cells} cells, each composed of n_{RU} RUs, numbered from bottom to top with the inlet and outlet being at the bottom, is as follows:

$$\begin{cases} Q_{\text{in}}^k - \sum_j^{n_{\text{RU}}} Q_{\text{RU j}}^k = 0 & k = n_{\text{cells}} \\ Q_{\text{in}}^k - Q_{\text{in}}^{k+1} - \sum_j^{n_{\text{RU}}} Q_{\text{RU j}}^k = 0 & k \neq n_{\text{cells}} \end{cases} \qquad [78]$$

$$\begin{cases} Q_{\text{out}}^k - \sum_j^{n_{\text{RU}}} Q_{\text{RU j}}^k = 0 & k = n_{\text{cells}} \\ Q_{\text{out}}^k - Q_{\text{out}}^{k+1} - \sum_j^{n_{\text{RU}}} Q_{\text{RU j}}^k = 0 & k \neq n_{\text{cells}} \end{cases} \qquad [79]$$

$$\begin{cases} Q_{\text{in}}^k - Q_{\text{tot}} = 0 & k = 1 \\ p_{\text{tot,in}}^{k-1} + \Delta p_{\text{W,in}}^{k-1} + \Delta p_{\text{CSt}}^{k-1} - p_{\text{tot,in}}^k = 0 & k \neq 1 \end{cases} \qquad [80]$$

$$\begin{cases} p_{\text{out}}^k - P_0 = 0 & k = 1 \\ p_{\text{tot,out}}^k - p_{\text{tot,out}}^{k-1} + \Delta p_{\text{W,out}}^{k-1} + \Delta p_{\text{StC}}^{k-1} = 0 & k \neq 1 \end{cases} \qquad [81]$$

and for $j \in [1, n_{\text{RU}}]$

$$\begin{cases} p_{\text{tot,in}}^k + \Delta p_{\text{cell j}}^k + \Delta p_{\text{B,in}} + \Delta p_{\text{B,out}} - p_{\text{tot,out}}^k = 0 & k = n_{\text{cells}} \\ p_{\text{tot,in}}^k + \Delta p_{\text{cell j}}^k + \Delta p_{\text{CS}}^k + \Delta p_{\text{SC}}^k - p_{\text{tot,out}}^k = 0 & k \neq n_{\text{cells}} \end{cases} \qquad [82]$$

with $p_{\text{tot}} = p + \rho\, u^2/2$, $p_{\text{tot,in}}^k$ and $p_{\text{tot,out}}^k$ the total pressures before and after the k-th cell, $Q_{\text{RU j}}^k$ the flow rate through the j-th RU of the k-th cell, $\Delta p_{\text{cell j}}^k$ the pressure loss across the j-th RU of the k-th cell, Δp_{CS} and Δp_{SC} the turning losses in T-junctions at the inlet and outlet of the stack, Δp_{CSt} and Δp_{StC} straight passage losses in T-junction at the inlet and outlet of the stack, $\Delta p_{\text{B,in}}$ and $\Delta p_{\text{B,out}}$ turning losses at the top of the stack, Δp_{W} the wall friction losses in a straight Section of the inlet or outlet manifold, P_0 the static pressure at the outlet of the stack and Q_{tot} the total flow rate fed to the stack.

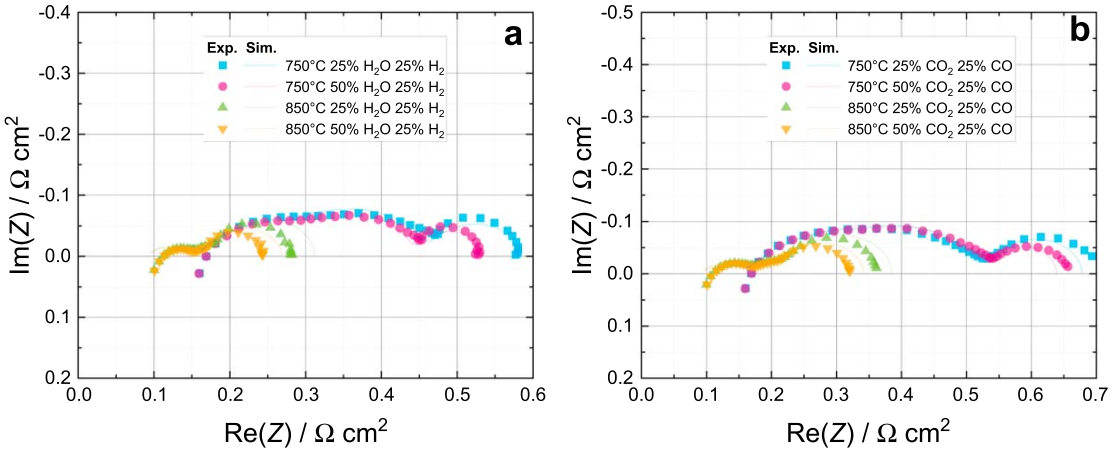

Figure 5. Fit of the button cell model to EIS of the cell of Ebbesen et al.[61] for operation with (a) H_2, H_2O and Ar and with (b) CO, CO_2 and Ar.

The system of equations is solved iteratively using the secant method. This extension of a previously published model[60] is designed to consider the flow maldistribution between the RUs of a same cell, which is caused by variations in the properties of the fluid due to temperature differences. Examples of pressure loss coefficients used to compute the pressure losses in this set of equations can be found in Eqs. 83–90.

In order to map the results of the network model to a computational cell of the homogenized stack model, especially the inlet flow velocities, a bilinear interpolation from the four closest channels to the center of the computational cell is performed. Conversely, the fluid properties inside the homogenized model are mapped to the channels of the flow model through barycentric interpolation of the three closest computational cell centers to the centerline of a channel.

Results and Discussion

Cell model parametrization.—In this section, it is explained how the model described in the previous Sections is parametrized in order to model the fuel-electrode-supported LSM-YSZ/YSZ/Ni-YSZ cell manufactured and characterized by Ebbesen, Knibbe and Mogensen.[61]

Cell structure.—In the referenced publication, the composition of the layers of the MEA and their approximate thickness is provided. Since no detailed description of the electrode microstructure is provided, some educated guesses have to be made about the exact construction of the electrodes. The supporting fuel electrode was assumed to have been manufactured as a thick but more porous support layer and a thin functional layer optimized for the electrochemical reaction. Assumed structural parameters of the cell are listed in Table I. From these parameters, the additional structural parameters required to solve the full set of differential equations is derived using the microstructure model for cermet electrodes presented before.

Electronic and ionic conductivities of common SOC materials can be found in the literature. Therefore, DETCHEM^{SOC} includes built-in expressions for the ionic and electronic conductivities of such materials, as well as the option to define custom conductivities as functions of temperature and gas partial pressures. The electrical properties of all the materials comprised in the present SOC model are listed in Table II.

EIS simulations.—The greatest advantage of a transient SOC model is the intrinsic ability to reproduce EIS, which are inherently transient. Herein, EIS are determined according to the potential step and current relaxation method outlined by Bessler.[65] EIS are a popular characterization tools for electrochemical devices because they provide information about individual physical phenomena, instead of characterizing the overall performance of the cell. While polarization curves allow to measure the ASR of a cell as a

Table I. Structural parameters of the cell assumed in this study.

Layer	Parameter	Unit	Value
Air electrode	Thickness	μm	20
	Porosity	%	35
	LSM volume fraction[a)]	%	50
	YSZ volume fraction[a)]	%	50
	Particle diameter	μm	1
	Tortuosity[c)]	—	3.9
Electrolyte	Thickness	μm	15
Fuel electrode			
Functional layer	Thickness	μm	15
	Porosity	%	20
	Ni volume fraction[a)]	%	50
	YSZ volume fraction[a)]	%	50
	Particle diameter	μm	1
	Tortuosity[c)]	—	21
Support layer	Thickness	μm	300
	Porosity[b)]	%	32
	Ni volume fraction[a)]	%	50
	YSZ volume fraction[a)]	%	50
	Particle diameter	μm	10
	Tortuosity[c)]	—	5.3

a) In the solid phase b) This parameter was adapted in order to reach the correct concentration overpotentials. c) Computed according to Eq. 46

Table II. Conductivities of the SOC materials used in this study.

Material	Electronic conductivity σ_{el} S cm^{-1}	Ionic conductivity σ_{io} S cm^{-1}	References
Ni	$32700 - T \cdot 10.653\ \mathrm{K}^{-1}$	—	62
YSZ	—	$334\, e^{-\frac{10300\ \mathrm{K}}{T}}$	63
LSM	$\frac{885500\ \mathrm{K}}{T}\, e^{\frac{-9000\ \mathrm{J\,mol^{-1}}}{RT}}$	—	64
Crofer 22H	$6950\, e^{\frac{307.7\ \mathrm{K}}{T}}$	—	14

Journal of The Electrochemical Society, 2025 172 074508

Table III. Parameters of the electrochemical model.

Reaction	Exchange current density i_0/A cm^{-1}	Charge-transfer coefficients	
		β_a	β_c
OER/ORR	$3\cdot10^6 \exp\left(-\frac{253769\ \text{J mol}^{-1}}{R\,T}\right)\left(\frac{p_{O_2}}{1\ \text{Pa}}\right)^{0.18}$	0.5	1.5
HOR/H_2ORR	$250 \exp\left(-\frac{160000\ \text{J mol}^{-1}}{R\,T}\right)\left(\frac{p_{H_2}}{1\ \text{Pa}}\right)^{-0.1}\left(\frac{p_{H_2O}}{1\ \text{Pa}}\right)^{0.33}$	0.5	0.5
COOR/CO_2RR	$7\cdot10^3 \exp\left(-\frac{180000\ \text{J mol}^{-1}}{R\,T}\right)\left(\frac{p_{CO}}{1\ \text{Pa}}\right)^{0.25}\left(\frac{p_{CO_2}}{1\ \text{Pa}}\right)^{-0.25}$	1.5	0.5

function of its polarization, an EIS allows to distinguish how much of the ASR is due to the electrochemical reaction kinetics, as opposed to mass transport inhibition.[66] Therefore, EIS are an invaluable tool for the calibration of cell models.

Despite the described modeling methodology being fully parametrized by physical parameters, some physical properties of SOC cannot be measured directly and need to be determined through fitting of simulation results to the experiments. This is typically the case for the coefficients of the Butler-Volmer equation, such as activation energy and pre-exponential factors in the exchange current density.

Reproducing experiments from literature also often requires determining some of the microstructural properties of the cell through fitting, since this data is often not included in publications. In the present case, reproducing the experiments of Ebbesen et al.,[61] only electrode thicknesses are provided and at least the support layer porosity needs to be determined due to its large impact on concentration overpotentials.

Fortunately, despite the multitude of fitted variables, calibrating the cell model on EIS prevents overfitting in multiple ways:

1. The contributions of polarization resistance, ohmic resistance and mass transport inhibition on the total cell ASR can be fitted individually.
2. The double-layer capacitance of an electrode has no influence on the local activation overpotential, only on the frequency response. The capacitance and exchange current density can therefore be fitted independently.
3. The very thin electrodes, such as the oxygen electrode in the present cell, have a minor influence on mass transport. In electrode-supported cells, the porosity and tortuosity of the support layer have a dominant influence on concentration overpotentials. In such cases where nothing of the cell microstructure is known, the microstructure of thin layers may thus be guessed without introducing significant errors, and the concentration overpotentials fitted solely based on the support layer.
4. Theoretically, the triple phase boundary length λ^V_{TPB} of the electrodes have a major impact on the cell performance, but in practice, this parameter cannot be separated from the exchange current density pre-exponential factor through fitting (see Eq. 22). When fitting the pre-exponential factor of the exchange current density, it is actually the product of pre-exponential factor and triple phase boundary length (or electrode/gas boundary area in the case of mixed electronic-ionic conducting electrodes) which is fitted.

Figure 5 depicts the finalized cell model compared to the experimental EIS data of Ebbesen et al.[61] Overall, the agreement between the model and the experiments is excellent.

As outlined by the authors of the experimental study, the open circuit voltage (OCV) observed during the experiments is different than the OCV computed from the gas compositions, which is likely the result from a gas or current leak through the MEA. Herein, it was assumed to be fully caused by a current leak and an electronic conductivity of $0.4 \exp\left(\frac{-9500}{T}\right)$ S cm^{-1} in the electrolyte was found to accurately reproduce the measured OCV.

The ohmic resistance of the cell, determined by the real part of the leftmost point of the spectrum, can be reproduced with great accuracy. Only a small contact resistance of 0.045 Ω cm^2 was determined through fitting, while literature data for material conductivities accounts for most of the ohmic ASR. On the experimental EIS plots, the high frequency data points exhibit a positive imaginary part, which is only due to the inductance of the measurement setup,[67] and is therefore not desired in the cell model. Since such an inductance does not contribute to the cell resistance, it does not impact the fitting procedure significantly.

An excellent fit was also achieved on the activation overpotentials. This requires fitting a greater number of values, namely the pre-exponential factor, activation energy and pressure exponents of the exchange current densities. Fortunately, the experimental dataset includes experiments at different temperatures, allowing to fit the activation energy, and different partial pressures in the feed gas, allowing to fit the pressure exponents reliably. These parameters need to be determined independently for the oxygen evolution reaction/oxygen reduction reaction (OER/ORR), hydrogen oxydation reaction/water reduction reaction (HOR/H_2ORR) and CO oxidation reaction/CO_2 reduction reaction (COOR/CO_2RR) independently, which is fortunately not too challenging since they can be distinguished as significantly distinct arcs in the EIS. The fitted exchange current densities are listed in Table III. The charge transfer coefficients β_a and β_c are the last remaining parameters of the Butler-Volmer equation that need to be fitted, but their influence is most noticeable at higher current densities. Therefore, in the absence of EIS measured under higher polarization, the present charge transfer coefficients were fitted using polarization curves, although the simulation results were noted to be rather insensitive to changes in charge transfer coefficients.

Finally, a satisfactory fit was achieved regarding concentration overpotential by fitting the fuel electrode support layer porosity. However, a slight mismatch in the influence of the temperature on the low frequency arc can be observed, as the concentration overpotential is slightly overestimated at high temperatures. This is likely due to the low flow rate of 20 sL/h used in the experiments, which is inconsistent with the assumption of perfectly mixed gas phase above the electrode. This suggests the need for a more detailed gas compartment model.

Due to the wealth of experimental data available, four datasets could be conserved as validation data. These remaining experiments all include gases that react on the surface of the nickel electrode, so that the heterogeneous chemistry model needs to be activated in those cases. A 42-step elementary reaction mechanism for methane reforming and water-gas shift on Ni-YSZ is used.[39] It provides 42 reaction rate equations for the thermocatalytic heterogeneous chemistry model (expressed in generic form as Eq. 19), which in turn influences species conservation through the species production rate $\dot{s}_{\text{m}}$ of Eq. 15. No additional calibration is needed. Comparison between experiments and simulations is shown in Fig. 6.

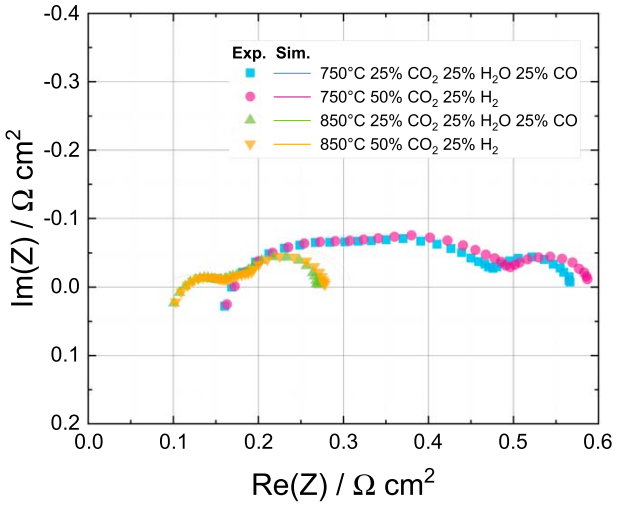

Figure 6. Fit of the button cell model to EIS of the cell of Ebbesen et al.[61] under conditions with mixed HOR/H_2ORR and COOR/CO_2RR charge-transfer reactions and thermocatalytic surface reactions on the Ni-YSZ electrode.

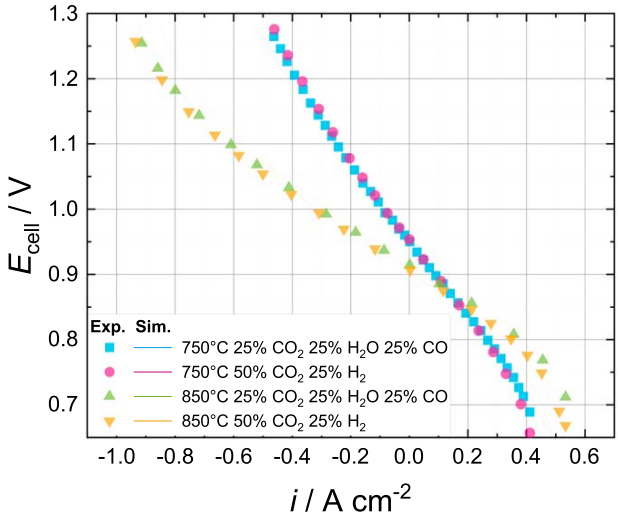

Figure 7. Fit of the button cell model to experimental polarization curves of Ebbesen et al.[61] under conditions with mixed HOR/H_2ORR and COOR/CO_2RR charge-transfer reactions and thermocatalytic surface reactions on the Ni-YSZ electrode.

The agreement between experiments and simulations on this validation dataset is very good, and showcases that the mixed H_2O/CO_2 electrolysis model works without need for additional fitting or other special treatment. In addition, the heterogeneous chemistry model is also demonstrated to work adequately in this case, although a case that is more strongly influenced by surface reaction kinetics would be required for proper testing, as the low flow rates used in the experimental setup lead to a composition of the gas phase close to equilibrium in the active layer of the fuel electrode.

Validation of polarization curves.—While the EIS data is the most useful for fitting the unknown parameters of the model, the polarization curves remain a useful tool to verify the adequacy of the fitted parameters under different polarization conditions, especially since the published dataset on which the present model is based provides only EIS measured at OCV, which is common practice. Comparison between simulated polarization curves and the experimental data of Ebbesen et al.[61] under conditions with mixed H_2ORR/HOR and CO_2RR/COOR charge-transfer reactions and surface reactions on the Ni-YSZ electrode is shown in Fig. 7.

Excellent agreement between the simulated and experimental polarization curves is reached for all cases over most of the simulated potential range. Notably, the OCV is predicted reliably despite the current leakage. The agreement is weakest at high current densities, negative and positive, which is where concentration overpotential dominates the losses in the cell. This is congruent with the flow model at the surface of button cells showing larger errors at low flow rates, as identified in the previous section.

Overall, this verification step confirms the ability to calibrate the cell model using solely EIS measured at OCV.

Stack model parametrization.—In this study, a stack of the LSM-YSZ/YSZ/Ni-YSZ cells is considered, on which the cell model was calibrated in the previous section.

A stack of 40 cells with an active area of 90×175 cm^2 is considered. In this arrangement, the number of cells in the stack is high enough so that flow maldistribution due to friction losses in the manifold can be expected, but not high enough to have turbulent flow in parts of the manifolds under reasonable operating conditions.

The interconnects are assumed to be made of Crofer 22 H, and the stack is insulated on all sides by a 5 cm layer of the Promalight-1000X material. The effect of the gaps in the insulation due to the inlets and outlets of the manifolds is neglected. The electric conductivity of Crofer 22 H is shown in Table II, and no additional contact resistance was considered.

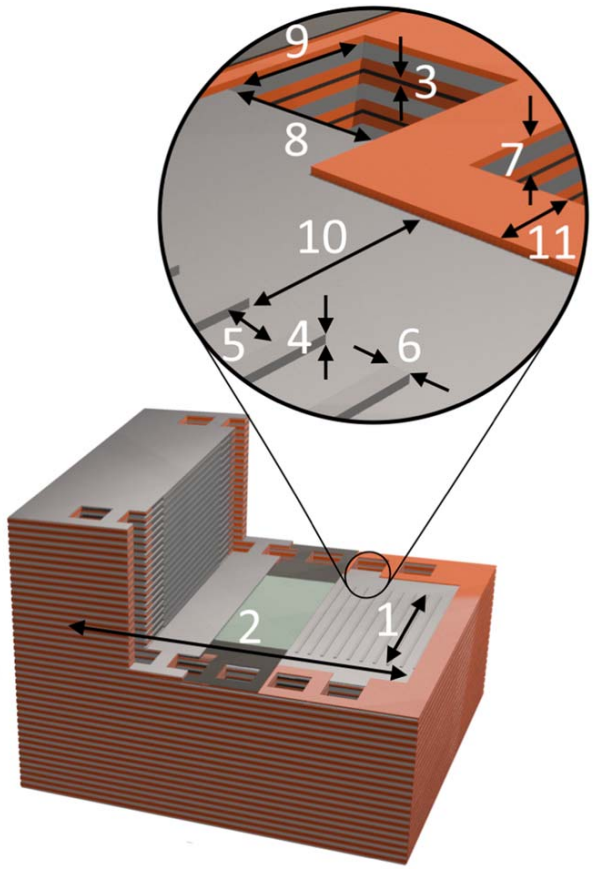

Figure 8. Sectional view of the SOC stack showing the geometry of the interconnects (in gray), sealing gaskets (in orange) and the SOC (in green) in its guide frame (in black). Measurements are annotated according to the numbered labels of Table IV.

Table IV. Dimensions of the SOC stack. The dimensions of the manifold are adopted from a prior publication presenting a flow model for this specific geometry.[60]

#	Dimension	Value	Unit
1	Cell length	90	mm
2	Cell width	175	mm
3	MEA thickness	350	μm
4	Air and fuel channel height	1	mm
5	Air and fuel channel width	4.75	mm
6	Interconnect rib width	1.5	mm
7	Interconnect total height	4.1	mm
8	Manifold channel width	17	mm
9	Manifold channel depth	17	mm
10	Inlet & outlet header length	17	mm
11	Sealing width	8	mm

Table V. Thermal properties of the stack components. Their values were assumed to be constant and evaluated at 1100 K.

Material	Specific heat capacity c_p J/kg/K	Thermal conductivity λ W/m/K	Density ρ kg/m^3	References
Ni	561.0	68.1	8900	68, 69
YSZ	620	2.1	5938	70, 71
LSM[a)]	610	3.4	6300	72, 73
Crofer 22H	660	26.1	7800	14, 74
Promalight-1000X	1070	0.036	280	75

a) In the absence of published data, the thermal properties of LSM were assumed to be similar to those of LSCF.

The geometry of the stack is illustrated in Fig. 8 and measurements are provided in Table IV. The thermal properties of all the materials comprised in the SOC stack are listed in Table V.

The pressure loss coefficients, required to characterize the geometry of the stack manifold in the flow model (Eqs. 78–82), are computed using the expressions listed as Eqs. 83–90 uncovered in a previous study.[60]

$$\zeta_{\mathrm{CSt}} = \frac{\overline{p}_{\mathrm{tot,St}} - \overline{p}_{\mathrm{tot,C}}}{\rho \overline{u}^2_{z,\mathrm{C}/2}} \approx 39.67 \left(\frac{Q_{\mathrm{S}}}{Q_{\mathrm{C}}}\right)^2 \frac{Q_{\mathrm{St}}}{Q_{\mathrm{C}}} - 0.4069 \quad [83]$$

$$\zeta_{\mathrm{CS}} = \frac{\overline{p}_{\mathrm{tot,S}} - \overline{p}_{\mathrm{tot,C}}}{\rho \overline{u}^2_{z,\mathrm{C}/2}} \approx -\frac{Q_{\mathrm{S}}/Q_{\mathrm{C}}}{Re_{\mathrm{C}}}(226 Re_{\mathrm{S}} + 3574) - 0.9842 \quad [84]$$

$$\zeta_{\mathrm{StC}} = \frac{\overline{p}_{\mathrm{tot,C}} - \overline{p}_{\mathrm{tot,St}}}{\rho \overline{u}^2_{z,\mathrm{C}/2}} \approx \frac{Re_{\mathrm{S}} Q_{\mathrm{C}}/Q_{\mathrm{St}} + 15.59/Re_{\mathrm{S}} - 14.79}{Re_{\mathrm{C}} Q_{\mathrm{St}}/Q_{\mathrm{C}}} \quad [85]$$

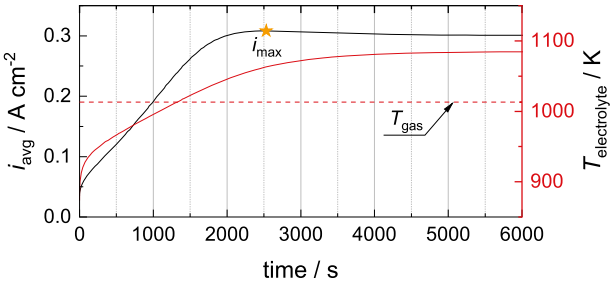

Figure 9. Evolution over time of the average electrolyte temperature and current density in a repeating unit starting at a constant temperature of 873 K being fed with humidified ammonia and air at 1023 K under a potential of 0.8 V.

$$\zeta_{\mathrm{SC}} = \frac{\overline{p}_{\mathrm{tot,C}} - \overline{p}_{\mathrm{tot,S}}}{\rho \overline{u}^2_{z,\mathrm{C}/2}} \approx \frac{2845\, Q_{\mathrm{S}}/Q_{\mathrm{C}}}{1.01 - Re_{\mathrm{C}}} + 0.7872 \quad [86]$$

$$\zeta_{\mathrm{B,in}} = \frac{\overline{p}_{\mathrm{tot,cell,in}} - \overline{p}_{\mathrm{tot,M_{in}}}}{\rho \overline{u}^2_{z,\mathrm{M_{in}}/2}} \approx -5727/Re_{\mathrm{M_{in}}} \quad [87]$$

$$\zeta_{\mathrm{B,out}} = \frac{\overline{p}_{\mathrm{tot,M_{out}}} - \overline{p}_{\mathrm{tot,cell,out}}}{\rho \overline{u}^2_{z,\mathrm{M_{out}}/2}} \approx -4702/Re_{\mathrm{M_{out}}} \quad [88]$$

$$f_{D,\mathrm{in}} = \frac{63.13}{Re_{\mathrm{M}}}\left(Re_{\mathrm{cell}}\frac{z}{h_{\mathrm{tot}}} + 0.3544 - \frac{z}{h_{\mathrm{tot}}}\right) \quad [89]$$

$$f_{D,\mathrm{out}} = \frac{31.47}{Re_{\mathrm{M}}}(Re_{\mathrm{cell}} + 1.4735). \quad [90]$$

Pressure losses in the channels are evaluated using analytical solutions for Poiseuille flow in rectangular channels.[76]

Simulation of the start-up of ammonia-fed repeating units.— Since no cell-specific calibration is needed for the heterogeneous chemistry model as long as the catalyst surface area is known or estimated well, it is possible to study the performance of the cell when it is fueled with ammonia by simply adopting a validated mechanism for ammonia decomposition on Ni-YSZ for from the literature such as the thermodynamically consistent 6-step elementary kinetic mechanism from Appari et al.[77]

The performance of a perfectly insulated RU fed with 0.65 sL/h mixture of 97% NH_3/3% H_2O at 1023 K is discussed in this section. The cell is operated at 0.8 V, in which case it reaches a fuel conversion of approximately 90%. 6.5 sL/h of 79% N_2/21% O_2 is fed to the air channel.

Figure 9 depicts the evolution of the average current density and MEA average temperature in the cell during the start up process, starting from a pre-heated cell at 873 K. Initially, the cell heats up through heat transport from the hot gas to the MEA and a small amount of resistive heating due to the electric conductivity of the MEA. Once the MEA reaches a sufficient ionic conductivity, the electrochemical reaction starts contributing to the temperature rise of the cell. In the steady state, the gas flow cools down the cell which produces heat through resistive heating and the electrochemical reactions. Ammonia cracking, which is an endothermic reaction, also helps to cool down the cell at high temperatures.

Interestingly, the highest average current density is not reached in the steady state where the average electrolyte temperature is highest. Therefore, the performance of the RU once it reaches steady

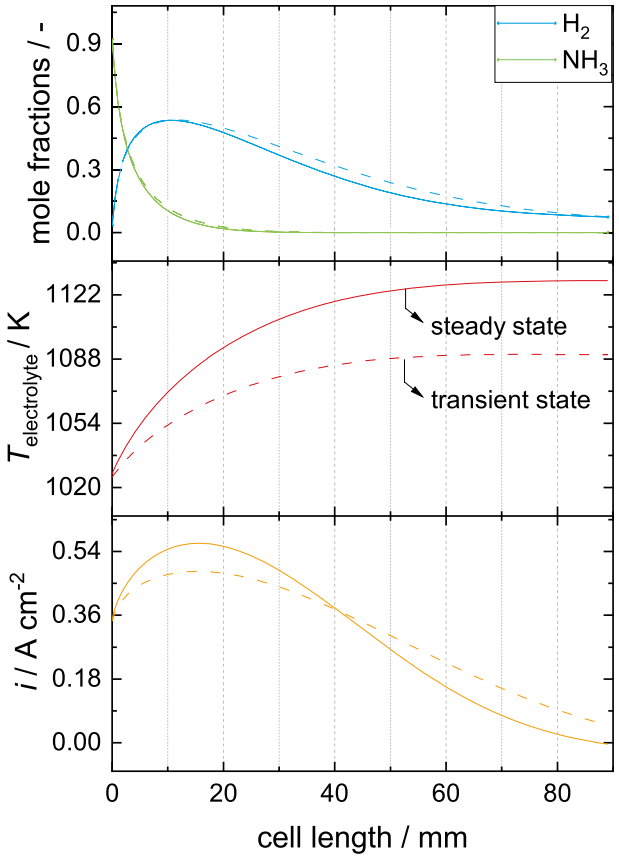

Figure 10. Axial current density, fuel channel species mole fraction and MEA temperature profiles of a RU fed with 0.65 sL/h mixture of 97% NH_3/3% H_2O at 1023 K under 0.8 V. Continuous lines represent the steady state while the dashed lines represent the state of highest current density during the heat-up of the cell.

operating conditions is studied in further detail and compared to its performance at its peak current density through the axial profiles of the MEA temperature, current density and gas channel species concentrations depicted in Fig. 10.

In the steady state, studying the species mole fractions reveals that ammonia is decomposed rapidly as soon as it enters the cell, allowing for a high current density right from the inlet. Still, as the hydrogen concentration continues to increase, so does the current density. However, the highest current density is not reached where the hydrogen concentration is highest. Since the temperature of the cell increases over its length due to the exothermic electrochemical reaction, so does the activity of the cell. Therefore, the highest current density, 0.56 A/cm^2, is reached approximately 17 mm into the cell, while the cell has reached a higher temperature but the hydrogen concentration is still high.

At the end of the cell, the current density drops to 0 A/cm^2 as the equilibrium potential reaches 0.8 V due to the low hydrogen concentration and high temperature. At this point, a hydrogen conversion of 89.8% is achieved. At the outlet, both the electrolyte and gas temperature reaches 1130 K, with the highest temperature gradient in the electrolyte being 14.2 K/mm directly at the inlet.

At the point in time where the maximum current density is reached, the MEA is significantly cooler, with a maximum temperature of 1090 K at the end of the cell. The decreased temperature toward the inlet leads to a lower peak current density where the hydrogen concentration is high, likely due to the increased ohmic overpotential. However, the lower temperature toward the outlet compared to the steady state ensures that the equilibrium potential does not drop too strongly. The current density does not drop to zero at the outlet and on average a slightly higher current density is achieved.

In order to provide a better understanding of the chemical reactions inside of the anode, the gas composition and catalyst surface coverage is shown in Fig. 11 at the inlet of the cell, at the 10 mm mark where the hydrogen concentration reaches its maximum and at the end of the cell. Therein, the active layer of the electrode can be clearly distinguished from the support layer by the sudden change in mole fraction gradients at a depth of 300 μm caused by the increased catalytic surface area. At the inlet of the cell, the high ammonia decomposition rate results in an increase in hydrogen mole fraction even close to the electrolyte, in spite of the competing electrochemical reaction. With the decreasing ammonia fraction along the channel length, this trend quickly inverts. At first, the hydrogen mole fraction increases throughout the support layer and decreases inside of the active layer. Once the maximum hydrogen fraction in the channel is achieved, approximately 10 mm from the inlet, the flow of hydrogen inverts and its mole fraction decreases monotonously over the thickness of the anode.

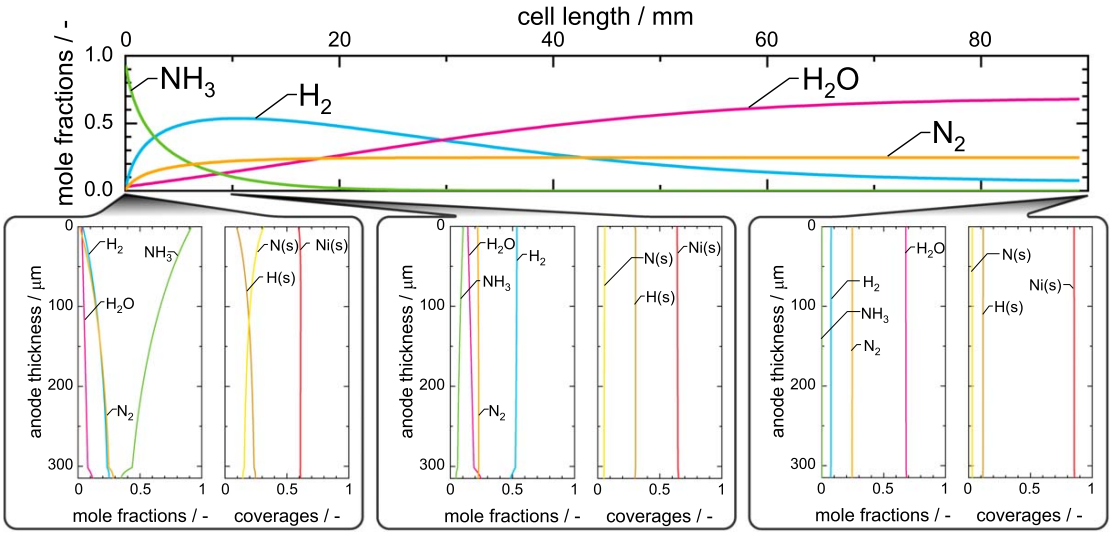

Figure 11. Gas species mole fractions along the length of the fuel channel at the steady state, accompanied by mole fractions and surface coverages through the thickness of the anode at the inlet, 10 mm from the inlet and at the end of the cell.

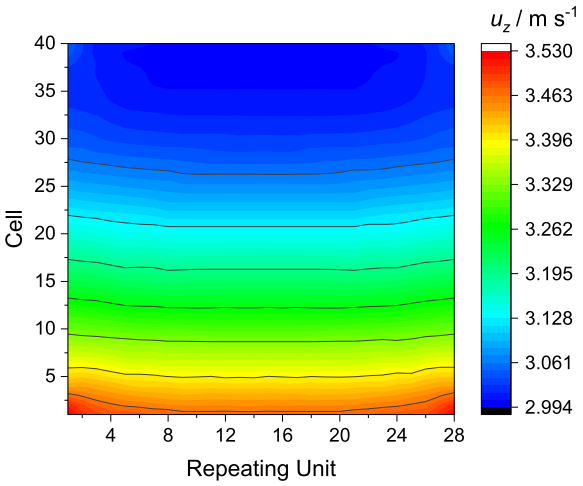

Figure 12. Contour plot of the inlet flow velocity of the air channels through all the repeating units of the stack.

Figure 11 also reveals good coverage of the Ni surfaces by N(s) and H(s) at the inlet, while the coverages by NH_3(s), NH_2(s) and NH(s) were not depicted because they are negligible due to their fast reaction rates. While the coverage by N(s) decreases as the ammonia depletes along the channel and through the anode, the coverage by H(s) is instead more greatly influenced by the hydrogen concentration. The increase in open Ni(s) sites toward the end of the channel seems therefore to be a result of the fuel depletion as well as the increased temperature.

Evaluation of the influence of flow maldistribution on stack performance.—By virtue of the stack flow model described by Eqs. 78–82, the influence of the manifold on the performance of a stack of 40 cells of the type manufactured by Ebbesen et al.[61] can be studied. The geometry of the stack considered herein was described in Table IV.

In this section, the analysis is performed on an electrolysis stack fed with a steam mixture of 90 vol% H_2O and 10 vol% H_2 at 1023 K. The fuel flow rate is adjusted to an average 7.78 sL/h, which amounts to a total fuel flow rate to the stack of 8709 sL/h, distributed to the individual channels according to the manifold model. A mixture of 21 vol% O_2 and 79 vol% N_2 is fed to the air channels with an average flow rate per channel of 15.6 sL/h, a relatively high sweep gas flow rate used for temperature management. The stack is operated at an average current density of -2.11 A cm^{-2} in the active area, resulting in an average cell potential of 1.40 V and a steam conversion rate of 72.5%. Of the achieved current density of -2.11 A cm^{-2}, -0.10 A cm^{-2} does not contribute to the electrolysis process due to the current leak of the electrolyte observed previously.

This shows that high current densities may be achieved with the present cell architecture under optimized operating conditions. However, such operating conditions also accelerate the degradation of the cell, which must be studied experimentally or with complementary simulation methods. In addition, the scale-up of single cells to full stacks introduces multiple engineering challenges such as ensuring good electrical contact between electrodes and interconnects, as well as preventing gas leakage. In the present simulation, no additional contact resistance nor gas leakage was introduced.

The flow distribution to the individual air channels of the stack is shown through a contour plot of the velocity at the inlet of the repeating units in Fig. 12. Therein, flow maldistribution is noticeable both in the vertical and horizontal direction.

Flow maldistribution along the height of the SOC stack can be expected due to the geometry of a U-type manifold such as the one studied herein. The previous study on an isothermal flow using an identical stack geometry showed that the friction inside the manifold

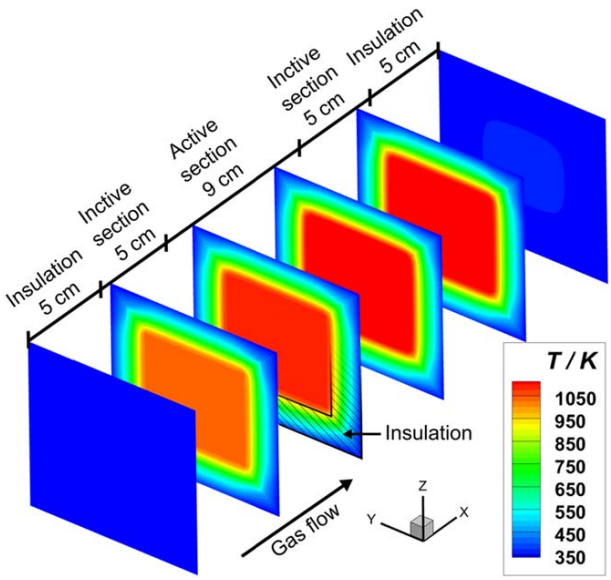

Figure 13. Temperature profiles of the SOEC stack at steady state. 5 equidistant slices are taken from the front to the back of the stack and the x-axis is stretched by a factor 3 for a better visualization.

generally causes a decrease in flow rates through cells more distant from the inlet of the manifold.[60] However, in the present case, the temperature distribution observed in Fig. 13 also introduces a slight maldistribution in the horizontal direction in which no geometric pressure losses are considered. Since the viscosity of gases increase with temperature, the flow in the central, hotter region of the stack suffers from an increased hydraulic resistance. Conversely, the highest flow velocities are found in the coldest corners of the stack.

In the present case, maldistribution in the vertical direction, which is mostly due to the manifold geometry, is much larger in scale than the maldistribution in horizontal direction which is solely due to the temperature distribution.

The temperature distribution in the stack is depicted in Fig. 13. The temperature within the stack increases by 75 K over the active area in flow direction while the temperature gradients in other directions are negligible in comparison. This is due to the highly exothermic operation of the stack, with the gases in the channel outlets 121 K above the inlet temperature on average.

Comparison with a simulation using homogeneous flow distribution shows no significant change in temperature distribution nor in conversion rate, despite a variation of 18% in sweep gas velocity. Fuel maldistribution has a magnitude of only 4% and the results indicate that it is not enough to meaningfully impact the stack performance through concentration overpotentials. As can be seen in the plot of cell potentials along the height of the stack shown in Fig. 14, only minute differences in cell performance are caused by

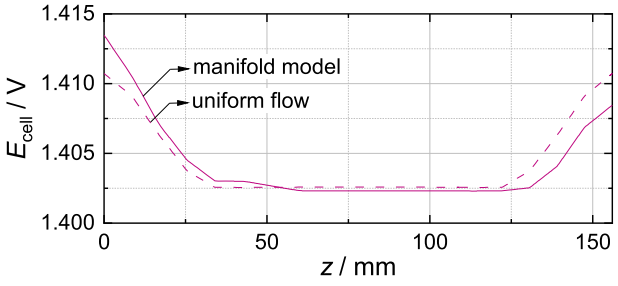

Figure 14. Cell potentials as a function of the height of the stack. The stack simulation with manifold model is compared to a simulation with uniform flow distribution.

the flow maldistribution in this case. Even then, the loss in performance at the bottom of the stack, manifested through an increase in cell potential of 3 mV in order to reach a current density of -2.11 A cm^{-2}, is compensated by an equivalent increase in cell performance at the top. The averages of cell potentials is therefore only different by 0.06 mV, or 0.004%.

Conclusions

The multi-scale framework for the transient simulation of solid oxide button cells, repeating units and stack modules integrated in DETCHEM was presented. This model was shown to effectively bridge the gap between button cell experiments and performance predictions of large-scale stacks, providing a comprehensive tool for analyzing SOC performance under various operating conditions.

The workflow of using such a model was demonstrated, starting with the calibration and validation using experimental EIS and polarization curves of a Ni-YSZ/YSZ/LSM-YSZ button cell followed by a performance analysis of the scaled-up repeating unit and stack.

The versatility of the tool was demonstrated by providing EIS of button cells, replicating experiments with both common fuel-side electrochemical reactions, validating the model on experimental data of a case that includes thermocatalytic chemistry, performing transient simulations of repeating units and simulating the flow maldistribution and potential field in a stack module.

The main shortcomings of the presented methodology is the limited geometry it is able to model. Tubular cells, as well as cross-flow and counter-flow stack configurations are widespread, but cannot yet be simulated by DETCHEM^{SOC}. In addition, the simplified geometry assumed by a two-dimensional cell model and homogenized stack model induces a loss of information on small-scale phenomena caused by tree-dimensional geometrical features.

The multi-scale SOC modeling framework integrated in DETCHEM not only enhances our understanding of cell performance but also paves the way for the scale-up of the SOC technology. By bridging the gap between experimental data and large-scale applications, such models stand as pivotal tools for researchers and engineers alike. The demonstrated versatility and robustness of the framework underscore its potential to drive innovation and optimize SOC systems for a wide range of industrial applications.

Acknowledgments

The authors acknowledge support by the state of Baden-Württemberg through bwHPC.

Omegadot software and consulting GmbH is gratefully acknowledged for a cost-free academic license of DETCHEM.

The authors extend their sincere gratitude to Professor Robert J. Kee for his invaluable insights and continuous engagement in discussions throughout the course of this research. We deeply appreciate his time, guidance, and unwavering support in advancing our work on this topic.

The authors also thank Mr. Felix Ehrlich and Dr. Steffen Tischer for constructive and fruitful discussions, which have provided meaningful perspectives and enriched the quality of this research. Their contributions are greatly appreciated.

ORCID

Oscar Furst https://orcid.org/0009-0007-7772-3660
Olaf Deutschmann https://orcid.org/0000-0001-9211-7529

References

1. P. R. Shukla et al., *IPCC, 2022: Climate Change 2022: Mitigation of Climate Change. Contribution of Working Group III to the Sixth Assessment Report of the Intergovernmental Panel on Climate Change* (Cambridge University Press) (2022).
2. A. Hauch, R. Küngas, P. Blennow, A. B. Hansen, J. B. Hansen, B. V. Mathiesen, and M. B. Mogensen, "Recent advances in solid oxide cell technology for electrolysis." *Science*, **370**, eaba6118 (2020).
3. *Topsoe A/S Herning SOEC Manufacturing Facility*, Accessed 02.06.2024.
4. *Bloom Energy Demonstrates Hydrogen Production with the World's Most Efficient Electrolyzer and Largest Solid Oxide System* (2023), Accessed 02.06.
5. "Sunfire - World's largest high-temperature electrolyzer achieves record efficiency." Accessed 02.06.2024.
6. F. Safari and I. Dincer, "Assessment and optimization of an integrated wind power system for hydrogen and methane production." *Energy Conversion and Management*, **177**, 693 (2018).
7. C. Drechsler and D. W. Agar, "Intensified integrated direct air capture - power-to-gas process based on H_2O and CO_2 from ambient air." *Applied Energy*, **273**, 115076 (2020).
8. Y. Chi, Q. Hu, J. Lin, Y. Qiu, S. Mu, W. Li, and Y. Song, "Numerical simulation acceleration of flat-chip solid oxide cell stacks by data-driven surrogate cell submodels." *Journal of Power Sources*, **553**, 232255 (2023).
9. Y. Chi, K. Yokoo, H. Nakajima, K. Ito, J. Lin, and Y. Song, "Optimizing the homogeneity and efficiency of a solid oxide electrolysis cell based on multiphysics simulation and data-driven surrogate model." *Journal of Power Sources*, **562**, 232760 (2023).
10. L. Wang, M. Pérez-Fortes, H. Madi, S. Diethelm, J. V. herle, and F. Maréchal, "Optimal design of solid-oxide electrolyzer based power-to-methane systems: A comprehensive comparison between steam electrolysis and co-electrolysis." *Applied Energy*, **211**, 1060 (2018).
11. M. A. Khaleel, Z. Lin, P. Singh, W. Surdoval, and D. Collin, "A finite element analysis modeling tool for solid oxide fuel cell development: coupled electrochemistry, thermal and flow analysis in MARC®." *Journal of Power Sources*, **130**, 136 (2004).
12. S. B. Beale, H.-W. Choi, J. G. Pharoah, H. K. Roth, H. Jasak, and D. H. Jeon, "Open-source computational model of a solid oxide fuel cell." *Comput. Phys. Commun.*, **200**, 15 (2016).
13. J. D. Duhn, A. D. Jensen, S. Wedel, and C. Wix, "Optimization of a new flow design for solid oxide cells using computational fluid dynamics modelling." *Journal of Power Sources*, **336**, 261 (2016).
14. L. Wehrle, Y. Wang, P. Boldrin, N. P. Brandon, O. Deutschmann, and A. Banerjee, "Optimizing solid oxide fuel cell performance to Re-evaluate its role in the mobility sector." *ACS Environmental Au*, **2**, 42 (2022).
15. A. Donazzi, S. De Pascali, F. Garavaglia, and M. Bracconi, "A quasi 2D model for the interpretation of impedance and polarization of a planar solid oxide fuel cell with interconnects." *Electrochimica Acta*, **365**, 137346 (2021).
16. J. Fan, J. Shi, R. Zhang, Y. Wang, and Y. Shi, "Numerical study of a 20-cell tubular segmented-in-series solid oxide fuel cell." *Journal of Power Sources*, **556**, 232449 (2023).
17. H. Zhu, R. J. Kee, V. M. Janardhanan, O. Deutschmann, and D. G. Goodwin, "Modeling elementary heterogeneous chemistry and electrochemistry in solid-oxide fuel cells." *J. Electrochem. Soc.*, **152**, A2427 (2005).
18. A. Banerjee and O. Deutschmann, "Elementary kinetics of the oxygen reduction reaction on LSM-YSZ composite cathodes." *J. Catal.*, **346**, 30 (2017).
19. H. Zhu and R. J. Kee, "Modeling protonic-ceramic fuel cells with porous composite electrodes in a button-cell configuration." *J. Electrochem. Soc.*, **164**, F1400 (2017).
20. J. A. Ortiz-Corrales and J. Otomo, "Simulating transport of charged defects in $BaZr_{0.8}Y_{0.2}O_{3-\delta}|BaZr_{0.1}Ce_{0.7}Y_{0.1}Yb_{0.1}O_{3-\delta}$ bilayer electrolytes using a Nernst-Planck-Poisson model." *Solid State Ionics*, 116680 (2024).
21. O. Deutschmann et al., *DETCHEM* (2022), Accessed 05.06.2024.
22. *DETCHEM-Mechanisms*, Accessed 05.06.2024.
23. V. Menon, Q. Fu, V. M. Janardhanan, and O. Deutschmann, "A model-based understanding of solid-oxide electrolysis cells (SOECs) for syngas production by H_2O/CO_2 co-electrolysis." *Journal of Power Sources*, **274**, 768 (2015).
24. A. Banerjee, Y. Wang, J. Diercks, and O. Deutschmann, "Hierarchical modeling of solid oxide cells and stacks producing syngas via H_2O/CO_2 Co-electrolysis for industrial applications." *Applied Energy*, **230**, 996 (2018).
25. L. Wehrle, D. Schmider, J. Dailly, A. Banerjee, and O. Deutschmann, "Benchmarking solid oxide electrolysis cell-stacks for industrial Power-to-Methane systems via hierarchical multi-scale modelling." *Applied Energy*, **317**, 119143 (2022).
26. S. E. Bechtel and R. L. Lowe, *Fundamentals of continuum mechanics: with applications to mechanical, thermomechanical, and smart materials* (Academic Press, an imprint of Elsevier, Amsterdam Boston) (2015).
27. L. L. Raja, R. J. Kee, O. Deutschmann, J. Warnatz, and L. D. Schmidt, "A critical evaluation of navier-stokes, boundary-layer, and plug-flow models of the flow and chemistry in a catalytic-combustion monolith." *Catal. Today*, **59**, 47 (2000).
28. R. J. Kee, M. E. Coltrin, P. Glarborg, and H. Zhu, *Chemically Reacting Flow: Theory, Modeling, and Simulation* (Wiley) 1 ed. (2017).
29. M. S. Day and J. B. Bell, "Numerical simulation of laminar reacting flows with complex chemistry." *Combust. Theory Modelling*, **4**, 535 (2000).
30. H. Zhu and R. J. Kee, "Modeling electrochemical impedance spectra in SOFC button cells with internal methane reforming." *J. Electrochem. Soc.*, **153**, A1765 (2006).
31. E. A. Mason and A. P. Malinauskas, *Gas Transport in Porous Media: The Dusty-gas Model* (1983), Chemical engineering monographs 17 (Elsevier, Amsterdam; New York).
32. V. M. Janardhanan and O. Deutschmann, "Numerical study of mass and heat transport in solid-oxide fuel cells running on humidified methane." *Chemical Engineering Science*, **62**, 5473 (2007).
33. S. S. Rathore, S. Biswas, D. Fini, A. P. Kulkarni, and S. Giddey, "Direct ammonia solid-oxide fuel cells: A review of progress and prospects." *International Journal of Hydrogen Energy*, **46**, 35365 (2021).

34. L. Wehrle, A. Ashar, O. Deutschmann, and R. J. Braun, "Evaluating high power density, direct-ammonia SOFC stacks for decarbonizing heavy-duty transportation applications." *Applied Energy*, **372**, 123646 (2024).
35. Y. Lin, Z. Zhan, J. Liu, and S. A. Barnett, "Direct operation of solid oxide fuel cells with methane fuel." *Solid State Ionics*, **176**, 1827 (2005).
36. L. Wang et al., "Power-to-methane via co-electrolysis of H_2O and CO_2: The effects of pressurized operation and internal methanation." *Applied Energy*, **250**, 1432 (2019).
37. M. E. Coltrin, R. J. Kee, and F. M. Rupley, "Surface CHEMKIN (Version 4. 0): A Fortran package for analyzing heterogeneous chemical kinetics at a solid-surface—gas-phase interface." *Technical Report*, **SAND-90-8003B**, 6128661 (1991), http://www.osti.gov/servlets/purl/6128661-UX6iLD/.
38. L. Maier, B. Schädel, K. Herrera Delgado, S. Tischer, and O. Deutschmann, "Steam reforming of methane over nickel: development of a multi-step surface reaction mechanism." *Topics in Catalysis*, **54**, 845 (2011).
39. V. M. Janardhanan and O. Deutschmann, "CFD analysis of a solid oxide fuel cell with internal reforming: Coupled interactions of transport, heterogeneous catalysis and electrochemical processes." *Journal of Power Sources*, **162**, 1192 (2006).
40. G. Narasimhaiah and V. M. Janardhanan, "Modeling CO_2 electrolysis in solid oxide electrolysis cell." *Journal of Solid State Electrochemistry*, **17**, 2361 (2013).
41. "Chapter 3: fuel cell reaction kinetics." *Fuel Cell Fundamentals* ch. 3, 77 (John Wiley & Sons, Ltd) (2016).
42. C. H. Wendel, Z. Gao, S. A. Barnett, and R. J. Braun, "Modeling and experimental performance of an intermediate temperature reversible solid oxide cell for high-efficiency, distributed-scale electrical energy storage." *Journal of Power Sources*, **283**, 329 (2015).
43. D. Ferrero, A. Lanzini, P. Leone, and M. Santarelli, "Reversible operation of solid oxide cells under electrolysis and fuel cell modes: Experimental study and model validation." *Chemical Engineering Journal*, **274**, 143 (2015).
44. Y. Wang, A. Banerjee, L. Wehrle, Y. Shi, N. Brandon, and O. Deutschmann, "Performance analysis of a reversible solid oxide cell system based on multi-scale hierarchical solid oxide cell modelling." *Energy Conversion and Management*, **196**, 484 (2019).
45. L. Wehrle, *Multiscale Modeling as a Tool to Optimize the Design and Performance of Solid Oxide Cells for Industrial Applications* (Karlsruher Instituts fuer Technologie (KIT)) (2023), PhD thesis.
46. H. Zhu and R. J. Kee, "Modeling distributed charge-transfer processes in SOFC membrane electrode assemblies." *J. Electrochem. Soc.*, **155**, B715 (2008).
47. A. Bertei and C. Nicolella, "A comparative study and an extended theory of percolation for random packings of rigid spheres." *Powder Technology*, **213**, 100 (2011).
48. A. Bertei and C. Nicolella, "Percolation theory in SOFC composite electrodes: effects of porosity and particle size distribution on effective properties." *Journal of Power Sources*, **196**, 9429 (2011).
49. P. Vijay, M. O. Tadé, Z. Shao, and M. Ni, "Modelling the triple phase boundary length in infiltrated SOFC electrodes." *International Journal of Hydrogen Energy*, **42**, 28836 (2017).
50. J. H. Nam and D. H. Jeon, "A comprehensive micro-scale model for transport and reaction in intermediate temperature solid oxide fuel cells." *Electrochimica Acta*, **51**, 3446 (2006).
51. P.-Y. Lanfrey, Z. Kuzeljevic, and M. Dudukovic, "Tortuosity model for fixed beds randomly packed with identical particles." *Chemical Engineering Science*, **65**, 1891 (2010).
52. R. E. Hayes, *Introduction to Catalytic Combustion* (Routledge, London) (2021).
53. P. Deuflhard, E. Hairer, and J. Zugck, "One-step and extrapolation methods for differential-algebraic systems." *Numerische Mathematik*, **51**, 501 (1987).
54. M. Mortada, H. S. Ramadan, J. Faraj, A. Faraj, H. El Hage, and M. Khaled, "Impacts of reactant flow nonuniformity on fuel cell performance and scaling-up: Comprehensive review, critical analysis and potential recommendations." *International Journal of Hydrogen Energy*, **46**, 32161 (2021).
55. Y. Wang, J. Shi, X. Gu, O. Deutschmann, Y. Shi, and N. Cai, "Toward mobility of solid oxide fuel cells." *Progress in Energy and Combustion Science*, **102**, 101141 (2024).
56. S. Tischer and O. Deutschmann, "Recent advances in numerical modeling of catalytic monolith reactors." *Catal. Today*, **105**, 407 (2005).
57. V. Menon, V. M. Janardhanan, S. Tischer, and O. Deutschmann, "A novel approach to model the transient behavior of solid-oxide fuel cell stacks." *Journal of Power Sources*, **214**, 227 (2012).
58. F. P. Incropera and D. P. DeWitt, *Fundamentals of Heat and Mass Transfer, 4th Edition* 4th ed. (Wiley, New York, NY U.A) (1996).
59. P. Von Böckh and T. Wetzel, *Wärmeübertragung: Grundlagen und Praxis* (Springer, Berlin, Heidelberg) (2014).
60. O. Furst and O. Deutschmann, "Development and calibration of a fast flow model for solid oxide cell stack internal manifolds." *Journal of Power Sources*, **613**, 234857 (2024).
61. S. D. Ebbesen, R. Knibbe, and M. Mogensen, "Co-electrolysis of steam and carbon dioxide in solid oxide cells." *J. Electrochem. Soc.*, **159**, F482 (2012).
62. V. M. Janardhanan and O. Deutschmann, "Modeling diffusion limitation in solid-oxide fuel cells." *Electrochimica Acta*, **56**, 9775 (2011).
63. J. R. Ferguson, J. M. Fiard, and R. Herbin, "Three-dimensional numerical simulation for various geometries of solid oxide fuel cells." *Journal of Power Sources*, **58**, 109 (1996).
64. W. Kiatkittipong, T. Tagawa, S. Goto, S. Assabumrungrat, and P. Praserthdam, "Oxygen transport through LSM/YSZ/LaAlO system for use of fuel cell type reactor." *Chemical Engineering Journal*, **106**, 35 (2005).
65. W. G. Bessler, "Rapid impedance modeling via potential step and current relaxation simulations." *J. Electrochem. Soc.*, **154**, B1186 (2007).
66. A. Nechache, M. Cassir, and A. Ringuedé, "Solid oxide electrolysis cell analysis by means of electrochemical impedance spectroscopy: A review." *Journal of Power Sources*, **258**, 164 (2014).
67. R. Barfod, M. Mogensen, T. Klemenso, A. Hagen, Y.-L. Liu, and P. Vang Hendriksen, "Detailed Characterization of Anode-Supported SOFCs by Impedance Spectroscopy." *J. Electrochem. Soc.*, **154**, B371 (2007).
68. R. Powell, R. Tye, and M. Hickman, "The thermal conductivity of nickel." *International Journal of Heat and Mass Transfer*, **8**, 679 (1965).
69. T. C. Allison, *NIST-JANAF Thermochemical Tables - SRD 13*, **258**, 164 (2013), Accessed 05.06.2024 https://janaf.nist.gov/.
70. M. Radovic, E. Lara-Curzio, R. M. Trejo, H. Wang, and W. D. Porter, "Thermophysical properties of YSZ and Ni-YSZ as a function of temperature and porosity.", ed. N. P. Bansal et al. *Ceramic Engineering and Science Proceedings* 79 (John Wiley & Sons, Inc., Hoboken, NJ, USA) (2008).
71. K. W. Schlichting, N. P. Padture, and P. G. Klemens, *J. Mater. Sci.*, **36**, 3003 (2001).
72. A. Esquirol, N. P. Brandon, J. A. Kilner, and M. Mogensen, "Electrochemical characterization of $La_{0.6}Sr_{0.4}Co_{0.2}Fe_{0.8}O_3$ cathodes for intermediate-temperature SOFCs." *J. Electrochem. Soc.*, **151**, A1847 (2004).
73. Y.-C. Shin, S.-ichi Hashimoto, K. Yashiro, K. Amezawa, and T. Kawada, "Thermal properties of perovskite-type oxides $La_{0.6}Sr_{0.4}Co_1$-XFex$O_{3-\delta}$ ($0 \leqslant x \leqslant 1.0$)." *ECS Trans.*, **72**, 105 (2016).
74. *VDM Crofer 22 H Data Sheet* (2021), Accessed 04.07.2024 https://www.vdm-metals.com/fileadmin/user_upload/Downloads/Data_Sheets/Data_Sheet_VDM_Crofer_22_H.pdf.
75. *PROMALIGHT: Rigid microporous insulation boards*, Accessed 04.07.2024 https://www.promat.com/en/industry/products-solutions/high-temperatureinsulation/rigid-panels/promalight/.
76. H. Bruus, *Theoretical Microfluidics* (2008), Oxford master series in physics 18 (Oxford University Press) "Oxford; New York."
77. S. Appari, V. M. Janardhanan, S. Jayanti, L. Maier, S. Tischer, and O. Deutschmann, "Micro-kinetic modeling of NH3 decomposition on Ni and its application to solid oxide fuel cells." *Chemical Engineering Science*, **66**, 5184 (2011).

APPENDIX C

Attached publication of Furst et al. [95]

Title: Modeling, optimization and comparative assessment of power-to-methane and carbon capture technologies for renewable fuel production
Journal: Applied Energy
Authors: Oscar Furst, Lukas Wehrle, Daniel Schamider, Julian Dailly, Olaf Deutschmann

Applied Energy 375 (2024) 123972

Contents lists available at ScienceDirect

Applied Energy

journal homepage: www.elsevier.com/locate/apenergy

Modeling, optimization and comparative assessment of power-to-methane and carbon capture technologies for renewable fuel production

Oscar Furst [a], Lukas Wehrle [a], Daniel Schmider [b], Julian Dailly [b], Olaf Deutschmann [a,*]

[a] Karlsruhe Institute of Technology, Kaiserstraße 12, Karlsruhe, 76131, Baden-Württemberg, Germany
[b] European Institute for Energy Research, Emmy-Noether-Straße 11, Karlsruhe, 76131, Baden-Württemberg, Germany

GRAPHICAL ABSTRACT

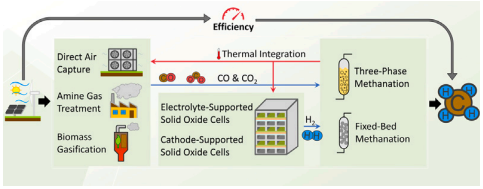

ARTICLE INFO

Keywords:
Power-to-methane
Solid oxide electrolysis cells
Catalytic methanation
Direct air capture
Amine gas treatment
Biomass gasification

ABSTRACT

Power-to-X systems which convert electrical energy into stable chemical energy carriers are a promising solution to the long-term energy storage challenge posed by the increasing market penetration of intermittent renewable power sources. In this paper, a systematic and flexible method for optimizing the steady-state operating conditions of Power-to-Methane (PtM) plant concepts is showcased and applied to perform a comparative assessment of a multitude of PtM process chains. As opposed to existing studies, a large number of comprehensive PtM system models integrating multiple carbon capture technologies and Solid Oxide Electrolysis Cell (SOEC) stacks are optimized. Using detailed 3D SOEC stack simulations and interpolation-based model reduction, the performance of electrolyte-supported (ESC) and cathode-supported cells (CSC) integrated in a variety of PtM systems with air and pure oxygen sweep gas concepts is compared. A total of 20 plant concepts using different combinations of carbon capture (biomass gasification, amine gas treatment, direct air capture) and methanation (fixed-bed, slurry bubble column) technologies are investigated using the pinch method. The results demonstrate that thermal integration of the carbon capture process in PtM systems can raise the total efficiency of the process chains by up to 10.9% for direct air capture and 10.4% for amine gas treatment, with the plants reaching high heating value efficiencies of 70.2% and 84.6% respectively. Endothermic, high temperature operation of SOECs is shown to consistently yield the highest PtM efficiencies due to the minimization of cell overpotentials and power inverter losses. Conversely, exothermic operation of SOECs thermally integrated with energy-intensive carbon capture processes is shown to significantly lower capital expenditures (CAPEX) while incurring an efficiency loss lower than 1% compared to thermoneutral operation.

* Corresponding author.
E-mail addresses: oscar.furst@kit.edu (O. Furst), lukas.wehrle@kit.edu (L. Wehrle), daniel.schmider@eifer.org (D. Schmider), dailly@eifer.org (J. Dailly), deutschmann@kit.edu (O. Deutschmann).
URL: https://www.itcp.kit.edu/deutschmann/ (O. Deutschmann).

https://doi.org/10.1016/j.apenergy.2024.123972
Received 16 October 2023; Received in revised form 10 June 2024; Accepted 19 July 2024
Available online 7 August 2024

Nomenclature

Abbreviations

3PM	Three-phase methanation
AGT	Amine gas treatment
BG	Biomass gasification
CAPEX	Capital expenditure
CC	Carbon capture
CNG	Compressed natural gas
CSC	Cathode-supported cell
DAC	Direct air capture of CO2
ESC	Electrolyte-supported cell
FBM	Fixed bed methanation
HHV	High heating value
OPEX	Operating expense
PEM	Polymer electrolyte membrane
PtM	Power to methane
RU	Repeating unit
SNG	Synthetic natural gas
SOC	Solid oxide cell
SOEC	Solid oxide electrolysis cell

Sub- and superscripts

blow	Blower
cool	Methanation unit coolant
elec	Electric
in	Inlet
meth	Methanation
out	Outlet

Physical quantities

$\dot{m}$	Mass flow rate
$\dot{V}$	Volumetric flow rate
η	Efficiency
ϕ	Sweep gas to fuel ratio
E	Voltage
i	Current density
P	Power
p	Pressure
Q	Heat
SC	Steam conversion
T	Temperature

1. Introduction

In order to mitigate global emissions of greenhouse gasses, renewable energy production grows consistently, albeit slowly, across the globe. On average, the proportion of renewable energies in the primary energy supply of OECD countries has risen by 4 percentage points (pp) between 2010 and 2020, reaching 7.9% in the USA, 9.68% in China and 15.18% in the European Union [1].

Power-to-X systems which convert electrical energy into chemical energy carriers address the lack of long-term energy storage posed by the increasing market penetration of intermittent renewable power sources and the decarbonization of hard-to-abate industrial sectors [2–4].

While electrolytic hydrogen is the cornerstone of Power-to-Gas systems, further processing into products with higher volumetric energy density, like methane (22.2 $MJ\,L^{-1}$) [5], methanol (15.6 $MJ\,L^{-1}$) [6], ammonia (11.5 $MJ\,L^{-1}$) [7] or formic acid (6.4 $MJ\,L^{-1}$) [8–10], helps to cover the needs of a broader range of end-users (energy densities referring to the liquid state). Hydrogen is also used in emergent solid-state energy storage technologies through reduction of iron oxides (40.7 $MJ\,L^{-1}$) [11,12] or direct storage in metal hydrides [13,14], but these storage methods suffer from low gravimetric energy densities.

Due to the consistent demand for natural gas [15], the existing infrastructure [16] and the emerging need for sustainable fuels in the transportation sector [17], the Power-to-Methane (PtM) process, which converts electricity into synthetic natural gas (SNG) via electrolysis, carbon capture and methanation, is a promising technology for the renewable production of a versatile compound [18]. Compared to other hydrocarbons, methane has the highest hydrogen to carbon ratio, resulting in a high volumetric energy density and low CO_2 emissions.

Owing to the low maturity of the technology, only pilot-scale PtM plants are operated, with the installed capacity totaling 47 MW_{el} worldwide as of 2019 [19]. Multiple projects demonstrating methane production through biogas upgrading were launched since 2011 [20–23]. The HELMETH project [24], which ran from 2014 to 2017, was the first to demonstrate thermal integration of pressurized Solid Oxide Electrolysis Cell (SOEC) stacks (10 kW, 15 bar) with fixed bed catalytic methanation reactors. Presupposing optimization of process conditions and heat losses, system high heating value (HHV) efficiencies were projected to reach 80%.

Lowering the cost of the produced SNG requires an improvement of the dynamic operation capability of plants, increase of the process efficiency and decrease of the electrolyzer capital expenditures (CAPEX) [25,26]. Therefore, all technologies available for the electrolysis, carbon capture and methanation processes that constitute a PtM system are under active development.

Solid Oxide Electrolysis Cells (SOECs) are in the demonstration stage (TRL7 according to the International Energy Agency in 2022) [27]. The deployment of efficient high-temperature electrolyzers with progressively higher capacities, e.g., the 720 kW unit operated by the Salzgitter AG [28] and the more recent 2.6 MW SOEC by Sunfire [29], demonstrate the growing interest in the technology. They offer an excellent electrical efficiency [30–32], which reaches 84% (based on the lower heating value (LHV) of H_2) in commercial units, producing hydrogen at 3.6 $kWh\,N\,m^{-3}$ [33], compared to 4.5 $kWh\,N\,m^{-3}$ [34] for PEM and 3.8 $kWh\,N\,m^{-3}$ [35,36] for alkaline electrolyzers. In addition, high system efficiencies can be achieved by coupling SOECs with the exothermic methanation process due to the advantageous thermal integration [37] and possibility of CO_2-electrolysis [38]. Apart from process integration, current research on SOECs has a strong focus on performance and durability improvements through the development of new and improved electrode and electrolyte materials [39].

Carbon capture (CC) technologies, which allow the separation of CO_2 from gases, are crucial components in order to reach a low-carbon economy [4,40], designed and implemented as parts of a large variety of carbon capture, utilization and storage systems [41]. The viability of the wide range of commercially available CC technologies is mostly dependent on geographical factors [42,43], which include the local presence of stationary CO_2 emitters, availability of waste heat and electricity costs. For the decarbonization of hard-to-abate industries, CO_2 can be captured from flue gases [4] with technologies such as Amine Gas Treatment (AGT), in which organic solvents like monoethanolamine (MEA) are used to absorb CO_2 to form weakly bonded chemical compounds that can be regenerated using heat [44]. For the CO_2 removal from the atmosphere, CC through the sustainable production of carbon-rich biomass is promising due to its ability to provide energy [45] and valuable industrial feedstock [4] after processing, e.g., synthesis gas obtained through biomass gasification (BG) or biogas production through anaerobic digestion [46] and subsequent pyrolysis [47]. However, the high land-use of biomass-based solutions, which compete with food production [48], leaves room for more expensive technological alternatives like Direct Air Capture (DAC) [49],

which enable the separation of CO_2 from air using physical adsorption on solid sorbent materials and later regeneration through heat and/or vacuum [50,51].

Methanation, which is a key technology in carbon capture and utilization processes [4], can be performed biologically and catalytically. Biological methanation reactors use microbial cultures to turn biogas into methane at low temperatures and have the advantage of being robust against feedstock impurities [52]. Catalytic methanation in Fixed-Bed Methanation (FBM) reactors is a well-established technology [53,54] and is now considered for the production of SNG. In order to improve the dynamic behavior of catalytic methanation reactors, alternative reactor types have been developed to address the heat management issues of FBM [55], e.g., Three-Phase Methanation (3PM) reactors [56,57] and honeycomb reactors [58].

Due to the large variety of available PtM processes [59,60] and the complex interactions between processes of thermally integrated plants, the performance and optimal design-point of plant concepts composed of selected electrolysis, methanation and CC technologies is not easily determined. PtM plant models are useful to evaluate the energetic efficiency and economic viability of plant concepts. Therefore, modeling of such plants is a dynamic research field. Several studies perform a detailed investigation of a specific plant design using multi-scale models for most system components [25,37,61,62], sometimes coupled to optimization algorithms in order to determine optimal operating conditions [38,63–66]. On the other hand, simplified modeling approaches are used by some researchers in order to perform comparative assessments between different plant concepts [67] or more complex optimization tasks, such as solving scheduling problems for the dynamic operation of plants powered by intermittent renewable energy sources [5,68–71]. In order to enable the use of multi-physics component models for computationally intensive optimization studies, Chi et al. [72,73] demonstrated the use of surrogate SOEC models calibrated on detailed simulation data.

However, such SOEC surrogate models have not yet been leveraged to include more accurate 3D stack models in PtM process optimizations. PtM system optimization studies commonly assume fixed electrolyzer operating conditions and therefore cannot study energetic trade-offs and synergies between electrolyzer and methanation reactor operating conditions [68,71,74,75]. At most, studies include simple 0D or 1D electrolyzer models [69,76] which allow the optimization of a small subset of the electrolyzer operating parameters.

Additionally, literature on integration of CC technologies into PtM systems is scarce. While the integration of PtM systems with the BG process has been studied [37,68,75,77], DAC and AGT integration has only been studied in combination with PEM electrolysis [76,78,79]. The majority of PtM system studies, especially optimizations, assume an upstream CO_2 separation process which is independent of the PtM plant and provides a stable supply of CO_2 [69–71,74,80].

In this paper, a systematic and flexible method for optimizing the steady-state operating conditions of PtM process chains is showcased. The method is based on a combination of process simulation, pinch analysis and derivative-free multivariate optimization. Process simulation is used to determine the material and energetic interactions between plant components by solving mass and energy conservation equations. Pinch analysis is used to evaluate the highest achievable efficiency of the plant concepts. Finally, multivariate optimization is used to determine the optimal operating conditions that maximize the energy efficiency of the process chains.

The selected methodology is used to conduct a comparative assessment of PtM plant concepts using SOEC stacks for hydrogen production via steam electrolysis [39]. Using multi-physics 3D SOEC stack models [81,82] built upon electrolyte-supported (ESC) and cathode-supported (CSC) cell designs, aided by interpolation-based model reduction, fully-integrated simulations of processes comprising different CC technologies (BG, AGT, DAC) and catalytic methanation technologies (FBM, 3PM) are performed.

This study aims to elucidate synergies among process components and identify energetically advantageous trade-offs by comparing optimized process chains. These insights aspire to deepen our understanding of how operating certain process components under sub-optimal conditions can enhance the overall energy balance of PtM plants. By uncovering these process interdependencies, this work can contribute to the design of plants that are more commercially viable. By optimizing energy use throughout the plant, PtM facilities can reduce their operational costs and become more competitive in the renewable energy sector.

The novelties provided by this study include the (i) systematic optimization and comparative energy assessment of a large number of PtM process chains (ii) with material and thermal integration of multiple CC technologies, notably the amine gas treatment and direct air capture processes whose thermal integration with SOECs, according to the author's best knowledge, have not been reported yet in the literature. (iii) The benefit of CC thermal integration in PtM process chains is evaluated by comparison with isolated CC and PtM processes simulated using the same methodology. (iv) Simultaneously, a detailed stack model is used to compare the performance of CSCs and ESCs, both standalone and integrated in PtM systems.

2. Methodology

The optimization of the PtM plant concepts is implemented in three abstraction layers depicted in Fig. 1: the individual plant component models, the fully integrated plant simulation and the optimization algorithm. Hereafter, these layers and their interactions are explained.

2.1. System simulation

Power-to-methane plants are built around a methanation process, which produces methane-rich SNG from CO, CO_2 and H_2. The product SNG is then dried and conditioned for storage, transport or direct use [83–85]. The structure of PtM process chains is schematically depicted in Fig. 2.

Multiple PtM system concepts are investigated in this paper, which are realized by combining the different methanation, electrolysis and carbon capture technologies listed in Table 1. Fig. 3 illustrates the process chain for a plant concept using CO_2 from AGT, the 3PM unit and using air as a sweep gas in the SOEC. Plant concepts containing the remaining technologies considered in this study can be found in Appendix A. Detailed descriptions, process diagrams and modeling methodology of all considered technologies are in Section 2.2.

In order to simulate different power-to-SNG plant concepts under various operating conditions, a flexible simulation tool was developed in Matlab. From a given set of methanation, electrolysis and carbon capture technologies, the tool produces a full plant model by selecting the necessary intermediary conditioning processes: (i) The CO_2, syngas, H_2, electrolyzer sweep gas (air or oxygen) and SNG are dried, compressed and/or expanded according to the subsystem operating conditions. (ii) The balance between steam produced through methanation reactor cooling and utilized in the electrolyzer and BG unit is computed and any deficit is compensated by an additional steam source. (iii) Additionally the SNG output of every plant concept is dried to 50 $\mathrm{mg\,N\,m^{-3}}$ H_2O, which is the requirement for compressed H-gas in Germany [86], and compressed to 200 bar, which corresponds to the pressure of CNG used in vehicles [87].

In order to quantitatively compare the performance of the different plant configurations (i.e., combinations of main process technologies and specific operating conditions), an energetic assessment of each concept is performed by means of thermal integration. The comparability of the results is ensured through the use of the pinch method [88], which enables the computation of the heating and cooling requirements of a perfectly thermally integrated plant. In this study, the hot utility is assumed to be provided by 100% efficient electrical heaters [37,65],

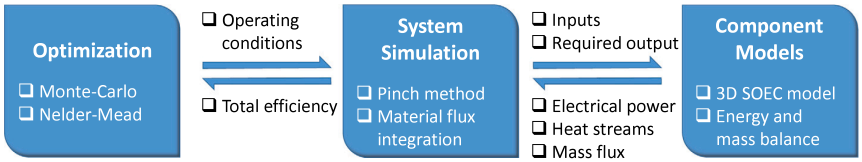

Fig. 1. Diagram of the hierarchy and relationship between the three abstraction layers of the modeling and optimization methodology.

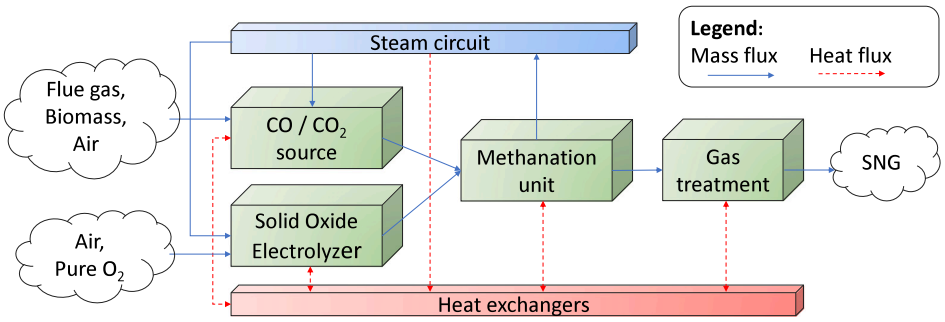

Fig. 2. Schematic representation of the main process components of thermally integrated power-to-methane plants.

Table 1
Summary of the different technologies assessed for the electrolysis, methanation and carbon capture with their respective optimization variables.

Process	Technologies	Variables	Range
Electrolysis	Cathode supported Electrolyte supported	Pressure Inlet temperature Current density Steam conversion Air-to-fuel ratio	1–20 bar 1073–1173 K (ESC) 923–1023 K (CSC) 0.3–1.2 A cm^{-2} (ESC) 0.3–1.5 A cm^{-2} (CSC) 70%–90% 1–6
Methanation	Fixed catalyst bed Slurry bubble column	Inlet temperature Pressure Coolant pressure	523–623 K 1–30 bar 1–30 bar
Carbon capture	Biomass gasification	Gasifier pressure	1 and 20 bar
	Amine gas treatment Direct air capture	No parameter with significant interactions with other process components, state-of-the-art process is used.	

while the cold utility is assumed to be available at 293 K. A minimal temperature difference between heating and cooling medium of $\Delta T_{min} = 20$ K was defined [37,89,90], which limits the size of the heat exchanger used at the pinch point.

Anghilante et al. [37] comparatively assessed system efficiencies of several Power-to-SNG bio-syngas-based plant concepts, which were either computed via the pinch method, or via a full explicit thermal integration using a functional, yet conservative heat exchanger layout. Modeled discrepancies between the two approaches were found to be below 2 pp for all cases, emphasizing that pinch analysis provides an upper, yet representative Power-to-SNG efficiency computation. Due to the congruent numerical approach, similar discrepancies are expected for the simulations performed in this work.

Following the pinch analysis, the efficiency of a plant η_{HHV} is computed through Eq. (1), which includes the HHV of the produced SNG (at least 95% CH_4, up to 2% H_2 and residual amounts of CO and C_2H_4) HHV_{SNG}, the heating requirement as computed by the pinch analysis $P_{heating}$, the electrical power consumption of all plant components $\sum P_{elec}$ and the HHV of the feedstock used in the gasification unit $HHV_{biomass}$ if present.

$$\eta_{HHV} = \frac{HHV_{SNG}}{P_{heating} + \sum P_{elec} + HHV_{biomass}} \quad (1)$$

2.2. System component models

For the system model to be able to perform the thermal integration and compute the PtM efficiency, each component model needs to produce the following set of information: temperature and enthalpy of the required heat stream $T_{cold}(Q)$, available heat stream $T_{hot}(Q)$, electrical power consumption P_{elec} and outlet properties (mole fractions X_{out}, mass flow $\dot{m}_{out}$, pressure p_{out}, temperature T_{out}). These results are functions of the inlet properties (mole fractions X_{in}, mass flow $\dot{m}_{in}$, pressure p_{in}^{SOEC}, temperature T_{in}^{SOEC}) and operating conditions found in Table 1.

In this section, all subsystem models are introduced, accompanied by process diagrams in which the cold streams and hot streams considered in the pinch analysis are depicted as heaters and coolers respectively.

2.2.1. Carbon capture

Contrary to the majority of PtM system models [25,65,71,91,92], in the present approach, the CC technology is integrated in the plant. The considered CC technologies, which supply carbon monoxide and carbon dioxide to the methanation process, are BG, AGT and DAC. This allows thermal and material integration with the other plant components, which is beneficial for all selected CC technologies: DAC and AGT require large amounts of low-temperature heat [93,94], while

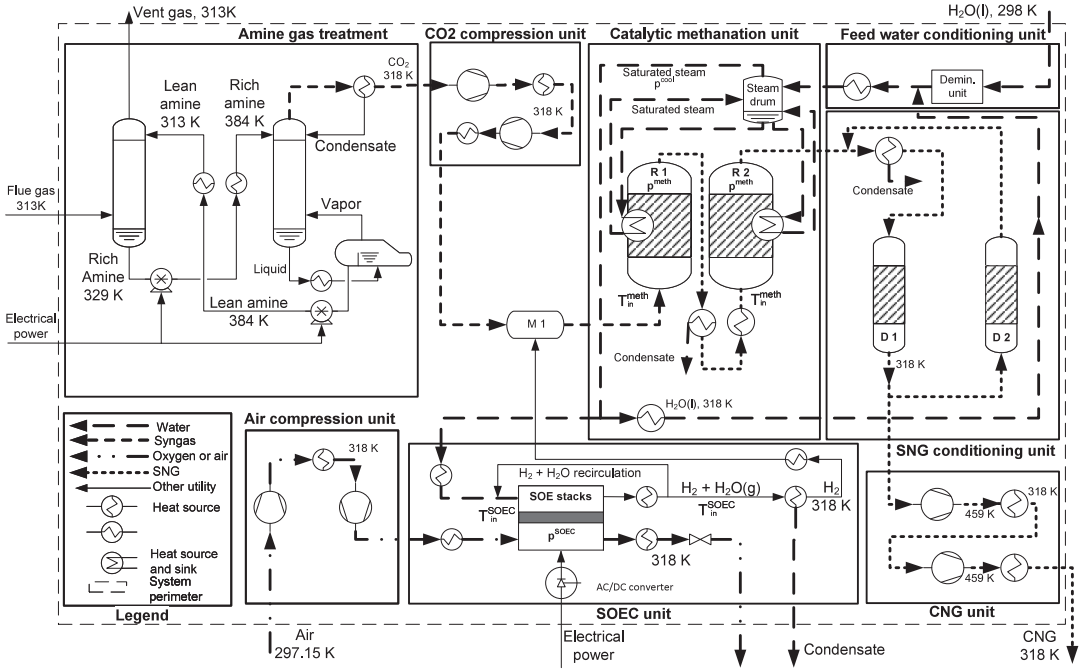

Fig. 3. Power-to-gas process chain with AGT, 3PM and without SOEC sweep gas recirculation.

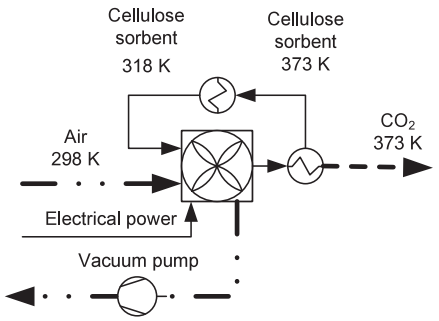

Fig. 4. Direct air capture process diagram.

autothermal BG utilizes the high-temperature oxygen produced by the electrolyzer to produce nitrogen-lean syngas [95].

Direct air capture (DAC) captures CO_2 (and approximately 0.5% water vapor [96]) from the ambient air. The chosen DAC technology, which is commercially applied by Climeworks [93], is based on the temperature-vacuum swing process using an amine-functionalized cellulose sorbent to separate CO_2 from the ambiant air. In this cyclic process, air is first circulated through the adsorbent bed until the sorbent is saturated. The sorbent bed is then evacuated. After heating up the sorbent to 373 K, the adsorbed CO_2 is released and can be isolated. In our model, the semi-batch process is implemented in a continuous form by the equivalent stationary model depicted in Fig. 4, which was designed to yield identical results to a cyclic model averaged over time.

Heat streams are computed using material properties of amine-functionalized cellulose sorbent published by Wurzbacher et al. [96] and provided in Table 2. The electricity consumption of the DAC unit was assumed to be directly proportional to the amount of CO_2 produced, at 1.8 MJ $kg^{-1}_{CO_2}$, with data released by Climeworks [93] used as reference. The same reference predicts a thermal power consumption

Table 2
Selected amine-functionalized cellulose sorbent properties [96].

Property	Unit	Value
Specific heat capacity	kJ kg^{-1} K^{-1}	$c_p^{ads} = 2.07$
CO_2 loading (48% humidity)	mol kg^{-1}	$q_{CO_2} = 1.222$
H_2O loading (48% humidity)	mol kg^{-1}	$q_{H_2O} = 3.0$
CO_2 adsorption enthalpy	kJ mol^{-1}	$\Delta H_{ads,CO_2} = 60$
H_2O adsorption enthalpy	kJ mol^{-1}	$\Delta H_{ads,H_2O} = 49$

of 5.4 MJ $kg^{-1}_{CO_2}$ for their optimized systems, matched closely by the pinch analysis of the present model which yields 5.34 MJ $kg^{-1}_{CO_2}$.

Amine gas treatment (AGT) is a technology that is used to separate CO_2 (and approximately 10% water vapor [94]) from flue gases. A piperazine activated methyldiethanolamine (45 wt.% MDEA/5 wt.% PZ) solution was chosen as CO_2 sorbent in this analysis because its CO_2 absorption reaction has a low enthalpy (≈70 kJ $mol^{-1}_{CO_2}$) and fast kinetics [94,97–99]. The component model, depicted in Fig. 5, is adapted from the detailed numerical analysis by Zhao et al. [94], which was used as reference for the process, the material properties of the solvent and the eclectic power consumption of 13.5 kJ $kg^{-1}_{CO_2}$. The study assumes a flue gas composition of 12 vol.% CO_2, 78 vol.% N_2 and 10 vol.% H_2O which corresponds to the output of a coal-fired power plant after treatment. The pinch analysis of the simplified model with ΔT_{min} = 10 K yields a minimum thermal power consumption of 2.8 MJ $kg^{-1}_{CO_2}$ compared to 3.3 MJ $kg^{-1}_{CO_2}$ (captured CO_2) in the referenced explicit thermal integration. With the pinch temperature ΔT_{min} = 20 K used herein, the predicted heat requirement is 3.7 MJ $kg^{-1}_{CO_2}$.

Trace amounts of hydrogen sulfide (H_2S) can be present in the AGT output (depending on the flue gas composition), which acts as a catalyst poison for the methanation reactor [100]. Therefore, the output is cleaned in a ZnO column, for which the gas is heated to 593 K [101].

Biomass gasification (BG) with subsequent gas cleaning and impurity separation (see Fig. 6) is a process that converts carbon-based organic materials (e.g., wood chips or straw) into a mixture consisting of H_2, CO, CO_2, CH_4 and steam (syngas).

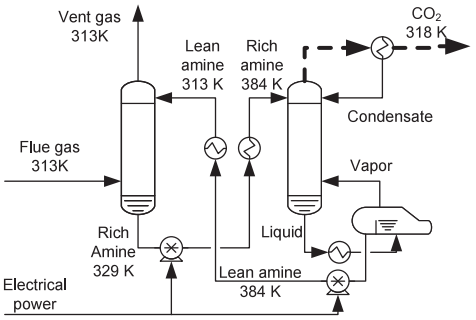

Fig. 5. Amine gas treatment process diagram.

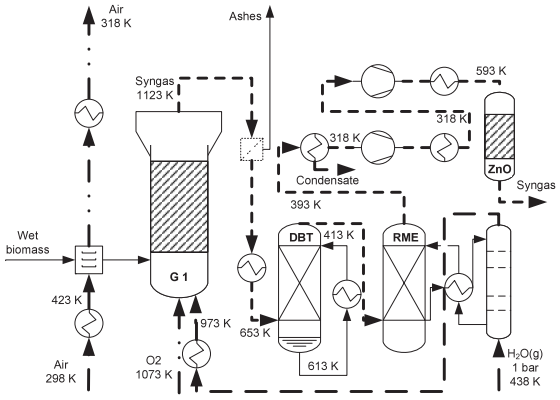

Fig. 6. Gasification process diagram.

The biomass gasification model herein is based on literature data from wood (the most widespread source of biomass on the market [102,103]) gasification experiments under autothermal conditions leading to low tar concentrations [95,104], achieved through the addition of steam (steam/carbon ratio = 1) and oxygen (equivalence ratio = 0.25). The resulting syngas composition and temperature is provided for gasification at 1 bar and 20 bar, which were treated as fixed setpoints in this study due to a lack of experimental data at intermediate pressure levels.

In the present model, the required oxygen is provided by the SOEC and a gas expander is placed between the SOEC and BG unit if the electrolysis module is operated under elevated pressure. Unless specified otherwise, the presented results were obtained with gasification at 1 bar.

For the production of syngas in a plant producing 20 MW of methane, approximately 10.5 MW (HHV) of wood is required with a power consumption of 208 kW for drying, which is congruent with the study of Anghilante et al. [37] with 10.8 MW (HHV) and 210 kW respectively.

The gasifier output contains a significant amount of contaminants, including H_2S (0.01%), tar (0.2%) and Ashes (0.04%) [105]. Therefore, the gas is treated in multiple steps. First, the ashes are removed using a filter. Then, a dibenzyltoluene (DBT) cleaning unit and rapeseed methyl ester (RME) cleaning unit remove Tar and the majority of H_2S [104]. The remaining H_2S is then removed in a ZnO column [101].

2.2.2. Catalytic methanation reactor

Catalytic methanation reactors convert CO, CO_2 and H_2 into methane and steam through the Sabatier, CO-methanation and water gas shift reactions (Eqs. (2)–(4)) in presence of a catalyst, usually Nickel [106].

$$CO_2 + 4\,H_2 \longleftrightarrow CH_4 + 2\,H_2O \qquad \Delta H_R = -165\ \mathrm{kJ\,mol^{-1}} \tag{2}$$

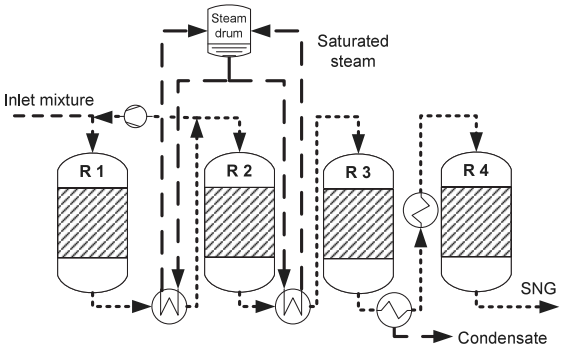

Fig. 7. Fixed-bed methanation process diagram.

$$CO + 3\,H_2 \longleftrightarrow CH_4 + H_2O \qquad \Delta H_R = -206\ \mathrm{kJ\,mol^{-1}} \tag{3}$$

$$CO + H_2O \longleftrightarrow CO_2 + H_2 \qquad \Delta H_R = -41\ \mathrm{kJ\,mol^{-1}} \tag{4}$$

Methanation reactors perform best below 823 K to favor methane formation and avoid deactivation of the catalyst by sintering and carbon formation temperatures above 673 K reduce the ethane selectivity and prevent the formation of nickel carbonyl. Further, elevated pressures improve CO and CO_2 conversion [56]. Since the methanation process is highly exothermic, reaction heat removal is crucial to the stability of the catalyst and improves the thermodynamic equilibrium of the reaction [56]. Heat can be removed effectively by cooling pipes using pressurized water as working fluid, taking advantage of two-phase heat transfer while also producing steam [104].

In order to reasonably limit the computational requirements of the system analysis, every methanation reactor is assumed to yield chemical equilibrium at its output, computed through Gibbs free energy minimization. The gas input into the methanation unit consists of a stoichiometric mixture of dried CO_2 or syngas and electrolytic H_2. For both reactor designs, the reaction heat is recovered by a steam circuit, which produces the superheated steam needed for the SOEC.

Two types of catalytic methanation reactors, and corresponding processes, are considered in this study: FBM reactors and 3PM slurry bubble column reactors.

Fixed-bed methanation (FBM) reactors, which are an established technology for carbon oxide removal in process gases [53,55], operate adiabatically and the reaction heat is removed from the product gas. The process chosen for the FBM unit, shown in Fig. 7, is analogous to the Haldor Topsoe TREMP process, consisting of four reactors with intermediate cooling and recirculation of the first reactor output [107]. Adiabatic reactor operation is assumed, whilst imposing an equivalent inlet gas temperature $T_{\mathrm{in}}^{\mathrm{meth}}$ and operating pressure $p_{\mathrm{in}}^{\mathrm{meth}}$ for all reactors, which are both set as optimization variables. Compared to experimental results of Schaaf et al. [56] on a single FBM reactor with an inlet temperature of 523 K, 20 bar and 27.7 vol.% CH_4, 33.8 vol.% H_2, 8.5 vol.% CO_2, 30.0 vol.% H_2O gas composition, which attained a CO_2 conversion of 64%, the adiabatic equilibrium model predicts a conversion of 66%.

The cooling between the first three reactors is performed by the steam circuit and returns the gas to the appropriate inlet temperature $T_{\mathrm{in}}^{\mathrm{meth}}$ with only small amounts of condensation. Before entering the last reactor, the process gas is dried by cooling to 319 K, which further increases the final methane yield. The dried gas is then reheated to $T_{\mathrm{in}}^{\mathrm{meth}}$ before entering the fourth reactor.

Three-phase methanation (3PM) reactors are filled with an inert cooling fluid, e.g., dibenzyltoluene, which allows heat removal from within the reactor and isothermal operation [55,57,108]. Both the thermodynamics and the dynamic operation capability benefit from the improved

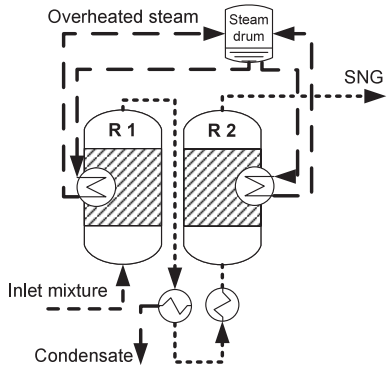

Fig. 8. Three-phase methanation process diagram.

thermal management across the reactor [109,110], which is crucial for PtM plants designed to adapt to the intermittent renewable electricity supply. The selected process, shown in Fig. 8 is composed of two reactors, with a single condensation and reheating step in between [37, 104]. In this reactor concept, the steam circuit directly recovers the reaction heat while maintaining a constant temperature T_{in}^{meth} in the reactors. Although the isothermal equilibrium model overestimates the conversion of 3PM reactors, predicting close to full CO_2 conversion at 593 K and 20 bar for a stoichiometric mixture as opposed to 82% [111], the two-step process is anticipated to achieve near-complete conversion. Due to isothermal operation, the integration of heat streams from both reactors in the pinch analysis implies minimal disparity in plant efficiency whether conversion is attained through one or two reactors.

2.2.3. Solid oxide electrolysis cell (SOEC) stacks

The SOECs used for H_2 production in the analyzed plant concepts utilize the steam produced from the methanation process, which significantly reduces the amount of heating required to operate the electrolyzer. Herein, the performance of two SOEC architectures is compared: electrolyte-supported cells (ESC) and cathode-supported cells (CSC).

In ESCs, the mechanical stability of the cell is provided by a thick electrolyte layer, which simplifies the manufacturing of the cells and provides a durable seal against gas leakage. However, the thick electrolyte increases the ohmic resistance of the cell, which is why ESCs need to operate at temperatures above 1073 K to reach acceptable area specific resistances (ASR) [112]. This cell type is nonetheless attractive for commercial applications, e.g., Sunfire and BloomEnergy electrolyzer product portfolion, due to their excellent long-term and thermal cycling stability [113,114], reducing the maintenance cost of the electrolyzers. For instance, a 30-cell ESC stack operated at $-0.5\ A\,cm^{-2}$ and 1103 K for 4000 h shows a low degradation of $0.8\%\,kh^{-1}$ [115].

CSCs, whose mechanical stability is provided by a thicker cathode, show better electrochemical performance at the cost of long-term stability [116]. They reach higher current densities at significantly lower temperatures: Riedel et al. [112] were able to operate a 10 CSC stack at up to $-1.2\ A\,cm^{-2}$ at 1023 K, while a similar 10 ESC stack only reached $-0.7\ A\,cm^{-2}$ at 1073 K. With higher current densities, fewer cells are required to produce a given amount of hydrogen, leading to reduced CAPEX.

In order to capture the influence of all five SOEC operating parameters selected for the present optimization, the electrochemical behavior of the stack needs to be modeled with sufficient detail. To ensure that all relevant physical processes are taken into consideration, the multi-scale SOC stack simulation tool [81,82] which is part of the DETCHEM [117] software package was used.

The simulation software is built around a 1D+1D cell model that comprises a plug flow model for the gas channels, a dusty gas model for

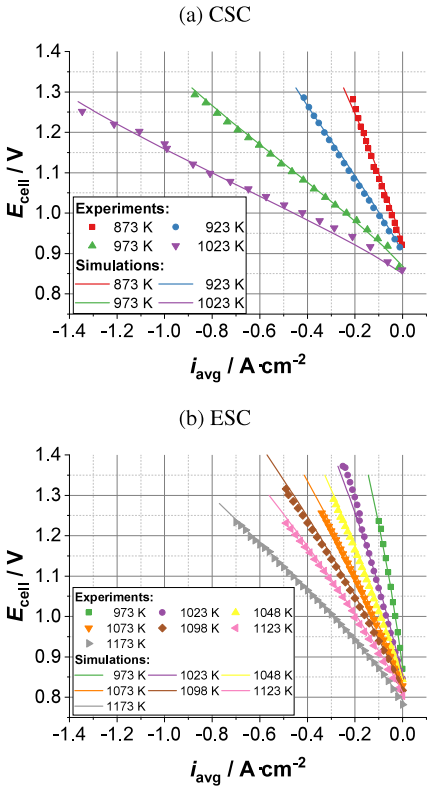

Fig. 9. Validation of the cell model via the measurement and simulation of steady-state polarization curves of 10.18 cm^2 cells for p = 1 atm, 9 : 1 H_2O to H_2 volume ratio, $\dot{V}_{air,in}$ = 114.5 N mL min^{-1} and $\dot{V}_{fuel,in}$ = 76.6 N mL min^{-1} (ESC)/$\dot{V}_{fuel,in}$ = 44.0–171.6 N mL min^{-1} (CSC). Adapted from Wehrle et al. [82]. Copyright 2022, with permission from Elsevier.

mass transport in the electrodes, a distributed charge transport model across the electrodes and electrolyte, global Butler-Volmer kinetics for the electrochemical reactions and a 2D heat transport model for the solid phase. This cell model is then used by a stack model to simulate single repeating units (RU) in the SOEC stack [81,82].

Microstructural analysis and electrochemical characterization of the CSC (provided by the commercial supplier Elcogen) and the ESC (provided by the commercial supplier Kerafol) have been performed in a previous study by Wehrle et al. [82] in order to calibrate and validate the cell models. A comparison between planar cell experimental data and simulation results is provided in Fig. 9 and shows good agreement. Based on the experimentally validated single cell models, two (CSC- and ESC-) stack models were built, comprising 150 cells each with an active area of 128 cm^2 (9 cm × 14.2 cm). The stack was assumed to be insulated with a 5 cm layer of Promalight-1000X [118] and heat loss through free convection in ambient air at 298 K was considered.

In order to perform the PtM system simulations, the required stack model outputs are the average cell voltage E_{cell}, average gas temperature at the outlet T_{out}^{SOEC} and maximum temperature gradient inside the stack ∇T_{max} as a function of the five optimization variables defined in Table 1. Thus, the in- and output interrelation can be summarized as Eqs. (5)–(7).

$$E_{cell} = f_1(i_{stack}, T_{in}^{SOEC}, p_{in}^{SOEC}, SC, \phi) \quad (5)$$

$$T_{out}^{SOEC} = f_2(i_{stack}, T_{in}^{SOEC}, p_{in}^{SOEC}, SC, \phi) \quad (6)$$

$$\nabla T_{max} = f_3(i_{stack}, T_{in}^{SOEC}, p_{in}^{SOEC}, SC, \phi) \quad (7)$$

The output of the SOEC stack model is used to calculate the electrical consumption of the stack and the heat demand or heat availability

Table 3
Varied parameters used to establish the performance maps of the SOEC stacks with a full factorial numerical experiment on the 3D stack models.

Parameter	Symbol	Unit	Values	
			CSC	ESC
Average current density	i_{stack}	A cm^{-2}	−0.3, −0.6, −0.9, −1.2, −1.5	−0.3, −0.6, −0.9, −1.2
Inlet gas temperature	T_{in}	K	923, 973, 1023	1073, 1123, 1173
Operating pressure	p	bar	1, 10, 20	1, 10, 20
Steam conversion	SC	%	70, 80, 90	70, 80, 90
Air-to-fuel ratio	ϕ	–	1, 3, 6	1, 3, 6

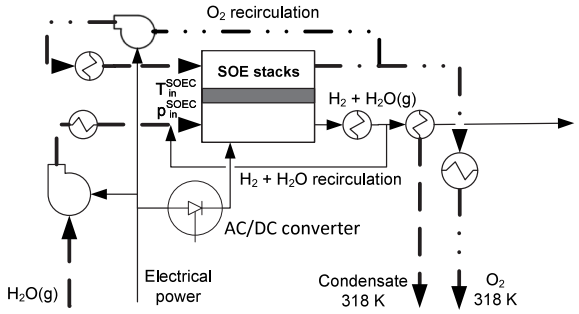

Fig. 10. Process diagram of the electrolysis units using oxygen as sweep gas.

generated by the gas flow at the output. Moreover, it is ensured that the temperature gradients inside the stack do not exceed 10 K cm^{-1} in order to limit degradation through thermal stress [119].

Since a large number of plant simulations have to be performed during an optimization, the long computation times of detailed stack simulations were circumvented by using simplified stack models implemented through multi-dimensional linear interpolation of detailed simulation results. The interpolation is performed on the results of a full factorial numerical experiment using the possible discrete variable values listed in Table 3, resulting in 1458 simulations and 3 multi-dimensional performance maps per combination of cell type and sweep gas.

The outputs of this reduced model are still functions of all the selected operating parameters, while the computation times are greatly reduced. The loss in accuracy depends on the amount of points computed, the interpolation method used and the behavior of the exact solutions to f_1, f_2 and f_3 in the region of interest. Since E_{cell} and T_{out}^{SOEC} are expected to be monotonous functions of the optimization variables inside the chosen domain [120–122], the linear interpolation method is expected to yield good approximations. However, ∇T_{max} is not a monotonous function of i_{stack} due to the transition between endothermic and exothermic operation, therefore the corresponding loss in accuracy is alleviated by the increased number of samples for the current density i_{stack}.

Ultimately, a very fast reduced stack model is obtained which accuracy is shown to be satisfactory in Section 3.1.

In the PtM plant, the electrolysis units includes multiple recirculation loops. The fuel (cathode) off-gas recycle loop regulates the inlet gas composition to 90% H_2O and 10% H_2, which is required to prevent re-oxidation of the nickel particles in the fuel electrode [123]. Thermal management of SOEC stack can be accomplished in multiple ways, including operation with air and pure oxygen as sweep gases. Feeding the stack with pure O_2 is achieved by implementing an anode off-gas recycle loop driven by a recycle blower, as depicted in Fig. 10. Full sweep gas recirculation (i) eliminates the need for sweep gas compression during pressurized operation, (ii) reduces the energy required to heat the sweep gas up to T_{in}^{SOEC} and (iii) produces pure O_2 as a byproduct, which is used in the BG unit for efficient N_2-lean syngas production [37].

For all other plant concepts, operation with air (without recirculation) is also simulated, since this simpler design better reflects the state-of-the-art.

The steam, sweep gas and recirculation blower work is computed using Eq. (8), which comprises the fan and electric motor efficiencies $\eta_{fan} = 0.8$ [124] and $\eta_{el} = 0.95$ [62], the required volumetric flow rate $\dot{V}_{blow}$ and the pressure drop Δp_{stack}.

$$P_{el,blow} = \eta_{fan} \cdot \eta_{el} \cdot \Delta p_{stack} \cdot \dot{V}_{blow} \tag{8}$$

The latter was obtained by implementing the manifold and stack flow model proposed by Koh et al. [125], which was further improved to take into account (i) the thermal volume expansion/contraction of the gases caused by temperature fluctuations across the stack and (ii) the density variation in the gas channels due to mass transport through the electrolyte.

Since a continuous current needs to be supplied to the SOEC stack, losses from a power inverter ($\eta_{AC/DC} = 96\%$) are also accounted for. The heat dissipated by the electric inverter is expected to be of low quality and is therefore not included in the pinch analysis.

2.2.4. Condensers and compressors

Because the operating pressure between system components can vary significantly, mechanical gas compression is needed at varying points in the plant. In order to reduce compression work, gases are cooled to 319 K (with condensation of excess steam) before each compression step. A maximal compression ratio of 6 was chosen, above which compression is performed in multiple steps with identical compression ratios and intermediate cooling. An isentropic compression efficiency of 75% and a mechanical efficiency of 90% was assumed in the adiabatic compressors [65]. All hot gas cooling duties resulting from compression processes are considered in the pinch analysis.

When condensation is required, e.g., downstream the methanation for product separation, the gases are cooled down to 319 K for water knock-out with a minimum allowed steam partial pressure of 0.1 bar. The cooling duties are also included in the pinch analysis.

In the SNG conditioning unit, the CH_4-rich product gas is condensed and then further dried to 50 mg$_N$ m^{-3} H_2O in a zeolite-based molecular sieve [126] (see *SNG conditioning unit* in Fig. 3) to comply with the DIN EN 16726 European standard for H-gas [86,104]. A minimal methane content of 95% and maximum hydrogen content of 2% is achieved through suitable selection of methanation process operating conditions. Finally, the SNG is compressed to 200 bar, which corresponds to the pressure used in European vehicles [87].

2.3. Optimization algorithm

The use of optimization algorithms enables a systematic, target-oriented and automatized determination of optimal operation conditions for all plant components. Specifically, setting up a systematic procedure largely facilitates the execution of a robust comparative energy assessment of different plant concepts without relying on guesses or intuition. Because some subsystems are simulated using complex external models, derivative-free constrained optimization algorithms are required.

Eight operation parameters were selected for optimization, five for the electrolyzer and three for the methanation unit (see Table 1). The

optimization was performed with the aim of maximizing the net PtM system efficiency with respect to the output HHV, as defined in Section 2.1. Additionally, the optimum was constrained by the maximum temperature gradient in the electrolyzer (10 K cm^{-1} [119]) and an SNG output suitable for use as an automotive fuel.

It was found that the solution space of the present optimization problem contains a large number of local optima, which makes the determination of the global optimum difficult. Although it is not possible to ensure that the global optimum of the optimization problem is found, the reliability of the results of the optimization methods was assessed by performing the optimizations multiple times (starting from random initial points for the deterministic optimization algorithms) while ensuring that the results are identical. A tolerance of 0.1% for the optima and 1% for the optimization variables is allowed in order to account for the convergence criterion of the optimization algorithm.

The PDFO optimizer suite [127–129] was first tested for the optimizations in this study, as it contains specialized tools for derivative-free constrained optimization. Unfortunately, the presence of local optima proved to be a hurdle for this method, as multiple optimizations started from random initial points of the parameter space yielded different optima. Therefore, the simulated annealing routine from the Matlab optimization toolbox was tested, as the algorithm is designed with the express purpose of global optimization in the presence of local optima. However, the optimizer settings required to reach reliable results led to very high computation times, with the number of computed data points approaching the millions. Recognizing that the local optima were reasonably distant from each other inspired the combination of Monte-Carlo and Nelder–Mead [130] algorithms ultimately used in this study, which allowed to reach reliable results with reasonable computation times.

The implemented method starts with a Monte Carlo optimization that samples random points in the parameter space. Such a stochastic optimization method converges toward the global optimum for an infinite number of samples, but sampling only 10 000 points was found to already provide good enough coverage of the parameter space to serve as a basis for a method that converges toward the closest local optimum. The Nelder–Mead algorithm is the gradient-free simplex optimization method chosen for this local optimization task. It was selected because it is a well-documented method that is easy to implement, and therefore to customize. The custom implementation made for this study uses the nine best (highest efficiency) sample points of the Monte-Carlo algorithm as starting points, and comprises an added penalty system that constrains the parameter space by rejecting invalid plant operating conditions. As the algorithm struggled to converge toward optima located directly at the limits of the parameter space, the Nelder–Mead algorithm was also modified to specifically consider points directly at the boundaries of the parameter space whenever the method converged toward them. The resulting algorithm converges in approximately 200 steps, resulting in a method that is much faster and, for this specific application, just as reliable as simulated annealing. The approximately 10 200 simulations required for an optimization resulted in single-core computation times of about 4 h for cases with 3PM reactors and 8 h for cases with FBM reactors. Simulations of FBM reactors are more computationally intensive because the gas composition at the inlet of the first reactor is computed iteratively due to the recirculation of the output of the first reactor. The memory requirement for these computations is minimal.

The final results reported in this study were obtained by performing each of the optimizations at least twice and never observing any significant change in the results. Although these results cannot be proven to be the global optima of the optimization problems, the flawless replication of over 50 optimizations, which always start from random samples, lends credibility to the assumption that the results represent the global optima.

Table 4
ASR of the CSC and ESC stacks for $i_{stack} = -0.3$ A cm^{-2}, $SC = 80\%$, $\phi = 1$ and fuel composition of 90% H_2O/10% H_2.

Case	CSC stack at 973 K	ESC stack at 1123 K
1 bar, O_2	0.283 Ω cm^2	0.408 Ω cm^2
1 bar, air	0.290 Ω cm^2	0.427 Ω cm^2
20 bar, O_2	0.220 Ω cm^2	0.381 Ω cm^2
20 bar, air	0.229 Ω cm^2	0.390 Ω cm^2

3. Results and discussion

3.1. SOEC stack performance maps

Exemplary slices from the interpolated performance maps of the ESC and CSC, operated with air and oxygen as sweep gases, are depicted in Fig. 11. The contour plots represent the average cell potential E_{cell} in the stack, which is inversely proportional to its electrical efficiency, as a function of the average current density i_{stack} and the gas inlet temperature T_{in}^{SOEC}. The depicted slices correspond to operation at constant inlet pressure $p_{in}^{SOEC} = 1$ bar, conversion rate $SC = 80\%$ and air-to-fuel ratio $\phi = 1$. Moreover, Fig. 12 shows simulated polarization curves for the two stack designs for $T_{in}^{SOEC} = 1023$ K (CSC)/$T_{in}^{SOEC} = 1173$ K (ESC) at $p_{in}^{SOEC} = 1$ bar and $p_{in}^{SOEC} = 20$ bar. Area-specific resistances (ASR) of both stack designs calculated at $i_{stack} = -0.3$ A cm^{-2} for varying sweep gases and absolute pressures are provided in Table 4.

As can be seen in Fig. 11, the electrical efficiency of the stack improves as the thermal energy input increases, whilst increasing current density at a fixed gas inlet temperature requires to supply a higher cell voltage due to the overpotential losses.

In the low current density regime ($i_{stack} = -0.3$ A cm^{-2}), a similar cell potential $E_{cell} \approx 1.23$ V results from the ESC stack at $T_{in}^{SOEC} = 1173$ K and the CSC stack at $T_{in}^{SOEC} = 1023$ K. Since the CSC stack is characterized by a lower ASR ($ASR_{CSC,1023\ K} = 0.290$ Ω cm^2 and $ASR_{ESC,1173\ K} = 0.427$ Ω cm^2 at 1 bar, see also Fig. 12), the performance of the ESC stack decreases further at higher current densities compared to the CSC stack. Accordingly, a higher cell potential $E_{cell} = 1.42$ V and higher inlet temperature $T_{in}^{SOEC} = 1173$ K have to be supplied to the ESC stack to match the current density $i_{stack} = 1.2$ A cm^{-2} of the CSC ($E_{cell} = 1.32$ V, $T_{in}^{SOEC} = 1023$ K).

Comparing air with oxygen as sweep gases for the stack, a slight reduction of the cell potential can be distinguished in case of air supply to the anode-side channels. The largest benefit can be observed for the ESC at high current density and low temperature, with a reduction of the cell potential of up to 20 mV.

For the selected set of operating conditions depicted in Fig. 12, the CSC achieves a lower electricity consumption than the ESC in a large part of the polarization regime. Only at very low current density and under atmospheric pressure, the ESC shows partially superior electrical efficiency than the CSC, which is due to the increased open circuit voltage (OCV) at higher temperatures. The ASR of the CSC is lower in all cases, despite a 150 K lower operating temperature. As numerically investigated by Wehrle et al. [82] and in congruence with the experimental results from Riedel et al. [112], the two cell types show an opposing behavior under pressurized operation: the efficiency of the ESC decreases under pressure, while the CSC is more efficient under pressure at higher current densities ($i_{stack} > 0.7$ A cm^{-2}) and less efficient at low current densities ($i_{stack} < 0.5$ A cm^{-2}). For both cell types, the OCV increases at higher pressures due to the pressure dependence of the Gibbs free energy of reaction [112,131]. However, the ASR generally decreases under increasing pressure, as can be observed in Table 4, which is due to the faster electrochemical kinetics and reactant density in the electrodes [82]. In the case of the CSC, in which the impact of activation and concentration overpotentials is more severe, the ASR improves significantly. For the cases listed in Table 4, pressurized operation reduces the ASR by approximately 21% for the CSC and only 8% for the ESC.

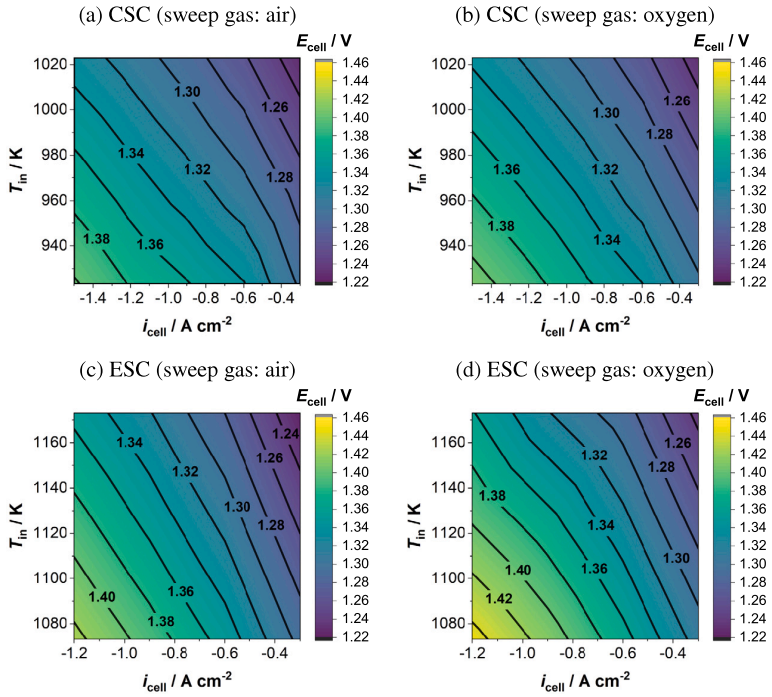

Fig. 11. Stack average cell potential as a function of gas inlet temperature and average current density for $p = 1$ bar, $SC = 80\%$, $\phi = 1$ and fuel composition of 90% H_2O/10% H_2.

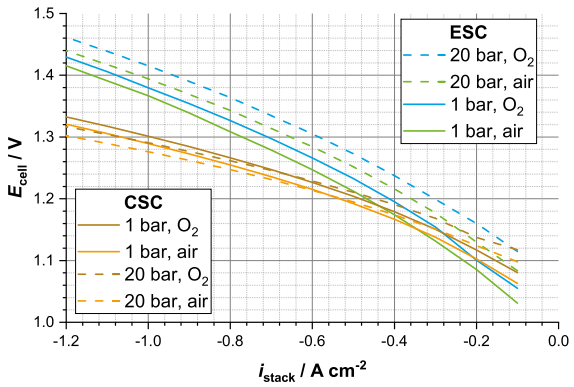

Fig. 12. Polarization curves of the CSC and ESC stacks for $SC = 80\%$, $\phi = 1$, $T_{in}^{SOEC} = 1023$ K (CSC)/$T_{in}^{SOEC} = 1173$ K (ESC) and fuel composition of 90% H_2O/10% H_2.

Table 5
Comparison of simulated and interpolated values for the air-fed CSC stack for $i_{stack} = -0.45$ A cm^{-2}, $p = 5$ bar, $T_{in}^{SOEC} = 998$ K, $SC = 75\%$ and $\phi = 2$.

Output	Unit	Simulated	Interpolated	Deviation
E_{cell}	V	1.267	1.248	1.5%
T_{out}	K	956.2	956.5	−0.031%
∇T_{max}	K cm^{-1}	5.31	4.89	7.9%

In order to estimate the accuracy of the interpolated values, an additional computation has been performed that does not correspond to a simulated point of the performance map (see Section 2.2.3). All the parameters for this simulation lie between discrete values listed in Table 3, which represents a worst-case scenario. The comparison between simulated and interpolated values is shown in Table 5 and the temperature profile of the simulated stack is depicted in Fig. 13.

While E_{cell} and T_{out} show excellent agreement, the highest deviation between simulated and interpolated values is found for ∇T_{max} with a relative deviation of 8%. Fortunately, the identified optimal process conditions (see Section 3.2) correspond to SOEC operation regimes with low temperature gradients, such that the limited accuracy in this value is not critical here.

3.2. Comparative assessment of PtM plant concepts

3.2.1. Plant concepts with oxygen-operated stacks

Table 6 lists the highest achievable PtM system efficiencies that can be reached for all plant concepts considering SOEC stacks operated with pure oxygen, alongside the respective operation parameters that minimize the system energy consumption. Fig. 14 depicts a cumulative bar chart representing the electricity consumers in the plants and their contribution to the total power requirement of the plant configurations for the production of 1 MW of SNG. A summary of the plant mass balances can be found in Appendix B, Table 12.

The CC process has the highest impact on the efficiency of the plant, with plants utilizing AGT and BG yielding higher efficiencies than DAC by approximately 10 pp.

Despite the selected BG process being autothermal, its thermal integration with the remaining plant is beneficial. In plants with BG, over 40% of the energy is provided by biomass, which significantly reduces the amount of electrolytic H_2 required. In optimized plants with both BG and CSC stacks, no electrical heating is required. Due to the lower number of SOECs required, the methanation heat is sufficient to evaporate and superheat the steam necessary for the gasification process and to operate the electrolyzer at lower steam conversion rates of $SC = 70\%$. In addition, the high temperature of the syngas stream exiting the gasification reactor ($T_{out}^{BG} = 1123$ K) can be used to heat up the SOEC inlet streams ($T_{in}^{SOEC} = 1023$ K), while the heat requirements of biomass drying and syngas cleaning can be fulfilled by lower temperature heat. When ESCs are used instead, a small amount of electrical heating is required between 1103 K and 1173 K due to their higher operating temperatures.

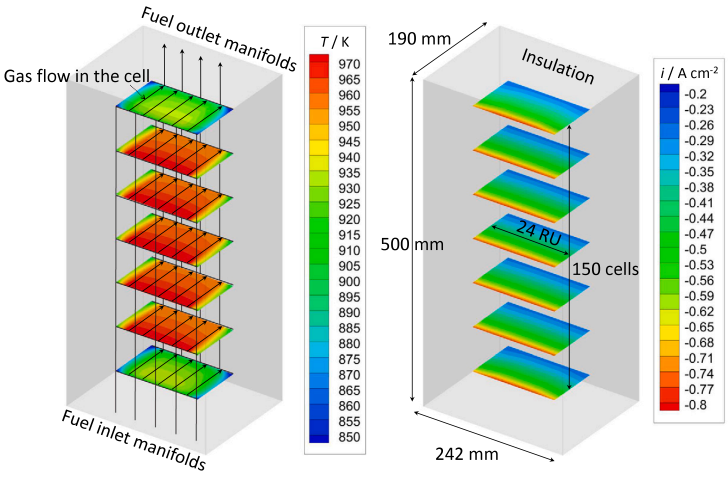

Fig. 13. Slices of the 3D solid phase temperature and current density distribution in the air-fed CSC stack active region for $i_{stack} = -0.45$ A cm^{-2}, $p = 5$ bar, $T_{in}^{SOEC} = 998$ K, $SC = 75\%$ and $\phi = 2$. The fuel gas flow, through the 5 inlet channels, 24 repeating units (RU) and 4 outlet channels is schematically depicted. Sweep gas flows in the same direction in a mirrored pattern (4 inlet channels, 5 outlet channels).

Table 6
Highest achievable efficiency and optimized operating conditions for every plant concept considered with oxygen-operated stacks.

Plant concept			Eff.	Stack					Methanation		
CO_2	Meth.	SOEC	η_{HHV} %	p bar	T_{in} K	$\lvert i_{stack}\rvert$ A cm^{-2}	SC %	ϕ –	p bar	T_{in} K	p_{cool} bar
BG	FBM	ESC	80.9	17.9	1173	0.300	70	6.0	19.9	523	21.8
		CSC	82.9	19.9	1023	0.300	70	6.0	19.9	523	21.1
	3PM	ESC	81.6	7.9	1173	0.300	70	6.0	10.0	525	20.4
		CSC	83.3	10.0	1023	0.300	70	6.0	10.0	526	17.4
AGT	FBM	ESC	81.2	4.4	1173	0.300	90	6.0	26.0	537	29.9
		CSC	81.5	5.1	1023	0.300	90	6.0	29.2	526	30.0
	3PM	ESC	84.3	2.6	1173	0.300	90	6.0	15.5	532	28.7
		CSC	84.6	19.2	1023	0.300	70	6.0	19.2	537	29.9
DAC	FBM	ESC	71.9	1.2	1173	0.300	90	6.0	27.7	535	29.9
		CSC	72.3	20.0	1023	0.300	70	6.0	21.0	523	29.9
	3PM	ESC	74.3	2.1	1173	0.300	90	6.0	12.4	531	29.4
		CSC	74.8	16.2	1023	0.300	70	6.0	16.4	549	29.7

BG: biomass gasification, AGT: amine gas treatment, DAC: direct air capture
FBM: fixed-bed methanation, 3PM: three-phase methanation
ESC: electrolyte-supported, cell CSC: cathode-supported cell.

Table 7
Highest achievable efficiency and optimized operating conditions for plant concepts with BG at 20 bar.

Plant concept			Eff.	Stack					Methanation		
CO_2	Meth.	SOEC	η_{HHV} %	p bar	T_{in} K	$\lvert i_{stack}\rvert$ A cm^{-2}	SC %	ϕ –	p bar	T_{in} K	p_{cool} bar
BG	FBM	ESC	84.9	20.0	1173	0.300	70	6.0	20.0	524	23.7
		CSC	86.8	20.0	1023	0.300	74	6.0	20.0	529	29.1
	3PM	ESC	84.9	20.0	1173	0.300	71	6.0	20.0	576	25.1
		CSC	87.0	20.0	1023	0.300	70	6.0	20.0	578	23.2

BG: biomass gasification, AGT: amine gas treatment, DAC: direct air capture
FBM: fixed-bed methanation, 3PM: three-phase methanation
ESC: electrolyte-supported, cell CSC: cathode-supported cell.

In order to investigate the system integration opportunities with pressurized BG, a set of optimizations was performed with the assumption that the BG process and the SOECs are both operated at 20 bar. Therefore, no O_2 compression is required. The results are depicted in Table 7. The corresponding mass balances can be found in Appendix B, Table 13.

Pressurized BG is highly beneficial, as the efficiencies achieved are superior by approximately 4 pp for all plant concepts. At 20 bar,

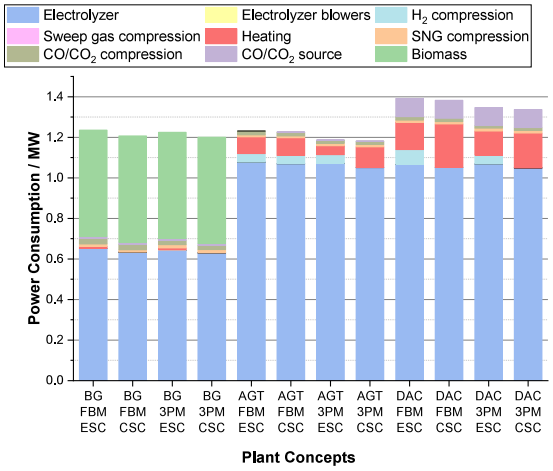

BG: biomass gasification, AGT: amine gas treatment, DAC: direct air capture, FBM: fixed-bed methanation, 3PM: three-phase methanation, ESC: electrolyte-supported, cell CSC: cathode-supported cell

Fig. 14. Breakdown of the power consumption of all sub-processes with oxygen-operated stacks for the production of 1 MW of SNG. BG: biomass gasification, AGT: amine gas treatment, DAC: direct air capture, FBM: fixed-bed methanation, 3PM: three-phase methanation, ESC: electrolyte-supported, cell CSC: cathode-supported cell.

the BG yields a much higher amount of CH_4 (16.7 vol% at 20 bar, 6.0 vol% at 1 bar) while the H_2, CO_2, CO yield drop from 35.4%, 25.5%, 21.9% at 1 bar to 28.7%, 34.0%, 18.6% at 20 bar respectively. As long as the electrolysis process is performed under pressure and with recirculated O_2 as sweep gas, pressurized BG is a net improvement, which is congruent with the observation of Anghilante et al. [37].

Plants using AGT as CC technology reach the highest efficiency. The heating duties of the CC process and H_2O evaporation are fully covered by the methanation reaction heat, while a moderate amount of electrical heating is required to heat up O_2 and steam to the SOEC inlet temperature. The power consumption of the sorbent pumps is also negligible.

Conversely, process integration of DAC increases the power consumption of the plant by up to 12% compared to the process using AGT (see Fig. 14). The majority of the power requirement of the DAC process is thermal [93,96,132], although approximately 10% of the

total plant power consumption is the electricity needed to operate the large amount of fans and vacuum pumps required for the process due to the low concentration of CO_2 in air (approximately 420 ppm [133]).

3PM yields the highest plant efficiencies in all presented cases. The reasons are twofold: (i) The product gas of the FBM is hotter, leading to a shift of the thermodynamic equilibrium toward the reactants which must be compensated with higher methanation pressures in order to reach the desired methane yield. Hence, the methanation pressure is higher in all plants including FBM reactors, leading to the increase in compression work most noticeable for the AGT plant concepts in Fig. 14. Conversely, operating the methanation units at the higher temperatures and pressures close to the SOEC leads to maximum system efficiency. (ii) Due to the higher reactant conversion, 3PM reactors produce larger amounts of heat at a lower temperature. In plant concepts with AGT or DAC, where a significant quantity of low temperature heat is needed, 3PM presents a significant advantage.

The discrepancy between both methanation processes is much smaller in plant concepts with BG because the gasification process increases the methane yield and reduces the heat requirement of the plant.

Under optimized conditions, the PtM system efficiency increases by up to 2.5% when using CSCs instead of ESCs due to the reduction of the electric power consumption of the stack. CSCs also perform well at elevated pressures, which is an advantageous mode of operation in plants using O_2 as sweep gas: pressurized operation of the SOEC reduces the total compression work required in the plant, since the output pressure of the produced H_2 matches the methanation reactor pressure more closely, and the O_2 does not need to be compressed due to the recirculation. While the maximum system efficiencies do not differ much between both cell types, the optimal operating pressure of the stack does depend on the cell design. While CSCs benefit from better performance at high pressures, ESCs should rather be operated at slightly lower pressures (see Table 6), which is a trade-off between H_2 compression work and stack performance.

The optimal steam conversion rate for a given plant configuration depends on the availability of surplus heat. For plants in which sufficient heat is available for water evaporation, operating the SOECs with a steam conversion of 70% decreases concentration overpotential losses and increases the plant efficiency (see Table 6). However, in plants with DAC and AGT units, the interactions are more complex, since the CSC are operated at lower steam conversion rates despite the need for additional heating. In these plants, the model indicates that the methanation heat is better utilized to reduce the concentration overpotential across the cells rather than minimizing electrical heating.

For every case, the optimal current density with respect to plant efficiency is at the lower boundary, $i_{stack} = -0.3\ A\,cm^{-2}$. Those conditions correspond to the endothermic operation regime at the upper boundary temperatures of 1173 K for the ESC and 1023 K for the CSC. The elevated oxygen-to-fuel ratio $\phi = 6$ maintains practical stack temperatures, which also keeps temperature gradients well below the defined limit of 10 $K\,cm^{-1}$. High gas temperatures improve the electrochemical performance of the SOECs by reducing the ASR. Endothermic, low current density operation maximizes the efficiency due to the reduction of overpotential losses and the utilization of thermal energy. Low current densities and high operating pressures also lead to lower volume flow through the stack, which minimizes blower work.

Although low current densities and high gas temperatures yield the highest plant efficiencies, these operating conditions raise CAPEX due to the higher number of SOEC stacks required to produce a given amount of SNG [134]. Further, operation at high temperatures leads to a cost enhancement of SOEC module and heating apparatus materials (interconnects, sealing, insulation, etc.) [135]. The preferred point of operation of SOEC stacks is the thermoneutral voltage because it simplifies the thermal management and system design [136]. Therefore, a similar set of optimizations was performed with electrolyzers operated under thermoneutral conditions, presented in Table 8.

Table 8
Highest achievable efficiency and optimized operating conditions for every plant concept considered with oxygen-operated stacks under thermoneutral conditions.

Plant concept			Eff.	Stack					Methanation		
CO_2	Meth.	SOEC	η_{HHV} %	p bar	T_{in} K	$\lvert i_{stack}\rvert$ A cm^{-2}	SC %	ϕ –	p bar	T_{in} K	p_{cool} bar
BG	FBM	ESC	77.9	19.9	1172	0.559	83	6.0	20.1	523	22.6
		CSC	78.4	20.0	1022	0.999	73	6.0	20.0	523	26.9
	3PM	ESC	78.1	10.0	1157	0.521	85	6.0	10.0	526	22.2
		CSC	78.6	10.0	1022	1.012	70	3.0	10.0	526	16.8
AGT	FBM	ESC	76.2	20.0	1169	0.525	90	6.0	23.7	532	30.0
		CSC	76.6	19.8	1018	0.838	90	4.4	22.7	528	29.7
	3PM	ESC	78.9	19.0	1173	0.545	90	6.0	19.0	555	30.0
		CSC	79.3	19.9	1019	0.852	90	3.9	19.9	552	29.7
DAC	FBM	ESC	68.0	19.8	1170	0.530	90	6.0	21.9	525	29.7
		CSC	68.3	20.0	1015	0.811	90	6.0	20.5	523	29.6
	3PM	ESC	70.1	19.4	1171	0.538	90	6.0	19.4	568	29.8
		CSC	70.4	18.6	1017	0.834	90	5.3	18.8	560	29.5

BG: biomass gasification, AGT: amine gas treatment, DAC: direct air capture
FBM: fixed-bed methanation, 3PM: three-phase methanation
ESC: electrolyte-supported, cell CSC: cathode-supported cell.

The average current density in the stack was selected such that the temperature T_{out}^{SOEC} of the gas output of the stack matches the temperature T_{in}^{SOEC} of the gas input, which yields average cell voltages $E_{cell,TNV}$ between 1.29 V and 1.3 V depending on the heat loss to the environment and the electric potential distribution along the height of the stack.

Enforcing thermoneutral operation causes a large reduction in achievable plant efficiency between 3 and 5 pp, which would lead to a significant increase in operating costs. In particular, plant concepts with AGT experience the largest efficiency loss since the additional heat production by the SOECs cannot be utilized as effectively as the plant concepts with DAC. The efficiency of plant concepts with BG does not change as much because of the lower amount of electrolytic H_2 produced.

As can be extracted from Table 8, under optimized conditions, CSCs reach distinctly higher current densities ($\Delta i_{stack} \approx 50\%–90\%$) at thermoneutral conditions compared to ESCs whilst operating at lower temperatures ($\Delta T_{stack} \approx 130–150$ K). In the present cases, the superior electrochemical performance of the CSC is amplified by the pressurized operating conditions leading to highest system efficiencies, similarly to the previous results.

Additionally, thermoneutral SOEC operations allows for lower air-to-fuel ratios, which enables the operation of the SOECs at slightly higher pressures in the AGT plant concepts due to the reduction of the sweep gas compression work.

3.2.2. Plant concepts with air-operated stacks

Table 9 and Fig. 15 deliver a similar overview of the results as in the previous section, but for process chains in which air is used as SOEC sweep gas instead of pure oxygen. Since oxygen is required to operate the selected biomass gasification technology, the plant concepts in this section are limited to AGT and DAC as CC technologies. A summary of the plant mass balances can be found in Appendix B, Table 14.

Despite the slight improvement in stack performance when air is used as sweep gas, as noted in Section 3.1, the absence of a sweep gas recirculation loop causes a major system performance reduction, as seen in Table 9 and shown by Wang et al. [38]. PtM efficiencies are approximately 5 pp lower for plants with AGT and approximately 4 pp lower for plants with DAC. This represents an increase of the energy consumption of up to 6.8% in the AGT 3PM ESC process chain.

Contrary to the first case, the highest efficiencies are achieved with stacks operated at atmospheric pressure, as the sweep gas compression work performed during pressurized operation with air outweighs the savings of H_2 compression work. This is congruent with the finding of

Table 9
Highest achievable efficiency and optimized operating conditions for every plant concept considered with air-operated stacks.

Plant concept			Eff.	Stack					Methanation		
CO_2	Meth.	SOEC	η_{HHV} %	p bar	T_{in} K	$\lvert i_{stack}\rvert$ A cm^{-2}	SC %	ϕ –	p bar	T_{in} K	p_{cool} bar
AGT	FBM	ESC	76.6	1.0	1172	0.300	90	3.0	29.9	533	29.4
		CSC	76.5	1.0	1023	0.300	90	3.0	29.9	531	29.6
	3PM	ESC	79.0	1.0	1173	0.300	90	3.0	29.2	590	29.8
		CSC	79.0	1.0	1023	0.302	90	3.0	28.8	581	29.8
DAC	FBM	ESC	68.2	1.0	1173	0.300	90	2.8	30.0	534	29.9
		CSC	68.2	1.0	1023	0.300	90	3.0	29.8	531	29.3
	3PM	ESC	70.2	1.0	1173	0.302	90	3.0	23.1	582	29.4
		CSC	70.2	1.0	1023	0.300	90	3.0	24.9	588	29.8

BG: biomass gasification, AGT: amine gas treatment, DAC: direct air capture
FBM: fixed-bed methanation, 3PM: three-phase methanation
ESC: electrolyte-supported, cell CSC: cathode-supported cell.

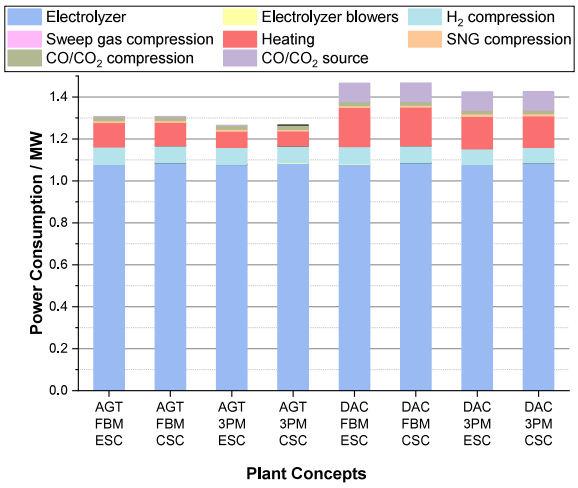

Fig. 15. Breakdown of the power consumption of all sub-processes with air-operated stacks for the production of 1 MW of SNG. BG: biomass gasification, AGT: amine gas treatment, DAC: direct air capture, FBM: fixed-bed methanation, 3PM: three-phase methanation, ESC: electrolyte-supported, cell CSC: cathode-supported cell.

Wehrle et al. [82]. With the reduced operating pressure, no difference between the efficiencies reached with CSCs and ESCs is observed. Although the electrical power consumption of ESCs is marginally lower than CSCs at −0.3 A cm^{-2}, their higher operating temperatures lead to a slight increase in heating requirements.

Due to the absence of sweep gas recirculation, additional heat is required to heat up air from the ambient temperature to T_{in}^{SOEC}, which cannot be fully covered by heat exchangers at the electrolyzer output. Therefore, lower air-to-fuel ratios of $\phi \approx 3$ are optimal in most cases, although the operating conditions are still endothermic. This additional heat requirement is also the reason why higher steam conversions of $SC \approx 90$ percent are required.

Compared to the previous section, the optimal methanation pressure is lower for all plant concepts. While reducing the compression work at the cost of a less favorable thermodynamic equilibrium is a worthwhile design choice in the first case, these plant concepts can utilize the low temperature heat generated during the compression, making higher methanation pressures more attractive.

A similar set of optimizations was performed with electrolyzers operated under thermoneutral conditions, presented in Table 10.

Table 10
Highest achievable efficiency and optimized operating conditions for every plant concept considered with air-operated stacks under thermoneutral conditions.

Plant concept			Eff.	Stack					Methanation		
CO_2	Meth.	SOEC	η_{HHV} %	p bar	T_{in} K	$\lvert i_{stack}\rvert$ A cm^{-2}	SC %	ϕ –	p bar	T_{in} K	p_{cool} bar
AGT	FBM	ESC	75.3	1.0	1173	0.715	90	1.0	29.2	533	29.7
		CSC	75.4	1.0	1023	0.868	90	1.0	29.5	531	29.7
	3PM	ESC	77.7	1.0	1173	0.716	90	1.1	26.1	570	30.0
		CSC	77.8	1.0	1021	0.857	90	1.0	26.0	572	29.4
DAC	FBM	ESC	67.2	1.0	1172	0.711	90	1.0	29.1	537	29.8
		CSC	67.3	1.0	1023	0.867	90	1.0	26.8	540	29.6
	3PM	ESC	69.1	1.0	1173	0.714	90	1.0	21.0	546	29.7
		CSC	69.3	1.0	1020	0.851	90	1.0	21.7	571	29.6

BG: biomass gasification, AGT: amine gas treatment, DAC: direct air capture
FBM: fixed-bed methanation, 3PM: three-phase methanation
ESC: electrolyte-supported, cell CSC: cathode-supported cell.

Table 11
Highest achievable efficiency for every plant concept considered with and without thermal integration of the CC process into the PtM plant.

	Plant concept			CC integration	
	CO_2	Meth.	SOEC	Yes	No
				η_{HHV} %	η_{HHV} %
Sweep gas: Oxygen	BG	FBM	ESC	80.9	80.7
			CSC	82.9	81.6
		3PM	ESC	81.6	81.3
			CSC	**83.6**	**82.0**
	AGT	FBM	ESC	81.2	75.9
			CSC	81.5	76.9
		3PM	ESC	**84.3**	**76.9**
			CSC	84.6	78.1
	DAC	FBM	ESC	71.9	67.3
			CSC	72.3	67.8
		3PM	ESC	74.3	68.2
			CSC	74.8	69.0
Sweep gas: Air	AGT	FBM	ESC	76.6	70.3
			CSC	76.5	70.0
		3PM	ESC	**79.0**	**70.8**
			CSC	79.0	70.9
	DAC	FBM	ESC	68.2	62.4
			CSC	68.2	62.4
		3PM	ESC	**70.2**	**63.3**
			CSC	**70.2**	**63.3**

BG: biomass gasification, AGT: amine gas treatment, DAC: direct air capture, FBM: fixed-bed methanation, 3PM: three-phase methanation, ESC: electrolyte-supported, cell CSC: cathode-supported cell, CC: carbon capture.

As opposed to the process chains compared in Section 3.2.1, the efficiency of the present plant concepts with thermoneutral SOEC operation (Table 9) is close to the efficiency of the same plant concepts with endothermic operation (Table 10), with a difference of up to 1 pp. This can be attributed to the higher heat requirement of these plant concepts, as illustrated in Fig. 15, in which the additional heat produced by the SOECs reduces the amount of additional electric heating required in the plant.

3.3. Comparison with PtM plants without CC integration

To evaluate the efficiency gain provided by thermal integration of CC technologies into the PtM process chains, the optimizations of the plant concepts presented in Sections 3.2.1 and 3.2.2 were repeated while thermally integrating the CC process and the remaining PtM process separately, thereby computing the efficiency of a system comprising a standalone CC plant delivering syngas or CO_2 to a PtM plant. In process chains with BG, the SOEC is still assumed to deliver O_2 to the process. The results are listed in Table 11.

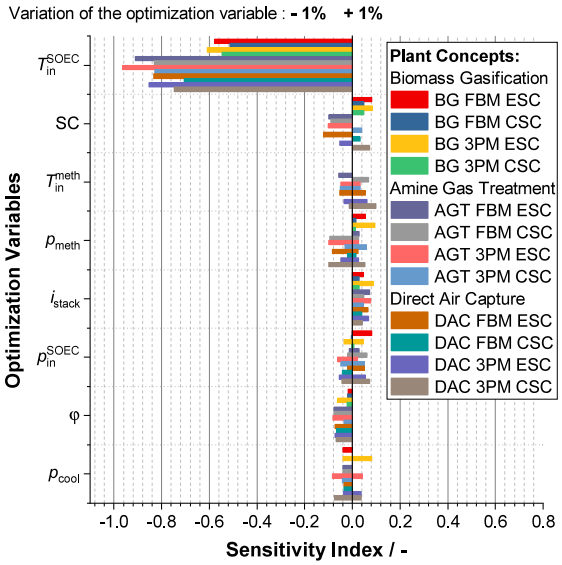

BG: biomass gasification, AGT: amine gas treatment, DAC: direct air capture, FBM: fixed-bed methanation, 3PM: three-phase methanation, ESC: electrolyte-supported, cell CSC: cathode-supported cell

Fig. 16. Tornado diagram of the impact of a variation of the optimization variables on the efficiency of plant concepts using oxygen-operated stacks. BG: biomass gasification, AGT: amine gas treatment, DAC: direct air capture, FBM: fixed-bed methanation, 3PM: three-phase methanation, ESC: electrolyte-supported, cell CSC: cathode-supported cell.

Separating the two processes has a small impact on the efficiency of the BG process chains, with the largest efficiency loss being 1.6 pp in the BG 3PM CSC plant concept. This is easily explained by the fact that the BG process is autothermal, so that thermal integration of this process into the PtM plant mainly serves to recuperate moderate amounts of high-temperature heat in order to superheat steam above the temperature provided by the methanation process. However, the main advantage of the integration of the BG process into PtM plants is that the oxygen produced as a byproduct of the electrolysis process is utilized.

Conversely, the DAC and AGT processes benefit greatly from their thermal integration into PtM plants, which raises their respective total efficiencies by as much as 10.9% and 10.4%. Since these CC processes require large amounts of heat for the desorption of CO_2, they utilize the surplus of heat produced by the methanation process effectively.

3.4. Sensitivity analysis

In order to quantitatively assess the influence of the optimization variables on the plant efficiency, a sensitivity analysis was performed on every plant concept examined in Section 3.2.1. The optimized plant configurations were used as baseline while each optimization variable was increased and reduced by 1% to compute a sensitivity index SI according to Eq. (9).

$$\mathrm{SI} = -\frac{\Delta\eta_{\mathrm{HHV}}/\eta_{\mathrm{HHV}}}{\Delta P_i/P_i} \tag{9}$$

η_{HHV} is the efficiency of the optimized plant, while $\Delta\eta_{\mathrm{HHV}}$ is the change in efficiency when the parameter i of value P is varied by ΔP. Since $\Delta\eta_{\mathrm{HHV}}$ is always negative, SI is defined so that it is positive for an increase of P and negative for a decrease of P. The results of this analysis are depicted in Fig. 16.

Because some variables have their optimal values at the edge of the range defined in Table 1, variations that would exceed this range or

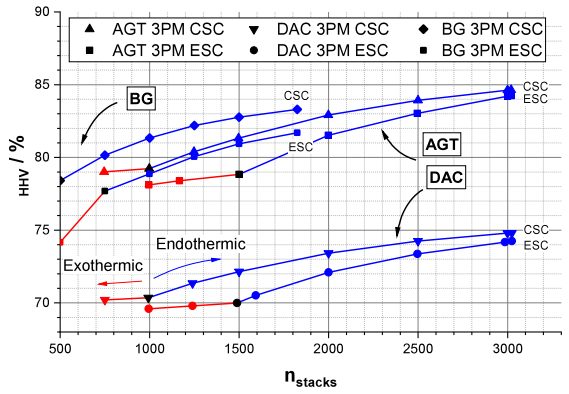

BG: biomass gasification, AGT: amine gas treatment, DAC: direct air capture, 3PM: three-phase methanation, ESC: electrolyte-supported, cell CSC: cathode-supported cell

Fig. 17. Pareto front of plant efficiency and number of SOEC stacks in 20 MW_{SNG} BG 3PM, AGT 3PM and DAC 3PM plant concepts for ESCs and CSCs with O_2 sweep. BG: biomass gasification, AGT: amine gas treatment, DAC: direct air capture, 3PM: three-phase methanation, ESC: electrolyte-supported, cell CSC: cathode-supported cell.

invalidate the constraints of the optimization (CH_4 and H_2 content, $\nabla T_{\max}$) were not performed. In cases where the SOEC pressure $p_{\mathrm{in}}^{\mathrm{SOEC}}$ would exceed the methanation pressure $p_{\mathrm{in}}^{\mathrm{meth}}$, both variables are varied simultaneously.

For every plant concept, lowering the stack inlet temperature $T_{\mathrm{in}}^{\mathrm{SOEC}}$ has the largest impact on the plant efficiency. This is related to the assumption that high temperature heat can be produced electrically at 100% efficiency [37,65], making it advantageous to supply the SOEC with higher amounts of thermal energy instead of electrical energy, which would lead to higher electric inverter losses. However, the plant efficiency has a much lower sensitivity to the current density i_{stack}, which correlates directly with the electrical energy supplied to the stack. In other words, the stack efficiency is more sensible to changes in temperature than to changes in current density. Therefore, it can be deduced that the observed sensitivity is rather a result of the increased electrochemical performance of the SOEC at elevated temperatures, where the ASR is reduced.

The sensitivity of the plant efficiency relative to the remaining optimization variables is approximately equal. In agreement with the literature [24,64], the efficiency loss observed when increasing the steam conversion SC (which leads to slight reductions in the performance of the SOECs), is of similar magnitude than the loss observed when reducing the steam conversion SC (which increases the amount of superheated steam required). This trend showcases that the efficiency of SOEC systems can be improved using residual low-temperature heat to evaporate water.

3.5. Bi-objective optimization of the plant efficiency and number of SOEC stacks

The previous sections focused entirely on maximizing the system efficiency, i.e. minimizing the electrical energy requirement (an therefore reducing OPEX) of the selected plant concepts. However, CAPEX are still a relevant part of the SNG production costs, and the capital investment is dominated by the SOEC stacks [104,134] and the CC system [137,138]. Therefore, a bi-objective optimization of the achievable efficiency and the minimal number of installed SOEC stacks for the production of 20 MW of SNG is performed and the resulting Pareto fronts are depicted in Fig. 17.

In all of the depicted plant concepts, CSCs permit to reach higher efficiencies than ESCs and can attain equivalent plant efficiencies while

reducing the amount of SOEC stacks required by up to 35% in low current density regions and 50% in high current density regions.

The use of CSCs increasingly benefits the plant efficiency when the number of stacks is reduced toward the thermoneutral point of CSCs (1000 stacks in plants with AGT and DAC, 500 stacks in the plant with BG), which corresponds to current densities of approximately $i_{stack} \approx -0.6\ A\,cm^{-2}$. Beyond this current density, endothermic operation of the CSC is not possible within the given constraints which leads to a change in slope. For ESCs, similar behavior is observed at current densities of approximately $i_{stack} \approx -0.9\ A\,cm^{-2}$.

In plants with DAC the excess heat generated by the exothermic electrolysis can be utilized effectively, leading to a plateau of $\eta_{HHV} \approx 70\%$ between thermoneutral and highly exothermic operation where the efficiency decreases by less than 0.5%. The same phenomenon is observed in the plants with AGT, with the plant efficiency dropping by no more than 1 pp while reducing the number of stacks by 33%. In plants with BG, exothermic operation leads to more significant losses due to the production of excess heat which cannot be utilized. Since the BG 3PM ESC process chain does not require a significant amount of electrical heating, the plant efficiency drops further as the SOEC performance degrades under inefficient operating conditions.

The observed trend demonstrates that in systems that can utilize heat effectively, exothermic operation of the SOECs can allow a significant reduction of the required number of stacks without significant increase of energy consumption compared to thermoneutral operation. The reduced number of stacks is expected to result in a reduction in plant CAPEX, as the only plant components that need to be adapted to the modified operating conditions are the heat exchangers at the SOEC gas outlets.

3.6. Comparison of results with existing literature

In order to validate the results of this study, the PtM efficiencies computed herein are compared to results of similar system simulation studies.

Wang et al. [64] report achieving energy efficiencies of up to 85.2% HHV in a PtM system comprising an isothermal methanation reactor ($p_{in}^{meth} = 26$ bar, $T_{in}^{meth} = 563$ K) and CSC stack ($i_{cell} = 0.34\ A\,cm^{-2}$, $p_{in}^{SOEC} = 26$ bar, $T_{in}^{SOEC} = 973$ K, $SC = 80\%$). The similar AGT 3PM CSC (air sweep) process, which was treated in Section 3.2.2, was shown to be 79.0% HHV efficient. Although this plant concept includes an AGT process, which reduces the plant efficiency significantly, the difference in efficiency of 7.3% (6.2 pp) is expected to be caused in equal measure by the power inverter losses of 4% which are accounted for in this study.

Anghilante et al. [37] compute efficiencies for three PtM plants with integrated BG. The most similar plant concept to this study is comprised of CSC stacks under thermoneutral conditions, a pressurized BG process and a methanation process comprising a 3PM reactor and a honeycomb reactor. A HHV efficiency of 81% is reported. For the comparison of results, a system simulation was performed using the BG 3PM CSC process chain with thermoneutral operation of the SOEC and the following operating conditions, which match the ones used in the Ref. [37]: $T_{in}^{SOEC} = 1023$ K, $p_{in}^{SOEC} = 20$ bar, $SC = 80\%$, $\phi = 1$, $T_{in}^{meth} = 563$ K, $p_{in}^{meth} = 20$ bar, $p_{cool} = 20$ bar. An efficiency of 82.2% is obtained. The difference can be attributed to the higher performance of the CSC in this study, which achieves a current density of $-0.958\ A\,cm^{-2}$ as compared to the $-0.8\ A\,cm^{-2}$ of the Ref. [37] at lower gas inlet temperatures (1023 K compared to 1073 K) under thermoneutral conditions. The pinch diagram produced by Anghilante et al. is compared to the process chain simulated herein in Fig. 18.

The differences in the hot stream and cold stream composite curves are due to (i) the lower temperature of the first 3PM reactor considered in this study, which results in a higher carbon utilization of 99.6% (as opposed to 97.8%) and hence a higher heat production, (ii) the honeycomb methanation process, which is not isothermal and hence

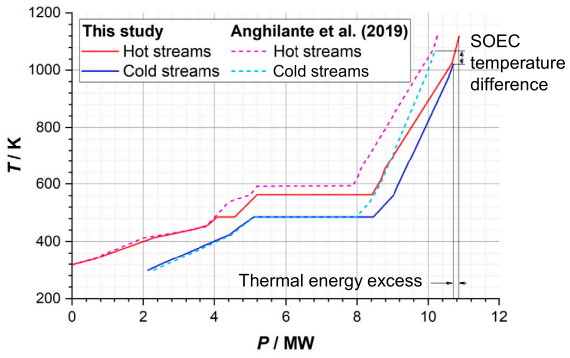

Fig. 18. Pinch diagram with the composite curves reported by Anghilante et al. compared to the similar system computed herein. Adapted from Anghilante et al. [37]. Copyright 2019, with permission from Elsevier.

results in a different slope of the hot stream composite curve before the isothermal methanation threshold and (iii) the difference in SOEC inlet temperature.

The only published data on energy efficiency of PtM plants with integrated DAC process stems from Coppitters et al. [78,139], which report a HHV energy efficiency of up to 59.5% for a system including PEM electrolyzers and a series of four adiabatic methanation reactors. Process chains with DAC units and adiabatic methanation reactors simulated herein reached HHV efficiencies ranging between 67.2% and 72.3%. The difference in efficiency is mostly due to the superior performance of SOEC, as the PEM electrolyzers are reported to constitute 93% of the power consumption of the PtM system, as opposed to approximately 77% in the similar plants considered in this study.

Even though a study considering a PtM system with integrated AGT process can be found in the literature [79], it is specific to the integration in steelmaking plants. Therefore, no direct quantitative comparison can be made to the results produced herein.

4. Conclusion

A methodology for optimizing the operating conditions of PtM plants was presented and used to comparatively assess 20 different PtM plant concepts producing SNG suitable for use as a fuel.

A multi-scale SOEC stack model was used to compare the performance of an ESC stack and a CSC stack integrated into PtM plants. Operation with two sweep gas concepts, air and pure oxygen, was considered for both stack types. Fast SOEC stack models were build from simulated performance maps of detailed 3D models (provided in the Supplementary Information). The reduced models were integrated in the system simulations and shown to lead to a small loss in accuracy compared to the full models. Furthermore, the computed system efficiencies represent an upper limit, as the thermal integration through pinch analysis does not account for heat exchanger layout and heat loss through pipes.

The system simulation results indicate that with proper thermal integration, plants using BG and AGT as CO_2 sources can reach excellent HHV efficiencies of up to 87.0% and 84.6%, respectively, while plants with DAC units achieved up to 74.8% HHV efficiency. Sweep gas recirculation was shown to increase plant efficiency by up to 6.8%, both by reducing the amount of heating required and by allowing the advantageous pressurized operation of CSCs without the need for sweep gas compression. Thermal integration of the DAC and AGT processes into PtM plants was demonstrated to increase the efficiency of the complete system by a large margin of up to 10.9% and 10.4% respectively.

Endothermic SOEC stack operation leads to the highest PtM efficiencies due to reduced overpotential losses at low current densities,

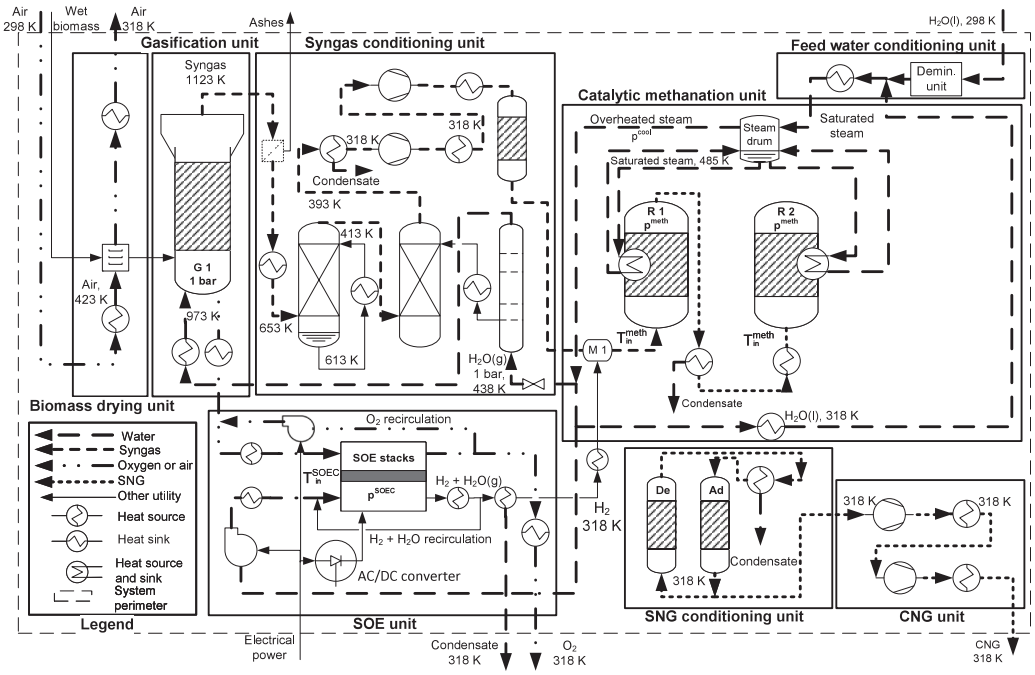

Fig. 19. PtM plant concept with BG, 3PM and sweep gas recirculation.

increased electrochemical performance at high gas temperatures, and reduced power inverter losses. Achievable system efficiencies with CSC and ESC stacks do not differ significantly, despite large differences in operating temperature ranges.

However, a Pareto optimization revealed that PtM plants with CSCs can achieve the same efficiency as plants with ESCs with half the number of SOEC stacks. Systems that effectively utilize heat were shown to benefit from a reduction in CAPEX with exothermic SOEC operation, while incurring an efficiency loss of less than 1% compared to thermoneutral operation. Considering the delicate balance between power density and degradation rate required for the commercially viable operation of SOECs, this observation warrants further investigation by means of techno-economic analysis.

The presented methodology provides valuable insights into synergistic process interactions that can be exploited to improve the system efficiency of PtM plant concepts. In particular, pressurized operation of ESC stacks resulted in higher PtM efficiencies, which is suboptimal for stand-alone operation, but advantageous at plant scale.

These results underline the significance of the present modeling and optimization approach for the design of thermally integrated PtM processes. Clearly, the methodological combination of optimization, pinch analysis and process modeling is a very powerful tool that can be easily adapted to other Power-to-X concepts.

CRediT authorship contribution statement

Oscar Furst: Writing – original draft, Validation, Software, Methodology, Investigation. **Lukas Wehrle:** Writing – review & editing, Software, Conceptualization. **Daniel Schmider:** Writing – review & editing. **Julian Dailly:** Resources. **Olaf Deutschmann:** Writing – review & editing, Supervision, Software, Funding acquisition, Conceptualization.

Declaration of competing interest

The authors declare that they have no known competing financial interests or personal relationships that could have appeared to influence the work reported in this paper.

Data availability

Data will be made available on request.

Acknowledgments

Funding

This work was supported by the German federal ministry for economic affairs and energy (Bundesministerium für Wirtschaft und Energie, BMWi) [grant numbers 03EIV041D, 03EIV041E] in the “MethFuel” group of the collaborative research project “MethQuest”. The authors acknowledge support by the state of Baden-Württembergthrough bwHPC.

Omegadot software and consulting GmbH is gratefully acknowledged for a cost-free academic license of DETCHEM.

Parts of this work have been presented at the 18th International Symposium on Solid Oxide Fuel Cells in Boston, May 28–June 2 2023 [140].

Appendix A. Full plant process diagrams

See Figs. 19 and 20.

Appendix B. System mass balance tables

See Tables 12–14.

Appendix C. Supplementary data

The performance maps of the ESC and CSC stacks, for both air and oxygen as sweep gas, are provided as supplementary tables.

Supplementary material related to this article can be found online at https://doi.org/10.1016/j.apenergy.2024.123972.

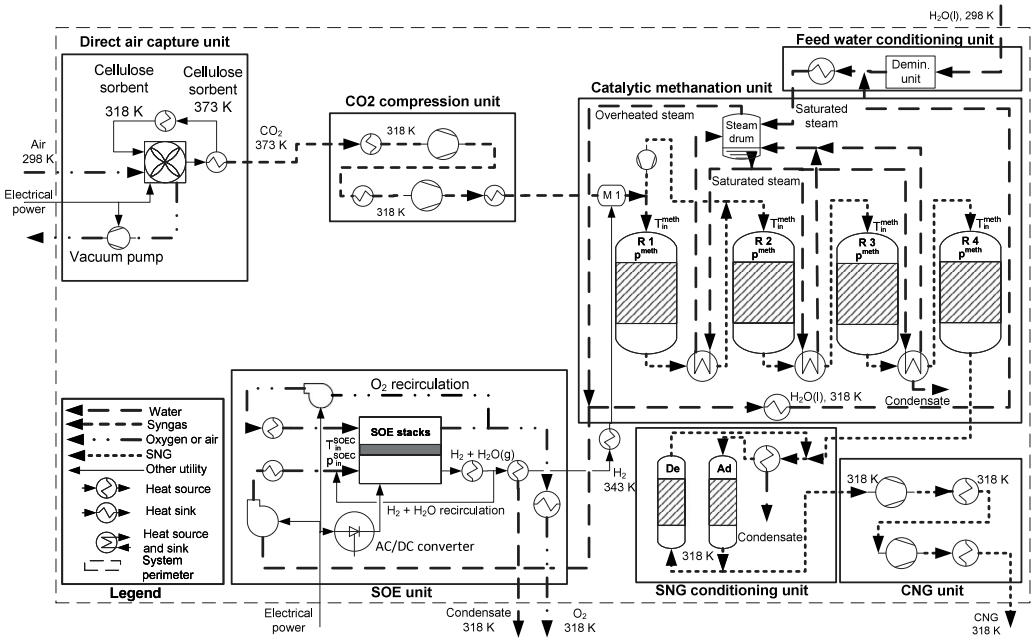

Fig. 20. PtM plant concept with DAC, FBM and sweep gas recirculation.

Table 12
Main mass streams at the inlet and outlet of the CC, SOEC and methanation units for every optimized plant concept considered with oxygen-operated stacks.

Plant concept			Carbon capture			SOEC				Methanation				
CO_2	Meth.	SOEC	$\dot{m}^{in}_{Bio.}$	$\dot{m}^{out}_{CO_2}$	$\dot{m}^{out}_{H_2O}$	$\dot{m}^{in}_{H_2O}$	$\dot{m}^{out}_{H_2}$	$\dot{m}^{out}_{H_2O}$	$\dot{m}^{out}_{O_2}$	$\dot{m}^{out}_{CH_4}$	$\dot{m}^{out}_{H_2O}$	$\dot{m}^{out}_{CO_2}$	$\dot{m}^{out}_{H_2}$	$\dot{m}^{out}_{C_2H_4}$
BG	FBM	ESC	0.569	0.454	0.073	1.346	0.110	0.363	0.702	0.360	0.252	0.006	0.001	0.000
		CSC	0.569	0.454	0.073	1.346	0.110	0.363	0.702	0.360	0.252	0.006	0.001	0.000
	3PM	ESC	0.568	0.453	0.073	1.344	0.110	0.363	0.701	0.360	0.241	0.005	0.001	0.000
		CSC	0.568	0.453	0.073	1.344	0.110	0.363	0.701	0.360	0.241	0.005	0.001	0.000
AGT	FBM	ESC	–	0.994	0.045	1.792	0.182	0.163	1.446	0.360	0.175	0.006	0.001	0.000
		CSC	–	0.993	0.045	1.789	0.182	0.164	1.444	0.360	0.146	0.004	0.001	0.000
	3PM	ESC	–	0.992	0.045	1.790	0.182	0.165	1.443	0.360	0.134	0.003	0.001	0.000
		CSC	–	0.991	0.045	2.224	0.182	0.601	1.442	0.360	0.104	0.003	0.001	0.000
DAC	FBM	ESC	–	0.994	0.002	1.790	0.182	0.163	1.446	0.360	0.160	0.005	0.001	0.000
		CSC	–	0.994	0.002	2.226	0.182	0.598	1.446	0.360	0.232	0.006	0.001	0.000
	3PM	ESC	–	0.993	0.002	1.788	0.182	0.162	1.444	0.360	0.180	0.004	0.001	0.000
		CSC	–	0.993	0.002	2.226	0.182	0.600	1.444	0.360	0.128	0.004	0.001	0.000

Table 13
Main mass streams at the inlet and outlet of the CC, SOEC and methanation units for every optimized plant concept considered with oxygen-operated stacks and 20 bar gasification.

Plant concept			Carbon capture			SOEC				Methanation				
CO_2	Meth.	SOEC	$\dot{m}^{in}_{Bio.}$	$\dot{m}^{out}_{CO_2}$	$\dot{m}^{out}_{H_2O}$	$\dot{m}^{in}_{H_2O}$	$\dot{m}^{out}_{H_2}$	$\dot{m}^{out}_{H_2O}$	$\dot{m}^{out}_{O_2}$	$\dot{m}^{out}_{CH_4}$	$\dot{m}^{out}_{H_2O}$	$\dot{m}^{out}_{CO_2}$	$\dot{m}^{out}_{H_2}$	$\dot{m}^{out}_{C_2H_4}$
BG	FBM	ESC	0.569	0.468	0.003	1.281	0.105	0.346	0.701	0.360	0.242	0.005	0.001	0.000
		CSC	0.569	0.468	0.003	1.226	0.105	0.290	0.702	0.360	0.244	0.006	0.001	0.000
	3PM	ESC	0.568	0.467	0.003	1.270	0.105	0.335	0.701	0.360	0.099	0.005	0.001	0.000
		CSC	0.568	0.468	0.003	1.281	0.105	0.346	0.701	0.360	0.100	0.005	0.001	0.000

Table 14
Main mass streams at the inlet and outlet of the CC, SOEC and methanation units for every optimized plant concept considered with air-operated stacks.

Plant concept			Carbon capture		SOEC				Methanation				
CO_2	Meth.	SOEC	$\dot{m}^{out}_{CO_2}$	$\dot{m}^{out}_{H_2O}$	$\dot{m}^{in}_{H_2O}$	$\dot{m}^{out}_{H_2}$	$\dot{m}^{out}_{H_2O}$	$\dot{m}^{out}_{O_2}$	$\dot{m}^{out}_{CH_4}$	$\dot{m}^{out}_{H_2O}$	$\dot{m}^{out}_{CO_2}$	$\dot{m}^{out}_{H_2}$	$\dot{m}^{out}_{C_2H_4}$
AGT	FBM	ESC	0.993	0.045	1.788	0.182	0.161	3.686	0.360	0.144	0.005	0.001	0.000
		CSC	0.993	0.045	1.788	0.182	0.162	3.676	0.360	0.144	0.004	0.001	0.000
	3PM	ESC	0.993	0.045	1.789	0.182	0.163	3.689	0.360	0.072	0.004	0.001	0.000
		CSC	0.992	0.045	1.788	0.182	0.162	3.690	0.360	0.071	0.004	0.001	0.000
DAC	FBM	ESC	0.993	0.002	1.788	0.182	0.161	3.542	0.360	0.144	0.005	0.001	0.000
		CSC	0.993	0.002	1.787	0.182	0.161	3.691	0.360	0.144	0.005	0.001	0.000
	3PM	ESC	0.993	0.002	1.788	0.182	0.161	3.692	0.360	0.090	0.005	0.001	0.000
		CSC	0.993	0.002	1.788	0.182	0.161	3.692	0.360	0.084	0.005	0.001	0.000

References

[1] Energy - Renewable energy - OECD data, URL https://data.oecd.org/chart/6ZhT.

[2] Varone A, Ferrari M. Power to liquid and power to gas: An option for the German Energiewende. Renew Sustain Energy Rev 2015;45:207–18. http://dx.doi.org/10.1016/j.rser.2015.01.049, URL https://www.sciencedirect.com/science/article/pii/S1364032115000593.

[3] Wulf C, Linßen J, Zapp P. Review of power-to-gas projects in Europe. Energy Procedia 2018;155:367–78. http://dx.doi.org/10.1016/j.egypro.2018.11.041, URL https://www.sciencedirect.com/science/article/pii/S1876610218309883.

[4] Shukla P, Skea J, Slade R, Al Khourdajie A, van Diemen R, McCollum D, Pathak M, Some S, Vyas P, Fradera R, Belkacemi M, Hasija A, Lisboa G, Luz S, Malley J. IPCC, 2022: Climate change 2022: Mitigation of climate change. Contribution of working group III to the sixth assessment report of the intergovernmental panel on climate change, Cambridge University Press; 2022, http://dx.doi.org/10.1017/9781009157926, URL https://www.ipcc.ch/report/sixth-assessment-report-working-group-3/.

[5] Blanco H, Nijs W, Ruf J, Faaij A. Potential of Power-to-Methane in the EU energy transition to a low carbon system using cost optimization. Appl Energy 2018;232:323–40. http://dx.doi.org/10.1016/j.apenergy.2018.08.027, URL https://www.sciencedirect.com/science/article/pii/S0306261918311826.

[6] Bos MJ, Kersten SRA, Brilman DWF. Wind power to methanol: Renewable methanol production using electricity, electrolysis of water and CO2 air capture. Appl Energy 2020;264:114672. http://dx.doi.org/10.1016/j.apenergy.2020.114672, URL https://www.sciencedirect.com/science/article/pii/S0306261920301847.

[7] Küngas R, Blennow P, Heiredal-Clausen T, Nørby TH, Rass-Hansen J, Hansen JB, Moses PG. Power-to-X activities at Haldor Topsoe: our approach for electrification of the chemicals industry. Zenodo; 2021, http://dx.doi.org/10.5281/zenodo.5115854, URL https://zenodo.org/record/5115854.

[8] Supronowicz W, A. Ignatyev I, Lolli G, Wolf A, Zhao L, Mleczko L. Formic acid: a future bridge between the power and chemical industries. Green Chem 2015;17(5):2904–11. http://dx.doi.org/10.1039/C5GC00249D, URL https://pubs.rsc.org/en/content/articlelanding/2015/gc/c5gc00249d, Publisher: Royal Society of Chemistry.

[9] Chatterjee S, Dutta I, Lum Y, Lai Z, Huang K-W. Enabling storage and utilization of low-carbon electricity: power to formic acid. Energy Environ Sci 2021;14(3):1194–246. http://dx.doi.org/10.1039/D0EE03011B, URL https://pubs.rsc.org/en/content/articlelanding/2021/ee/d0ee03011b, Publisher: Royal Society of Chemistry.

[10] Dutta I, Chatterjee S, Cheng H, Parsapur RK, Liu Z, Li Z, Ye E, Kawanami H, Low JSC, Lai Z, Loh XJ, Huang K-W. Formic acid to power towards low-carbon economy. Adv Energy Mater 2022;12(15):2103799. http://dx.doi.org/10.1002/aenm.202103799, URL https://onlinelibrary.wiley.com/doi/abs/10.1002/aenm.202103799 _eprint: https://onlinelibrary.wiley.com/doi/pdf/10.1002/aenm.202103799.

[11] Bergthorson JM. Recyclable metal fuels for clean and compact zero-carbon power. Prog Energy Combust Sci 2018;68:169–96. http://dx.doi.org/10.1016/j.pecs.2018.05.001, URL https://www.sciencedirect.com/science/article/pii/S0360128518300327.

[12] Kuhn C, Düll A, Rohlfs P, Tischer S, Börnhorst M, Deutschmann O. Iron as recyclable energy carrier: Feasibility study and kinetic analysis of iron oxide reduction. Appl Energy Combust Sci 2022;12:100096. http://dx.doi.org/10.1016/j.jaecs.2022.100096, URL https://www.sciencedirect.com/science/article/pii/S2666352X22000395.

[13] Møller KT, Sheppard D, Ravnsbæk DB, Buckley CE, Akiba E, Li H-W, Jensen TR. Complex metal hydrides for hydrogen, thermal and electrochemical energy storage. Energies 2017;10(10):1645. http://dx.doi.org/10.3390/en10101645, URL https://www.mdpi.com/1996-1073/10/10/1645 Number: 10 Publisher: Multidisciplinary Digital Publishing Institute.

[14] Düll A, Rohlfs P, Deutschmann O, Börnhorst M. Performance evaluation of KBH4 as energy carrier for shipping applications. Chem Ing Tech 2022;94(5):747–59. http://dx.doi.org/10.1002/cite.202100193, URL https://onlinelibrary.wiley.com/doi/abs/10.1002/cite.202100193 _eprint: https://onlinelibrary.wiley.com/doi/pdf/10.1002/cite.202100193.

[15] Imports of natural gas by partner country | Eurostat. 2023, URL https://ec.europa.eu/eurostat/databrowser/view/nrg_ti_gas/default/table?lang=en.

[16] System development map, URL https://www.gie.eu/publications/maps/system-development-map/.

[17] Sustainable aviation fuels, URL https://www.energy.gov/eere/bioenergy/sustainable-aviation-fuels.

[18] Sterner M, Stadler I. Energiespeicher - Bedarf, technologien, integration. Berlin, Heidelberg: Springer Berlin Heidelberg; 2014, http://dx.doi.org/10.1007/978-3-642-37380-0, URL http://link.springer.com/10.1007/978-3-642-37380-0.

[19] Thema M, Bauer F, Sterner M. Power-to-Gas: Electrolysis and methanation status review. Renew Sustain Energy Rev 2019;112:775–87. http://dx.doi.org/10.1016/j.rser.2019.06.030, URL https://www.sciencedirect.com/science/article/pii/S136403211930423X.

[20] Martin MR, Fornero JJ, Stark R, Mets L, Angenent LT. A single-culture bioprocess of *methanothermobacter thermautotrophicus* to upgrade digester biogas by CO_2-to-CH_4 conversion with H_2. Archaea 2013;2013:e157529. http://dx.doi.org/10.1155/2013/157529, URL https://www.hindawi.com/journals/archaea/2013/157529/, Publisher: Hindawi.

[21] Bailera M, Lisbona P, Romeo LM, Espatolero S. Power to Gas projects review: Lab, pilot and demo plants for storing renewable energy and CO2. Renew Sustain Energy Rev 2017;69:292–312. http://dx.doi.org/10.1016/j.rser.2016.11.130, URL https://www.sciencedirect.com/science/article/pii/S1364032116307833.

[22] Carmeuse, ENGIE and John Cockerill join forces to reduce industrial CO2 emissions in Wallonia. 2020, URL https://www.carmeuse.com/eu-en/newsroom/global/carmeuse-engie-and-john-cockerill-join-forces-reduce-industrial-co2-emissions.

[23] Review EI. Electrochaea and the European innovation council accelerate rollout of biological methanation technology. 2021, URL https://energyindustryreview.com/power/electrochaea-and-the-european-innovation-council-accelerate-rollout-of-biological-methanation-technology/.

[24] Gruber M, Weinbrecht P, Biffar L, Harth S, Trimis D, Brabandt J, Posdziech O, Blumentritt R. Power-to-Gas through thermal integration of high-temperature steam electrolysis and carbon dioxide methanation - Experimental results. Fuel Process Technol 2018;181:61–74. http://dx.doi.org/10.1016/j.fuproc.2018.09.003, URL https://www.sciencedirect.com/science/article/pii/S037838201831155X.

[25] Becker WL, Penev M, Braun RJ. Production of synthetic natural gas from carbon dioxide and renewably generated hydrogen: A techno-economic analysis of a power-to-gas strategy. J Energy Resour Technol 2018;141(2). http://dx.doi.org/10.1115/1.4041381.

[26] Guilera J, Ramon Morante J, Andreu T. Economic viability of SNG production from power and CO2. Energy Convers Manage 2018;162:218–24. http://dx.doi.org/10.1016/j.enconman.2018.02.037, URL https://www.sciencedirect.com/science/article/pii/S019689041830147X.

[27] Electrolysers – analysis, URL https://www.iea.org/reports/electrolysers.

[28] GrInHy2.0 - green industrial hydrogen via steam electrolysis. 2022, URL https://www.green-industrial-hydrogen.com/.

[29] Sunfire. Renewable Hydrogen Project "MultiPLHY": World's largest high-temperature electrolyzer from sunfire successfully installed. 2023, URL https://www.sunfire.de/en/news/detail/renewable-hydrogen-project-multiplhy-worlds-largest-high-temperature-electrolyzer-from-sunfire-successfully-installed. [Accessed 24 April 2023].

[30] Brisse A, Schefold J, Zahid M. High temperature water electrolysis in solid oxide cells. Int J Hydrog Energy 2008;33(20):5375–82. http://dx.doi.org/10.1016/j.ijhydene.2008.07.120, URL https://www.sciencedirect.com/science/article/pii/S0360319908008355.

[31] Mogensen MB. Thermodynamics of high temperature H2O and CO2 electrolysis. 2020, 4887975. http://dx.doi.org/10.6084/M9.FIGSHARE.12652322.V1, URL https://figshare.com/articles/Thermodynamics_of_high_temperature_H2O_and_CO2_electrolysis/12652322/1, BytesArtwork Size: 4887975 Bytes Publisher: figshare.

[32] Sunfire - World's largest high-temperature electrolyzer achieves record efficiency, URL https://www.sunfire.de/en/news/detail/worlds-largest-high-temperature-electrolyzer-achieves-record-efficiency.

[33] SUNFIRE-HYLINK SOEC, URL https://www.sunfire.de/files/sunfire/images/content/Sunfire.de%20(neu)/Sunfire-Factsheet-HyLink-SOEC-20210303.pdf.

[34] Nel - PEM electrolyser. 2018, URL https://nelhydrogen.com/product/m-series-3/.

[35] Nel - atmospheric alkaline electrolyser. 2018, URL https://nelhydrogen.com/product/atmospheric-alkaline-electrolyser-a-series/.

[36] Buttler A, Spliethoff H. Current status of water electrolysis for energy storage, grid balancing and sector coupling via power-to-gas and power-to-liquids: A review. Renew Sustain Energy Rev 2018;82:2440–54. http://dx.doi.org/10.1016/j.rser.2017.09.003, URL https://linkinghub.elsevier.com/retrieve/pii/S136403211731242X.

[37] Anghilante R, Müller C, Schmid M, Colomar D, Ortloff F, Spörl R, Brisse A, Graf F. Innovative power-to-gas plant concepts for upgrading of gasification biosyngas through steam electrolysis and catalytic methanation. Energy Convers Manage 2019;183:462–73. http://dx.doi.org/10.1016/j.enconman.2018.12.101, URL https://linkinghub.elsevier.com/retrieve/pii/S0196890419300172.

[38] Wang L, Pérez-Fortes M, Madi H, Diethelm S, herle JV, Maréchal F. Optimal design of solid-oxide electrolyzer based power-to-methane systems: A comprehensive comparison between steam electrolysis and co-electrolysis. Appl Energy 2018;211:1060–79. http://dx.doi.org/10.1016/j.apenergy.2017.11.050, Publisher: Elsevier Ltd.

[39] Hauch A, Küngas R, Blennow P, Hansen AB, Hansen JB, Mathiesen BV, Mogensen MB. Recent advances in solid oxide cell technology for electrolysis. Science 2020;370(6513):eaba6118. http://dx.doi.org/10.1126/science.aba6118, URL https://www.science.org/doi/full/10.1126/science.aba6118, Publisher: American Association for the Advancement of Science.

[40] Metz B, Davidson O, de Coninck H, Loos M, Meyer L. IPCC special report on carbon dioxide capture and storage. Tech. rep., Intergovernmental Panel on Climate Change; 2005.

[41] Nagireddi S, Agarwal JR, Vedapuri D. Carbon dioxide capture, utilization, and sequestration: Current status, challenges, and future prospects for global decarbonization. ACS Eng Au 2024;4(1):22–48. http://dx.doi.org/10.1021/acsengineeringau.3c00049, URL https://pubs.acs.org/doi/10.1021/acsengineeringau.3c00049.

[42] Leonzio G, Zondervan E. Analysis and optimization of carbon supply chains integrated to a power to gas process in Italy. J Clean Prod 2020;269:122172. http://dx.doi.org/10.1016/j.jclepro.2020.122172, URL https://linkinghub.elsevier.com/retrieve/pii/S0959652620322198.

[43] Lux B, Gegenheimer J, Franke K, Sensfuß F, Pfluger B. Supply curves of electricity-based gaseous fuels in the MENA region. Comput Ind Eng 2021;162:107647. http://dx.doi.org/10.1016/j.cie.2021.107647, URL https://www.sciencedirect.com/science/article/pii/S0360835221005519.

[44] Wang M, Lawal A, Stephenson P, Sidders J, Ramshaw C. Post-combustion CO2 capture with chemical absorption: A state-of-the-art review. Chem Eng Res Des 2011;89(9):1609–24. http://dx.doi.org/10.1016/j.cherd.2010.11.005, URL https://linkinghub.elsevier.com/retrieve/pii/S0263876210003345.

[45] Bioenergy with carbon capture and storage – analysis, URL https://www.iea.org/reports/bioenergy-with-carbon-capture-and-storage.

[46] Khan MU, Lee JTE, Bashir MA, Dissanayake PD, Ok YS, Tong YW, Shariati MA, Wu S, Ahring BK. Current status of biogas upgrading for direct biomethane use: A review. Renew Sustain Energy Rev 2021;149:111343. http://dx.doi.org/10.1016/j.rser.2021.111343, URL https://www.sciencedirect.com/science/article/pii/S1364032121006298.

[47] Çelik A, Othman IB, Müller H, Lott P, Deutschmann O. Pyrolysis of biogas for carbon capture and carbon dioxide-free production of hydrogen. React Chem Eng 2023. http://dx.doi.org/10.1039/D3RE00360D, URL https://pubs.rsc.org/en/content/articlelanding/2023/re/d3re00360d, Publisher: Royal Society of Chemistry.

[48] Lovett AA, Sünnenberg GM, Richter GM, Dailey AG, Riche AB, Karp A. Land use implications of increased biomass production identified by GIS-based suitability and yield mapping for miscanthus in England. BioEnergy Res 2009;2(1):17–28. http://dx.doi.org/10.1007/s12155-008-9030-x.

[49] de Coninck H, Revi A, Babiker M, Bertoldi P, Buckeridge M, Cartwright A, Dong W, Ford J, Fuss J, Hourcade J-C, Ley D, Mechler R, Newmann P, Revokatowa A, Schultz S, Steg L, Sugiyama T. Strengthening and implementing the global response. In: Global warming of 1.5° c. an IPCC special report on the impacts of global warming of 1.5° c above pre-industrial levels and related global greenhouse gas emission pathways, in the context of strengthening the global response to the threat of climate change, sustainable development, and efforts to eradicate poverty. 2018, URL https://www.ipcc.ch/sr15/chapter/chapter-4/.

[50] Wurzbacher J. Capturing CO2 from air. In: Liebl J, Beidl C, editors. Internationaler motorenkongress 2017. Wiesbaden: Springer Fachmedien Wiesbaden; 2017, p. 499–511. http://dx.doi.org/10.1007/978-3-658-17109-4_32, URL http://link.springer.com/10.1007/978-3-658-17109-4_32, Series Title: Proceedings.

[51] McQueen N, Gomes KV, McCormick C, Blumanthal K, Pisciotta M, Wilcox J. A review of direct air capture (DAC): scaling up commercial technologies and innovating for the future. Prog Energy 2021;3(3):032001. http://dx.doi.org/10.1088/2516-1083/abf1ce, URL https://iopscience.iop.org/article/10.1088/2516-1083/abf1ce.

[52] Bellini R, Bassani I, Vizzarro A, Azim AA, Vasile NS, Pirri CF, Verga F, Menin B. Biological aspects, advancements and techno-economical evaluation of biological methanation for the recycling and valorization of CO2. Energies 2022;15(11):4064. http://dx.doi.org/10.3390/en15114064, URL https://www.mdpi.com/1996-1073/15/11/4064, Number: 11 Publisher: Multidisciplinary Digital Publishing Institute.

[53] Rehmat A, Randhava SS. Selective methanation of carbon monoxide. Prod RD 1970;9(4):512–5. http://dx.doi.org/10.1021/i360036a009, Publisher: American Chemical Society.

[54] Schmider D, Maier L, Deutschmann O. Reaction kinetics of CO and CO2 methanation over nickel. Ind Eng Chem Res 2021;60(16):5792–805. http://dx.doi.org/10.1021/acs.iecr.1c00389, Publisher: American Chemical Society.

[55] Rönsch S, Schneider J, Matthischke S, Schlüter M, Götz M, Lefebvre J, Prabhakaran P, Bajohr S. Review on methanation – From fundamentals to current projects. Fuel 2016;166:276–96. http://dx.doi.org/10.1016/j.fuel.2015.10.111, URL https://www.sciencedirect.com/science/article/pii/S0016236115011254.

[56] Schaaf T, Grünig J, Schuster MR, Rothenfluh T, Orth A. Methanation of CO2 - storage of renewable energy in a gas distribution system. Energy Sustain Soc 2014;4(1):2. http://dx.doi.org/10.1186/s13705-014-0029-1.

[57] Lefebvre J. Three-phase CO2 methanation: methanation reaction kinetics and transient behavior of a slurry bubble column reactor (Ph.D. thesis), München: Verlag Dr. Hut; 2019.

[58] Schollenberger D, Bajohr S, Gruber M, Reimert R, Kolb T. Scale-Up of innovative honeycomb reactors for power-to-gas applications – The project store&go. Chem Ing Tech 2018;90(5):696–702. http://dx.doi.org/10.1002/cite.201700139, URL https://onlinelibrary.wiley.com/doi/abs/10.1002/cite.201700139, _eprint: https://onlinelibrary.wiley.com/doi/pdf/10.1002/cite.201700139.

[59] Ghaib K, Ben-Fares F-Z. Power-to-Methane: A state-of-the-art review. Renew Sustain Energy Rev 2018;81:433–46. http://dx.doi.org/10.1016/j.rser.2017.08.004, URL https://linkinghub.elsevier.com/retrieve/pii/S1364032117311346.

[60] Hidalgo D, Martín-Marroquín J. Power-to-methane, coupling CO2 capture with fuel production: An overview. Renew Sustain Energy Rev 2020;132:110057. http://dx.doi.org/10.1016/j.rser.2020.110057, URL https://linkinghub.elsevier.com/retrieve/pii/S1364032120303488.

[61] Wendel CH, Kazempoor P, Braun RJ. Novel electrical energy storage system based on reversible solid oxide cells: System design and operating conditions. J Power Sources 2015;276:133–44. http://dx.doi.org/10.1016/j.jpowsour.2014.10.205, URL https://www.sciencedirect.com/science/article/pii/S0378775314018242.

[62] Reznicek E, Braun RJ. Techno-economic and off-design analysis of stand-alone, distributed-scale reversible solid oxide cell energy storage systems. Energy Convers Manage 2018;175:263–77. http://dx.doi.org/10.1016/j.enconman.2018.08.087, URL https://linkinghub.elsevier.com/retrieve/pii/S019689041830952X.

[63] Jeanmonod G, Wang L, Diethelm S, Maréchal F, Van herle J. Trade-off designs of power-to-methane systems via solid-oxide electrolyzer and the application to biogas upgrading. Appl Energy 2019;247:572–81. http://dx.doi.org/10.1016/j.apenergy.2019.04.055, URL https://www.sciencedirect.com/science/article/pii/S0306261919307020.

[64] Wang L, Düll J, Maréchal F, Van herle J. Trade-off designs and comparative exergy evaluation of solid-oxide electrolyzer based power-to-methane plants. Int J Hydrog Energy 2019;44(19):9529–43. http://dx.doi.org/10.1016/j.ijhydene.2018.11.151, URL https://www.sciencedirect.com/science/article/pii/S0360319918337832.

[65] Wang L, Rao M, Diethelm S, Lin TE, Zhang H, Hagen A, Maréchal F, Van herle J. Power-to-methane via co-electrolysis of H2O and CO2: The effects of pressurized operation and internal methanation. Appl Energy 2019;250:1432–45. http://dx.doi.org/10.1016/j.apenergy.2019.05.098, Publisher: Elsevier Ltd.

[66] Jalili M, Ghazanfari Holagh S, Chitsaz A, Song J, Markides CN. Electrolyzer cell-methanation/Sabatier reactors integration for power-to-gas energy storage: Thermo-economic analysis and multi-objective optimization. Appl Energy 2023;329:120268. http://dx.doi.org/10.1016/j.apenergy.2022.120268, URL https://www.sciencedirect.com/science/article/pii/S0306261922015252.

[67] Uebbing J, Rihko-Struckmann L, Sager S, Sundmacher K. CO2 methanation process synthesis by superstructure optimization. J CO2 Util 2020;40:101228. http://dx.doi.org/10.1016/j.jcou.2020.101228, URL https://www.sciencedirect.com/science/article/pii/S221298202030278X.

[68] Gassner M, Maréchal F. Thermo-economic optimisation of the integration of electrolysis in synthetic natural gas production from wood. Energy 2008;33(2):189–98. http://dx.doi.org/10.1016/j.energy.2007.09.010, URL https://www.sciencedirect.com/science/article/pii/S0360544207001764.

[69] Safari F, Dincer I. Assessment and optimization of an integrated wind power system for hydrogen and methane production. Energy Convers Manage 2018;177:693–703. http://dx.doi.org/10.1016/j.enconman.2018.09.071, URL https://www.sciencedirect.com/science/article/pii/S0196890418310744.

[70] Gorre J, Ortloff F, van Leeuwen C. Production costs for synthetic methane in 2030 and 2050 of an optimized Power-to-Gas plant with intermediate hydrogen storage. Appl Energy 2019;253:113594. http://dx.doi.org/10.1016/j.apenergy.2019.113594, URL https://www.sciencedirect.com/science/article/pii/S0306261919312681.

[71] Morgenthaler S, Ball C, Koj JC, Kuckshinrichs W, Witthaut D. Site-dependent levelized cost assessment for fully renewable Power-to-Methane systems. Energy Convers Manage 2020;223:113150. http://dx.doi.org/10.1016/j.enconman.2020.113150, URL https://linkinghub.elsevier.com/retrieve/pii/S0196890420306944.

[72] Chi Y, Hu Q, Lin J, Qiu Y, Mu S, Li W, Song Y. Numerical simulation acceleration of flat-chip solid oxide cell stacks by data-driven surrogate cell submodels. J Power Sources 2023;553:232255. http://dx.doi.org/10.1016/j.jpowsour.2022.232255, URL https://www.sciencedirect.com/science/article/pii/S0378775322012320.

[73] Chi Y, Yokoo K, Nakajima H, Ito K, Lin J, Song Y. Optimizing the homogeneity and efficiency of a solid oxide electrolysis cell based on multiphysics simulation and data-driven surrogate model. J Power Sources 2023;562:232760. http://dx.doi.org/10.1016/j.jpowsour.2023.232760, URL https://www.sciencedirect.com/science/article/pii/S0378775323001350.

[74] Qi M, Lee J, Hong S, Kim J, Liu Y, Park J, Moon I. Flexible and efficient renewable-power-to-methane concept enabled by liquid CO2 energy storage: Optimization with power allocation and storage sizing. Energy 2022;256:124583. http://dx.doi.org/10.1016/j.energy.2022.124583, URL https://www.sciencedirect.com/science/article/pii/S0360544222014864.

[75] Koytsoumpa EI, Karellas S, Kakaras E. Modelling of Substitute Natural Gas production via combined gasification and power to fuel. Renew Energy 2019;135:1354–70. http://dx.doi.org/10.1016/j.renene.2018.09.064, URL https://www.sciencedirect.com/science/article/pii/S0960148118311273.

[76] Drechsler C, Agar DW. Intensified integrated direct air capture - power-to-gas process based on H2O and CO2 from ambient air. Appl Energy 2020;273:115076. http://dx.doi.org/10.1016/j.apenergy.2020.115076, URL https://www.sciencedirect.com/science/article/pii/S0306261920305882.

[77] Martínez I, Romano MC. Flexible sorption enhanced gasification (SEG) of biomass for the production of synthetic natural gas (SNG) and liquid biofuels: Process assessment of stand-alone and power-to-gas plant schemes for SNG production. Energy 2016;113:615–30. http://dx.doi.org/10.1016/j.energy.2016.07.026, URL https://www.sciencedirect.com/science/article/pii/S0360544216309501.

[78] Coppitters D, Costa A, Chauvy R, Dubois L, De Paepe W, Thomas D, De Weireld G, Contino F. Energy, exergy, economic and environmental (4E) analysis of integrated direct air capture and CO2 methanation under uncertainty. Fuel 2023;344:127969. http://dx.doi.org/10.1016/j.fuel.2023.127969, URL https://www.sciencedirect.com/science/article/pii/S0016236123005823.

[79] Perpiñán J, Bailera M, Peña B, Romeo LM, Eveloy V. Technical and economic assessment of iron and steelmaking decarbonization via power to gas and amine scrubbing. Energy 2023;276:127616. http://dx.doi.org/10.1016/j.energy.2023.127616, URL https://www.sciencedirect.com/science/article/pii/S0360544223010101.

[80] Peters R, Baltruweit M, Grube T, Samsun RC, Stolten D. A techno economic analysis of the power to gas route. J CO2 Util 2019;34:616–34. http://dx.doi.org/10.1016/j.jcou.2019.07.009, URL https://linkinghub.elsevier.com/retrieve/pii/S2212982019304731.

[81] Zhu H, Kee RJ, Janardhanan VM, Deutschmann O, Goodwin DG. Modeling elementary heterogeneous chemistry and electrochemistry in solid-oxide fuel cells. J Electrochem Soc 2005;152(12):A2427. http://dx.doi.org/10.1149/1.2116607, URL https://iopscience.iop.org/article/10.1149/1.2116607.

[82] Wehrle L, Schmider D, Dailly J, Banerjee A, Deutschmann O. Benchmarking solid oxide electrolysis cell-stacks for industrial Power-to-Methane systems via hierarchical multi-scale modelling. Appl Energy 2022;317:119143. http://dx.doi.org/10.1016/j.apenergy.2022.119143, URL https://www.sciencedirect.com/science/article/pii/S0306261922005190.

[83] Khan MI, Yasmin T, Shakoor A. Technical overview of compressed natural gas (CNG) as a transportation fuel. Renew Sustain Energy Rev 2015;51:785–97. http://dx.doi.org/10.1016/j.rser.2015.06.053, URL https://www.sciencedirect.com/science/article/pii/S1364032115006255.

[84] Sun L, Wang Y, Guan N, Li L. Methane activation and utilization: Current status and future challenges. Energy Technol 2020;8(8):1900826. http://dx.doi.org/10.1002/ente.201900826, URL https://onlinelibrary.wiley.com/doi/abs/10.1002/ente.201900826, _eprint: https://onlinelibrary.wiley.com/doi/pdf/10.1002/ente.201900826.

[85] Qi M, Liu Y, He T, Yin L, Shu C-M, Moon I. System perspective on cleaner technologies for renewable methane production and utilisation towards carbon neutrality: Principles, techno-economics, and carbon footprints. Fuel 2022;327:125130. http://dx.doi.org/10.1016/j.fuel.2022.125130, URL https://www.sciencedirect.com/science/article/pii/S0016236122019718.

[86] DIN EN 16726:2019-11, gasinfrastruktur_- beschaffenheit von gas_- gruppe_H; deutsche fassung EN_16726:2015+A1:2018. Tech. rep., Beuth Verlag GmbH, http://dx.doi.org/10.31030/2867769, URL https://www.beuth.de/de/-/-/292011490.

[87] Gröschl F. Daten und fakten gas-mobilität PKW, LKW, bus. 2018, URL https://www.dvgw.de/leistungen/publikationen/publikationsliste/daten-und-fakten-erdgasmobilitaet.

[88] Ebrahim M, Kawari A. Pinch technology: an efficient tool for chemical-plant energy and capital-cost saving. Appl Energy 2000;65(1):45–9. http://dx.doi.org/10.1016/S0306-2619(99)00057-4, URL https://www.sciencedirect.com/science/article/pii/S0306261999000574.

[89] Im-orb K, Arpornwichanop A. Comparative techno-economic assessment of bio-methanol and bio-DME production from oil palm residue. Energy Convers Manage 2022;258:115511. http://dx.doi.org/10.1016/j.enconman.2022.115511, URL https://www.sciencedirect.com/science/article/pii/S0196890422003077.

[90] Bou Malham C, Zoughaib A, Rivera Tinoco R, Schuhler T. Hybrid optimization methodology (exergy/pinch) and application on a simple process. Energies 2019;12(17):3324. http://dx.doi.org/10.3390/en12173324, URL https://www.mdpi.com/1996-1073/12/17/3324, Number: 17 Publisher: Multidisciplinary Digital Publishing Institute.

[91] Parra D, Zhang X, Bauer C, Patel MK. An integrated techno-economic and life cycle environmental assessment of power-to-gas systems. Appl Energy 2017;193:440–54. http://dx.doi.org/10.1016/j.apenergy.2017.02.063, URL https://www.sciencedirect.com/science/article/pii/S0306261917302064.

[92] Perna A, Moretti L, Ficco G, Spazzafumo G, Canale L, Dell'Isola M. SNG generation via power to gas technology: Plant design and annual performance assessment. Appl Sci 2020;10(23):8443. http://dx.doi.org/10.3390/app10238443, URL https://www.mdpi.com/2076-3417/10/23/8443, Number: 23 Publisher: Multidisciplinary Digital Publishing Institute.

[93] Deutz S, Bardow A. Life-cycle assessment of an industrial direct air capture process based on temperature–vacuum swing adsorption. Nat Energy 2021;6(2):203–13. http://dx.doi.org/10.1038/s41560-020-00771-9, URL http://www.nature.com/articles/s41560-020-00771-9.

[94] Zhao B, Liu F, Cui Z, Liu C, Yue H, Tang S, Liu Y, Lu H, Liang B. Enhancing the energetic efficiency of MDEA/PZ-based CO2 capture technology for a 650MW power plant: Process improvement. Appl Energy 2017;185:362–75. http://dx.doi.org/10.1016/j.apenergy.2016.11.009, URL https://www.sciencedirect.com/science/article/pii/S0306261916315951.

[95] Müller C, Ortloff F, Graf F. Final report of the baden-wurttemberg project Res2CNG - innovative production of SNG and CNG from biogenic waste and residues. 2018, URL https://pudi.lubw.de/detailseite/-/publication/92291.

[96] Wurzbacher JA, Gebald C, Brunner S, Steinfeld A. Heat and mass transfer of temperature–vacuum swing desorption for CO2 capture from air. Chem Eng J 2016;283:1329–38. http://dx.doi.org/10.1016/j.cej.2015.08.035, URL https://linkinghub.elsevier.com/retrieve/pii/S138589471501116X.

[97] Ibrahim AY, Ashour FH, Ghallab AO, Ali M. Effects of piperazine on carbon dioxide removal from natural gas using aqueous methyl diethanol amine. J Natl Gas Sci Eng 2014;21:894–9. http://dx.doi.org/10.1016/j.jngse.2014.10.011, URL https://www.sciencedirect.com/science/article/pii/S1875510014003102.

[98] Frailie PT. Modeling of carbon dioxide absorption/stripping by aqueous methyldiethanolamine/piperazine (Thesis), Austin: University of Texas; 2014, URL https://repositories.lib.utexas.edu/handle/2152/25019, [Accepted: 2014-07-03T20:58:39Z].

[99] Svensson H, Hulteberg C, Karlsson HT. Heat of absorption of CO2 in aqueous solutions of N-methyldiethanolamine and piperazine. Int J Greenh Gas Control 2013;17:89–98. http://dx.doi.org/10.1016/j.ijggc.2013.04.021, URL https://www.sciencedirect.com/science/article/pii/S1750583613002016.

[100] Bartholomew CH, Weatherbee GD, Jarvi GA. Sulfur poisoning of nickel methanation catalysts: I. in situ deactivation by H2S of nickel and nickel bimetallics. J Catal 1979;60(2):257–69. http://dx.doi.org/10.1016/0021-9517(79)90147-7, URL https://www.sciencedirect.com/science/article/pii/0021951779901477.

[101] Robinson VS. Process for desulfurization using particulate zinc oxide shapes of high surface area and improved strength. 1978, URL https://patents.google.com/patent/US4128619/en.

[102] Solarte-Toro JC, González-Aguirre JA, Poveda Giraldo JA, Cardona Alzate CA. Thermochemical processing of woody biomass: A review focused on energy-driven applications and catalytic upgrading. Renew Sustain Energy Rev 2021;136:110376. http://dx.doi.org/10.1016/j.rser.2020.110376, URL https://linkinghub.elsevier.com/retrieve/pii/S136403212030664X.

[103] García R, Pizarro C, Lavín AG, Bueno JL. Biomass sources for thermal conversion. Techno-economical overview. Fuel 2017;195:182–9. http://dx.doi.org/10.1016/j.fuel.2017.01.063, URL https://www.sciencedirect.com/science/article/pii/S0016236117300698.

[104] Anghilante R. Flexibilisation and integration of solid oxide electrolysis units in power to synthetic natural gas plants (Ph.D. thesis), Toulouse: Institut national polytechnique; 2020, URL http://www.theses.fr/2020INPT0094/document.

[105] Schmid M, Beirow M, Schweitzer D, Waizmann G, Spörl R, Scheffknecht G. Product gas composition for steam-oxygen fluidized bed gasification of dried sewage sludge, straw pellets and wood pellets and the influence of limestone as bed material. Biomass Bioenergy 2018;117:71–7. http://dx.doi.org/10.1016/j.biombioe.2018.07.011, URL https://linkinghub.elsevier.com/retrieve/pii/S0961953418301752.

[106] Koytsoumpa EI, Karellas S. Equilibrium and kinetic aspects for catalytic methanation focusing on CO2 derived Substitute Natural Gas (SNG). Renew Sustain Energy Rev 2018;94:536–50. http://dx.doi.org/10.1016/j.rser.2018.06.051, URL https://linkinghub.elsevier.com/retrieve/pii/S1364032118304878.

[107] Jensen JH, Poulsen JM, Andersen NU. From coal to clean energy. In: Nitrogen+syngas. Vol. 310, 2011, p. 34–8.

[108] Siegfried DB, Frank D-IG, Rainer PDR. Methansynthese in einem Blasensäulenreaktor. 2012, URL https://patents.google.com/patent/DE102011009163A1/en?oq=three+phase+methanation.

[109] Lefebvre J, Götz M, Bajohr S, Reimert R, Kolb T. Improvement of three-phase methanation reactor performance for steady-state and transient operation. Fuel Process Technol 2015;132:83–90. http://dx.doi.org/10.1016/j.fuproc.2014.10.040, URL https://www.sciencedirect.com/science/article/pii/S0378382014004640.

[110] Lefebvre J, Bajohr S, Kolb T. A comparison of two-phase and three-phase CO2 methanation reaction kinetics. Fuel 2019;239:896–904. http://dx.doi.org/10.1016/j.fuel.2018.11.051, URL https://linkinghub.elsevier.com/retrieve/pii/S0016236118319379.

[111] Sauerschell S, Bajohr S, Kolb T. Methanation pilot plant with a slurry bubble column reactor: Setup and first experimental results. Energy Fuels 2022;36(13):7166–76. http://dx.doi.org/10.1021/acs.energyfuels.2c00655, URL https://doi.org/10.1021/acs.energyfuels.2c00655, Publisher: American Chemical Society.

[112] Riedel M, Heddrich M, Ansar A, Fang Q, Blum L, Friedrich K. Pressurized operation of solid oxide electrolysis stacks: An experimental comparison of the performance of 10-layer stacks with fuel electrode and electrolyte supported cell concepts. J Power Sources 2020;475:228682. http://dx.doi.org/10.1016/j.jpowsour.2020.228682, URL https://linkinghub.elsevier.com/retrieve/pii/S0378775320309861.

[113] Nechache A, Hody S. Alternative and innovative solid oxide electrolysis cell materials: A short review. Renew Sustain Energy Rev 2021;149:111322. http://dx.doi.org/10.1016/j.rser.2021.111322, URL https://www.sciencedirect.com/science/article/pii/S1364032121006080.

[114] Kusnezoff M, Trofimenko N, Müller M, Michaelis A. Influence of electrode design and contacting layers on performance of electrolyte supported SOFC/SOEC single cells. Materials 2016;9(11):906. http://dx.doi.org/10.3390/ma9110906, URL https://www.mdpi.com/1996-1944/9/11/906, Number: 11 Publisher: Multidisciplinary Digital Publishing Institute.
[115] Léon A, Micero A, Ludwig B, Brisse A. Effect of scaling-up on the performance and degradation of long-term operated electrolyte supported solid oxide cell, stack and module in electrolysis mode. J Power Sources 2021;510:230346. http://dx.doi.org/10.1016/j.jpowsour.2021.230346, URL https://www.sciencedirect.com/science/article/pii/S0378775321008582.
[116] Chelmehsara ME, Mahmoudimehr J. Techno-economic comparison of anode-supported, cathode-supported, and electrolyte-supported SOFCs. Int J Hydrog Energy 2018;43(32):15521–30. http://dx.doi.org/10.1016/j.ijhydene.2018.06.114, URL https://linkinghub.elsevier.com/retrieve/pii/S0360319918319864.
[117] Deutschmann O, Tischer S, S K, Janardhanan V, Correa C, Chatterjee D, Mladenov N, Minh HD, Karadeniz H, Hettel M, Menon V, Banerjee A, Gossler H, Shirsath A, E D. DETCHEM. 2022, URL https://www.detchem.com.
[118] PROMALIGHT: Rigid microporous insulation boards, URL https://www.promat.com/en/industry/products-solutions/high-temperature-insulation/rigid-panels/promalight/.
[119] Aguiar P, Adjiman CS, Brandon NP. Anode-supported intermediate-temperature direct internal reforming solid oxide fuel cell: II. Model-based dynamic performance and control. J Power Sources 2005;147(1):136–47. http://dx.doi.org/10.1016/j.jpowsour.2005.01.017, URL https://www.sciencedirect.com/science/article/pii/S0378775305001473.
[120] Udagawa J, Aguiar P, Brandon NP. Hydrogen production through steam electrolysis: Model-based steady state performance of a cathode-supported intermediate temperature solid oxide electrolysis cell. J Power Sources 2007;166(1):127–36. http://dx.doi.org/10.1016/j.jpowsour.2006.12.081, URL https://www.sciencedirect.com/science/article/pii/S0378775307001103.
[121] Motylinski K, Wierzbicki M, Kupecki J, Jagielski S. Investigation of off-design characteristics of solid oxide electrolyser (SOE) operating in endothermic conditions. Renew Energy 2021;170:277–85. http://dx.doi.org/10.1016/j.renene.2021.01.097, URL https://www.sciencedirect.com/science/article/pii/S096014812100104X.
[122] Chen H, Wang J, Xu X. Parametric study of operating conditions on performances of a solid oxide electrolysis cell. J Therm Sci 2023. http://dx.doi.org/10.1007/s11630-023-1772-4.
[123] Kim S-D, Seo D-W, Dorai AK, Woo S-K. The effect of gas compositions on the performance and durability of solid oxide electrolysis cells. Int J Hydrog Energy 2013;38(16):6569–76. http://dx.doi.org/10.1016/j.ijhydene.2013.03.115, URL https://www.sciencedirect.com/science/article/pii/S0360319913007556.
[124] Gülich JF. Kreiselpumpen: Handbuch für entwicklung, anlagenplanung und betrieb. 4th ed.. Berlin [u.a.]: Springer; 2013.
[125] Koh J-H, Seo H-K, Lee CG, Yoo Y-S, Lim HC. Pressure and flow distribution in internal gas manifolds of a fuel-cell stack. J Power Sources 2003;115(1):54–65. http://dx.doi.org/10.1016/S0378-7753(02)00615-8, URL https://www.sciencedirect.com/science/article/pii/S0378775302006158.
[126] Belviso C. Zeolites - useful minerals. Rijeka: InTechOpen; 2016.
[127] PDFO - Powell's derivative-free optimization solvers, URL https://www.pdfo.net/.
[128] Powell MJD. Developments of NEWUOA for minimization without derivatives. IMA J Numer Anal 2008;28(4):649–64. http://dx.doi.org/10.1093/imanum/drm047.
[129] Powell MJD. A direct search optimization method that models the objective and constraint functions by linear interpolation. In: Gomez S, Hennart J-P, editors. Advances in optimization and numerical analysis. Mathematics and its applications, Dordrecht: Springer Netherlands; 1994, p. 51–67. http://dx.doi.org/10.1007/978-94-015-8330-5_4.
[130] Nelder JA, Mead R. A simplex method for function minimization. Comput J 1965;7(4):308–13. http://dx.doi.org/10.1093/comjnl/7.4.308.
[131] Henke M, Willich C, Kallo J, Friedrich KA. Theoretical study on pressurized operation of solid oxide electrolysis cells. Int J Hydrog Energy 2014;39(24):12434–9. http://dx.doi.org/10.1016/j.ijhydene.2014.05.185, URL https://www.sciencedirect.com/science/article/pii/S0360319914016012.
[132] Terlouw T, Treyer K, Bauer C, Mazzotti M. Life cycle assessment of direct air carbon capture and storage with low-carbon energy sources. Environ Sci Technol 2021;55(16):11397–411. http://dx.doi.org/10.1021/acs.est.1c03263, Publisher: American Chemical Society.
[133] U.S. Department of Commerce N. Global monitoring laboratory - carbon cycle greenhouse gases. 2023, URL https://gml.noaa.gov/ccgg/trends/.
[134] Wang L, Chen M, Küngas R, Lin T-E, Diethelm S, Maréchal F, Van herle J. Power-to-fuels via solid-oxide electrolyzer: Operating window and techno-economics. Renew Sustain Energy Rev 2019;110:174–87. http://dx.doi.org/10.1016/j.rser.2019.04.071, URL https://www.sciencedirect.com/science/article/pii/S1364032119302928.
[135] Sohal MS, Herring JS. Oxygen handling and cooling options in high temperature electrolysis plants. Tech. rep. INL/EXT-08-14483, Idaho National Lab. (INL), Idaho Falls, ID (United States); 2008, http://dx.doi.org/10.2172/936626, URL https://www.osti.gov/biblio/936626.
[136] Yang Y, Tong X, Hauch A, Sun X, Yang Z, Peng S, Chen M. Study of solid oxide electrolysis cells operated in potentiostatic mode: Effect of operating temperature on durability. Chem Eng J 2021;417:129260. http://dx.doi.org/10.1016/j.cej.2021.129260, URL https://www.sciencedirect.com/science/article/pii/S1385894721008494.
[137] Fasihi M, Efimova O, Breyer C. Techno-economic assessment of CO2 direct air capture plants. J Clean Prod 2019;224:957–80. http://dx.doi.org/10.1016/j.jclepro.2019.03.086, URL https://www.sciencedirect.com/science/article/pii/S0959652619307772.
[138] Chauvy R, Verdonck D, Dubois L, Thomas D, De Weireld G. Techno-economic feasibility and sustainability of an integrated carbon capture and conversion process to synthetic natural gas. J CO2 Util 2021;47:101488. http://dx.doi.org/10.1016/j.jcou.2021.101488, URL https://www.sciencedirect.com/science/article/pii/S221298202100055X.
[139] Coppitters D, Costa A, Dubois L, Thomas D, Weireld GD, Contino F. Robust integration of direct air capture in power-to-methane systems: techno-economic feasibility study under uncertainty. In: Proceedings of ECOS 2022 35th International conference on efficiency, cost, optimization, simulation and environmental impact of energy systems. Vol. 35, 2022, p. 1497.
[140] Furst O, Wehrle L, Schmider D, Dailly J, Deutschmann O. Systematic determination of optimal design-points of fully integrated power-to-SNG process chains via detailed simulation of SOEC stacks. ECS Trans 2023;111(6):1965. http://dx.doi.org/10.1149/11106.1965ecst, URL https://iopscience.iop.org/article/10.1149/11106.1965ecst/meta, Publisher: IOP Publishing.

List of Figures

List of Publications and Presentations

Journal Publications

1. **O. Furst**, L. Wehrle, D. Schmider, J. Dailly, O. Deutschmann: Systematic Determination of Optimal Design-Points of Fully Integrated Power-to-SNG Process Chains Via Detailed Simulation of SOEC Stacks, *ECS Transactions*, **2023**, 111, 1965-1973.
DOI: 10.1149/11106.1965ecst
2. **O. Furst**, O. Deutschmann: Development and calibration of a fast flow model for solid oxide cell stack internal manifolds, *Journal of Power Sources*, **2024**, 613, 234857.
DOI: 10.1016/j.jpowsour.2024.234857
3. **O. Furst**, L. Wehrle, D. Schmider, J. Dailly, O. Deutschmann: Modeling, optimization and comparative assessment of power-to-methane and carbon capture technologies for renewable fuel production, *Applied Energy*, **2024**, 375, 123972.
DOI: 10.1016/j.apenergy.2024.123972
4. **O. Furst**, O. Deutschmann: A versatile multi-scale framework for transient simulations of solid oxide cells and stack modules integrated in DETCHEM, *Journal of The Electrochemical Society*, **2025**, 172, 074508.
DOI: 10.1149/1945-7111/ade56d
5. F. Ehrlich, A. Ashar, **O. Furst**, P. Blanck, H. Zhu, R.J. Kee, R.J. Braun, O. Deutschmann: Theoretical Insights into Equilibrium Potentials in Electrochemical Cells with Multiple Mobile Charge Carriers, *Journal of The Electrochemical Society*, **2025**.
DOI: 10.1149/1945-7111/ae2959

Oral Presentations

1. **O. Furst**, L. Wehrle, D. Schmider, J. Dailly, O. Deutschmann: Systematic Determination of Optimal Design-Points of Fully Integrated Power-to-SNG Process Chains Via Detailed Simulation of SOEC Stacks, *SOFC: Eighteenth International Symposium on Solid Oxide Fuel Cells (SOFC-XVIII)*, Boston, USA, 01.06.2023.
2. **O. Furst**, O. Deutschmann: Computationally inexpensive solid oxide cell stack internal manifold flow model, *European Fuel Cell Forum 2024*, Lucerne, Switzerland, 05.07.2024.
3. **O. Furst**, D. Schmider, J. Dailly, O. Deutschmann: Comparative assessment of power-to-methane technologies for sustainable synthetic natural gas production, *International Conference on Environmental Catalysis*, Isola delle Femmine, Italy, 05.06.2025.

Poster Presentations

1. **O. Furst**, L. Wehrle, D. Schmider, J. Dailly, O. Deutschmann: Systematic determination of optimal design-points of fully integrated Power-to-SNG process chains via detailed simulation of SOEC stacks, *Annual Meeting on Reaction Engineering 2023*, Frankfurt am Main, Germany, 15–17.05.2023.

2. **O. Furst**, O. Deutschmann: Development and calibration of a computationally inexpensive solid oxide cell stack internal manifold flow model, *Annual Meeting on Reaction Engineering 2024*, Würzburg, Germany, 06–08.05.2023.
3. **O. Furst**, O. Deutschmann: Numerical investigation of the influence of flow maldistribution on the performance of metal-supported solid oxide fuel cell stacks, *DECHEMA FORUM 2024*, Friedrichshafen, Germany, 11–13.09.2024.
4. P. Blanck, **O. Furst**, J. Dailly, O. Deutschmann: Electrochemically Enhanced Low-temperature Catalytic Ammonia Synthesis, *European Fuel Cell Forum 2024*, Lucerne, Switzerland, 02–05.07.2024.
5. F. Ehrlich, **O. Furst**, O. Deutschmann: Proton ceramic fuel cell stack simulations with three mobile charge carriers, *European Fuel Cell Forum 2024*, Lucerne, Switzerland, 02–05.07.2024.
6. **O. Furst**, O. Deutschmann: A hybrid surrogate and physical modeling methodology for accelerated solid oxide cell stack simulations, *Annual Meeting on Reaction Engineering*, Würzburg, Germany, 26–28.05.2025.
7. **O. Furst**, O. Deutschmann: Multiscale Simulation of a Solid Oxide Electrolysis Cell Stack: Evaluating the Influence of a Manifold on the Performance, *ModVal 2025 - 21st Symposium on Modeling and Experimental Validation of Electrochemical Energy Technologies*, Karlsruhe, Germany, 10–12.03.2025.